WELD CORROSION IN THIN CO_2-CONTAINING SOLUTION LAYERS

BY

RACHEL ADAMS

A THESIS SUBMITTED TO THE UNIVERSITY OF MANCHESTER INSTITUTE OF SCIENCE AND TECHNOLOGY FOR THE DEGREE OF DOCTOR OF PHILOSOPHY

SEPTEMBER 2002

Declaration

I declare that the work referred to in this thesis has not been submitted in support of an application of any other degree or qualification for this or any other institute of learning.

Rachel Adams

September 2002

Acknowledgements

The author would like to thank the following for their contribution, directly and indirectly, to the work leading to the completion of this thesis:

Dr Stephen Turgoose for his supervision and advice.

EPSRC, Total Technology and BP for their financial support.

The Sponsor Group for the informative meetings.

The staff of the Corrosion and Protection Centre for sharing their knowledge and providing practical assistance.

The students of the Corrosion and Protection Centre, especially Tony, for camaraderie, advice and entertainment.

My family and friends who like corrosion and those who don't care for it.

My employer, Serco Assurance, for their cooperation.

Mostly Sean, for his constant reassurance and support.

WELD CORROSION IN THIN CO_2-CONTAINING SOLUTION LAYERS

Preferential weldment corrosion in low-alloy steel oil and gas production flowlines and other equipment in the presence of CO_2 and saline solutions has been recognised as a persistent problem.

Previously, it was thought that adding small quantities of nobler elements such as Ni to the filler metal would prevent selective attack of weldment components by creating a cathodic weld metal and thus ensuring a small difference in rest potential (ΔE) between the weld and parent metals in CO_2 environments. Although this approach has proved effective, it has been found that preferential corrosion has occurred in weldments that are virtually identical to others that corrode acceptably in service. It is thought that this is due to the small quantities of Ni increasing the corrosion rate of the low-alloy steel.

A one-dimensional mathematical model was used, based on De Levie's transmission line theory, as a novel approach to the problem. The model is intended to show the current and potential distributions and local corrosion rates of weld and parent metals. The galvanic current between the weld and parent metals has been shown to decrease as the solution thickness is reduced on the surface of the weldment. This lowering of solution thickness has the effect of increasing the solution resistance and therefore decoupling the weld and parent metals, allowing them to corrode at their own intrinsic rates. It is possible to use the model to predict preferential attack in thin liquid films from measurements taken in bulk solutions.

Work was performed using two electrodes; an "artificial" weld and parent metals – low-alloy steels typically in common usage as parent base pipe and a "filler" metal that was slightly higher in alloying additions and a weldment specimen (Waveney) that had actually undergone preferential corrosion whilst in service.

The segmented weldment electrodes were tested in an electrochemical cell designed with a moveable spacer to adjust the liquid layer thickness. The galvanic current and potential behaviour of the weld and parent metals were studied using a zero resistance ammeter (ZRA). Polarization resistance (LPR) and ac impedance measurements were used to study local corrosion rates and non-uniformity of applied current along the length of the weld and parent components. The solutions used were NaCl of varying, mostly low, molarities and NaCl-free water (the Artificial electrode) purged with CO_2.

The effects of long-term coupling and surface analysis using SEM-EDX were also studied using coupons fabricated from the weld and parent metals of the actual weldment failure.

It has been possible to predict galvanic current behaviour and demonstrate that potential distributions, effective solution resistances and polarisation resistances can be approximated for both the weld and parent components on the Artificial electrode. But the approximations were only applicable to the parent (long) component of the Waveney electrode. This was due to the former having lower inherent solution conductivity and a larger potential difference between the weld and parent metals.

Flattening of the complex plots at high frequency was recorded in the ac impedance tests of the weld and parent components in low solution thicknesses, similar to plots of De Levie's porous electrodes, further validating the model.

Also, galvanic current monitoring suggests that long-term coupling creates a different surface on an electrode than if it remained uncoupled.

Contents

1.0 Introduction

Corrosion of carbon and low-alloy steel pipelines through weldment corrosion is a common and expensive concern of the oil and gas industry. It is not surprising to find that, although the base alloy may be resistant to corrosion in a specific environment, the welded counterpart is not, and it can often be as costly to repair the corroded weldment, as it is to replace the whole section of pipeline that is affected. There have been many investigations on the subject since early this century. The majority of preferential weld corrosion work has involved the heat-affected zone (HAZ) in the last 25 years and earlier work seems to be more widely concerned with weld metals that were anodic with respect to the parent metal. It has been established in many investigations that microstructures, formed via the welding process, have caused HAZ and weld metal corrosion because they are cathodic relative to the surrounding alloy and behaved like microcathodes. The anodic weld metal problem can be remedied, in most environments, by adding small quantities of nobler elements to the filler with the intention of the parent metal becoming a large anode to a small cathode. Other procedures to prevent weldment corrosion include preheating and postheating areas to be welded, slow-cooling and the addition of corrosion inhibitors to the oil/gas and water passing through the pipeline.

It has become apparent that some pipelines have suffered preferential corrosion in some weldments but other, apparently similar, weldments in the same pipeline have not undergone such attack. The contents of the pipelines are obviously the same; water, oil, gas, sodium chloride with dissolved and gaseous CO_2.

A mathematical model has been suggested that involves considering the thickness of the solution on the surface of the weldment. If the thickness of the solution on the metal surface is halved, the solution resistance will double and this can cause effective decoupling of the parent metals from the weld metal. The solution conductivity is a critical factor, in lower conductivity solutions the attack is more prominent in the weld centre and at the weld and parent interface, whilst in more conducting solutions the attack in these areas is less concentrated. The model also considers that although the weld may be cathodic with respect to the parent metal, its intrinsic corrosion rate may be greater than that of the parent. If the weld and parent are

decoupled, the parent and weld metals will corrode at their own rates; hence the centre of the weld will suffer metal loss more rapidly than the parent, resulting in the failure of the weldment. The two interfaces of the metals may also suffer severe preferential corrosion due to galvanic current, restricted by high solution resistance (or low "throwing-power") and concentrating attack on the fusion line.

Using the mathematical model it is possible, knowing the potential and Rp values of the individual weldment components and the solution resistance to predict whether the weldment will undergo preferential attack. The model may be applicable to other relevant systems, but this work has remained within the scope of an oil or gas flowline using NaCl solutions of varying concentration, saturated with CO_2 and often with HCO_3^{2-} added, intended to be typical of formation/produced water.

An "Artificial" weldment electrode was constructed from low-alloy steels typically used as weld and parent metals, and tests were performed using very low conductivity solutions. A weldment from an actual preferential corrosion failure, the Waveney spoolpiece, was tested in solution that was representative of the service environment. The electrodes consisted of 4.5 to 6 cm lengths of parent metal either side of 1 to 3 cm weld metals. Luggin probes were situated along the length of the parent and weld metals to monitor potential and galvanic current and the solution thickness (or liquid film thickness) was adjusted from outside a modified electrochemical cell via a side-arm.

Aspects of the model were investigated using linear polarisation resistance, ac impedance and zero resistance ammetry. The potential behaviour of long electrodes and how this is analogous with similar behaviour of porous electrodes and the galvanic current changes with varying solution thickness on the surface of segmented electrodes was studied. The effects of long term coupling on the potential and galvanic current of weld and parent metals in segmented electrodes led to further tests using weld and parent metal coupons and coupons were also examined to study the surface chemical compositions of the weld and parent metals using SEM-EDX.

2.0 Fundamentals of Corrosion

This chapter will explain the nature of aqueous corrosion using thermodynamics and kinetics. The metallurgical character of relevant materials susceptible to corrosion and corrosion rate measurement techniques are included. Previous work regarding weldment corrosion in oil and gas pipelines, CO_2 corrosion and the effect of alloying elements in low-alloy steels is reviewed. This is followed by a summary of the study of porous electrodes by De Levie, and its relevance to the mathematical model.

2.1 Thermodynamics of Corrosion in Aqueous Solutions[1]

Thermodynamics is the study of energy changes. This is useful in the study of corrosion as it can predict the state of equilibrium in a metal/solution system.

2.1.1 Free Energy

The free energy change is a measure of the maximum electrical energy from the system. The free energy ($\Delta G°$) is calculated from the standard energies of the reactants and indicates the direction of the reaction. In a closed system, a negative free energy ($-\Delta G$) would be an energetically favourable reaction and if positive, the reaction would require the input of energy to proceed.

The free energy states of all corrosion reactions are dependent on temperature and concentration it is therefore necessary to use the following equation to calculate ΔG:

$$\Delta G = \Delta G° + RT \ln K \qquad \textbf{2.1}$$

Where $\Delta G°$ is the free energy change in standard conditions, R is the gas constant (8.31 $Jmol^{-1}K^{-1}$), T is the absolute temperature and K is the activity product. K can be determined from the following reaction:

$$aA + bB \rightarrow cC + dD \qquad \textbf{2.2}$$

It can be calculated thus:

$$K = \frac{[C]^c[D]^d}{[A]^a[B]^b} \qquad 2.3$$

The free energy involved in an electrochemical reaction can be calculated using:

$$\Delta G^\circ = -nFE \qquad 2.4$$

Where n is the number of electrons involved in the reaction, F, is the Faraday constant and E is the equilibrium potential.

2.1.2 Cell Potentials

The change in free energy can be calculated using equilibrium potentials of reactions as Equation 2.4 illustrates. A reversible electrochemical cell as in the copper and zinc equation below indicates that the cell has equilibrium and is at unit activity.

$$Cu + Zn^{2+} = Cu^{2+} + Zn \qquad 2.5$$

This reaction is a summation of the two half reactions:

$$Cu = Cu^{2+} + 2e \qquad 2.6$$

And

$$Zn^{2+} + 2e = Zn \qquad 2.7$$

There is a potential difference between the zinc and copper electrodes of 1.1V, which is used to determine the free energy of the overall electrochemical reaction. The electrode potentials of individual half-cells are measured against the hydrogen-hydrogen ion reaction (Equation 2.8), which has an electrode potential of 0V.

$$2H^+ + 2e = H_2 \qquad 2.8$$

A platinum electrode may be used to determine the half-cell, emf or redox potential because it provides an inert solid surface for the reduction and oxidation of hydrogen to take place, as it is not possible to make an electrode from hydrogen gas.

The individual redox potentials can be used to calculate numerous electrochemical cell potentials at unit activity and 25°C.

The Nernst equation is used to find the potential of an electrochemical reaction when it is not at unit activity.

$$E = E° + 2.3\frac{RT}{nF}\log\frac{a_{oxid}}{a_{red}} \qquad \textbf{2.9}$$

Where E is the half-cell potential, E° is the half-cell potential at unit activity, R is the gas constant, T is the absolute temperature, n the number of electrons transferred, F is the Faraday constant and a_{oxid} and a_{red} are the activities of the oxidised and reduced species. The Nernst equation clearly shows that as the oxidised species increases, the half-cell potential will become more positive.

2.1.3 Corrosion Prediction using Thermodynamics

Although there is a relationship between free-energy change and cell potential the magnitude of the free-energy change is fairly unimportant when applied to corrosion prediction. The sign of the energy change is all that is required from Equation 2.4 to suggest that a reaction can or cannot take place.

A table of standard redox potentials can be used to predict the spontaneous direction of an electrochemical reaction. The most negative or active half-cell tends to be oxidised and the more positive or noble half-cell will tend to be reduced.

It can be predicted from the redox potentials of metals whether they will corrode in acid solutions or remain noble. If the reversible potential is more negative than that of hydrogen then they may spontaneously react but those more noble will not. If a solution has oxygen present then metals less noble than the O_2/H_2O reaction may also corrode as the half-cell potentials in Table 2.1 show.

Table 2.1 Standard redox potentials of selected half-cells.[2]

Standard half-cell reaction	E°/V (vs. NHE)
$Au \rightarrow Au + 3e^-$	+ 1.4
$O_2 + 4H^+ + 4e^- \rightarrow 2H_2O$	+ 1.23
$Cu \rightarrow Cu^{2+} + 2e^-$	+ 0.34
$H_2 \rightarrow 2H^+ + 2e^-$	0.0
$Fe \rightarrow Fe^{2+} + 2e^-$	- 0.44

It is imperative to remember that the half-cell potentials are stated at unit activities and changes in concentration will alter these values and it is therefore necessary to perform Nernst calculations for non-standard conditions. Pourbaix[3] prepared potential-pH plots (Pourbaix diagrams) using Nernst calculations and solubility data for various metal compounds (Figure 2.1). The diagrams show the most thermodynamically stable forms of the metal over the pH and potential range.

Pourbaix diagrams are mainly used for 1) predicting whether a spontaneous reaction will occur, 2) estimating what the corrosion product of the metal might be and 3) predicting environmental conditions that may cause or prevent corrosion of the metal.

They have the same limitations as thermodynamic calculations in that one cannot extract kinetic information from them. Also they fail to account for microstructures in the metal, aggressive ions, which might attack a passivated metal surface, and they cannot be applied to alloys. However Pourbaix diagrams give useful generalised information about the behaviour of metals in aqueous environments.

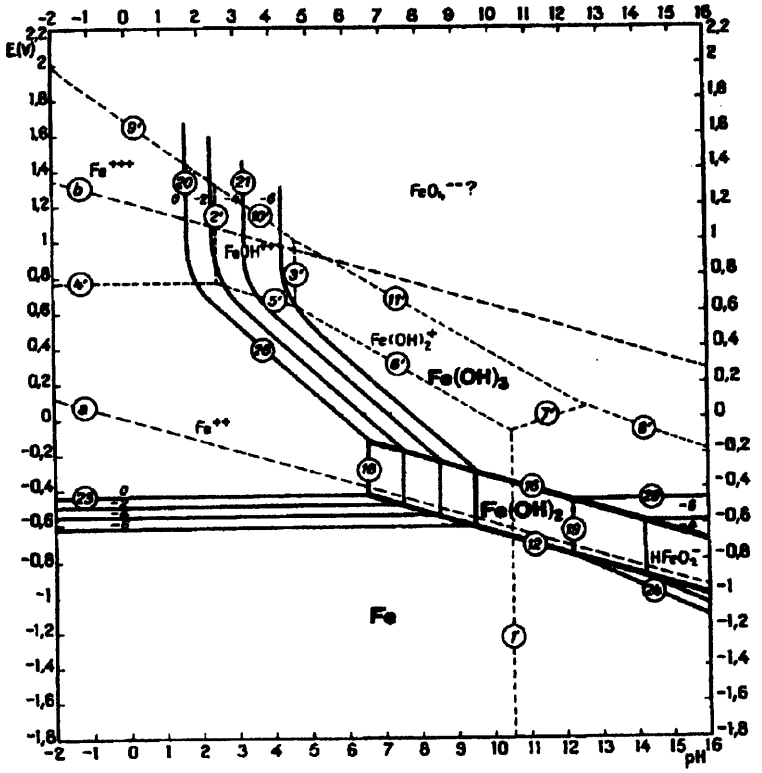

Figure 2.1 Potential-pH diagram for the iron-water system, at 25°C (Fe, $Fe(OH)_2$ and $Fe(OH)_3$).[3]

2.2 Reaction Kinetics

In order to manage corrosion, being able to predict the corrosion rate of a metal is essential. Corroding systems are not at equilibrium therefore thermodynamics cannot be used. Corrosion is observed when two cells at their equilibrium potential, E°, are short-circuited. The circuit enables electrons to flow from the more active cell or *anode* to the more noble or *cathode*. At the anode net oxidation of the metal occurs and at the cathode net reduction.

2.2.1 Kinetics of Activation Controlled Reactions

The rates of forward and reverse anodic reactions are equal at the equilibrium potential, $E°_a$. Away from the equilibrium potential, the magnitude of the polarisation is dictated by the overpotential (η), the difference between the applied potential and the equilibrium potential ($E - E°_a$). The Butler-Volmer Equation (2.10) gives the net anodic current, i_{net} at a given overpotential.

$$i_{net} = i_a - i_{ac} = i_{0,a}\left[\exp(\frac{\alpha\eta nF}{RT}) - \exp\frac{((1-\alpha)\eta nF)}{RT}\right] \qquad \textbf{2.10}$$

In Equation 2.10, $i_{o,a}$ is the exchange current density, the rate of the current densities of the forward (i_a) and reverse (i_{ac}) anodic reactions at equilibrium. α is a symmetry coefficient that reflects the way the forward and reverse reactions are influenced by the applied potential. The first term in the equation shows how the anodic reaction increases with the exponential of the positive overpotential and the second term indicates how the cathodic reaction increases with the negative overpotential. It follows that at high positive overpotentials the cathodic term in the equation can be omitted since cathodic current is negligible. Equation 2.10 then becomes:

$$i = i \circ \exp\frac{(B\eta nF)}{RT} \qquad \textbf{2.11}$$

Taking logarithms the equation becomes:

$$\ln i_a = \ln i_0 + \frac{(B\eta nF)}{RT} \qquad \textbf{2.12}$$

2.2.2 Activation Polarisation[4]

If the surface concentration of ions in solution does not differ appreciably from that in the bulk solution then the Butler-Volmer equation is used to calculate the net current. Assuming there are no mass-transfer effects, any overpotential will affect the activation energy for the redox process as reflected by the current. The lower the exchange current density for a system, the slower the reaction sequence and hence the larger the activation overpotential for the specific net current. The relationship between activation overpotential, η_a, and the effect on the anodic process is obtained from Equation 2.12 by rearranging and converting to the base 10 giving:

$$\eta_a = b_a \log_{10}\left(\frac{i_a}{i_0}\right) \qquad \textbf{2.13}$$

The anodic Tafel constant, b_a, is derived from:

$$b_a = \frac{2.303RT}{BnF} \qquad \textbf{2.14}$$

In a similar way the term for negative overpotentials in Equation 2.10 giving the cathodic Tafel constant can be defined thus:

$$b_c = \frac{2.303RT}{(1-B)nF} \qquad \textbf{2.15}$$

2.2.3 Concentration Polarisation

A high oxidation and reduction rate can lead to a concentration gradient in the solution, the surface of the electrode being depleted of oxidising species. If the rate of reduction is increased further then a limiting rate is reached which depends on the diffusion, migration and convection of the oxidising species to the electrode surface. This is known as concentration polarisation.

If the exchange current density is very large then the system may be able to supply the mass transfer limited current because the activation overpotential is very small, but the application of an overpotential to drive the reaction will also result in a limiting current density.

The limiting diffusion current density (i_{lim}), the maximum rate of reduction in a system is given by:

$$i_{\lim} = \frac{DnFC_B}{x} \qquad \textbf{2.16}$$

D is the diffusion coefficient of the reductant species, C_B is the concentration of the reductant species in the bulk solution and x is the diffusion-layer thickness. Agitation, the system geometry and the dimensions of the electrode influence the diffusion layer thickness. These factors will increase the limiting current diffusion

density because they reduce the diffusion-layer thickness. The movement of ions in one dimension in solution is governed by the Nernst-Planck equation:

$$J(x) = -D\frac{\partial C(x)}{\partial x} - \frac{nF}{RT}DC\frac{\partial \phi(x)}{\partial x} + Cv(x) \qquad \textbf{2.17}$$

Where $J(x)$ is the flux of ions (mol $s^{-1}cm^{-2}$), $\partial C(x)/\partial x$ is the concentration gradient across the diffusion layer, $\partial \phi(x)/\partial(x)$ is the potential gradient, due to electrostatic forces and $v(x)$ is the velocity (cm s^{-1}) of the solution moving in a one-dimensional axis. Ficks first law can be applied to electrochemistry to illustrate the diffusion of a chemical species in a solution:

$$J = -D\frac{\partial C}{\partial x} = \frac{i}{nF} \qquad \textbf{2.18}$$

Ficks first law states that the current at the electrode is related to the concentration gradient of the chemical species in the electrolyte near the electrode surface. It can be seen that Ficks law has been applied to produce Equation 2.16 to obtain the limiting diffusion current density.

The equation if there is only concentration polarization in a system is given as:

$$\eta_c = 2.3\frac{RT}{nF}\log\left(1 - \frac{i}{i_{lim}}\right) \qquad \textbf{2.19}$$

The overall reaction with both activation and concentration polarization is a combination of Equations 2.13 and 2.19:

$$\eta = -b_c \log_{10}\left(\frac{i_c}{i_0}\right) + b_c \log\left(1 - \frac{i}{i_{lim}}\right) \qquad \textbf{2.20}$$

2.3 Mixed Potentials[5]

Mixed potential theory is based on two factors; an electrochemical reaction consists of two partial redox reactions and during the electrochemical reaction there will be no net accumulation of charge, i.e. the rate of reduction must equal the rate of oxidation.

2.3.1 Mixed Electrodes

When an electrode is in contact with two or more redox systems, the net reduction and oxidation reactions of the individual systems are removed from their equilibrium values.

The E_{corr} value is found by determining the point where the net anodic and cathodic reactions intercept using an E-*log i* diagram. At this point the corresponding E value is E_{corr} and i_{corr} is obtained, as current density (A/cm^2) from the other axis. At E_{corr} the law of conservation of matter is apparent in that every two electrons from the release of a metal ion (Fe^{2+} for instance) one H_2 molecule is formed (in the case of the hydrogen evolution reaction, HER).

In more complicated systems, such as with the addition of ferric ions to oxidise the metal electrode, the sum of the oxidation currents equals the overall oxidation rate. Similarly the overall reduction rate of the system can be obtained from all the reduction reactions taking place. Once again, at E_{corr}, the sum of the reduction is equal to that of the oxidation occurring in the whole system.

2.4 Passivity

Passivity is a very useful phenomenon in terms of engineering. Passivation is observed in iron and other metals such as nickel and chromium, which is one reason why these metals are so beneficial when constituents of alloys.

The passive current density is independent of the applied potential, and it is observed that metal dissolution is significantly reduced. Polarisation curves can identify the region of passivity of a metal/alloy when a potentio-dynamic sweep is performed on the specimen. A polarisation curve will also show the active and transpassive regions as a plot of log current density versus potential.

The film formed on iron and its alloys in oxygenated environments reducing current density is an oxide film (Fe_2O_3). This occurs by a solid-state reaction at the metal-electrolyte interface.[6] The mechanism can be described as the transfer of protons from the water molecules adsorbed on the metal surface to the bulk solution leaving O^{2-} ions forming a monolayer with the metallic cations from the lattice. The metal cations continue to migrate and react with the also migrating O^{2-} ions supplied by the proton loss from the adsorbed water molecules. The oxide film grows inhibiting further metal dissolution in the passive region.

2.5 Linear Polarisation Resistance[1]

It has been observed in many corroding systems[7] that when the overpotential is the region of approximately ± 0.01V of E_{corr} the curve of a plot of η versus i_{net} is nearly linear (Figure 2.2). This has enabled linear polarisation resistance (LPR) to be a relatively accurate and rapid technique for measuring corrosion rates.

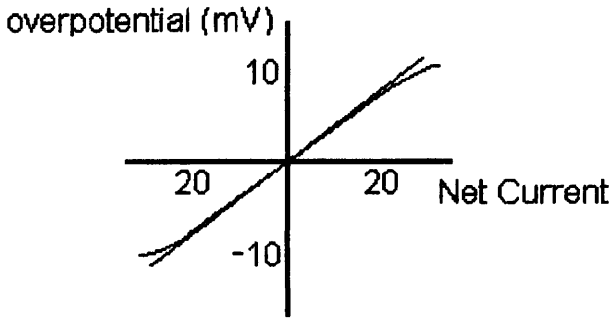

Figure 2.2 Overpotential against applied current for linear polarisation resistance measurements.

An equation derived from the Butler-Volmer Equation, 2.10, and Equations 2.14 and 2.15 can be used to determine the polarisation resistance, Rp, value thus:

$$Rp = \frac{b_a b_c}{2.3(i_{corr})(b_a + b_c)} \qquad \textbf{2.21}$$

Where:

$$Rp = \frac{\Delta\eta}{i_{net}} \qquad \textbf{2.22}$$

The i_{corr} value can be calculated using the Stern-Geary coefficient, B, and therefore the corrosion rate can be calculated thus.

$$i_{corr} = \frac{B}{Rp} \qquad \textbf{2.23}$$

where

$$B = \frac{babc}{2.3(ba + bc)} \qquad \textbf{2.24}$$

2.6 Zero Resistance Ammetry

The measurement of galvanic currents between galvanically coupled metals using a zero resistance ammeter (ZRA) was devised by Brown and Mears[8] in 1938.

Within the ZRA,[9] the galvanic current between working electrode (WE) 1 and 2 is measured by adjustment of the voltage or the resistance. The coupled potential of the working electrodes is measured in the solution with the reference electrode (RE), illustrated in Figure 2.3.

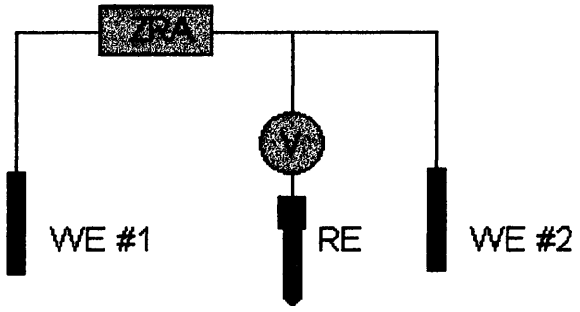

Figure 2.3 The schematic of the basic zero resistance ammeter set up.

2.7 Electrochemical Impedance Spectroscopy (EIS) [10]

Corrosion rate measurements using dc electrochemical techniques although often rapid and accurate are only able to produce a value for the Rp component of the equivalent circuit below. In addition, Rp measurements can be found to be excessively large in low conductivity electrolytes because of the inclusion of Rs. Using alternating applied voltages, it is possible for the resulting current to provide a value for the capacitance of the metal surface as well as individually distinguishing Rp and Rs.

2.7.1 The Impedance of Simple Circuits

The equivalent circuit (Figure 2.4) for the ac measurement shows the double-layer capacitance (C_{dl}) in parallel with the Rp because the current can 1) flow through the corroding interface and reduce/oxidise reactants or 2) charge or discharge the capacitance.

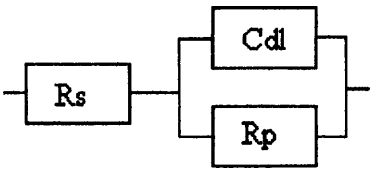

Figure 2.4 The equivalent circuit for a simple corrosion system, including solution resistance.

If solution resistance is currently ignored, the simple equivalent circuit the variation of current with potential can be described (the Rp current), also the variation of current with time when the potential is varied with time (the Cdl current). Therefore Equation 2.25 can describe the total current flowing through the metal/solution interface thus:

$$I(t) = \frac{V(t)}{Rp} + Cdl\frac{dV(t)}{dt} \qquad \textbf{2.25}$$

If the change in voltage with time is small then the total current can be described by the first term because the second would be negligible. By using a slow sweep rate (dV(t)/dt) the metals surface would remain unaltered with such a small amplitude of potential change – this also minimises the capacitance effects enabling a more linear response.

2.7.2 AC Potential

The applied voltage used for ac impedance is in the form of a sinusoidal signal described by:

$$V(t) = Vo\sin(\omega t) \qquad \textbf{2.26}$$

Vo is the maximum amplitude of the sine wave; ω is the angular frequency in radians s^{-1} and (ωt) is the angle in radians (2π radians = 360°). One cycle would take $2\pi/\omega$ seconds. The angular frequency is related to frequency (f) by:

$$\omega = 2\pi f \qquad \textbf{2.27}$$

The period of the sinusoidal cycles is given in seconds by:

$$period = \frac{1}{f} = \frac{2\pi}{\omega} \qquad \textbf{2.28}$$

The rate of change in sinusoidal voltage in Equation 2.26 is given by:

$$\frac{dV(t)}{dt} = Vo\omega\cos(\omega t) \qquad \textbf{2.29}$$

The current obtained from this applied voltage (V_0) is:

$$I(t) = \frac{Vo}{Rp}\sin(\omega t) + Vo\omega Cdl\cos(\omega t) \qquad \textbf{2.30}$$

If the two terms above were plotted as current against time then the "separate" current magnitudes would both be proportional to that of the applied voltage. However, the Rp term would be in-phase with V_0 whereas the Cdl signal would be 90° out of phase (at maximum current when V_0 is zero and zero current at peak V_0).

It is possible to plot the in phase and out of phase current responses if both the components are divided by V_0. If the in phase plotted on the x-axis and the out of phase on the y-axis, it can be said that the in phase is proportional to 1/Rp and the latter

proportional to $j\ \omega\ Cdl$ (the "j operator" indicates the 90° phase difference between the applied voltage and current output). Plotting these points at different frequencies produces what is similar to a Nyquist plot of admittance.

A simpler equation that describes the total measured current is:

$$I(t) = Io[\sin(\omega t)\cos\phi + \cos(\omega t)\sin\phi] \qquad \textbf{2.31}$$

From this equation:

$$I_0 \cos\phi = \frac{V_0}{R_p} \qquad \textbf{2.32}$$

and

$$I_0 \sin\phi = V_0 \omega C_{dl} \qquad \textbf{2.33}$$

If the amplitude of I_0 amps is shifted along the time axis compared to the voltage by the angle (ϕ), then another sine wave can be described by:

$$I(t) = I_0 \sin(\omega t + \phi) \qquad \textbf{2.34}$$

The admittance modulus (I_0/V_0) is often written as |Y|.

$$|Y| = \frac{I_0}{V_0} = \sqrt{\frac{1}{R_p^2} + \omega^2 C_{dl}^2} \qquad \textbf{2.35}$$

The phase angle, ϕ, can therefore be shown as:

$$\tan\phi = \omega R_p C_{dl} \qquad \textbf{2.36}$$

The total current given by Equation 2.34 describes a sine wave for $I_{(0)}$ shifted along the time axis by ϕ, the ϕ and |Y| are dependent on frequency.

The current response to the applied voltage can be represented by the above equations by two means: as in phase and out of phase components and admittance modulus and phase angle. These can also be used to describe the admittance of the circuit. The current response to the applied voltage is what has been measured *(I/V=1/R)*.

The symbol Y is used to represent the admittance and Equation 2.37 is used to describe it, viz:

$$Y(\omega) = \frac{1}{R_p} + j\omega C_{dl} \qquad \textbf{2.37}$$

or

$$Y(\omega) = Y' + jY'' \qquad \textbf{2.38}$$

Y' represents the real component and Y" is referred to as the imaginary component. The admittance is dependent on frequency (hence the inclusion of ω) and generally, Y' and Y" also depend on frequency, but not here. Y' is proportional to the in-phase and Y" to the out-of-phase current components. In the above equation, j is equal to the square root of −1 and the expression of admittance is a complex number.

It would appear logical to identify the current response from an applied voltage as admittance however it is normally referred to as impedance measurement. The analyser processes the data to provide the impedance modulus |Z| and phase angle or refers to the real and imaginary in-phase and out-of phase components as Z' and Z".

2.7.3 Responses of Simple Circuits

It is not necessary to consider the current-time response of more complicated circuit to provide an expected response. The impedances and admittances of the individual component parts can provide a response. The expressions for resistors and capacitors are listed in Table 2.2.

Table 2.2 The impedance and admittance of simple circuit components.[10]

	Impedance	**Admittance**
Resistor, R (Ohm)	R	1/R
Capacitor, C (Farad)	-j/ωC	jωC

Using the expressions in the Table 2.2 it is possible to write the Equation 2.38 above for the admittance of the parallel resistor and capacitor in the equivalent circuit.

The total impedance of the parallel RC circuit cannot be obtained by adding the individual impedances. It is only possible to add the admittances in parallel but impedances can be added in a series RC circuit. This is similar to calculating the total resistance of a circuit that has resistors in series or parallel. The admittances are added for parallel and impedances added for series.

To obtain the impedance of a circuit when the admittance is known the reciprocal of the admittance is taken.

$$Y = \frac{1}{R} + j\omega C$$

and **2.39**

$$Y = \frac{1 + j\omega CR}{R}$$

The impedance is given thus:

$$Z = \frac{R}{1 + j\omega CR} \qquad \textbf{2.40}$$

To define the real and imaginary parts in an impedance expression it is necessary to remove of the j term from the above equation. This is achieved by

multiplying the top and bottom of the expression by the complex conjugate of the bottom, (1-$j\omega CR$) resulting in:

$$Z = \frac{R}{1+\omega^2C^2R^2} - \frac{j\omega CR}{1+\omega^2C^2R^2} = Z' + j''Z \qquad \textbf{2.41}$$

From this, the impedance modulus and phase angle can be expressed thus:

$$|Z| = \frac{R}{\sqrt{1+\omega^2C^2R^2}}$$

$$\tan\phi = -\omega CR \qquad \textbf{2.42}$$

The phase angle for the impedance is identical to that of the admittance but of the opposite sign.

2.7.4 Solution Resistance Effect

Referring back to the simple equivalent circuit in Figure 2.4, it is clear that the solution resistance is in series with the parallel RC components. To calculate the impedance of the whole circuit, the impedance of the R_s is added to Equation 2.41:

$$Z = R_s + \frac{R}{1+\omega^2C^2R^2} - \frac{j\omega CR^2}{1+\omega^2C^2R^2} \qquad \textbf{2.43}$$

The admittance of the circuit is calculated by taking the reciprocal of the impedance expression:

$$Y = \frac{R_s(1+\omega^2C^2R^2)+R}{(R_s+R)^2+R_s^2\omega^2C^2R^2} + \frac{j\omega CR^2}{(R_s+R)^2+R_s^2\omega^2C^2R^2} \qquad \textbf{2.44}$$

2.7.5 Impedance Plots

There are two primary methods of presentation for impedance and admittance data, known as Bode and Nyquist plots. The former is provided by the impedance modulus, |Z| and the phase angle, ϕ plotted against frequency in Figure 2.5 and the latter

by the real plotted against the imaginary parts of the impedance, Z' and Z" in Figure 2.4. These parameters are related by the following expressions:

$$|Z|^2 = Z'^2 + Z''^2$$

$$\tan\phi = \frac{Z''}{Z'} \qquad \textbf{2.45}$$

$$Z' = |Z|\cos\phi$$

$$Z'' = |Z|\sin\phi$$

The frequency and the capacitance is obtainable from the maximum of Z" and Equation 2.46. The actual Rp is the high intercept on Z' minus the low intercept (R_s).

$$\omega_{max} = 2\pi f_{max} = \frac{1}{R_p C_{dl}} \qquad \textbf{2.46}$$

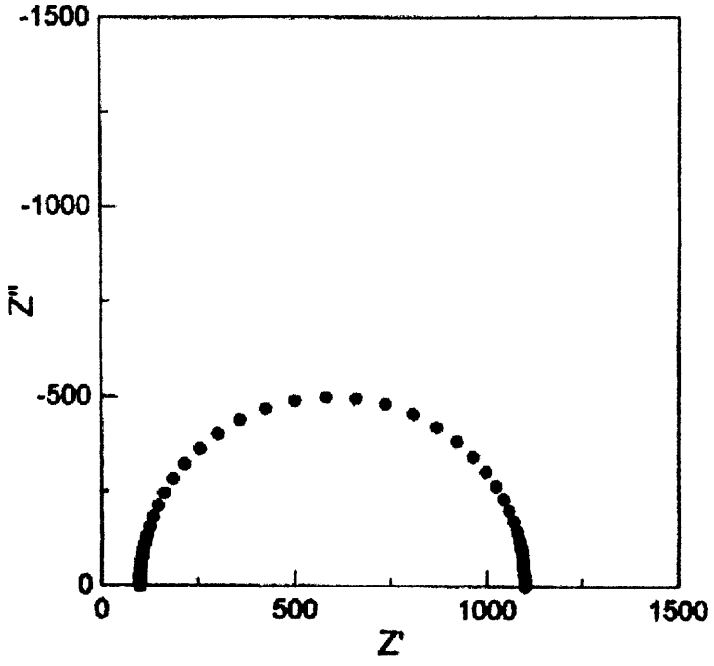

Figure 2.4 A typical Nyquist plot.[10]

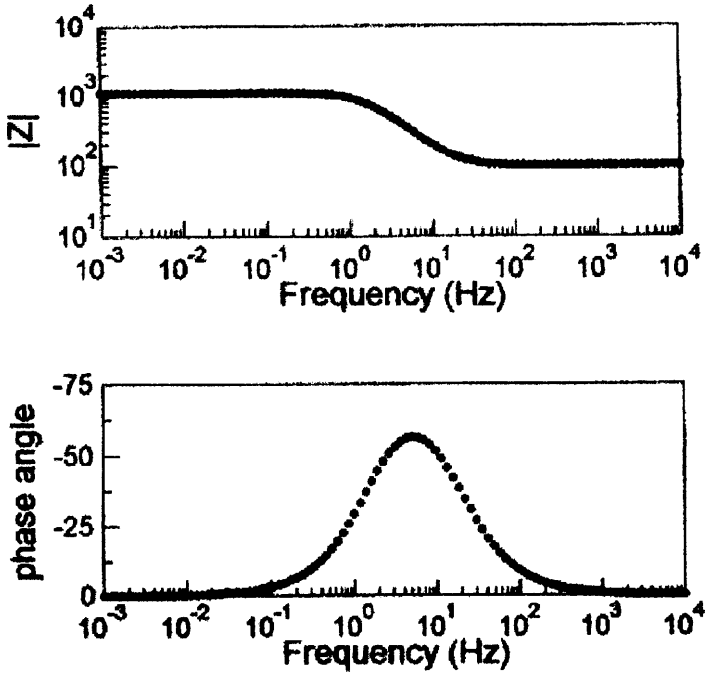

Figure 2.5 Bode plots - the impedance modulus and phase angle against frequency.[10]

2.8 Carbon Dioxide Corrosion in Oil and Gas Production[11]

There are two types of water associated with oil and gas production, condensed water and produced water. The former is water vapour condensed from the gas phase and the latter is the brine mixed with the hydrocarbon in the well stream. The presence of CO_2 has been increased by the use of enhanced oil recovery techniques involving injecting CO_2 into the reservoir as well as the CO_2 in the deeper hydrocarbon deposits.

CO_2 corrosion has been such a problem in wells and pipelines in the oil and gas industry because CO_2 corrosion is possible at near neutral pH whereas mineral acids are only of concern below pH 4. CO_2 corrosion can occur uniformly as a general thinning of the pipeline wall but localised attack caused by these conditions is most problematic.

2.8.1 Water Wetting

For corrosion to occur in an oil pipeline the water present in the hydrocarbon must wet the steel surface. This will happen if the emulsion formed is an oil-in-water instead of a water-in-oil emulsion. The oil-in-water emulsion is prevalent at 30-40 wt% water cut provided the pipe is straight, however in practice, water can drop out of the emulsion along the line. The occurrence of water wetting depends on: oil/water ratio, flow rate/regime, surface condition of the steel and changes in flow profile such as welds and bends.

2.8.2 The Hydration of Carbon Dioxide[12]

When CO_2 is purged in water (P_{CO2} = 1 Atm) and ambient temperature, the following reactions take place:

$$CO_{2\,(gas)} = CO_{2\,(aq)} \qquad \textbf{2.47}$$

K_d =0.034 mol dm^{-3} bar^{-1}.

Where CO_2 dissolves in the water, removing any dissolved oxygen.

The hydration of CO_2 takes place by the following reaction:

$$CO_{2(aq)} + H_2O \underset{K_{d1}}{\overset{K_{f1}}{\Leftrightarrow}} H_2CO_3 \qquad \textbf{2.48}$$

$K_{f1} = 0.044\ s^{-1}$ and $K_{d1} = 17.3\ s^{-1}$, therefore $K = 0.0025$ at 25°C.

Carbonic acid can be dissociated into bicarbonate, Equation 2.49 and then carbonate, Equation 2.50:

$$H_2CO_3 \Leftrightarrow H^+ + HCO_3^- \qquad pK_a = 3.77 \qquad \textbf{2.49}$$

$$HCO_3^- \Leftrightarrow H^+ + CO_3^{2-} \qquad pK_a = 10.3 \qquad \textbf{2.50}$$

The hydration of CO_2 is a slow step in the series of reactions and is therefore a rate-determining step. The ionisation of the acid occurs very much faster and remains in equilibrium because of the slow CO_2 hydration. The pK_a value of 3.77 is lower than that usually reported of 6.352. This is because dissolved CO_2 and H_2CO_3 are often considered and all CO_2 is counted as carbonic acid so the same value is obtained as if titrating with dissolved CO_2.[12]

The concentration of the CO_2 dissolved in the aqueous phase will be directly related to the partial pressure of the gas in equilibrium with the aqueous phase. The activity of the dissolved CO_2 will depend on the chemical composition of the aqueous phase but also the activity of the CO_2 in the gas phase (fugacity).

2.8.3 Proposed Mechanisms of CO_2 Corrosion

It is accepted that the corrosion rate of carbon steel in NaCl solutions, containing CO_2, is controlled by the hydrogen evolution reaction and there have been differing explanations for the electrode surface reaction that produces hydrogen atoms.

De Waard and Milliams[13] studied the corrosion rates of carbon steel in CO_2 environments and compared them with strong acids. They account for the differences by stating that the direct reduction of the undissociated carbonic acid is the rate-determining step of the cathodic process according to:

R-DS

$$H_2CO_{3(ad)} + e^- \Rightarrow H_{(ad)} + HCO_3^-{}_{(ad)} \qquad \textbf{2.51}$$

The carbonic acid is then catalytically regenerated:

$$HCO_3^-{}_{(ad)} + H^+_{(bulk)} \Leftrightarrow H_2CO_3 \qquad \textbf{2.52}$$

Also the adsorbed hydrogen atoms rapidly recombine thus:

$$H_{(ads)} + H_{(ads)} \Rightarrow H_2 \qquad \textbf{2.53}$$

The formation of carbonic acid from the bicarbonate at the electrode surface (Equation 2.52) may become the rate-determining step if there is a cathodic shift in potential and the diffusion of H^+ from the bulk solution cannot keep up with the amount of bicarbonate produced.

This model was criticised by Schmitt and Rothmann[14] because experimental work showed that the adsorbed hydrogen would more likely have entered the steel than from H_2, although this was dependent on the metallurgy of the particular metal. They also suggested that carbonic acid reduction (Equation 2.51) might not be the rate-determining step because the catalytic mechanism they suggested only explains the diffusion-limited component of the cathodic limiting current but not the reaction-controlled component.

The authors used rotating disc electrodes-unlike De Waard and Milliams to investigate the effect of rotation speed on the limiting current density. Their work on the kinetics of the release of hydrogen in the cathodic limiting current range found that this limiting current (i_{lim}) is composed of rate-determining diffusion of H^+ and undissociated H_2CO_3, (i_{diff}). Also contributing to the cathodic limiting current is the rate

determining reaction-controlled component, which is the hydration of adsorbed CO_2, and the subsequent rapid release of H^+ from the adsorbed H_2CO_3, i_R in Equation 2.54.

$$i_{lim} = i_{diff} + i_R \qquad \textbf{2.54}$$

The diffusion component is a linear function of the square root of the rotation speed (ω). In the absence of oxygen in a CO_2 saturated solution the diffusion component can be given as:

$$i_{diff} = i_{H+} + i_{H2CO3} \qquad \textbf{2.55}$$

The slow diffusion of the H^+ from the bulk solution, that is the i_{H+} component, are adsorbed and reduced according to:

R-DS

$$H^+_{(bulk)} \Rightarrow H^+_{(ad)} \qquad \textbf{2.56}$$

Followed by:

$$H^+_{(ad)} + e^- \Rightarrow H_{(ad)} \qquad \textbf{2.57}$$

The slow diffusion of H_2CO_3 from bulk solution to the surface of the electrode is the i_{H2CO3} component. It is adsorbed and then reduced producing $H_{(ad)}$:

R-DS

$$H_2CO_{3(bulk)} \Rightarrow H_2CO_{3(ad)} \qquad \textbf{2.58}$$

Equations 2.51 and 2.53 follow the previous reaction.

The diffusion independent component is the heterogeneous hydration of the adsorbed CO_2 on the metal surface that is shown in the following:

$$CO_{2(ad)} + H_2O \Leftrightarrow H_2CO_3 \qquad \textbf{2.59}$$

Hence rotation speed and CO_2 concentration influence the cathodic polarisation curve.

2.8.4 Protective Films

The protective scale compounds associated with CO_2 corrosion are Fe_3C, (cementite), $FeCO_3$, (siderite). The matrix of Fe_3C is present as an undissolved layer, from the dissolution of ferritic or martensitic components within the steel. A layer of $FeCO_3$ forms on the surface when the amount of Fe^{2+} has reached its solubility limit in the aqueous phase and the solid precipitates on top of the cementite to lower the corrosion rate.[15]

2.8.4.1 Factors Influencing Development and Effectiveness of Protective Films

The formation of a protective film on the steel surface depends on several factors. These are: temperature, pH, flow rate, flow regime and metallurgy of the steel.

Reservoir water is most beneficial to film formation due to the generally high concentration of bicarbonates, thus raising the pH. Condensed water has been reported to promote CO_2 corrosion.[16] There is a large decrease in the solubility of $FeCO_3$ between pH 5 and 6 from pH<5 resulting in the deposition of $FeCO_3$ on the metal substrate.[17] This scale offers protection from further corrosion, although the solubility of Fe^{2+} does not decrease.

Protective films form above pH 5 and there are three stages of corrosion depending on temperature[18] <60° C general corrosion, ~100° C some protection but pitting, ringworm and mesa attack are possible and >150° C a protective $FeCO_3$ film is formed that will have low porosity morphology and show good adherence to the metal surface in order to be effective.[19] Without the presence of $FeCO_3$ films, when the corrosion rate is low i.e. at low temperatures, so that any Fe^{2+} present is completely soluble, the Fe_3C film formed on the metal surface is thinned by high flow rates and may offer some protection if Cr, remaining from the steel dissolution, stabilizes the film.[20, 21, 22]

It is thought that the initial phase in developing a protective film, Fe_3C, can define whether the final layer will be protecting or not. It is conducting and can lead to galvanic coupling between itself and the steel, thus the cathodic corrosion reaction can

occur on the cementite as easily as on the steel. However, this also lowers the local pH because of the removal through electro migration of HCO_3^- ions from the steel surface.[23, 15]

At 60° C and above, pearlitic – ferritic (normalized) microstructure of steel generally has superior resistance to localized corrosion in CO_2 environments than a martensitic (quenched and tempered) microstructure.[24, 25, 26, 34] Initially pearlitic-ferritic structures experience more severe corrosion but this in turn promotes the formation of the protective $FeCO_3$ film before it is formed on martensite due to becoming supersaturated more rapidly.[27] The film is also more stable and less prone to localized corrosion because of the formation of lamellar cementite from the pearlite which may provide cathodic sites for the dissolution of the iron.[28] The pearlite phase enables cavities to form when the iron corrodes away and localises the build up of Fe^{2+} in conditions of low flow, this helps to anchor the $FeCO_3$ to the metal surface.[29, 30] It has been suggested that microstructure only affects corroding rates below 60° C.[32]

Flow rate is thought to have the most influence on the morphology of the protective film.[31] Thinner $FeCO_3$ films are found on carbon steel pipes subjected to slug flow which is more turbulent than those found on pipes in full pipe flow conditions leading to higher corrosion rates.

2.8.4.2 Film Failure and Localized Attack [33, 11]

Changes in any of the environmental and physical factors mentioned at the beginning of the previous section may also cause the film to fail depending on its intrinsic stability.

Uniform corrosion is experienced linearly up to approximately 60° C but in carbon and low-alloy steel pipelines localised corrosion is the main cause of failures. The common forms of localized attack from carbon dioxide corrosion in oil and gas pipelines are mesa-attack, pitting, flow-induced localised corrosion (FILC) and corrosion at welds.

Mesa attack is characterized by shallow, wide, flat-bottomed grooves with steep sides and can be attributed to instability and spallation of the $FeCO_3$ protective

film and may be caused by the following mechanisms. A poorly adhered film, such as that formed on martensite, can be scoured away in severe flow.[21, 34] Also the removal of protective films above 60° C can be the result of fracture stresses intrinsically within the film when it reaches a critical thickness if flow rates allow.[35, 38] The condition of the steel surface will affect the amount of corrosion that metal will receive. Roughened patches due to scratching, anodic polarisation and the surface finish can cause regions to be more vulnerable to localized attack.[36] The film may again reform, and be removed once more as the critical thickness is reached.

Pits were thought to occur in stagnant to moderate flow conditions in pipelines where the protective film is present, however it has been reported that their frequency increases at high flow rates.[37] Pitting can also be related to condensing conditions close to the dew point temperature in sweet gas wells and generally occurs in the temperature range 80 - 90° C depending on the alloy composition.

FILC initiated by mesa attack and pitting can cause further film removal. This mechanism however may be attributed to erosion-corrosion, which can be promoted by CO_2 but it is not unique to CO_2 environments.[39, 40] If the solution is close to the solubility limit of Fe^{2+} the protective film cannot reform in this area due to the high flow rate and corrosion continues.

Localised corrosion of welds can occur due to the geometry of the weld profile causing local turbulences.[11] It may also be possible that films of varying protectiveness or adherence are formed on the parts of the weldment with varying alloy composition or microstructure so that spallation is more likely to occur in some areas rather than others.[37] It is not certain whether welds serve as a nucleus for localised corrosion or autocatalytic galvanic coupling between the different corrosion deposits.[33]

2.9 The Principles of Welding[41]

Some of the main types of fusion welding are:

1. Manual Metal Arc (MMA).
2. Flux-cored arc welding (FCAW).
3. Tungsten inert gas (TIG) or (Gas Tungsten Arc Welding (GTAW)).

3. Shielded metal arc (SMAW).
4. Submerged arc (SAW).

In MMA welding, an arc between a flux-covered consumable electrode and the workpiece metal generates the heat for the welding. The flux provides gas shielding to protect the weld-pool from atmospheric contamination and must be easily removable. TiO_2 (rutile) fluxes improve the arc properties but leave oxide dispersions in the weld, whereas basic fluxes leave a cleaner weld deposit and fewer inclusions.

FCAW uses a continuous flux-filled consumable electrode wire that melts by heating the metals to be joined with an arc. Gas shielding can also be provided externally depending on the consumable electrode.

TIG or GTAW uses a tungsten electrode for the joining the metals but it is not consumed, therefore fusion is performed without a filler metal. Once again an inert gas, such as argon, protects the weld pool from atmospheric contamination but no slag is formed.

SMAW is an arc welding process that fuses the metals by heating with an arc and uses flux-covered stick electrodes that provide both filler metal and gas shielding. An ac/dc welder is recommended for using stick electrodes.

SAW is similar to MMA in that a flux is used to protect the arc and weld pool, however the flux is fed to the welding area via a hopper so that the filler wire can be constantly fed to welded joint. Sometimes a second filler rod is used instead of the electrode.

2.9.1 The Structure of Carbon and Low-Alloy Steel Weldments

A side view of a typical multi pass fusion weld is illustrated in Figure 2.6. The main components of a weld are the two parents i.e. the base metals that are fused together, The dilution zone where the weld metal has mixed with the parent, the heat-affected zones directly next to the filler and several welding sequences or runs of the filler metal which would also undergo mixing.

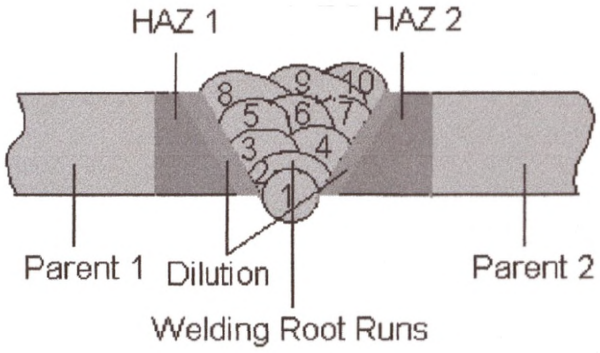

Figure 2.6 The different component parts of a typical butt-weld.

2.9.1.1 The Microstructure of the Filler Metal (Weld Pool)[42]

Low carbon steel forms pro-eutectoid ferrite from the cooling austenite, these appear as parallel laths. The remaining austenite, depending on the cooling rate and metal composition will form around the laths, which are normally acicular ferrite, fine pearlite, bainite and martensite. It is favourable to have the fine acicular ferrite because it improves the toughness of the material.

Inclusions in the filler metal can promote nucleation sites for the formation of the pro-eutectoid ferrite. Welds with a low oxygen content (0.01%) tend to have a low inclusion content but if oxygen is present at 0.03% then the number of nucleation sites increases. At higher oxygen content the amount of acicular ferrite is reduced perhaps because the nucleation sites are unsuitable. However inclusions are generally undesirable as they are a cause of corrosion in welds.

2.9.1.2 The Heat-Affected Zone (HAZ)[42]

The structure of the HAZ will vary depending on the alloy, composition, mechanical history and the thermal cycling of the parent metal, although the majority of the composition of the HAZ will be the same as that of the parent metal except for microstructural differences.

The HAZ can be defined as two regions, the grain growth region next to the fusion line and the grain-refined region further into the parent metal. At the fusion line

where the temperature is approximately 1200° C during the welding process there is a rapid growth of austenite. The austenitic grain size and its transformation structure control the microstructure. In turn, the coarsening temperature and thermal cycling control the austenitic grain size. The greater the energy input, the more coarse the grains.

The grain growth region will be composed of pro-eutectoid ferrite at the austenite grain boundaries with a ferritic and pearlitic or bainitic structure in the grains. At faster cooling rates, the pro-eutectoid ferrite is lost and in its place acicular bainite or martensite is formed. In the grain-refined region, the microstructure will be similar to the parent metal but with equiaxial ferrite and pearlite grains.

2.9.2 Causes of Weld Corrosion[43]

Weld corrosion has been known to occur even if the correct procedures have been observed. Welds often exhibit superior corrosion resistance compared to the untreated parent metal in a particular environment. They can also display erratic behaviour, displaying both resistance and susceptibility to corrosion attack. The following list of factors have often provided an explanation for weld corrosion:

- Fabrication technique
- Welding practice
- Welding sequence
- Moisture contamination
- Organic or inorganic chemical species
- Oxide film and scale
- Weld slag and spatter
- Incomplete weld penetration or fusion
- Porosity
- Cracks (crevices)
- Internal stress
- High residual stresses
- Improper choice of filler metal
- Final surface finish

2.9.2.1 Modes of Preferential Weldment Corrosion

The corrosion behaviour of carbon steel welds can vary depending on many considerations such as the composition of the parent and filler metal and the welding process employed. Because of the metallurgical transformations across the weld and HAZ, microstructures and morphologies become significant. The range of microstructures formed can develop on the cooling rate and are dependent on energy input, preheat treatment, metal thickness, weld bead size and reheating due to multipass welding. As a result, the filler metal microstructures are often different to the parent and HAZ, due to the chemical composition and weld inclusions. The modes of preferential corrosion are shown in Figure 2.7.

Small quantities of elements are added to carbon steel to alter certain properties of the metal in wet CO_2 and brine environments. Such changes might be:

- Electrochemical behaviour of ferrite and carbides.
- Microstructure - slower diffusion rate of elements such as Cr, Mn and Mo promotes finer structures such as bainite and martensite as a conversion product from ferrite. The formation of structural phases due to precipitation hardening that might have different electrochemical properties to ferrite.
- Surface corrosion products may be altered.

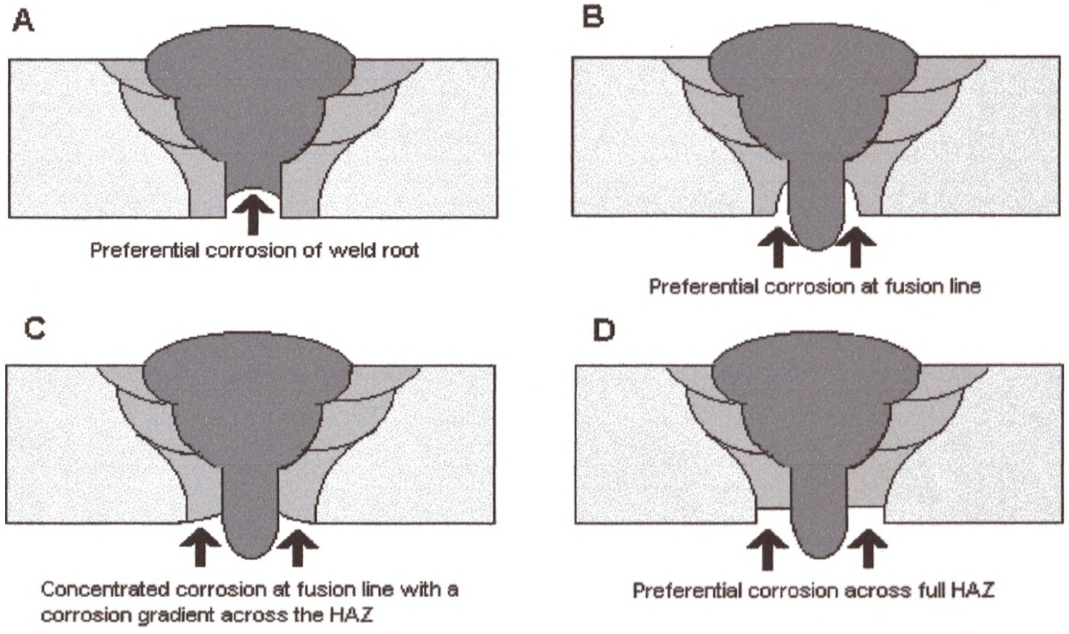

Figure 2.7 Modes of preferential weldment corrosion.[44]

2.9.2.2 Preferential Weld Corrosion

The microstructures present in weld metals are similar to those of the HAZ, although there are deoxidation products, the amount of which depends on the flux used in the welding process.

Corrosion in welds may in part be due to differences in the composition of individual welding rods.[45] Microgalvanic cells can form if re-melting of the weld or parent metal occurs. A narrow band of the weld pool develops a composition gradient on cooling creating an anodic region in some conditions, which can lead to galvanic attack.

Preferential corrosion of the weld may occur, of course, if the filler metal is less alloyed than the parent plate and may therefore have a lower potential.[46] If this were the case then the large cathode (parent plate), and the small anode (weld) would accelerate the weld attack further. Also the cathodic reaction is usually rate determining. Poor corrosion resistance can also be found in welds of similar composition and hardness to the parent, which may be due to the flux used to coat the electrode. Rutile (TiO_2) fluxes provide superior corrosion resistance to basic ones, although not to the standard of the parent plate. Differences in inclusion content between the two fluxes may cause this and heat treatment unfortunately has little effect at remedying it.

To counter preferential attack, alloying small quantities of Cu, Cr, Mo, Nb, Ti, Al, V and Ni with the intention of making the weld more noble[65] has been tested successfully even with basic electrodes.[61] The addition of these elements must be treated with caution as it is the synergistic behaviour of selected elements together that is more beneficial rather than assuming that optimum performance can be gained by adding all of them to a filler metal.

The effect of the environment where the weld is in service is crucial.[45] Accelerated corrosion of the weld is possible when the pH is low, with low bicarbonate content and hydrodynamic flow regimes. High turbulent flow gives high fluid to wall shear stresses and enhanced mass transfer hence greater weight loss per annum. The

effect of turbulent flow rates and their detrimental effect on welds have been known for many years, since high corrosion rates were noted in welds on the hulls of ships.[48]

2.9.2.3 Preferential Corrosion of the HAZ

Corrosion of the HAZ has usually occurred below between pH 7-8 in aqueous environments. It is apparent that the HAZ will corrode more severely than the parent metal; this fact has been connected with the microstructures formed when the steel has been hardened. It is thought that the hardened structures produce microcathodes that reduce H^+ in acid environments. The microstructures are the low-transformation products martensite, lower bainite and retained austenite.

Manganese, silicon, carbon and decreasing welding energy will increase the amount of retained austenite in the HAZ.[49, 50, 51] Retained austenite occurs in the HAZ of low alloy steels at moderate and slow cooling rates. Stress relieving at 575°C anneals the martensite and increases the corrosion resistance. Normalising for 20 minutes at 950°C followed by air-cooling may restore the HAZ to a ferritic-pearlitic structure and possess the corrosion resistance of the base metal.[52]

2.9.3 Recent Studies of Weldment Corrosion

Rothwell, Dawson, Eden and Palmer[53] first used simultaneous galvanic current measurements and electrochemical impedance spectroscopy (EIS) on a segmented weld to study corrosion rates and galvanic current. The workers concluded that microstructures could be listed in order of potential, solution annealed being the least noble and in order of increasing nobility were; martensitic, pearlitic, upper and lower bainite. Carbon-manganese steel welds suffered the highest corrosion rates and heat treatment was the major consideration in defining the microstructure of the HAZ. The key recommendations were to add Ni to the filler metal to make the weld more noble and to introduce inhibitors to the solution when in service.

Joosten, Kolts, Humble, Keifer and Marlow[54] also used the segmented electrode technique to investigate suitable materials and welding requirements to prevent preferential corrosion in CO_2 environments. They also established that carbon-manganese welds were subject to severe corrosion whatever the welding

technique. It was discovered that if Ni was present in the weld and also in the parent, in addition to Cu, then the HAZ could corrode preferentially if the welding energy is low. Therefore, it was stated that if an alloyed weld made in low-alloy steel with high fusion energy there would be no selective attack of any of the weldment components.

In an earlier study Joosten and Payne[57] cite minor differences in chemical composition in the weld and HAZ and not necessarily microstructures as the primary cause of galvanic corrosion. Like other authors they recommend adding Cu and Ni to the filler metal but also phosphorus. It was further concluded that P was beneficial to corrosion prevention but it had a negative effect when the quantity exceeded that of Ni.

Savva, Weatherly and Aust[58] found that by increasing the Mn content of steels, the corrosion depth of the HAZ was more pronounced. Niobium increased the HAZ corrosion in low-carbon steels (0.06%) but not significantly in steels with higher carbon contents (0.12%).

It is thought that carbon can increase the corrosion rate in quenched and tempered steels. They are mainly martensitic and bainitic so that more carbon is in solid solution and the carbides do not form a continuous grid. This may lead to a less adherent and thinner protective $FeCO_3$ film.[21] Others have reported that the carbides needle-like structure has promoted film adherence.[55, 56] In general the overall benefits of C content are inconclusive and may be irrelevant as low-carbon steels (<0.1% C) are increasingly used in new flowlines.

Silicon is known to promote graphite precipitation, restricts the gamma phase and increases strength and wear resistance. It also reduces the electrical conductivity of steels[5]. It was found that carbon steel alloyed with Si has a decreasing corrosion rate with increasing Si content. Si has been found to significantly reduce the effect of increasing corrosion rate with increasing carbon content in steel because of a shift in the open circuit potential on the noble direction. However studies fail to draw any clear conclusion as to the possible benefits of Si additions to carbon steel.

Corrosion of the fusion line has been described[49] and has been associated with the liquidation of sulphides along the grain boundaries by decreasing the surface

tension of the austenite grains. Tramline corrosion[46] also appears as grooving at the fusion line and occurs in acidic conditions. Post-weld heat treatment has been known to counter this problem or suitably arranging the weld runs.

2.9.4 Nobler Element Additions

The alloying additions intended to raise the potential of filler metals in weldments and carbon or low-alloy steels (corrosion resistant alloys – CRAs), namely Cr, Cu and Ni were added to steels is small quantities to prevent preferential weldment corrosion. However failures have shown that there are still problems. This section will discuss the viability of using Cr, Ni and Cu in addition to the previous section in terms of electrochemical behaviour and the influence on possible surface films in the context of weldments or other relevant situations. Examples of alloyed consumables often used in flowlines welds are listed in Table 2.3.

Table 2.3 Alloyed consumables used on oil and gas flowlines in the presence of CO_2.[60]

Consumable composition %	AWS classification	Commercial consumable used
0.9Ni	A5.5-81 E8016-C3	Metrode 1Ni.B (Mo-free)
0.7Ni-0.3Cu	A5.1-81 E7016	ESAB Weldshield
0.6Ni-0.4Cu	A5.5-81 E8018-G	ESAB OK 73.08
0.6Ni-0.3Cu-0.3Cr	A5.5-81 E7016	Filarc 86M
0.8Ni-0.4Cu	-	ESAB OK 13.26

2.9.4.1 Chromium[66]

Chromium is the considered to be the most beneficial alloy addition to carbon steel to improve corrosion resistance in CO_2 saturated environments.[62] It is thought that even small quantities (approx 0.5 %) of Cr stabilise the carbonate film below 90°C and halve the corrosion rate if added to carbon steel whilst minimising the loss of toughness

in the metal. Chromium containing steels (>0.5 %) show a decrease in corrosion rate with increasing Cr content and a reduction in mesa (uneven) corrosion.

It was found that a tight surface film containing Cr_2O_3 and $FeCO_3$ was protecting the metal's surface and therefore, by increasing the Cr content in the steel, the resistance of the film was increased.[22,63] It was also proposed[20, 21] that Cr forms a protective film of hydroxides or $(Fe,Cr)CO_3$ on the metal surface before the $FeCO_3$ film was able to develop which reduced mesa attack more effectively with increasing Cr content. This Cr-rich film consists mainly of Fe_3C particles that remain, un-oxidised on the metal's surface after the metal (ferrite) was removed and subsequently enriched the film with Cr and other elements.

An increase in flow rate is known to thin these films and other work[18] has suggested that the higher the Cr content of the metal, the thinner the corrosion product that is also adhesive, stiff and tough. The Cr is concentrated in the corrosion product i.e. above 2 % Cr bearing steel has 15 – 17 % Cr concentrated in the film.[59]

In low concentrations (0 – 1.4 %), Cr-bearing carbon steels have been found to exhibit an increase in corrosion rate with increasing Cr content at low flow rates at 60°C and pH 6.[21] At pH 4 and 5, the increase of Cr produced similar corrosion rates to the unalloyed carbon steel at low flow rates. However at higher Cr contents of 2 – 4 %, it has been found that corrosion rate is reduced by a factor of two in conditions of low flow.[59] This implies that at low Cr concentrations the reduction of general corrosion rates is observed at higher flow rates. Most studies regarding avoidance of preferential and CO_2 corrosion are in favour of using Cr as an alloying addition and that its effectiveness increases with the amount present in the metal.

2.9.4.2 Copper

Cu is added to carbon and low-alloy steel filler metals, usually in combination with Ni to avoid weld metal attack. The optimum amounts commonly used for effective protection are 0.6% Ni and 0.4% Cu. It is suggested that larger quantities of these metals will result in HAZ attack in some parent metals[60].

Although unlikely, it has been suggested[69] that Cu and Ni are enriched in a layer of mill scale after machining and provides a barrier that prevents corrosion when the metals are of a relatively low concentration in the steel. It has also been reported that Cu can prevent corrosion in combination with Cr, Si and Mo subject to microstructure and heat treatment.[65]

Cu is homogenously dissolved in the ferrite matrix and because Cu is more noble than Fe, enrichments of Cu can occur on the metal surface leading to faster general corrosion rates on the weld metal than on the parent metal surface if uncoupled.

Films formed on Cu containing steels have been reported as being vulnerable to mesa-attack because the films can be easily removed.[22] It was also noted that the addition of only 0.2% Cu to a 0.5% Cr steel caused the corrosion rate to be twice that of steel not containing Cu.

It is generally concluded that small percentages of Cu in the metal is maybe detrimental in terms of increased corrosion rate but more research is required into its effects.

2.9.4.3 Nickel

1 % Ni (if without Cu) is added to carbon steel filler metal for welding for two reasons, 1) to increase resistance to environmental cracking and 2) some believe that creating a cathodic weld metal relative to the parent (base) pipe will eliminate preferential corrosion of the weld, although, it does not necessarily mean that it is not susceptible to attack. 1% Ni has been used, for these reasons, as an alloying addition in carbon-manganese steels to provide protection from preferential weld corrosion.[54]

Studies using Ni enriched welds have found that in comparison to parent pipe there is a consistently higher corrosion rate of the weld metal with an increasing rate above 1.1% Ni,[63] (Figure 2.8). It has been concluded that the presence of even small amounts of Ni in the weld metal can cause preferential corrosion of the immediate parent and HAZ because the parent pipe has the less noble potential of the couple and, depending on the conductivity of the electrolyte, will be preferentially attacked.[57]

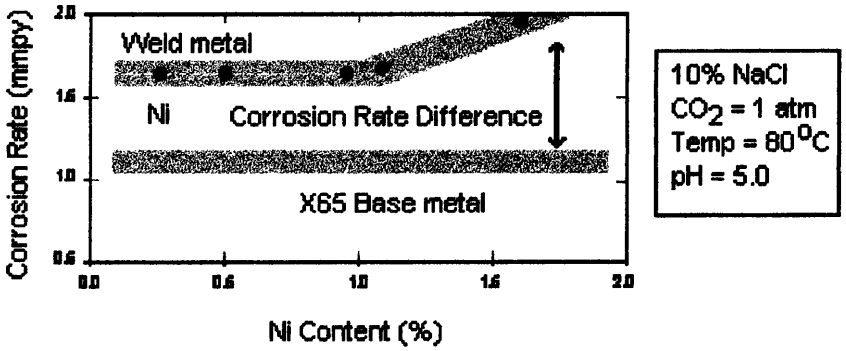

Figure 2.8 The effect of nickel on the corrosion rate of steel in aqueous CO_2 environments.[63]

The effects of Ni additions on corrosion rate may not be clear from many studies.[67] However the overall cathodic reaction on the Ni-rich weld is thought to be at a faster rate than the parent metal and increases with immersion time whereas the cathodic reaction rate on the parent metal remains relatively constant.[18, 21] This behaviour is thought to be due to Ni enrichment at the weld metal surface because of the slow dissolution of the ferrite in response to the hydrogen evolution reaction at the Ni that is homogenously dispersed within this ferrite. In addition to the hydrogen evolution reaction, the higher limiting current at the Ni-rich weld metal may also be explained by direct reduction of H_2CO_3 and/or HCO_3^- at the metal surface.[68] Ni may also accelerate mesa-attack at high pH and temperature.[64]

2.10 Waveney Spoolpiece Failure[70–73]

A 6'' spoolpiece flowline that had been in service for just over 1 year was replaced in 1999 after it was found to have suffered internal preferential corrosion in the weld metal and the HAZ. There were nine weldments, of which joints 1, 2, 3, 4 and 6 underwent some form of preferential corrosion leading to failure.

The parent pipe was a low alloy carbon steel, because most of the joints were fabricated in a workshop the welding method employed was flux cored arc welding (FCAW) with 1% Ni GTAW filler wire. Two of the weldments, joints 4 and 7 were fabricated offshore therefore SMAW was the welding technique used with matching

carbon steel GTAW filler wire. The nature of the preferential corrosion that occurred on the weldment at joint 3 is illustrated in Figure 2.9 and the attack on the weldments at joints 1, 2, 4 and 6 are also illustrated in Figure 2.11. Figure 2.10 is a photograph of the weld metal attack at joint 3 and Figure 2.12 illustrates the positions of the weldments in the structure of the spoolpiece and flow direction.

The weldments were tested metallographically and the solution was also examined to determine the cause of the failure. The microstructure of the forged tee parent metal of joint 3 was found to be ferrite with some pearlite at the grain boundaries, typical of normalised steels.

The composition and metallurgy of the root and hot passes were difficult to determine because most had been removed from the welds and was hard to predict because it was known that WPS D002 – TIG/PZ6513 Ni content may vary with welding technique. It was found that there were no adverse metallurgical factors present in the weldments that would cause such attack at the HAZ and the weld root. The solution may have contained sand, although the amount was unknown. Therefore depending on this and the flow rate it was thought that corrosion and or erosion might have caused the attack.

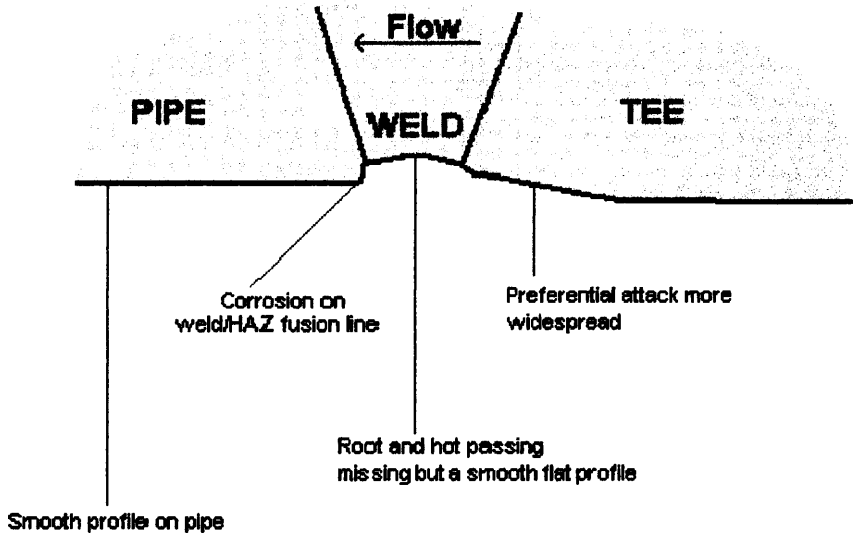

Figure 2.9 Joint 3 of the Waveney failure.[71]

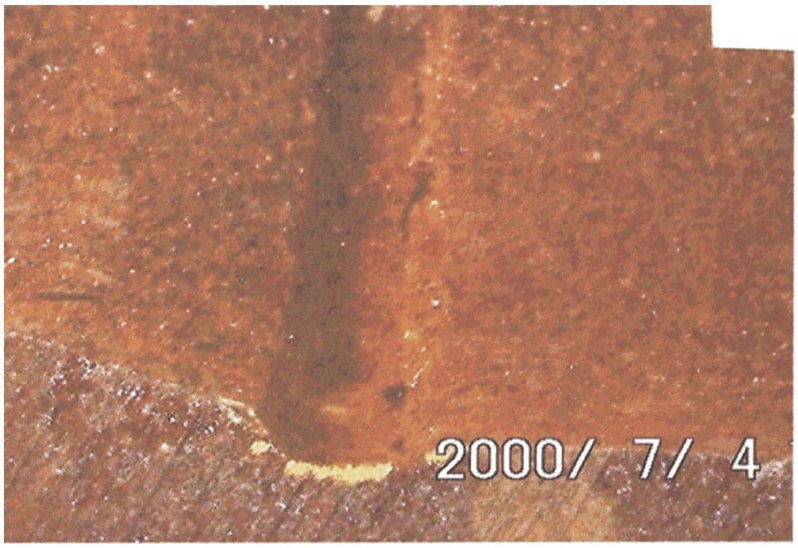

Figure 2.10 The preferential attack in the pipeline at joint 3.

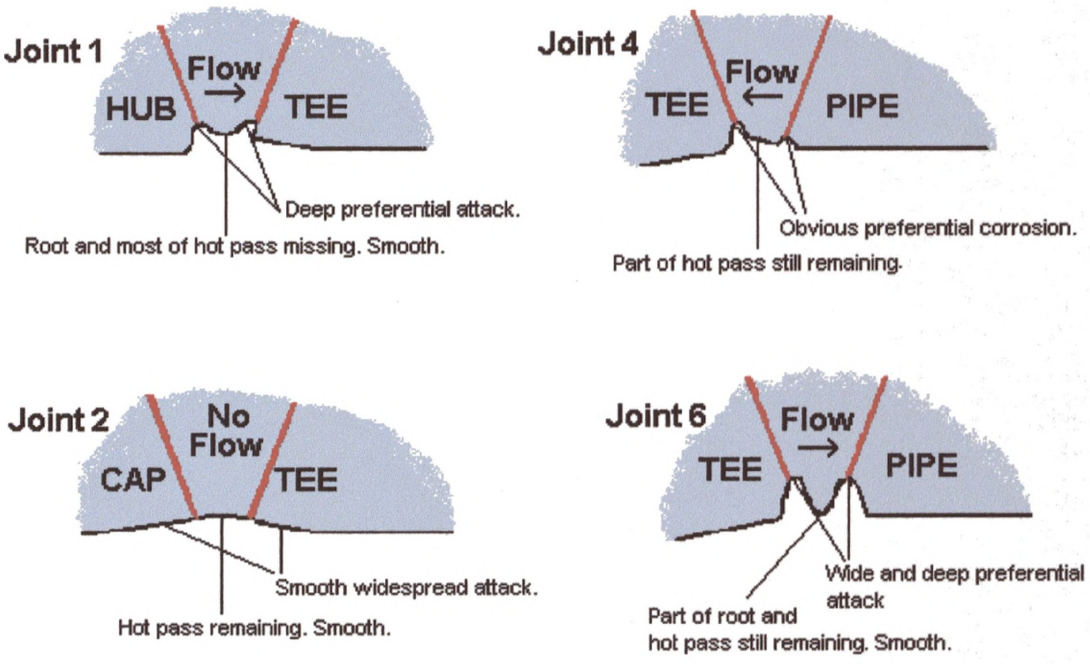

Figure 2.11 The preferential attack on some of the remaining weldments.[71]

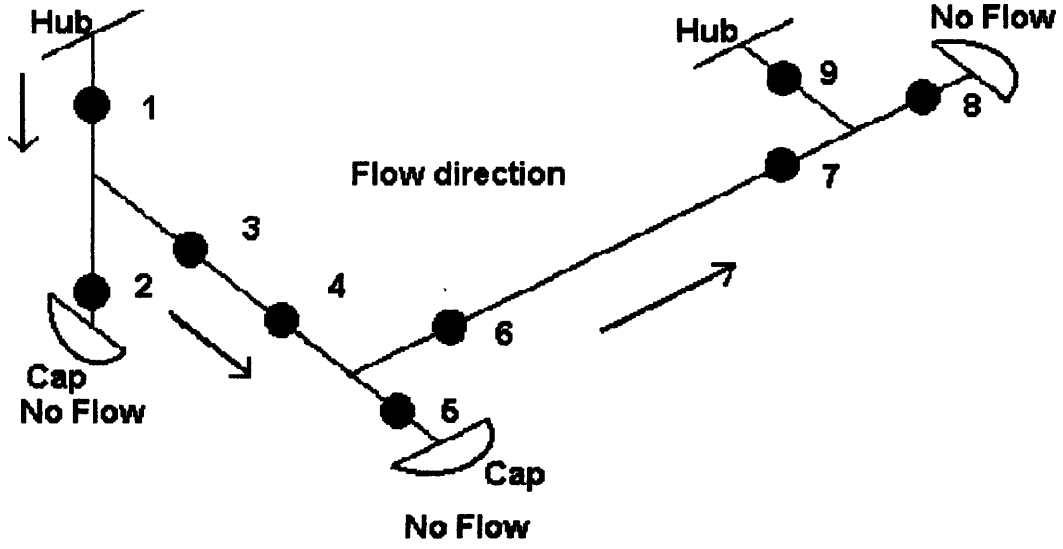

Figure 2.12 A small section of the structure of the Waveney spoolpiece indicating the numbered joints and the direction of flow.[70]

2.11 Predictive Testing of Weld Corrosion

Corrosion failures in oil production can be due to selective attack at or near the welds. Although there has been some success in corrosion prediction with segmented electrodes in laboratory tests, they fail to detect the possibility of selective attack on the weld, parent or heat-affected zone due to "thin film" conditions that occur in annular flow in pipelines. An illustration of the occurrence of thin film conditions as opposed to bulk solution is shown in Figure 2.13.

There is a need for a different approach to predictive testing because it has been observed in some failures that "identical" welds in the same line and fluid composition have not suffered preferential corrosion and at present there are no testing methods that could predict this. There is of course the possibility of subtle differences between the supposedly identical welds that have not been detected, but it is probable that a new approach to preferential weldment corrosion is needed.

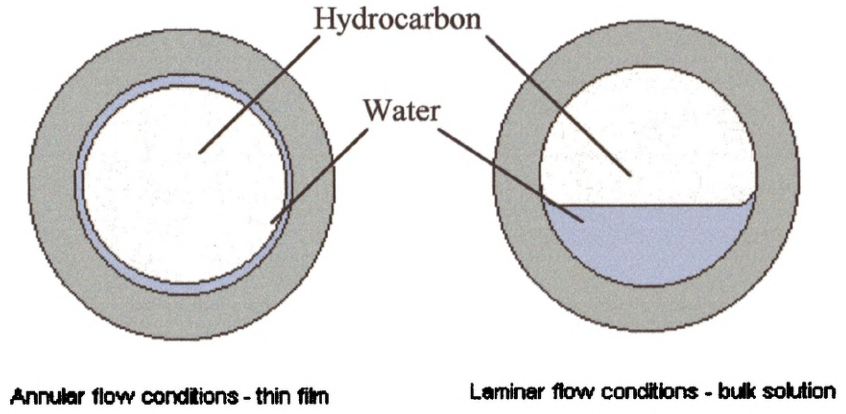

Figure 2.13 Annular flow can create thin film conditions possibly leading to preferential weldment corrosion.

2.11.1 Transmission Line Theory

Transmission line theory is used in corrosion measurement/monitoring techniques such as potential monitoring of rebar in concrete,[76] wires in solution[77] and porous electrodes. The transmission line can be understood as a one-dimensional equivalent circuit representing behaviour of current flow in long electrodes.

2.11.2 Equivalent Circuits of Porous Electrodes

A great deal of work on the current and potential distributions of porous electrodes was undertaken by De Levie.[78, 79, 74, 75] This work is of interest because a lot of the theory and equations can be considered to be analogous with predicting current and potential distributions on weldments in thin aqueous layers. Knowing values of current and potential distributions in porous electrodes enables incorporation into the electrode kinetics of a flat electrode.

De Levie performed experiments using dc and ac techniques but found that ac related the porous electrodes to corresponding flat electrodes with the simplest equations. The assumptions underlying the calculations for the flat electrodes are:

1. The pores are of uniform cross-section.
2. Also of semi-infinite length.
3. Homogenously filled with electrolyte.
4. Without cross-links.
5. A large amount of inert electrolyte is present.
6. The electrode material has no resistance.
7. Curvature of the equipotential surfaces in the pore can be neglected.

Using these assumptions, De Levie devised a transmission line equivalent circuit for a pore (Figure 2.14), where the impedance, Z, of the electrode interface depends of potential (in the case of a slow reaction) and time (in diffusion control).

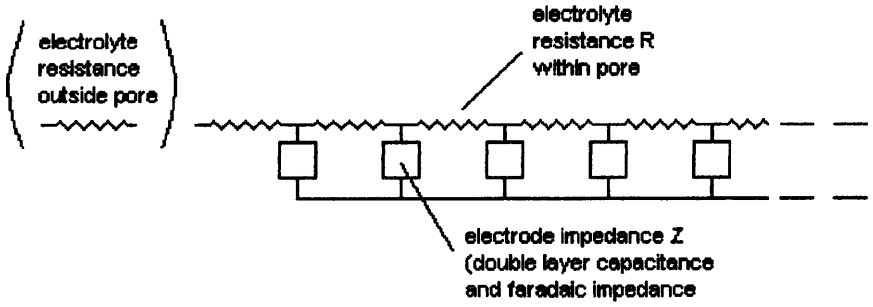

Figure 2.14 The equivalent circuit in the pore. [78, 79, 74, 75]

When a potentiostatic or galvanostatic step is applied to the pore orifice, the potential and current within the pore changes slowly due to damping of the pulse by the double layer capacitance resulting in a complicated analysis. The simpler analysis of the pore response to a smaller amplitude (≤5 mV) is given by the application of an alternating potential. Z is dependent on the angular frequency only and the Equations 2.60 and 2.61 below and illustrated in Figure 2.15 can describe an infinitely small section of pore, *dx*.

$$de = -iR\,dx \qquad \text{so} \qquad \frac{de}{dx} + iR = 0 \qquad \textbf{2.60}$$

$$di = -\frac{e}{Z}\,dx \qquad \text{so} \qquad \frac{di}{dx} + \frac{e}{Z} = 0 \qquad \textbf{2.61}$$

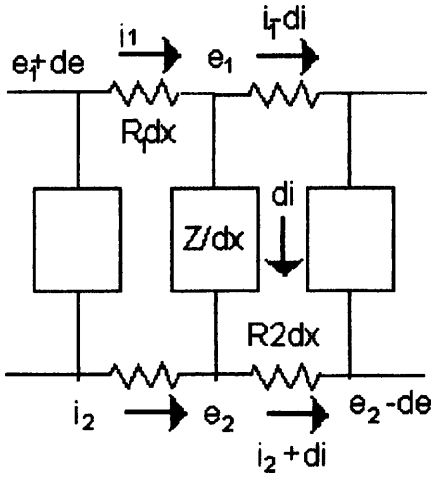

Figure 2.15 An small section, *dx*, of the pore equivalent circuit. Subscript 1 denote solution resistance, 2 denotes electrode impedance. [78, 79]

From Figure 2.15, *e* is the potential, *dx* is the small change in distance, *i* is the current, *x* is the distance along the pore axis ($x = 0$, at the mouth of the pore), *R* is the ohmic resistance of the pore per unit pore length and *Z* is the impedance of the electrolyte-electrode interface per unit pore length.

Combining Equations 2.60 and 2.61 gives:

$$\frac{d^2 i}{dz^2} - \frac{R}{Z} i = 0$$

and **2.62**

$$\frac{d^2 e}{dz^2} - \frac{R}{Z} e = 0$$

In terms of potential, e, for the semi-infinite pore;

$$e(\infty) = 0$$

$$e(0) = E$$

$$e(x) = E \exp\left(- z \sqrt{\frac{R}{Z}} \right) \quad \textbf{2.63}$$

$$i(z) = -\frac{1}{R} \frac{de}{dz} = \frac{E}{\sqrt{ZR}} \exp\left[- z \sqrt{\frac{R}{Z}} \right] \quad \textbf{2.64}$$

$$i(0) = \frac{E}{\sqrt{ZR}} \quad \textbf{2.65}$$

The pore behaves as an impedance, $(ZR)^{1/2}$, which can be called the apparent pore impedance, $Z_{measured}$.

2.11.3 Interpretation of Impedance Complex Plots of Porous Electrodes

In a Nyquist plot a flat electrode would be expected to have a Z with the modulus $|Z|$ and a phase angle, ϕ. For the corresponding porous electrode the measured Z is actually $Z^{1/2}$ and the modulus $|Z|^{1/2}$ with a phase angle of ½ ϕ. R is a scalar so $(ZR)^{1/2}$ and $Z^{1/2}$ differ only by vector-length. Therefore for porous electrodes:

1. The phase angle is half of the value for the equivalent flat electrode.

2. The absolute magnitude of the measured impedance is proportional to the square root of the equivalent flat electrode.

2.11.4 Pore Penetration Depth

From Equation 2.64 the reciprocal of $(R/Z)^{1/2}$ is used to quantify the fraction of the pore included in the ac measurement. Penetration depth can be defined as:

$$\lambda \equiv \frac{\sqrt{|Z|R}}{R\cos\frac{1}{2}\varphi} \qquad 2.66$$

The penetration depth increases with increasing radius and electrolyte conductivity within the pore.

Penetration depth of a pore is also influenced by the ac signal. At high frequencies, the electrode admittance is great and the signal is damped within a short distance, as the frequency decreases the pore is more deeply penetrated. Therefore the high frequency part of the Nyquist plot is linear and equal to the square root of the equivalent flat electrode. The Nyquist plot in a range of frequencies can then be correlated to the size of the pore.[80]

2.12 A Novel Approach to Preferential Weldment Corrosion

An alternative explanation to preferential weldment corrosion could lie in the differences in liquid film thickness. De Levies model describes the potential drop over the distance of a pore of a particular length, which takes into account penetration depth and solution resistance. This model can be applied in a similar manner to a thin liquid layer in a one-dimensional channel over a weldment to study the potential drop with distance as the thickness of the solution layer is varied.

It may be possible to switch the attack from the parent to the weld by varying the film thickness. This will alter the solution resistance of the electrolyte layer, which will change the galvanic current distribution across the weld and parent metals. Thus the local corrosion rate of the metals will also be changed in a similar way.

It should also be remembered that although a weld metal may be nobler than the parent, its kinetics can differ and it may corrode at a faster rate due to alloying additions.[74] Figures 2.16 a and b show the nature of the corrosion of the couple that would occur in with changes in the liquid film thickness on the interface of the metal surface.

a. Low liquid film thickness equivalent to a very high resistance electrolyte. The centre of the weld metal, the cathode corrodes as it is de-coupled from the parent metal, the anode, as it has the higher intrinsic corrosion rate of the two metals. The HAZ region is attacked because this is the join of the two metals and the parent metal is undergoing anodic dissolution to protect the weld metal. This weld might be referred to as having low "throwing power".

b. This weldment is in bulk solution or in a conducting electrolyte and if the weld metal has a higher intrinsic corrosion rate than the parent it does not matter because the weld and parent metals are fully coupled. The large area of anode i.e. parent metal can protect the weld metal and there will not be any selective attack.

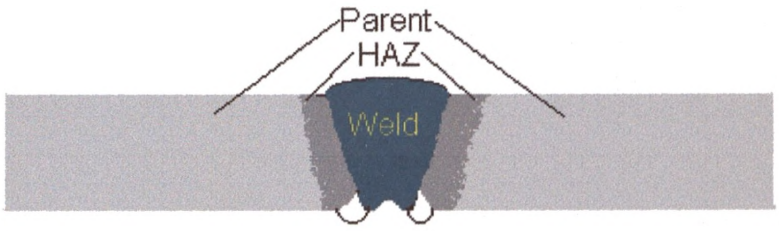

Figure 2.16 a) A representation of the current behaviour in a weldment where the solution resistance is high and the interfaces of the HAZ with the weld metal are preferentially attacked as well as the weld metal centre.

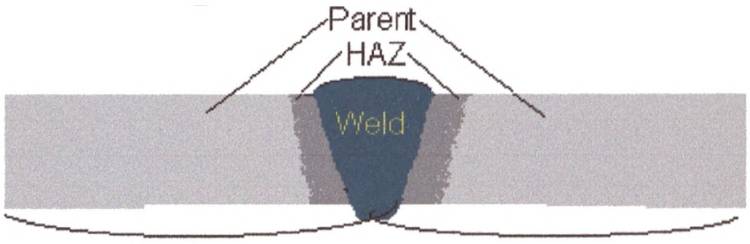

Figure 2.16 b) A representation of the current behaviour in a weldment where the solution resistance is low and there is no preferential attack.

Laboratory tests that reproduce the weld environment and geometry may not detect selective attack. It can be said the only way of predicting whether a weld is "safe" or not is to expose it to environments where the liquid film thickness varies.

2.12.1 The Principles of the Mathematical Model

The calculation for the mathematical model is one dimensional, assuming linear current-potential behavior and two different metals where the potential and current distributions in a thin liquid film on the weld surface are controlled by:

1. The uncoupled potential difference the weld and parent, ie $Ecorr_{weld} - Ecorr_{parent}$, ΔE,
2. The uncoupled polarization resistances (related to corrosion rates) of the weld, Rp_{weld}, parent, Rp_{parent}, and
3. The solution resistance of the aqueous phase per unit length of the solution, R_{soln}, which is dependent upon the conductivity of the solution and the liquid film thickness:

$$R_{soln} = 1/\sigma t$$

σ = Conductivity of the solution (S cm^{-1}).

t = Liquid film thickness (cm).

2.12.2 The Mathematical Model

The current distribution in thin liquid films covering a weldment inside a pipeline can be approximated using a one-dimensional model. Only the weld and parent components, which, for simplicity, are assumed to have a flat surface, are within the scope of the model described here. All parameters of the model are defined for a 1 cm width "slice" from the circumference of a pipe. R is the solution resistance for 1 cm width:

$$R = \frac{1}{\sigma t} \qquad \textbf{2.67}$$

t is the liquid film thickness in cm and σ is the solution conductivity in S cm^{-1}.

e is the solution "overpotential" so that if e = 0 no current flows across the interface. It is defined for each of the weldment components and is related to the electrode overpotential, $\eta = E - E_{corr}$, by:

$$\eta = -e \qquad \textbf{2.68}$$

Z, (Ohm cm^2) is the interfacial electrode impedance (or R_{ct}) for 1 cm width. It is taken to be constant for the different weldment components and equal to the actual polarisation resistance because the electrochemical kinetics are assumed to be linear. This assumption is valid if the metal is only polarised by a few millivolts from its corrosion potential. The symbol Z is used to avoid confusion with the solution resistance.

$$\frac{di}{dx} = -\frac{e}{Z} \qquad \textbf{2.69}$$

and

$$\frac{de}{dx} = -iR \qquad \textbf{2.70}$$

To define the current and potential distributions Equation 2.69 and 2.70 are combined and the equation solved resulting in Equation 2.71.

$$\frac{d^2e}{dx^2} = \frac{R}{Z}(e - e_{corr}) \qquad \textbf{2.71}$$

This can be solved for each of the weld and parent components and the combined results used to satisfy the system conditions of no potential discontinuities and no net current.

Defining:

$$\alpha^2 = \frac{R}{Z} \qquad \textbf{2.72}$$

The general solution to Equation 2.71 is:

$$e(x) = C_1 \exp(\alpha x) + C_2 \exp(-\alpha x) \qquad \textbf{2.73}$$

The solution potential at x = 0 can be defined as e_0 (further definition later) and, considering the weld metal, symmetry dictates that no current flows across the plane at the weld centre, therefore the other boundary condition is:

$$\left(\frac{de}{dx}\right)_{x=l} = 0 \qquad \textbf{2.74}$$

l is half the width of the weld metal i.e. the distance between the weld and parent junction and the weld centre. These boundary conditions give:

$$C_1 + C_2 = e_0$$

$$C_1 \exp(\alpha l) - C_2 \exp(-\alpha l) = 0 \qquad \textbf{2.75}$$

Solving for C_1 and C_2 and substituting into Equation 2.73 gives:

$$e(x) = \frac{E_0 \cosh[\alpha(l-x)]}{\cosh[\alpha l]} \qquad \textbf{2.76}$$

The total net current on one half of the weld, indicated by using the subscript *w*, is given by:

$$I_w = -\frac{1}{R}\left(\frac{de}{dx}\right)_{x=0} \qquad \textbf{2.77}$$

or by:

$$I_w = \int_0^l \frac{e}{Z_w} dx \qquad \textbf{2.78}$$

Both Equations 2.77 and 2.78 result in:

$$I_w = \frac{e_{0w}}{\sqrt{RZ_w}} \tanh(\alpha_w l) \qquad \textbf{2.79}$$

A positive value for I_w indicates a net cathodic current on the weld, and

$$\alpha_w = \sqrt{\frac{R}{Z_w}} \qquad \textbf{2.80}$$

Equations 2.76 and 2.80 are general expressions and are applicable for any length of electrode, including the parent metal. However the parent can be considered to be of infinite length. As *l* tends to infinity Equation 2.76 reduces to:

$$e(x) = e_{0p} \exp(-\alpha_p x) \qquad \textbf{2.81}$$

α_p is defined similarly to α_w and Equation 2.79 becomes:

$$I_p = \frac{e_{0p}}{\sqrt{RZ_p}} \qquad \textbf{2.82}$$

To define the behaviour of the coupled weld and parent metals it should be considered that there is no overall net current:

$$I_w + I_p = 0 \qquad \textbf{2.83}$$

Because there is no discontinuity in the solution potential at the weld and parent metal junction:

$$e_{0w} - e_{0p} = \Delta E = E_{corr,w} - E_{corr,p} \qquad \textbf{2.84}$$

Where the E_{corr} values are the uncoupled potentials of the individual weld and parent components.

Combining Equations 2.83 and 2.84 with 2.79 and 2.82 gives:

$$e_{0w} = \frac{\Delta E \sqrt{Z_w}}{\sqrt{Z_w} + \sqrt{Z_p}\tanh(\alpha l)} \qquad \textbf{2.85}$$

and

$$e_{0p} = \frac{-\Delta E \sqrt{Z_p}\tanh(\alpha l)}{\sqrt{Z_w} + \sqrt{Z_p}\tanh(\alpha l)} \qquad \textbf{2.86}$$

Where α is α_w as defined in Equation 2.80.

The galvanic current between the components of the segmented electrode is determined using Equations 2.79 and 2.85 (or 2.82 and 2.86).

$$I_g = \frac{\Delta E \tanh(\alpha l)}{\sqrt{R}\left[\sqrt{Z_w} + \sqrt{Z_p}\tanh(\alpha l)\right]} \qquad \textbf{2.87}$$

A positive I_g indicates that the weld metal is the net cathode. The R and α terms are dependent on liquid film thickness and therefore affect the resulting I_g.

The local electrode potential, E(x), is given by:

$$E(x) = E_{corr} - e(x) \qquad \textbf{2.88}$$

The local corrosion rates, or anodic dissolution rates, i_a, can be calculated from the uncoupled corrosion rates and the potential distribution, assuming linear current-potential relationships:

$$i_a = i_{corr}\left(1 - \frac{e(x)}{\beta_a}\right) \qquad \textbf{2.89}$$

β_a is the anodic Tafel slope.

It is therefore possible, knowing the polarisation resistances of the uncoupled weld and parent metals and the potential difference between them as well as the solution resistivity, to model the corrosion behaviour of a suitable electrode at different liquid film thicknesses.

3.0 Experimental

In this chapter the compositions of the specimen materials and the different test solutions will be described followed by the design of the electrodes and experimental set up. Finally a description of the electrochemical tests performed during each experiment will be detailed.

3.1 Materials

An Artificial weldment electrode was prepared to simulate real low-alloy parent and weld metals. The compositions of the two low-alloy steels are given in Table 3.1.

Table 3.1 The chemical compositions of the "weld" and "parent".[81]

	Elemental composition (%)								
	C	**Ni**	**Si**	**Mn**	**P**	**S**	**Cr**	**Mo**	**Fe**
"Weld"	0.36 /0.44	1.3 /1.7	0.1 /0.35	0.45 /0.7	0.035	0.04	1.0 /1.4	0.2 /0.35	96.52 /96.39
"Parent"	0.148	0.065	0.175	0.799	0.01	0.032	0.069	0.014	98.69

A weldment specimen from an actual weldment failure from joint 3 of the Arco/Waveney platform flowlines (referred to as the Waveney weld) was also tested to evaluate the model. The composition of the weld and parent (pipe and tee) metal are given in Table 3.2.

Table 3.2 The chemical compositions of the Waveney weld, pipe (parent) and tee metals.[71]

	Elemental composition (%)										
Component	**C**	**V**	**Si**	**Mn**	**P**	**S**	**Cr**	**Mo**	**Ni**	**Cu**	**Fe**
Weld	0.05	<0.003	0.31	1.19	0.012	0.008	<0.01	0.01	0.85	0.02	97.54
Pipe	0.15	0.033	0.32	1.39	0.015	<0.003	0.11	0.01	0.06	0.04	97.87
Tee	0.13	0.05	0.2	1.18	0.015	<0.003	0.08	0.03	0.1	0.21	98.00

The Cr and Ni content of the artificial weld metal was high in comparison to the parent metal, which is often typical of low-alloy steel weldments in oil and gas pipelines to ensure that the resulting weld is cathodic relative to the parent. It was the intention of this work to produce a situation where the weld metal had a higher intrinsic corrosion rate than the parent pipe because of the higher Ni content but had the more noble potential of the couple.

3.1.1 Electrode Fabrication

The weldment area of Waveney joint 3 was polished to 600 μm grit and etched with 3 % Nital to distinguish the parent pipe, heat-affected zone (HAZ) and weld metal. The weld and parent metal components of the Waveney electrodes were removed from the Waveney Spool (Figure 3.1) and machined to suitable dimensions, the HAZ was not used. Two lengths of parent metal for each electrode were 6 cm long and two pieces of weld metal were 3 cm and 1 cm in length. All widths were 1 cm and the heights of the components were 2 – 3 mm.

Two electrodes were assembled, a standard-sized weld metal using the 1 cm^2 piece of weld metal (referred to as Standard) and one wider than would be normally fabricated using the 3 cm^2 piece of weld metal (referred to as "Wide" rather than long because in a pipeline the length would be considered to be the circumference of the weld). The component dimensions of the two electrodes are shown in Figure 3.2 a.

The Artificial electrode in Figure 3.2 b) was constructed using the metals with the compositions tabulated in Table 3.1. The components had two parent metals of 4.5 cm long and a weld metal 1.2 cm long. The width of all components was 1 cm with heights of 2 - 3 mm.

Figure 3.1 A cross-section of joint 3 of the Waveney Spoolpiece after polishing and etching.

The following method for preparation of the electrodes applies to both the Waveney and artificial weldment electrodes. Polythene covered Nichrome wire was spot-welded to the rears of the components before the faces were fixed to the bottom of a Perspex mould with adhesive and the weld and parent metals were separated by acetate film, 12 - 13 μm thick.

Once firmly in position, the components were immersed in Araldite resin and when fully set, the mould was broken away. Two holes of 1.0 mm diameter were drilled at the top of the electrode, approximately 2.0 mm distance from the top parent metal in which the platinum wire auxiliary electrode (AE) was threaded through after the face of the electrode was polished to 1.0 μm grit.

Figures 3.2 a) and b) show the dimensions of the electrodes and the locations of the salt bridge Luggin probes in relation to the electrode surfaces. The connecting wires were spot-welded onto the rears of the three components.

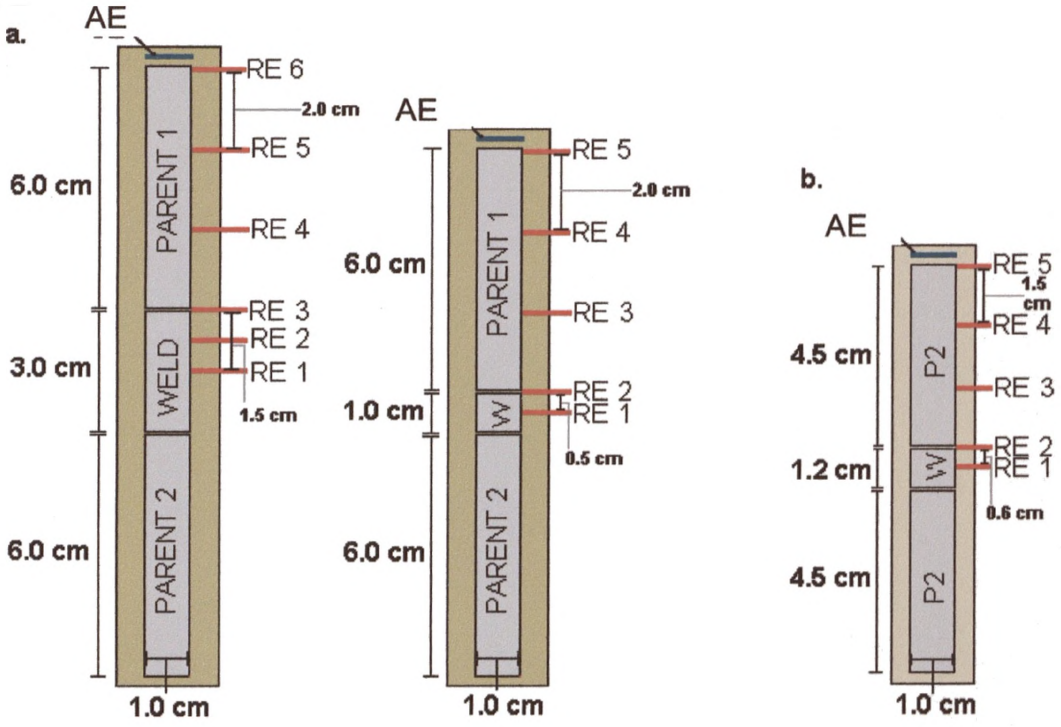

Figure 3.2 a) The Wide and Standard Waveney and **b)** the Artificial weldment electrodes.

3.2 Experimental Set-up

To allow one-dimensional current behaviour, two perspex side-walls were attached to the face of the electrode either side of the edges of the weld and parent metals along the length of the electrode. One of the lengths of perspex had holes drilled through the sides to secure the ends of the Luggin probes to be flush with the inside wall, so that when attached to the electrode, they would correspond to the desired location to measure potential. Another piece of perspex was attached to the top of the two lengths of perspex to secure them in place.

A 1 Litre electrochemical cell was modified by adding a side-arm which enabled manual adjustment the liquid film thickness using a perspex rod attached to a similar piece of square Perspex, as described above, that fitted snugly between the two perspex side walls and covered the electrode components. The perspex rod adjuster was calibrated by marking millimetre increments where the rod entered and exited the side-arm, this was done prior to sealing the cell and adding the solution. The set-up of

a typical experiment is illustrated in Figures 3.3 a) and b). Five Luggin probes are shown in the figure but there was an additional Luggin probe for the Wide weld electrode experiment.

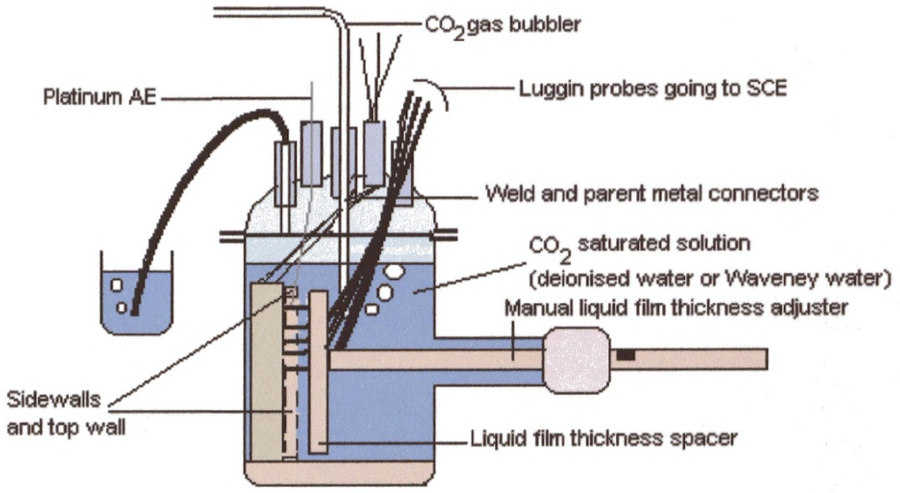

Figure 3.3 a) The set-up of a typical weldment electrode experiment.

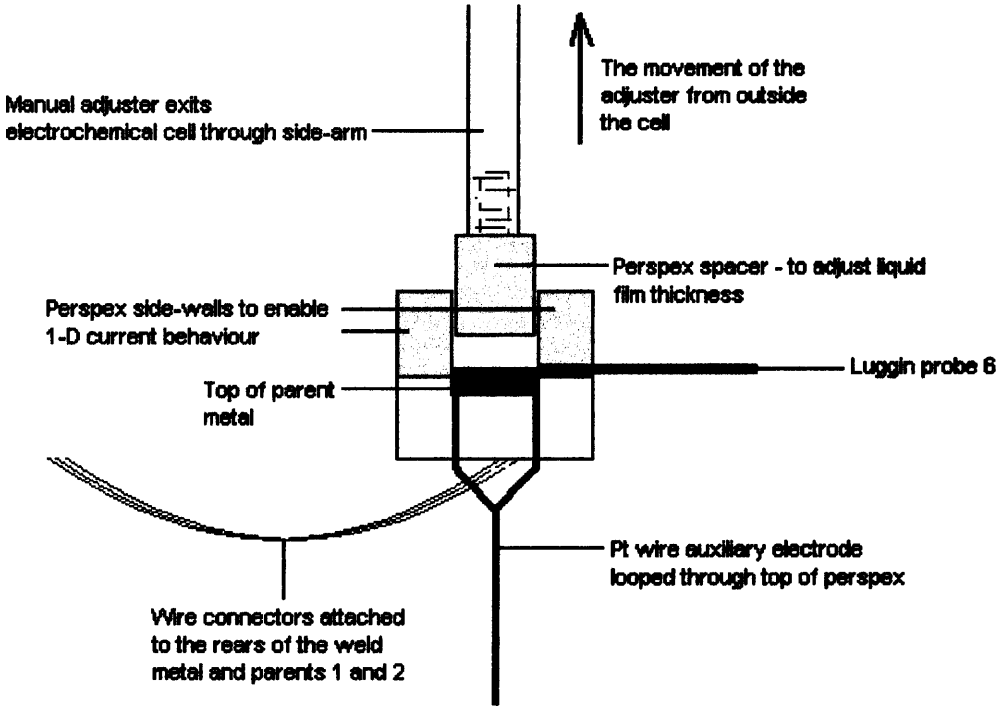

Figure3.3 b) The top view of an electrode in the electrochemical cell highlighting the spacer enabling one-dimensional current behaviour.

3.2.1 Solution Chemistry

The solution used in the Artificial weldment work was CO_2 saturated de-ionised water to minimise conductivity so that the behaviour of the current and potential distributions could be studied with high solution resistance. For the Waveney electrode experiments, a solution was prepared with NaCl and $NaHCO_3^-$ to have the chloride and bicarbonate content, but omit the other constituents of the formation water in which the failures occurred. The results of the actual solution analysis i.e. the solution composition are given in Table 3.3. The total dissolved solids in the solution were 414 ppm and the service temperature was 60° C. The solution was prepared using de-ionised water to contain 215 ppm Cl^-, 49 ppm HCO_3^- and 160 ppm Na^+. The solution, referred to as artificial Waveney solution, was also saturated with CO_2 prior to and during experimental work.

To obtain a solution containing 215 ppm Cl^- and 49 ppm HCO_3^-:

1 M NaCl = 58.44g

1 M $NaHCO_3$ = 83.98g

For Cl^-: 58.44g/35.5g=1.65

$\therefore$ 1.65*0.215g Cl^- =<u>0.355g NaCl</u>

For HCO_3^- : 83.98g/60.99g=1.38

$\therefore$ 1.38*0.049g HCO_3^-= <u>0.067g $NaHCO_3$</u>

Table 3.3 Waveney water content.[82]

Species	Na^+	K^+	Ca^{2+}	Mg^{2+}	Ba^{2+}	Sr^{2+}	Fe^{3+} (soluble)
$mg.L^{-1}$	0	1.5	116	<1	<1	<1	30

Species	Fe (total)	Cl^-	SO_4^{2-}	CO_3^{2-}	HCO_3^-	OH^-
$mg.L^{-1}$	45	215	1.9	<1	49	<1

The experiments for both types of electrode were performed at ambient temperature. It was not considered necessary to perform all of the experiments at the service temperature because the current and potential behaviour at ambient temperature would reflect the behaviour at the elevated temperature but with a larger galvanic current. However one experiment was performed with the Standard Waveney electrode at 60° C with the electrochemical cell immersed in a thermostatically controlled water bath.

3.3 Weldment Electrodes - Experimental Work

The duration of each experiment was one to three weeks. The galvanic current and potential monitoring was ongoing throughout this period and when these measurements indicated that the system had stabilised a series of tests were then performed daily, which involved ceasing the continuous monitoring. Some tests were only performed once during the whole test.

3.3.1 Galvanic Current and Potential Monitoring

An ACM GalvoGill 12 (12 Channel) zero resistance ammeter (ZRA) was used to measure the galvanic current between the weld and parent. The working electrode cable was connected to the weld and the ground cable to the two parent connections. This arrangement measured a cathodic galvanic current if the weld was cathodic relative to the parent and was applied in all experimental work. The galvanic current and coupled potentials measured with the references at all Luggins were logged every minute on a PC.

3.3.2 Liquid Film Thickness Measurements

The thickness of the solution on the surface of the weld and parent metals was adjusted by manually moving the spacer towards or away from the electrode surface. The liquid film thickness measurements were taken each day over the measurement period. For each measurement the spacer was above the electrode with 1.0 cm liquid film thickness initially and this was considered to be bulk solution. The liquid film thickness was then reduced by 0.1cm every minute by moving the spacer toward the electrode surface. The galvanic current and coupled potentials were recorded at each liquid film thickness and with the references at all of the Luggin probes. The measurements were repeated by moving the spacer in the same increments away from the electrode surface. The error in the gap spacing was taken to be ±0.25 mm due to possible movement of the electrode in the fixture on the bottom of the cell in relation to the perspex rod liquid film thickness adjuster.

3.3.3 Modified Linear Polarisation Resistance Measurements

After each galvanic current and coupled potential measurement at the different liquid film thicknesses the weld and parents metals were uncoupled in order to perform linear polarisation resistance (LPR) measurements using an ACM Gill DC potentiostat.

The LPR is referred to as "modified" because the intention of the test was not to directly gain an accurate value of Rp because area correction was not applied, but to study the potential behaviour of the weld and parent metals at different liquid film thicknesses. The schematic set up of the tests is shown in Figure 3.4 and a typical plot of a polarisation sweep of the Tafel region of an electrode is shown in Figure 3.5.

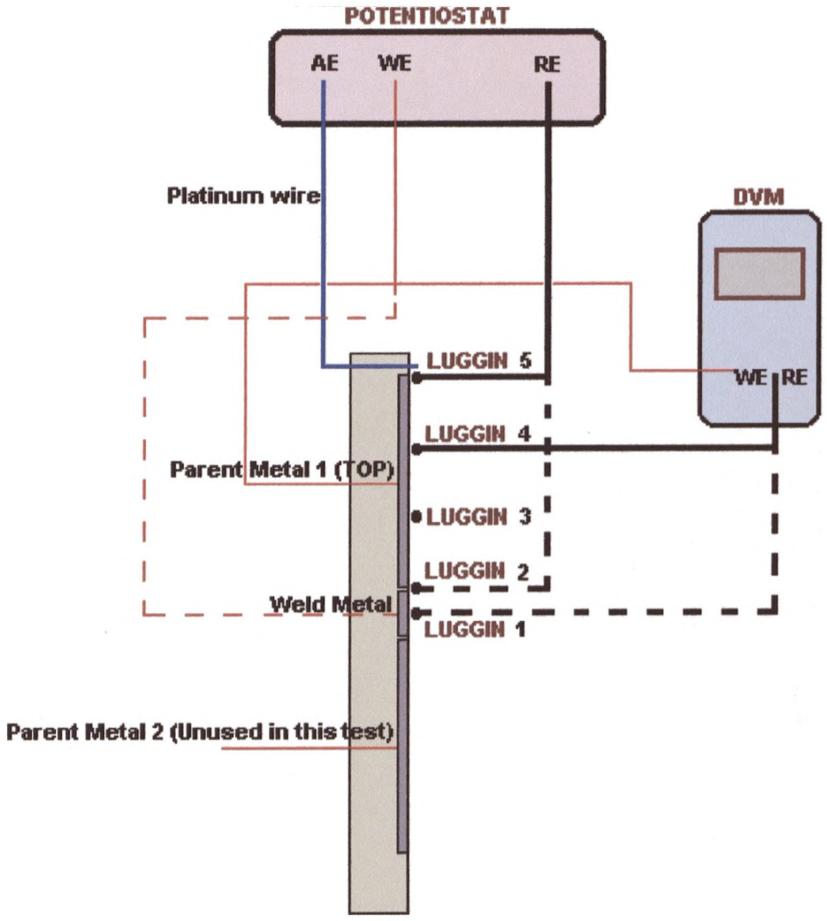

Figure 3.4 A schematic showing the weldment electrode and the modified LPR set up.

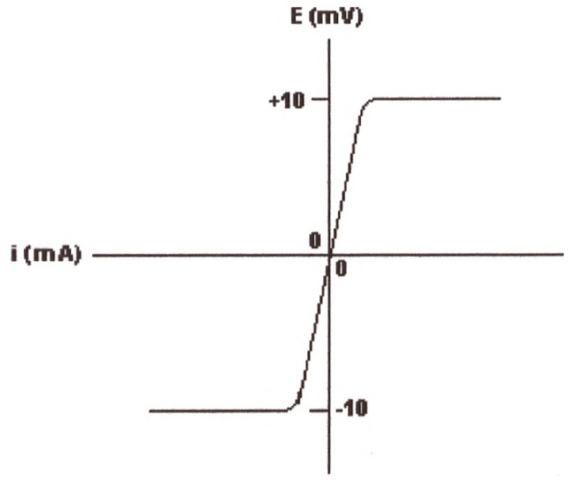

Figure 3.5 A representation of a 20 mV potential step.

3.3.3.1 The Parent Metal

For the parent metal, the working electrode (WE) was the top parent metal component of the electrode. The reference electrode (RE) was the Luggin at reference electrode 5 (6 for the Wide Waveney electrode) that was at the end of the parent metal component next to the platinum wire auxiliary electrode (AE). The uncoupled potential of the parent metal was measured at the locations of both Luggins prior to applying a potential step of 20 mV around E_{corr} to measure Rp (Figure 3.5). Each measurement was performed at the liquid film thicknesses 1 cm, 0.75 cm, 0.5 cm and 0.25 cm and lasted four minutes and were repeated twice for reproducibility.

The WE was also connected to a separate digital voltmeter (DVM) to measure the uncoupled potential on the metal surface with respect to the reference at Luggin 4 (5). When the potential step was performed, the potential measured with the reference at Luggin 4 (5) was recorded with the DVM when it was polarised cathodically, and then anodically to obtain values for potential change at the different liquid film thicknesses.

A reduction in potential change measured at Luggin 4 (5) would be expected with decreasing liquid film thickness for the parent and weld metals. The LPR measurement at varying liquid film thickness is illustrated in Figure 3.6.

3.3.3.2 The Weld Metal

The same procedure was performed using the weld metal as the WE, which was connected to the potentiostat and the DVM. Uncoupled rest potentials were obtained at the locations of both Luggin probes on the weld metal surface using the potentiostat and the DVM. The reference at Luggin 2 was connected to the potentiostat and Luggin 1 was connected to the DVM in order to measure the potential change in the centre of the weld metal when the potential step was performed using the reference at the weld and parent metal interface. The distance between the positions of Luggins 1 and 2 were much less than the distances between Luggins 5 (6) and 4 (5) so a larger potential change at the location of Luggin 1 would be measured at the equivalent liquid film thicknesses.

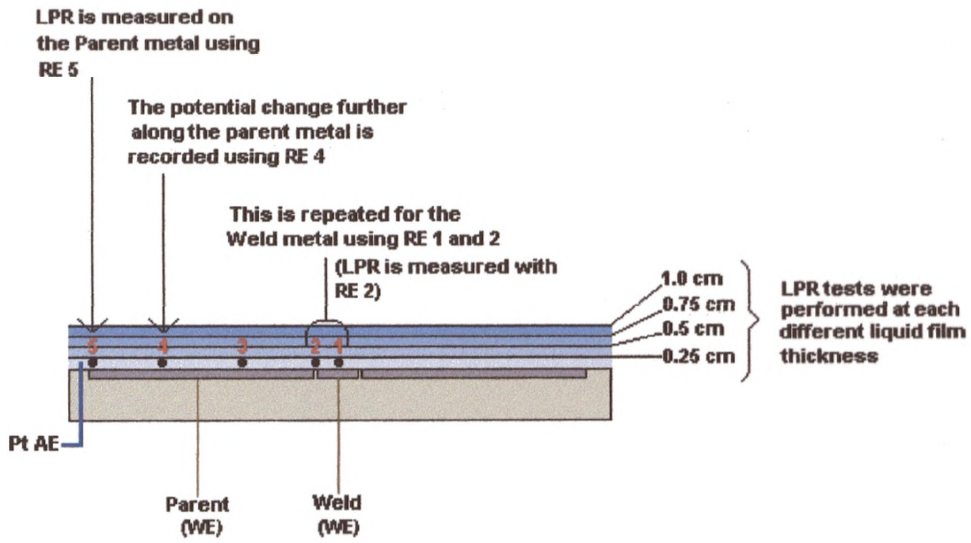

Figure 3.6 The modified LPR measured at varying liquid film thicknesses.

3.3.4 AC Impedance

AC measurement techniques were used to study the potential and current behaviour of the weld and parent metals of the Standard Waveney electrode in ambient conditions and at 60° C with liquid film thicknesses of 1.0, 0.75, 0.5 and 0.25 cm, without area correction. Impedance measurements were only taken once for each liquid film thickness and component during the whole experiment because they took considerably longer to perform than LPR tests.

The Pt wire was the AE and the REs were at Luggins 2 and 5 for the weld and parent metals (WEs) respectively. A Schlumberger SI 1280 Electrochemical Measuring Unit was used and the amplitude of the waveform was 10 mV and the frequency range was 10 kHz to 0.1 Hz. The set up was similar to that of the modified LPR testing without the DVM in Figure 3.4.

For the impedance measurement of the Standard Waveney weldment electrode at 60° C, the RE at Luggin 3 was used instead of Luggin 5 to study the ac current and potential distribution at a location on the parent metal further away from the AE.

3.3.5 Potentio-dynamic Measurements

At the end of the ZRA and modified LPR analyses, potentio-dynamic sweeps were performed on the weld and parent metals with area correction of all the weldment electrodes in bulk solution using an ACM Gill DC potentiostat.

The cathodic polarisation was undertaken first with sweep of 0 to -150 mV (SCE), where 0 mV was the free corrosion potential. The anodic polarisation was then performed from 0 to +1500 mV (SCE).

3.3.6 pH and Solution Conductivity

The pH was measured at the beginning and at the end of each experiment using a bench pH meter probe inserted into the electrochemical cell. The meter was calibrated with pH 4, 7 and 10 standard buffers before each measurement.

The conductivity was recorded with a hand held probe and a reading was taken every day of the experiment or whenever possible. The instrument was calibrated against KCl standards.

3.3.7 Additional Tests

LPR tests were also performed using the Artificial weldment electrode to study the effect of current and potential distribution with distance away from the auxiliary electrode.

For the Wide Waveney weldment electrode only, the Cl^- content of the artificial Waveney solution was increased from 215 ppm of the standard Waveney solution to 2150 ppm and then to 21500 ppm after approximately 9.6 and 11.5 days of immersion. The purpose of this was to study the effects of increasing solution conductivity on the galvanic current and potential.

A Potential step LPR measurement was performed using an ACM Gill DC potentiostat with the reference at Luggins 1 to 5 so that values for Rp were obtained at the location of each Luggin probe with the liquid film thickness fixed at 1.0 cm. The parent metal was the WE for LPR measurements with the reference at Luggins 2 to 5 and was exchanged for the weld metal when Luggins 1 and 2 served as the RE.

Luggin 2 was used as reference for the parent and the weld metal because of its location at the component interface.

3.4 Waveney Weld and Parent Metal Coupons

Individual coupons of the weld and parent metals from joint 3 of the Waveney failure were tested for three reasons:

1. To obtain actual individual corrosion rates and potentials for the Waveney weld and parent metals at the different temperatures and in the environments in which the weldment electrodes were tested.
2. To analyse the effect of long-term coupling on the weld and parent metal individual potentials and Rp values.
3. To obtain corroded specimens suitable for SEM-EDX analysis.

3.4.1 Preparing the Weld and Parent Metal Coupons

Four pieces of weld and four of parent metal, all approximately 1 cm^3, were cut from the failed weldment. One side of each piece was polished to 1200 grit so that it was flat enough to be positioned in a mould. 40 cm of Nichrome wire was spot-welded to the rear of the flat side and covered with a 30 cm length of polythene tube before Araldite resin was poured in to the mould and left to set for 24 hours. When the resin was hardened, the mould was removed and the flattened face of the electrode was polished to 1 μm with grinding paper and diamond paste and degreased with ethanol prior to testing.

3.4.2 Experimental Set-up

The four pairs of weld and parent metal coupons were set up in four electrochemical cells and immersed in 3.5% NaCl (to increase conductivity) with 49 ppm HCO_3^- solution (Figure 3.7) as follows:

1. Coupled at ambient temperature.
2. Uncoupled at ambient temperature.
3. Coupled at 60 °C.
4. Uncoupled at 60 °C.

A schematic of the coupled and uncoupled tests are shown in Figure 3.7 a and b. The experiments performed at 60 °C were immersed in a thermostatically controlled water bath and the surface areas of each of the weld and parent metal coupons are given in Table 3.4.

Table 3.4 Surface areas of parent and weld metal coupons (cm^2).

	Initially Coupled Ambient Temp.	**Initially Uncoupled Ambient Temp.**	**Initially Coupled 60° C**	**Initially Uncoupled 60° C**
Parent	1.08	1.2	1.2	1.1
Weld	1.2	1.8	0.84	0.8

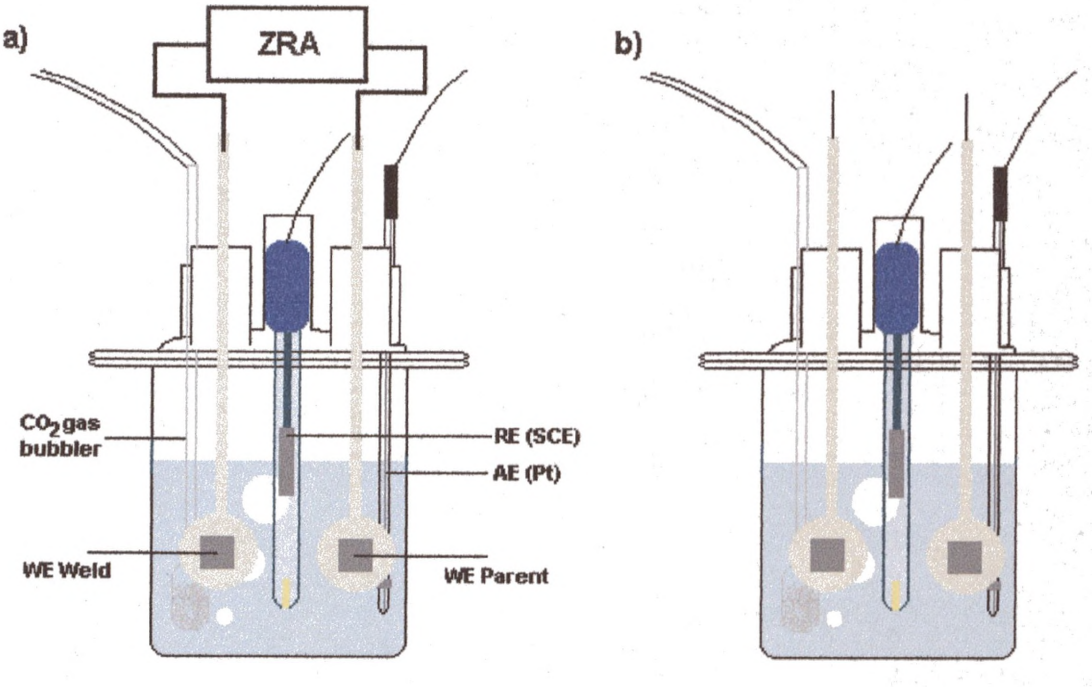

Figure 3.7 The coupled and uncoupled weld and parent metal coupon set-up.

3.4.3 Experiments

The following experiments were performed over a period of 23 days. After 15 days the coupling was swapped to the previously uncoupled pairs of electrodes to study the potential and Rp response of the coupons.

3.4.3.1 Galvanic Current and Potential Monitoring

The two pairs of coupled weld and parent metal coupons were connected to a ZRA, the GalvoGill 12, which continuously measured the galvanic current and coupled potential at a rate of one reading per minute. The data was logged directly onto a PC.

3.4.3.2 Linear Polarisation Resistance

The coupled coupons were uncoupled for a short time to take a potential step LPR measurement of all eight coupons to determine the Rp and individual potentials using an ACM Gill DC potentiostat. A potential step of 20 mV was applied, with area correction, each measurement lasted four minutes and was repeated twice per coupon for reproducibility. The Rp was measured in this manner for each coupon once every day.

3.4.3.3 AC Impedance

The ac impedance measurements were performed of all of the coupons on day 7, using a Schlumberger SI 1280 Electrochemical Measuring Unit, to compare the values of corrosion rate obtained with the measured LPR values. The amplitude of the waveform was 10 mV and the frequency range was generally 1000 Hz to 0.01 Hz. However for the weld metal coupons at ambient temperature it was appropriate to use the range 10 kHz to 0.01 Hz. The rest potentials of all of the coupons were also measured prior to the impedance measurements.

3.4.3.4 Potentio-dynamic Measurements

Once the ZRA and LPR analyses were completed, polarisation sweeps were performed on the weld and parent metals of all the weldment electrodes in bulk solution using an ACM Gill DC potentiostat with area correction.

In the same method as the weldment electrodes the cathodic polarisation was performed first with sweep from 0 to -150 mV (SCE), where 0 mV was the free corrosion potential and then the anodic polarisation from 0 to +1500 mV (SCE).

3.4.4 Scanning Electron Microscopy – Energy Dispersive X-ray (SEM-EDX)

EDX analysis is an elemental analysis technique used in conjunction with Scanning Electron Microscopy (SEM). The surface of a sample, which must be conducting, is bombarded with a finely focused beam of electrons, typically of 3-20 keV in energy. A transfer of energy occurs which excites a core electron into an orbital of higher energy, and once in this excited state the atom has two possible modes of relaxation: emission of a X-ray (EDX), or emission of an Auger electron. X-rays are emitted in the case of high-energy transitions involving inner electron orbitals. The X-rays emitted have energies characteristic of the target element, and by detecting them it is possible to obtain qualitative and/or quantitative chemical analysis of the target area.

The surfaces of the weld and parent metals were examined uncorroded, polished to 1 μm with diamond paste, following a corrosion test at ambient temperature and after testing at 60° C using an Amray 1810 scanning electron microscope equipped with EDX analysis facilities. Analyses of the surfaces were generally performed at 500X magnification, which gave an area of analysis of 65 μm x 65 μm using accelerating voltages of 10 and 20 keV.

4.0 Results of the Artificial Weldment Electrode Testing

The following chapter will describe the results obtained from the experiments performed using low-alloy steels typically used as the base metal and weld filler metal in pipelines. Throughout the experiment the "weldment" electrode was immersed in de-ionised water for the static CO_2 bubble test. This solution was used to study the effects of minimal solution conductivity on the current and potential distributions. The geometry of the weld metal part of the electrode was 1.0 cm by 1.2 cm and for the two parent components 4.5 cm by 1.0 cm.

The duration of the experiment was approximately 17 days and in this period the various tests were undertaken everyday if possible. For simplicity a typical three days of testing were taken from the experiment and used as examples in this chapter.

4.1 Coupled Potential and Galvanic Current with Time

Figure 4.1 shows the coupled potential of the weld and both parent metals when the salt bridge Luggin 1 (weld metal centre) is used as the reference for measuring this potential. The coupled potential is found to be predominantly between –685 and –694 mV for the duration of the measurement (approximately 17 days). Thin peaks are clearly visible at ten locations on the graph, coinciding with when the solution thickness on the surface of the weldment was reduced for the liquid film thickness measurements, prior to the weld and parent metals being briefly uncoupled for the modified linear polarisation resistance (LPR) experiments. These experiments appear to have affected the trend of the coupled potential with time on the ten occasions to a lesser or greater extent. The potential has increased slightly, by up to approximately 3 mV after some experiments and then returned to a stable coupled potential within 30 hours.

The potentials measured with the reference at Luggins 2 (weld and parent interface) and 5 (the remote parent) are shown in Figure 4.3. Both plots reveal an initial drop in potential and then relatively stable potentials measured throughout the experiment with some fluctuation due to the liquid film thickness and modified LPR tests. Generally, there is a measured potential difference of approximately 10 mV between the interface of the weld and parent metal and the end of the parent.

Figure 4.2 shows the galvanic current (*ig* μA) with time, again for the weld and both parent metals. The galvanic current is negative indicating that the weld metal is the cathode in the couple. The current increases linearly throughout the measurement from around –5 μA to –26 μA. This plot also highlights the effects of changes in solution thickness and uncoupling with greater clarity than the plot of coupled potentials by the ten peaks reaching zero current. A slight decrease in the current can be seen to coincide with the increase in potential in Figure 4.1 after some uncoupling and solution thickness experiments. The plots suggest that it appears to takes up to 30 hours for the uncoupling effect to subside and return the system to a stable coupled potential with steadily increasing galvanic current.

4.2 Liquid Film Thickness - Potentials and Galvanic Currents

Figure 4.4 a, b and c show the average value of two measured coupled potentials plotted against ten liquid film thicknesses (0.1 cm intervals) up to 1.0 cm. Three sets of data are shown corresponding to Luggin locations 1, 2 and 5 along the length of the artificial electrode. These results are summarised below in Table 4.4. The distances between the Luggins are 0.6 cm (1 and 2) and 5.0 cm (1 and 5).

It is clear from examining the graphs that there is a potential difference of approximately 25 mV between the weld centre and the remote parent (salt bridge 5) when the liquid film thickness is considerable and the two components are coupled. On all three of the days shown here, the weld centre and weld/parent interface show a potential increase by about 2 mV between 1.0 cm and 0.4 cm. The potential measured at Luggin 5 changes very little at high and low solution thickness. At a distance of 5.0 cm away from the weld centre, the remote parent potential remains unpolarised at low solution thicknesses and high solution resistance.

Table 4.4 Summary of measured coupled potentials against liquid film thickness.

	Day		
Luggin	**2**	**5**	**11**
1	From 1.0 to 0.4 cm, changes from -690.5 mV to -687.5 mV. To 0.1 cm, decreases to -693.5 mV	From 1.0 to 0.4 cm, increases to from -691 mV to -689 mV. To 0.1 cm, decreases to -693 mV.	From 1.0 to 0.4 cm, increases from -691 mV to -688 mV. To 0.1 cm, decreases to -693.5 mV.
2	From 1.0 to 0.3 cm, remains at -704 mV. To 0.1 cm, decreases to -707 mV	From 1.0 to 0.4 cm, remains at about -705 mV. To 0.1 cm, decreases to –707 mV.	From 1.0 to 0.4 cm, increases from -705 mV to -701 mV. To 0.1 cm, decreases to -701.5 mV
5	Remains at -716 mV at all thicknesses.	Remains at -716 mV at all thicknesses.	Remains at -716 mV at all thicknesses.

The data used to prepare Figure 4.5, galvanic current (ig μA) against liquid film thickness, was simultaneously gathered with the potentials for Figures 4.4 a, b and c described above. The plotted values are the average of two measurements at each solution thickness and are summarised in Table 4.5.

Table 4.5 Summary of measured coupled potentials against liquid film thickness.

Day		
2	**5**	**11**
From 1.0 to 0.1 cm, a smooth change from -14.8 to -7 μA.	From 1.0 to 0.1 cm, a smooth change from –17.8 to -6.5 μA.	From 1.0 to 0.6 cm, a smooth change from –23.5 to -20.5 μA. To 0.1 cm, a sharp change to –9 μA.

The galvanic current becomes increasingly negative with time and also can be seen to decrease smoothly with decreasing liquid film thickness.

4.3 Modified LPR Tests and the Application of the Mathematical Model

The data obtained from the modified LPR measurements were used in equations to generate a valid comparison of the model with the experimental data.

Table 4.1 a, b and c displays the polarisation resistance (Rp) data for the weld and parent metal surfaces at 1.0 cm and 0.5 cm liquid film thickness. The measured Rp ($Rp_{measured}$) values are taken directly from experimental work measurements. No area correction was given to these results because it was known that the current distribution was not uniform in these experiments.

The $Rp_{measured}$ at 1.0 cm are smaller than at 0.5 cm, however on day 5 the weld metal with a liquid film thickness of 0.5 cm has a value is approximately 100 Ohm lower than at 1.0 cm. This inconsistency in the electrochemical measurement results in a non-concurrent value for R_{calc}. Equation 2.81 was used to calculate α, where α is defined by Equation 2.80, for the parent and weld metals (disregarding the parent subscripts). Where e_0 is the applied potential of 20 mV. $e(x)$ is the potential change, in mV, recorded by the DVM at Luggin 4 (or 1) at a distance of x (1.5 cm or 0.5 cm) from Luggin 5 (or 2), further down the parent (or weld) metal. R_{calc}, the actual solution resistance, is calculated from $Rp_{measured}$ and the α values, using Equation 4.1.

$$R_{calc} = \alpha \times Rp_{measured} \qquad \textbf{4.1}$$

$$Z_{calc} = \left(\frac{Rp_{measured}}{\sqrt{R_{calc}}} \right)^2 \qquad \textbf{4.2}$$

Z_{calc}, the interfacial Rp is obtained using Equation 4.2. The corrosion rates, in mm y^{-1}, are listed Table 4.2 are calculated using Equation 4.3 where z = atomic mass, ρ = density (kgm^{-3}), $n = 2$, 96500 = Faraday's constant, a Stern-Geary constant of 17 mV, 3153600 is time in seconds and the Z_{calc} values from Table 4.1 a, b and c are the Rp values.

$$((((z \times (0.017 \div Rp))/(n \times 96500))/\rho) \times 10) \times 3153600 \qquad \textbf{4.3}$$

4.3.1 Polarisation Resistance at Different Locations on the Electrode

Figure 4.6 illustrates the different $Rp_{measured}$ recorded when Luggins 1 to 5 (RE) are used to measure the Rp at 0.5 cm liquid film thickness. In the circuit, the AE is closest to the parent metal (WE), at the location of Luggin 5 (Figure 3.2 b). The polarisation of the parent electrode is 20 mV at the location of Luggin 5 because of its proximity to the auxiliary electrode (AE).

Luggin 4 is 1.5 cm further away from the AE therefore the circuit has increased solution resistance. To polarise the metal surface at the location of Luggin 4 more current is applied that polarises the metal between the reference and the AE by more than 20 mV giving a Rp value of almost half of that measured using Luggin 5. The Rp measured for Luggin 3 is also approximately half of that at 4 and the Rp at Luggin 2 is less, but not half of Luggin 3. The Rp measured with Luggin 2 for the weld metal is 750 Ohm – over 100 Ohm more than at the location of Luggin 1.

4.3.2 Uncoupled Potentials

The individual electrode potentials of the weld and parent metals measured on days 2, 5 and 11 can be found in Table 4.3. The three values vary little with time and the average potentials are –712.17 and –686.5 mV for the parent and weld metals

respectively. The mean potential difference between the two components is 25.67 mV in these conditions.

4.4 Solution Conductivity

The solution conductivity in Figure 4.7 shows the calibration of the conductivity meter plotted against the standard conductivities of known KCl molar concentrations, which provides reasonably straight line. The plot against time on the second x-axis shows the change in conductivity of the solution measured throughout the experiment. The solution conductivity was also calculated from the weld and parent metal R_{calc} values using Equation 2.67, where t is the liquid film thickness (1 or 0.5 cm) and plotted against time in Figure 4.7.

The conductivity increases from about 650 μS to 5000 μS over 5 days, it then rises steadily until the end of the experiment reaching about 8500 μS. This increase in conductivity coincides with the increase in galvanic current shown from Figure 4.4 a, b and c at 1.0 cm liquid film thickness.

4.5 pH

On commencing the experiment (shortly after the electrode was immersed in the CO_2 deionised water) the solution pH was 4.9. At the end of the experiment, just before the potentio-dynamic sweeps were performed, the solution was pH 6.02.

4.6 Polarisation Curves

The results of the potentio-dynamic sweep of the weld metal and parent metal 1 are plotted in Figure 4.8. Only the 0 mV to –800 mV part of the curves are shown because resistance greatly affected both of the anodic sweeps. The anodic current of the parent metal appears to be greater than that of the weld metal.

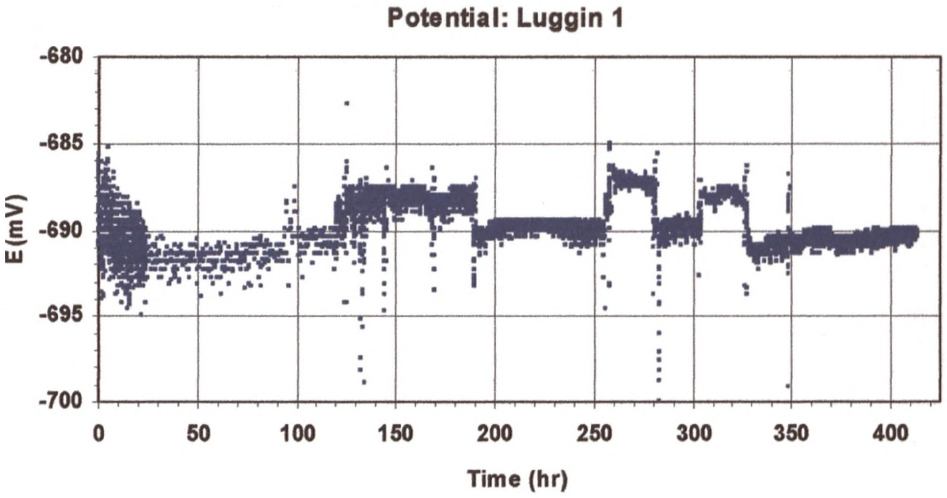

Figure 4.1 The coupled potential measured throughout the experiment with the reference in the weld metal centre.

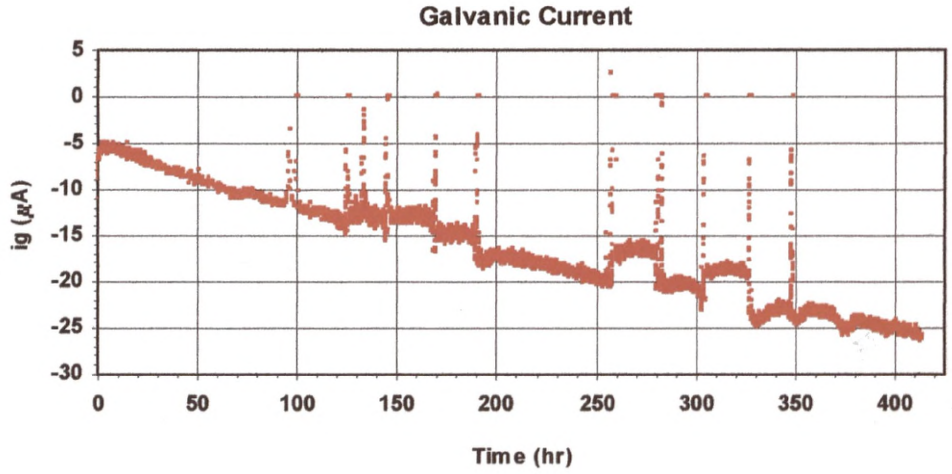

Figure 4.2 The galvanic current measured throughout the experiment between the weld and parent metals.

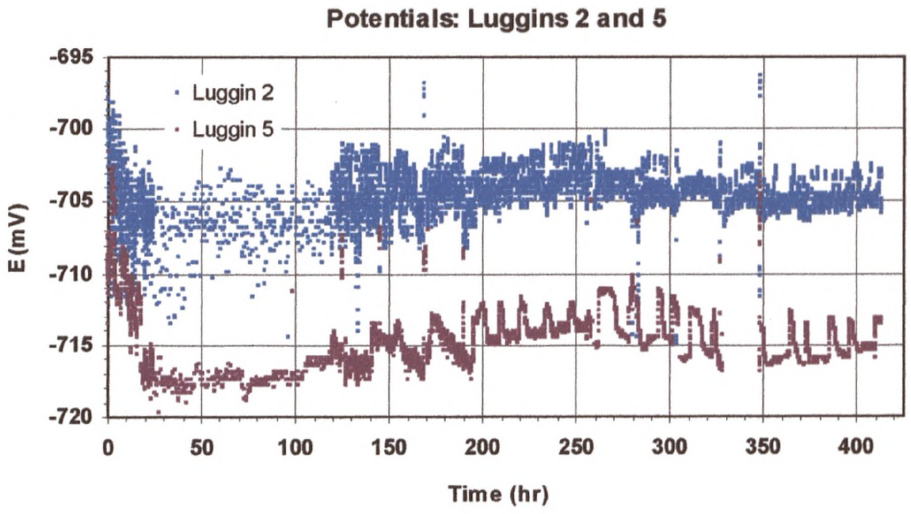

Figure 4.3 The coupled potentials measured throughout the experiment at the weld and parent interface (2) and the remote parent metal (5).

a)

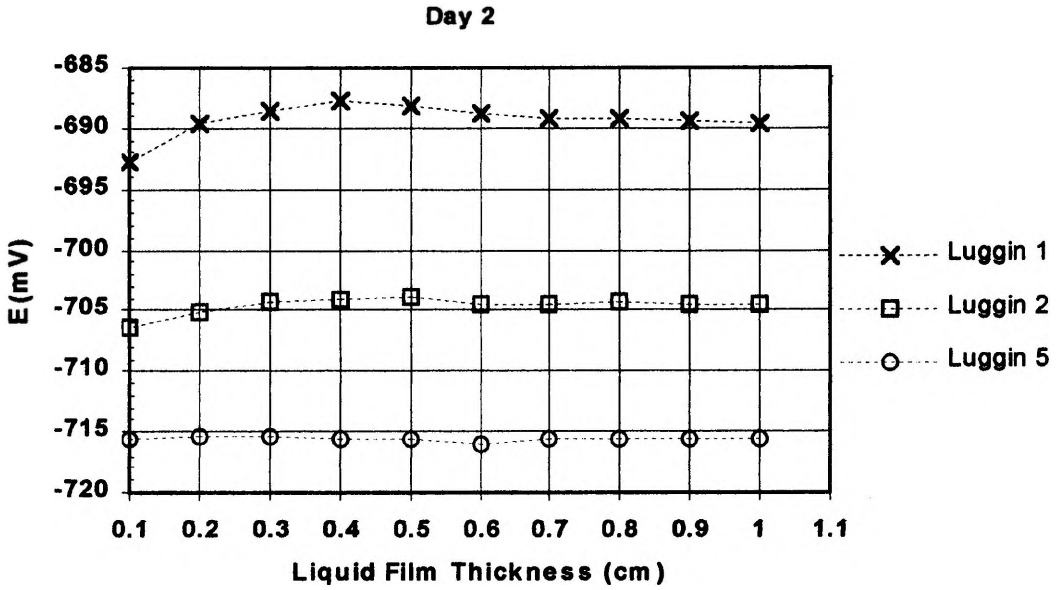

Figure 4.4 (a, b and c) The coupled potentials measured at the weld metal centre (1), the weld and parent interface (2) and the remote parent (5) at different liquid film thicknesses.

b)

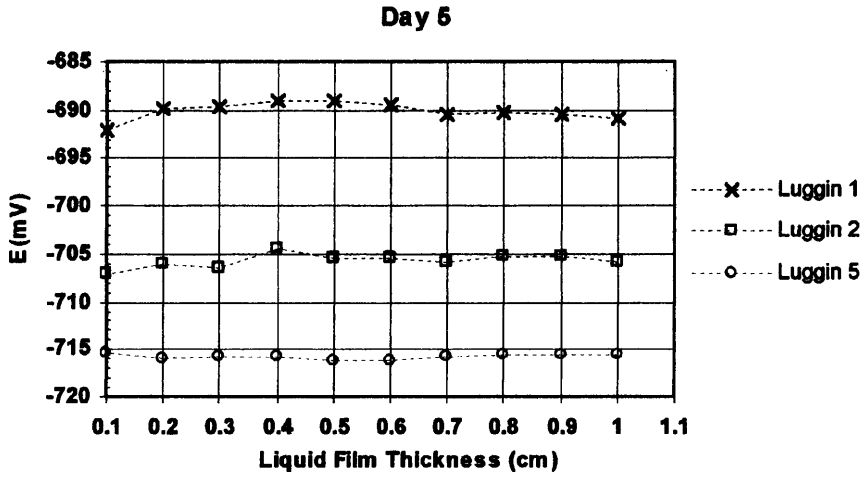

c)

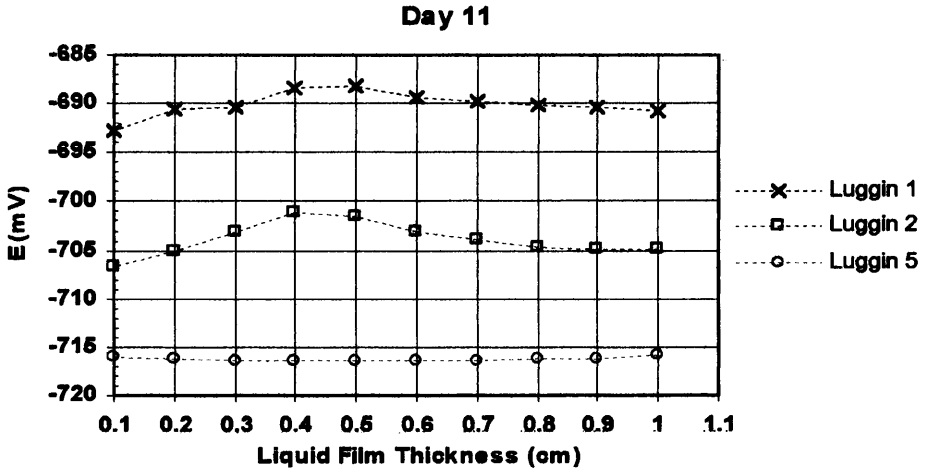

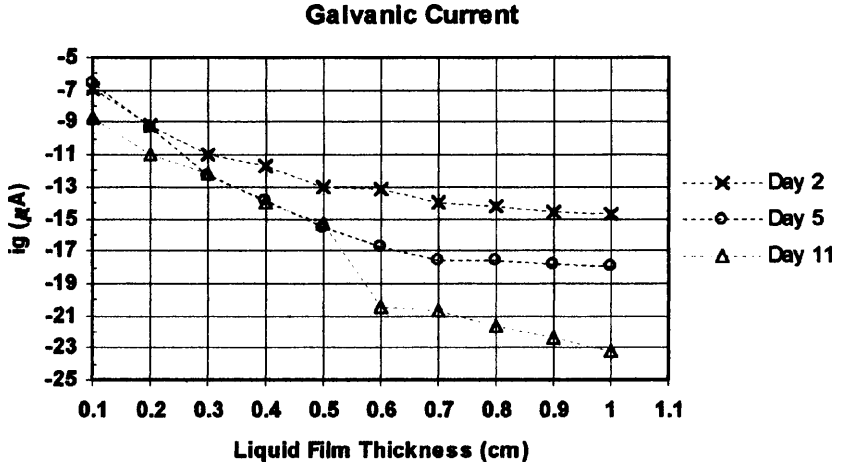

Figure 4.5 The galvanic current between the weld and parent metals measured at different liquid film thicknesses.

Luggin	1	2 (WM)	2 (PM)	3	4	5
$Rp_{measured}$	630	750	570	650	1230	2550

Figure 4.6 The Rp values measured with references at locations on the weld (1, 2) and parent metals (2, 3, 4 and 5) in 0.5 cm liquid film thickness.

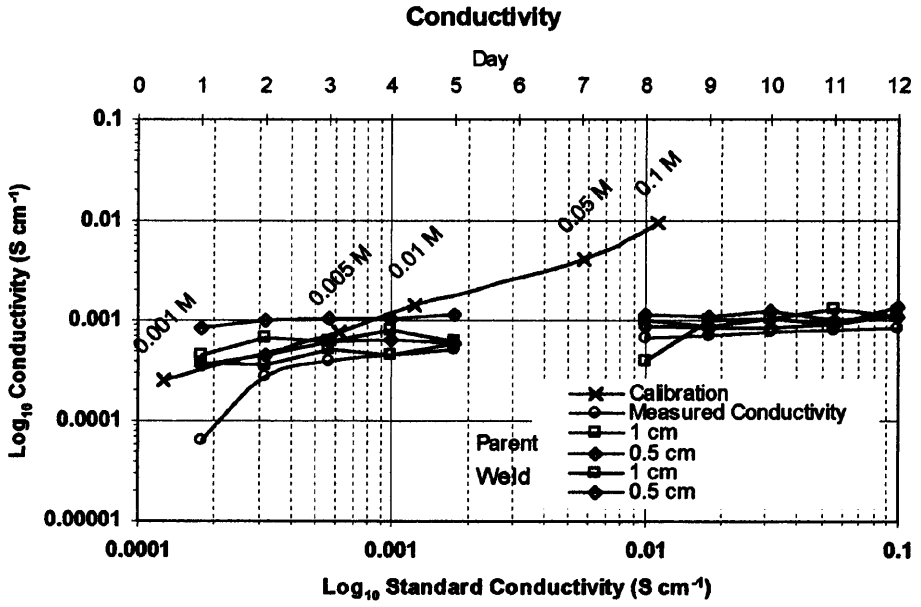

Figure 4.7 The measured conductivity of the solution and the calibration. The conductivities calculated from R_{calc} are also plotted.

Table 4.1 (a, b and c) The measured and calculated data from modified LPR tests.

a)

Day 2

	Liquid film thickness (cm)	$Rp_{measured}$ (Ohm)	e_x (x = 1.5 cm) e_0 = 20 mV	α calc	R_{calc} (Ohm)	Z_{calc} (Ohm cm^2)
Parent	1	1770	2	1.54	2717	1153
	0.5	2440	1.33	1.81	4405	1352
			e_x (x = 0.6 cm) e_0 = 20 mV			
Weld	1	1068	8.67	1.39	1489	766
	0.5	1137	7	1.75	1989	650

b)

Day 5

	Liquid film thickness (cm)	$Rp_{measured}$ (Ohm)	e_x (x = 1.5 cm) e_0 = 20 mV	α calc	R_{calc} (Ohm)	Z_{calc} (Ohm cm^2)
Parent	1	1213	2.5	1.39	1682	875
	0.5	1860	1.33	1.81	3358	1030
			e_x (x = 0.6 cm) e_0 = 20 mV			
Weld	1	1024	7.67	1.60	1636	641
	0.5	932	6.33	1.92	1786	486

c)

Day 11

	Liquid film thickness (cm)	$Rp_{measured}$ (Ohm)	e_x (x = 1.5 cm) e_0 = 20 mV	α calc	R_{calc} (Ohm)	Z_{calc} (Ohm cm^2)
Parent	1	851	2.83	1.30	1109	653
	0.5	1297	1.67	1.66	2148	783
			e_x (x = 0.6 cm) e_0 = 20 mV			
Weld	1	636	9.83	1.18	753	537
	0.5	1012	6	2.01	2031	504

Table 4.2 The corrosion rates calculated from Z_{calc}.

Corrosion rate (mm y^{-1})			
Day	L.F.T. (cm)	Parent	Weld
2	1	0.17	0.26
	0.5	0.15	0.31
5	1	0.23	0.31
	0.5	0.19	0.41
11	1	0.31	0.37
	0.5	0.25	0.40

Table 4.3 The uncoupled potentials of the weld (1) and parent 1 (4) metals.

	Uncoupled Potential (mV)	
Day	Luggin 4	Luggin 1
2	-711.9	-686.5
5	-712	-687
11	-712.6	-686

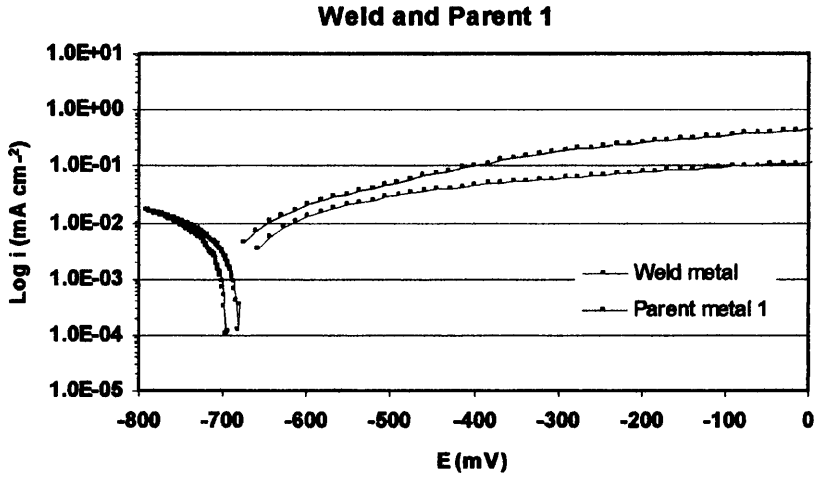

Figure 4.8 The polarisation curves of the weld and parent metals in bulk solution.

5.0 Results of the Waveney Weldment Electrodes Testing

The results from the experimental work performed using two weldment electrodes created from joint 3 of the Waveney failure are presented here. There are three parts to this section – work from the Standard weld and Wide weld in Waveney solution at ambient temperature and the Standard weld in Waveney solution at 60°C. The results are selected from a typical three days of testing from each of these experiments.

5.1 The Standard Weldment Electrode

This section details the results obtained from the experiments performed using the Standard weldment electrode, assembled from the parent metals (6 cm long, 1.0 cm wide) and weld (1.0 cm^2) metals of joint 3. The duration of the galvanic current and potential logging at five Luggins was approximately 224 hours (9.3 days) and for short periods in this time the weld metals and parent metals 1 and 2 underwent galvanic current and potential measurements with varying liquid film thickness and were uncoupled for modified LPR measurements. All potentials quoted here are with reference to saturated calomel electrodes (SCE).

5.1.1 Potential and Galvanic Current

The potential recorded at Luggin 1, at the weld metal centre (Figure 5.1) was recorded at a rate of one measurement per minute with the exception of a 48 hour period mid-experiment where the measurements were once every fifteen minutes. The potential can be seen to rise from about -725 mV to –710 mV in 150 hours after which it increases slightly to –706 mV and remains at this value for the final 40 hours of logging. Some of the more negative peaks of the potentials from the measurements at different liquid film thicknesses are visible at 68, 90, 140 and 160 hours into the experiment.

The initial galvanic currents recorded between the weld and parent metals 1 and 2 in Figure 5.2 are negative and within the first 100 hours of logging the current appear to hover largely between –2 and –5 μA. Over the remaining 124 hours the current changes, reaches zero and finally becomes positive measuring almost 1 μA at

the conclusion of the experiment. The current peaks from the liquid film thickness tests are also visible on this plot.

The potentials measured at Luggins 2 and 5, the weld/parent metal 1 interface and the top of parent metal 1 are plotted in Figure 5.3. The potential behaviour recorded using Luggin 2 is virtually identical to that at Luggin 1 and Luggin 5 also exhibits a similar pattern but with an overall potential approximately 5 mV more negative. The liquid film thickness measurement peaks are also clearly visible in these plots.

5.1.2 Liquid Film Thickness – Coupled Potentials and Galvanic Currents

The potential change with liquid film thickness (0.1 to 1.0 cm) is shown for three tests in Figure 5.4 a, b and c and a summary of the potential behaviour is given in Table 5.4. Each point is the average of two values measured at Luggins 1, 2 and 5.

Luggins 1 and 2, unsurprisingly exhibit similar potential behaviour although the Luggin 1 potentials appear to be slightly more positive. Luggin 5 potentials are noticeably more negative than the above by 3 – 4 mV at all thicknesses on days 1 and 3 and approximately 2 – 3 mV on day 5. All of the Luggins recorded an overall potential increase chronologically, which is consistent with the findings of Figures 5.1 and 5.3. The increase in potential at Luggin 5 on day 3 and 5 between 0.3 and 0.1 cm is unexpected and is perhaps associated with the Luggin interface in the sidewall being cut-off by the spacer.

Table 5.5 Summary of coupled potential behaviour at different liquid film thicknesses on the Standard Waveney electrode

	Luggin 1	**Luggin 2**	**Luggin 5**
Day 1	From 1.0 to 0.4 cm, a decrease from -718.7 to -719.6 mV. 0.4 to 0.2 cm, no change. 0.2 to 0.1 cm, increases to -719.3 mV	From1.0 to 0.3 cm, a decrease from -719.4 mV to -720.8 mV. 0.3 to 0.1 cm, increases to -720.6 mV.	Changes little from 1.0 to 0.4 cm. 0.4 to 0.1 cm, decreases from -723.1 mV to -723.7 mV
Day 3	From 1.0 to 0.3 cm, a decrease from -714 mV to -715.5 mV. From 0.3 to 0.2 cm, increases to –714.8 mV. –714.9 mV at 0.1 cm.	From 1.0 to 0.3 cm, a decrease from -714.3 mV to -715.6 mV. From 0.3 to 0.2 cm, increases to -715 mV. -715.3 mV at 0.1 cm.	From 1.0 to 0.7 cm, decreases from -718.4 mV to -719.3 mV. From 0.7 to 0.3 cm, little change. 0.3 to 0.1 cm, increases from -719.2 mV to -718.7 mV
Day 5	From 1.0 to 0.4 cm, a decrease from -711.4 mV to -712.7 mV. From 0.4 to 0.2 cm, increases to -711.7 mV. -711.8 mV at 0.1 cm.	From 1.0 to 0.3cm, a decrease from -711.7 mV to -713.3 mV. From 0.3 to 0.2 cm, increases to -712.3 mV. -712.6 mV at 0.1 cm.	Overall decrease from 1.0 to 0.3 cm, -714.2 mV to -715.7 mV. 0.3 to 0.2 cm increases to -714.3 mV. -714.4 mV at 0.1 cm.

The galvanic current (*ig*), also an average of two measurements recorded concurrently with the potentials above is shown in Figure 5.5, with a summary in Table 5.5.

Table 5.6 Summary of galvanic current behaviour at different liquid film thicknesses on the Standard Waveney electrode

Day		
1	**3**	**5**
From 1.0 to 0.7 cm, changes from –4 μA to – 3.8 μA. At 0.1 cm, -2.5 μA, a linear change.	From 1.0 to 0.7 cm, changes from -4.2 μA to – 4.4 μA. At 0.1 cm, -2.8 μA, a linear change.	From 1.0 to 0.6 cm, changes from -3.3 μA to – 3.7 μA. At 0.1 cm, -2.2 μA, a linear change.

It is unexpected that the *ig* on day 5 is generally lower than that of days 1 and 3, because the conductivity of the solution should increase with time due to the build up of corrosion products. However this result correlates with the galvanic current taken throughout the whole experiment in that the later liquid film thickness work (i.e. day 5) was performed when the current was tending towards zero.

5.1.3 Modified LPR Tests and the Application of the Mathematical Model

Table 5.1 a, b and c display the data obtained from the LPR measurements performed using the uncoupled weld and parent 1 metals at four liquid film thicknesses.

The $Rp_{measured}$ values of the parent metal at all four thicknesses are average of three values and are lower than those of the weld metal and by examining Figure 5.6 a, b and c, the plot of $Rp_{measured}$ against $1/t^{1/2}$ according to Equation 5.1, it is clear that the parent undergoes a greater change in measured Rp with decreasing liquid film thickness than the weld metal. The weld metal displays higher measured Rp but increases less with lowering liquid film thickness.

$$Rp_{measured} = Z^{\frac{1}{2}} \cdot \left(\rho^{\frac{1}{2}} \cdot \frac{1}{t^{\frac{1}{2}}} \right) \qquad \textbf{5.1}$$

The potential change on the electrode, e_x, is used to calculate α in Equation 2.81 for the weld and parent metal. e_x decreases with lowering of solution thickness on the parent and weld metals and e_0 is 20 mV (±10 mV), the linear polarisation step.

R_{calc}, the actual solution resistance caused by the changing liquid film thickness, is calculated using Equation 4.1 and plotted according to equation 5.2 in Figure 5.7 a, b and c.

$$R^{1/2} \cdot t^{1/2} = \rho^{1/2} \qquad \textbf{5.2}$$

There are, however, a few inconsistent measurements. On day 1, e_x of the weld metal at 1.0 and 0.75 cm are identical therefore giving the same value for α when the expected value would be slightly higher, this results in a lower R_{calc} at 0.75 cm on what might be expected to be a linear slope. Inconsistencies similar to this can be identified for the parent metal on day 3 giving three identical values of e_x at 0.75, 0.5 and 0.25 cm solution thickness leading to lower than expected calculated solution resistances. The weld metal on day 5 has an uncharacteristically low e_x of 7 mV at 0.25 cm; this results in a relatively high α of 2.10, which in turn produces an extremely high R_{calc} of 941 Ohm.

Z_{calc}, calculated using Equation 4.2, is the actual Rp of the individual metals and therefore should not appear to change with varying liquid film thickness. These values vary at different liquid film thickness measurements and on different days where there are inconsistent experimental results. Z_{calc} of the weld metal is found to be between 214 and 585 Ohm cm^2 and 266 and 540 Ohm cm^2 for the parent metal in all three tests. Z_{calc} decreases with time indicating an increase in corrosion rate on both metals surfaces with immersion time.

5.1.4 Corrosion Rates

The corrosion rates in Table 5.2 were calculated using Z_{calc} values and the same variables as the Artificial weldment electrode in Equation 4.3. The corrosion rates vary in accordance with Z_{calc} and would be expected to be similar for the same metal at all liquid film thicknesses.

Average rates for the weld and parent metals for each of the three days are found to be: 0.408 and 0.418 mm y^{-1}, 0.540 and 0.575 mm y^{-1}, 0.588 and 0.603 mm y^{-1} respectively. Although the corrosion rates of the parent metal are slightly higher than the weld metal, there is little difference and these values cannot be considered accurate.

5.1.5 Uncoupled Potentials

The individual potentials of the weld and parent metals in Table 5.3 indicate that the weld is cathodic with respect to the parent and the potential difference is 14, 8.75 and 8.75 mV for days 1, 3 and 5 respectively.

5.1.6 Solution Conductivity

The solution conductivity at the different liquid film thicknesses (1, 0.75, 0.5 or 0.25) was calculated from R_{calc} for the three days using Equation 2.67 and plotted against time in Figure 5.8. The conductivity, recorded by the meter was 6.2 mS cm^{-1} at the beginning of the experiment. The conductivities calculated from the weld metal data are lower than those of the parent metal data. The conductivity increases from days 1 to 3 and should not appear to vary with liquid film thickness.

5.1.7 pH

The pH of the Waveney solution shortly after electrode immersion was 4.8 and at the end of the experiment the solution was pH 5.9, prior to the potentio-dynamic sweep.

5.1.8 Polarisation Curves

The results of the cathodic and anodic potentio-dynamic sweeps for the uncoupled weld metal and parent 1 metal in bulk solution were plotted to produce the polarisation curves in Figure 5.9. The parent metal has a larger cathodic and anodic current than the weld metal and a less noble potential. Only up to 0 mV of the anodic curves are shown because resistance caused them to flatten.

5.1.9 AC Impedance

The Nyquist plots of the impedance responses and the impedance modulus and phase angles (ϕ) plotted against frequency of the parent 1 and weld metals at different

liquid film thicknesses are shown in Figures 5.11 a and b and 5.12 a and b. A linear region is apparent in the high frequency response of the complexes, highlighted by Figure 5.10.

Z_{Rmeas} and Z_{Imeas} are the measured real and imaginary parts of the impedance listed for each measurement at different liquid film thicknesses in Table 5.4. Z_{Rmeas} is the plot on the complex where it is no longer linear (an example shown in Figure 5.10). This point also marks the measurement on the x-axis where the $Z_R - R_s$ is taken and R_s (solution resistance) is the low intercept with the x-axis.

The calculations for the parent metal reveal increasing solution resistance and Z_{Rmeas} with decreasing liquid film thickness. The weld metal R_s also increases with decreasing thickness and is approximately half the amount measured for the parent metal, although the Z_{Rmeas} is larger. Z_{Imeas} generally does not change with varying liquid film thickness, except for the parent metal at 0.25 cm, which may be related to the size of the electrode (6 cm long).

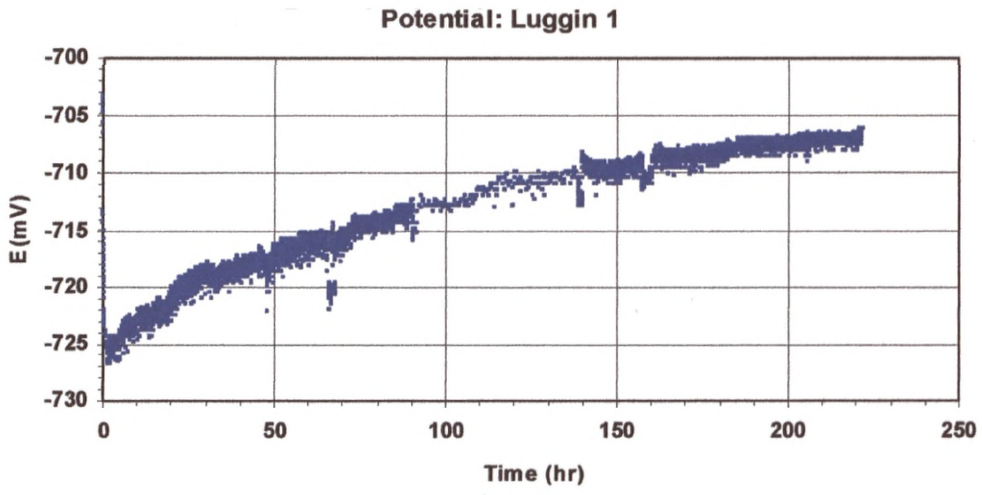

Figure 5.1 The coupled potential measured throughout the experiment with the reference in the weld metal centre.

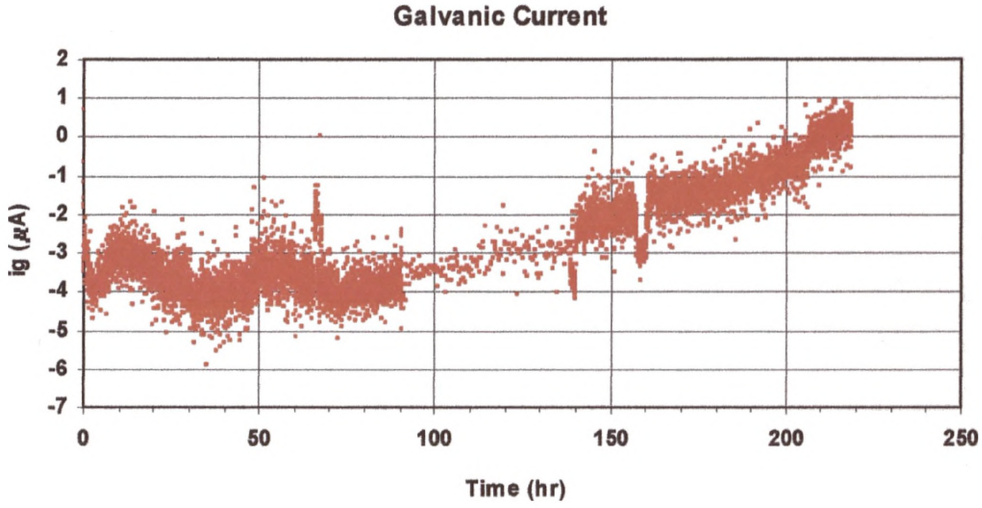

Figure 5.2 The galvanic current measured throughout the experiment between the weld and parent metals.

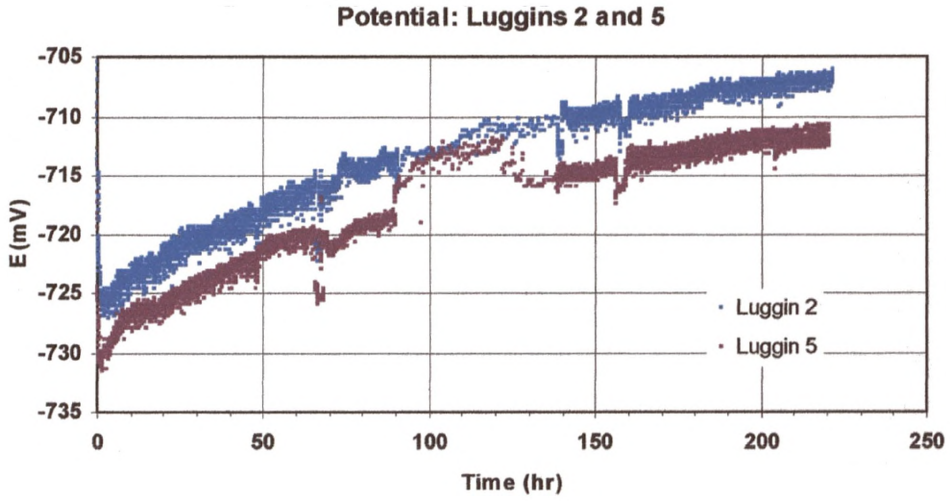

Figure 5.3 The coupled potentials throughout the experiment at the weld and parent interface (2) and the remote parent metal (5).

a)

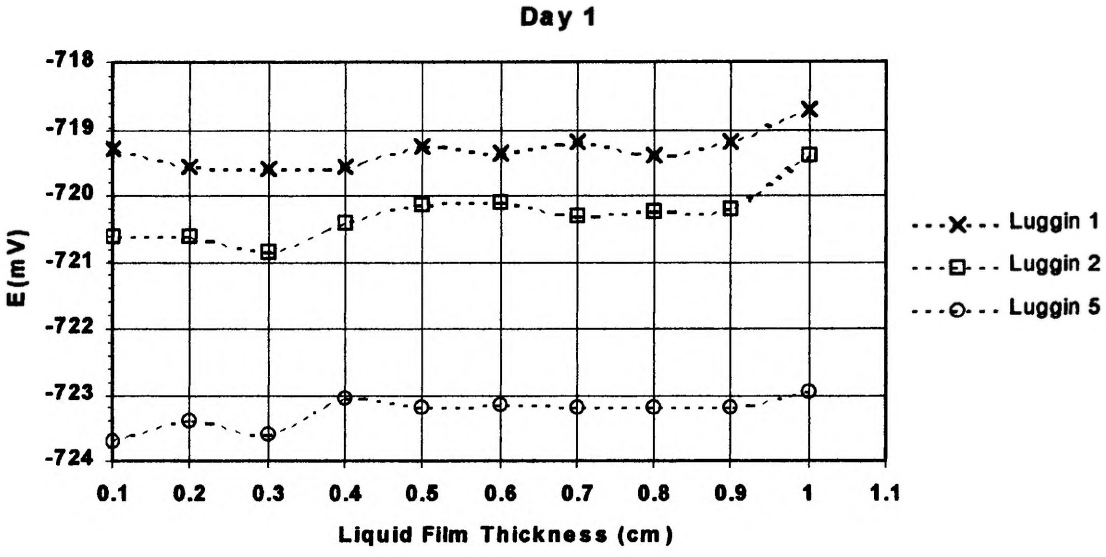

Figure 5.4 (a, b and c) The coupled potentials measured at the weld metal centre (1), the weld and parent interface (2) and the remote parent (5) at different liquid film thicknesses.

b)

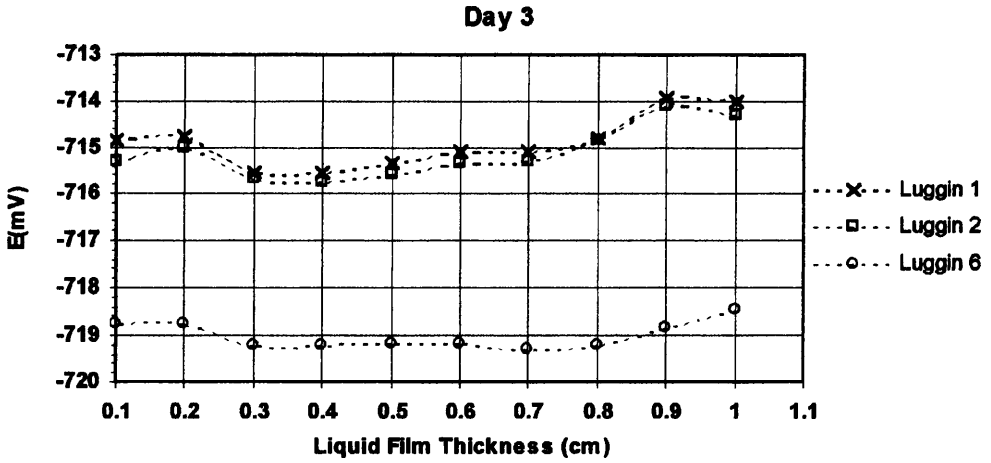

c)

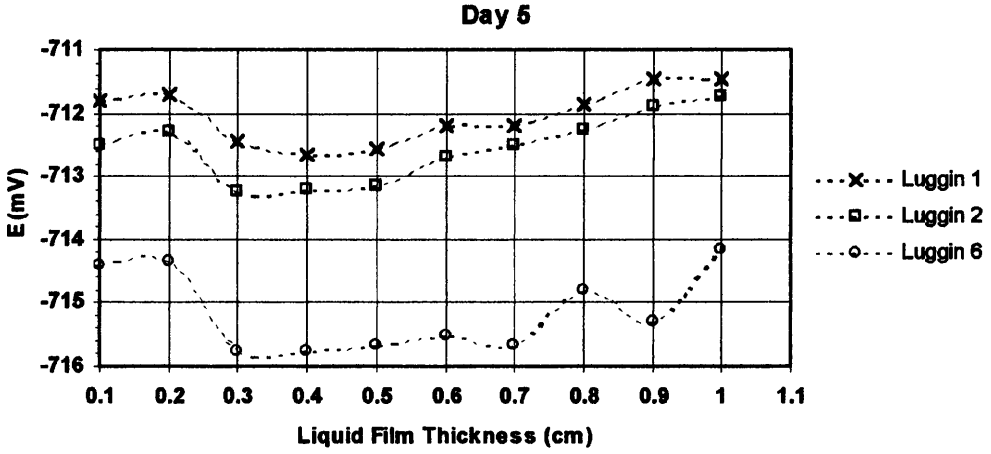

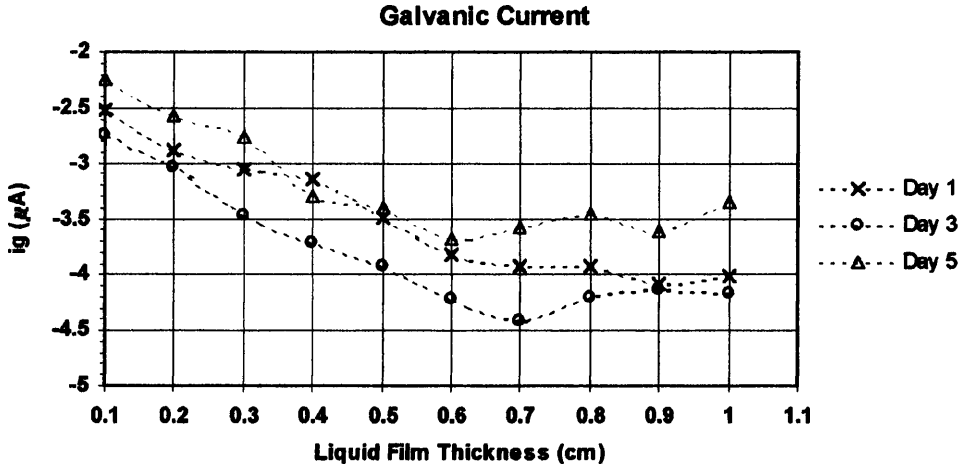

Figure 5.5 The galvanic current between the weld and parent metals measured at different liquid film thicknesses.

Table 5.1 (a, b and c) The measured and calculated data from the modified LPR tests.

a)

Day 1

	Liquid film thickness (cm)	$Rp_{measured}$ (Ohm)	e_x (x = 2.0 cm) e_0 = 20 mV	α calc	R_{calc} (Ohm)	Z_{calc} ($Ohmcm^2$)
Parent	1	168	10.00	0.35	58	483
	0.75	287	6.50	0.56	161	511
	0.5	313	5.50	0.65	202	485
	0.25	376	3.50	0.87	328	431
			e_x (x = 0.5 cm) e_0 = 20 mV			
Weld	1	486	13.00	0.86	418	564
	0.75	504	13.00	0.86	434	585
	0.5	489	11.50	1.11	541	442
	0.25	562	10.00	1.39	778	405

b)

Day 3

	Liquid film thickness (cm)	$Rp_{measured}$ (Ohm)	e_x (x = 2.0 cm) e_0 = 20 mV	α calc	R_{calc} (Ohm)	Z_{calc} ($Ohmcm^2$)
Parent	1	158	8.00	0.46	72	345
	0.75	214	5.50	0.65	138	331
	0.5	172	5.50	0.65	111	266
	0.25	349	5.50	0.65	225	540
			e_x (x = 0.5 cm) e_0 = 20 mV			
Weld	1	396	13.50	0.79	311	503
	0.75	391	12.50	0.94	368	416
	0.5	406	10.50	1.29	523	315
	0.25	428	10.00	1.39	593	309

c)

Day 5

	Liquid film thickness (cm)	$Rp_{measured}$ (Ohm)	e_x (x = 2.0 cm) e_0 = 20 mV	α calc	R_{calc} (Ohm)	Z_{calc} ($Ohmcm^2$)
Parent	1	119	8.67	0.42	50	285
	0.75	152	7.17	0.51	78	297
	0.5	218	6.00	0.60	131	362
	0.25	285	5.00	0.69	198	411
			e_x (x = 0.5 cm) e_0 = 20 mV			
Weld	1	376	13.67	0.76	286	493
	0.75	381	13.00	0.86	328	442
	0.5	397	11.33	1.14	451	349
	0.25	448	7.00	2.10	941	214

a)

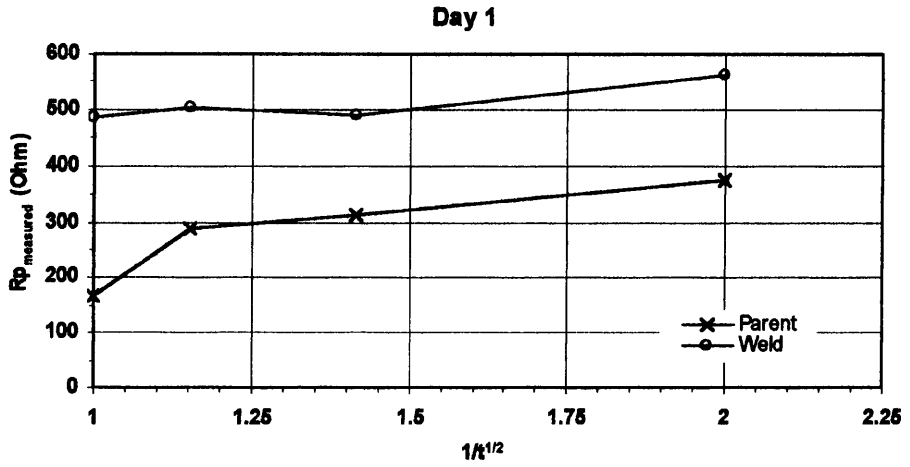

b)

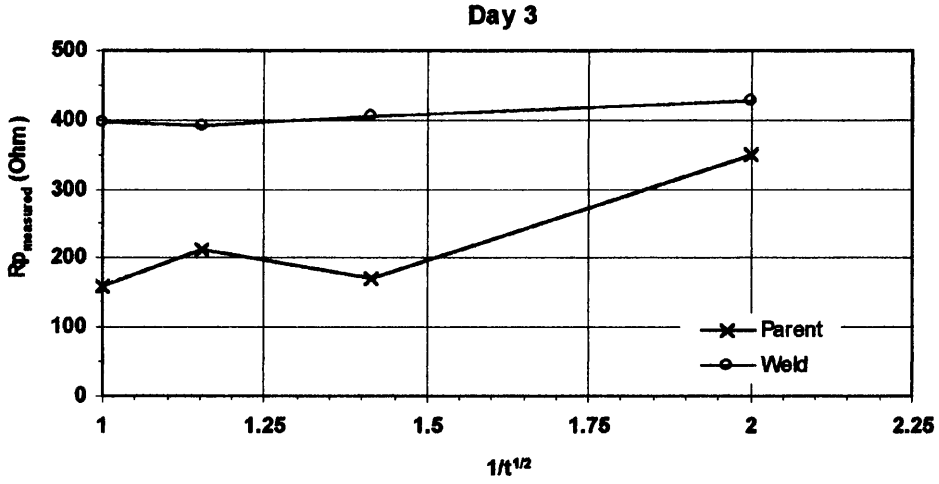

c)

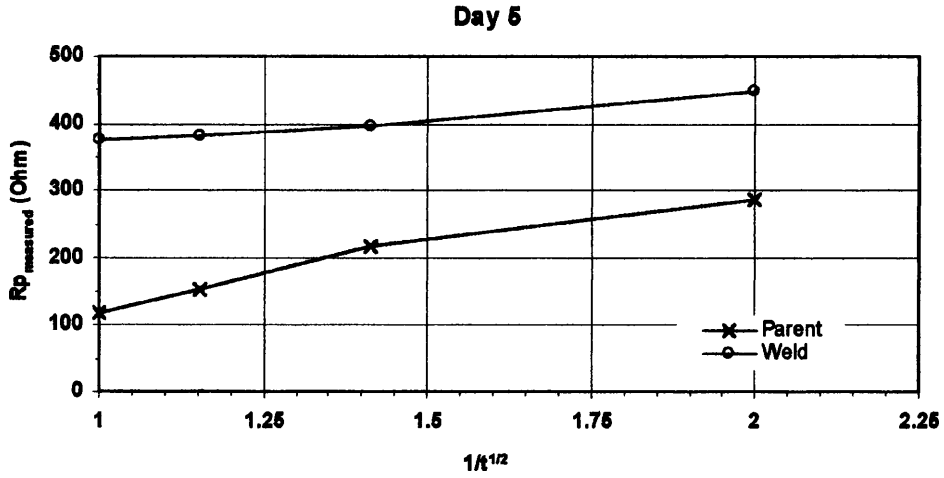

Figure 5.6 (a, b and c) The weld and parent metal 1 measured Rp against liquid film thickness.

a)

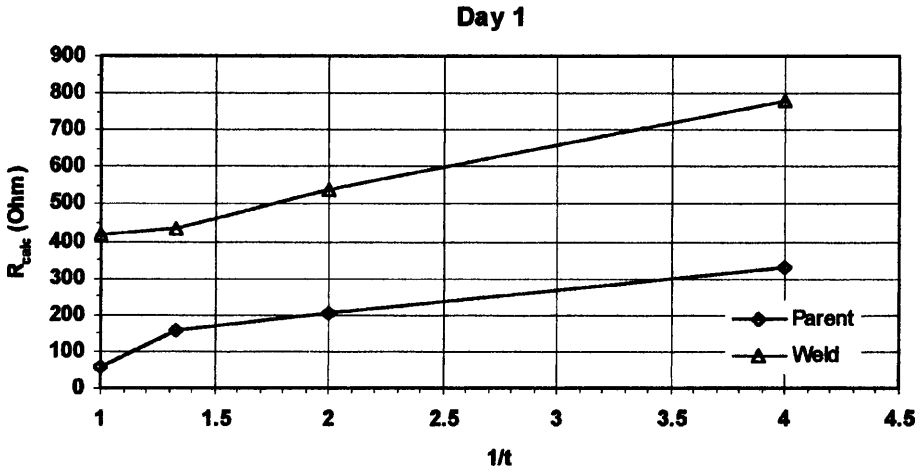

b)

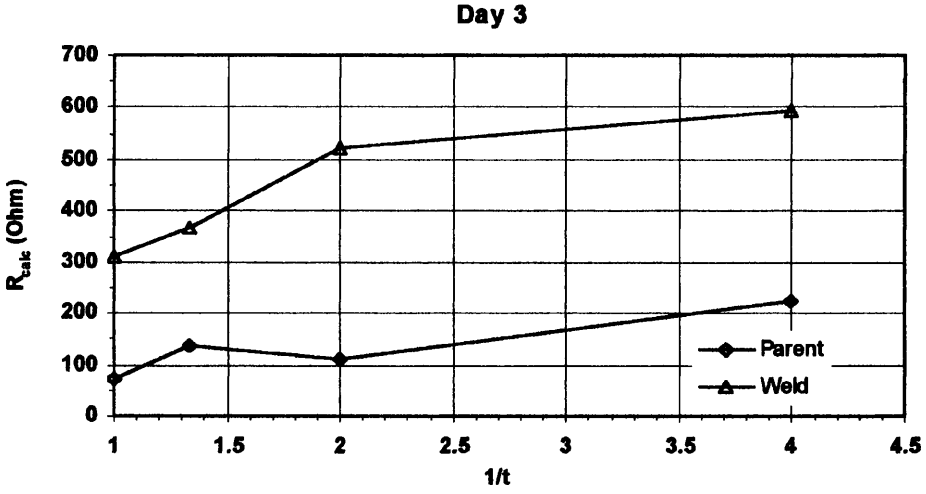

c)

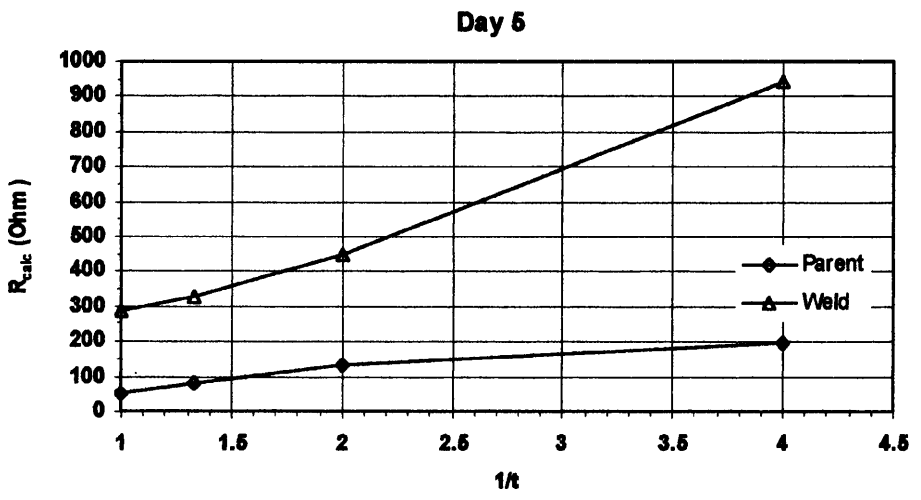

Figure 5.7 (a, b and c) The calculated solution resistance from weld and parent metal 1 data against liquid film thickness.

Table 5.2. The corrosion rates calculated using R_{calc}.

Corrosion rate (mm y^{-1})			
Day	**L.F.T. (cm)**	**Parent**	**Weld**
1	1	0.41	0.35
	0.75	0.39	0.34
	0.5	0.41	0.45
	0.25	0.46	0.49
3	1	0.58	0.40
	0.75	0.60	0.48
	0.5	0.75	0.63
	0.25	0.37	0.65
5	1	0.70	0.40
	0.75	0.67	0.45
	0.5	0.55	0.57
	0.25	0.49	0.93

Table 5.3 The uncoupled potentials of the weld (1) and parent 1 (4) metals.

	Luggin 4	Luggin 1
Day 1	-723.4	-715.3
Day 3	-719.0	-713.3
Day 5	-716.5	-709.8

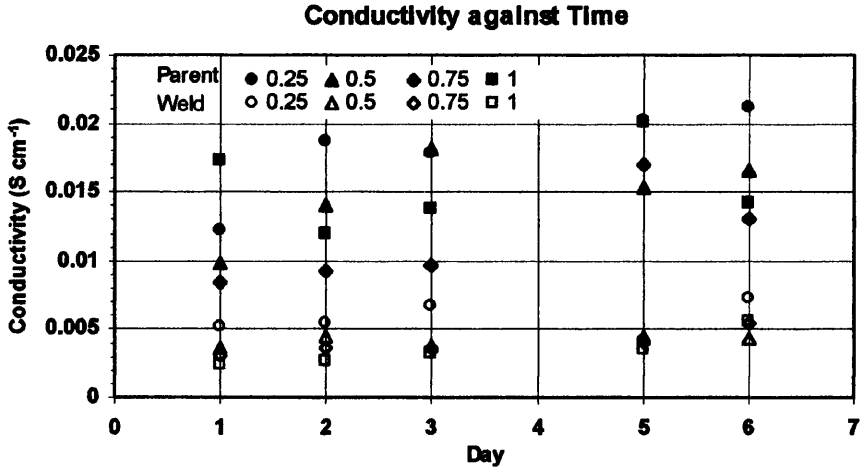

Figure 5.8 The solution conductivities calculated using R_{calc} from the weld and parent metal 1 data.

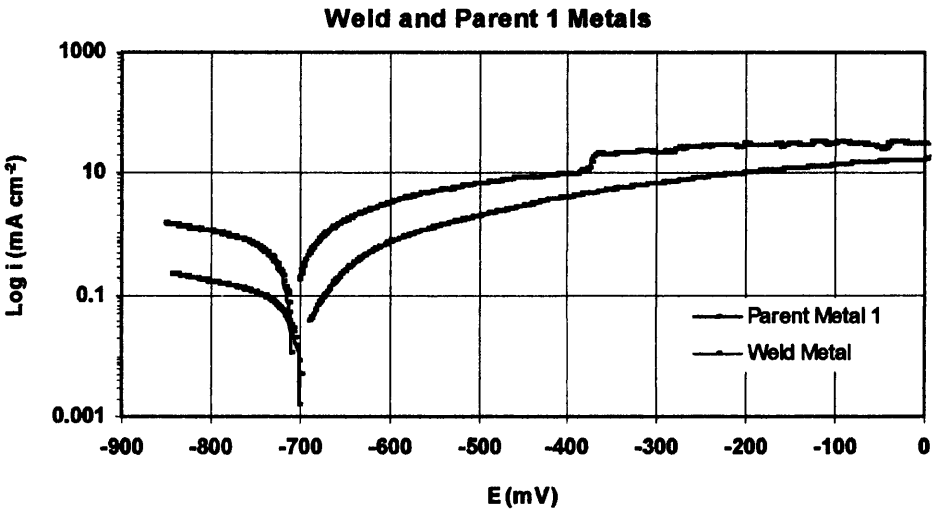

Figure 5.9 The polarisation curves of the weld and parent metal 1 in bulk solution.

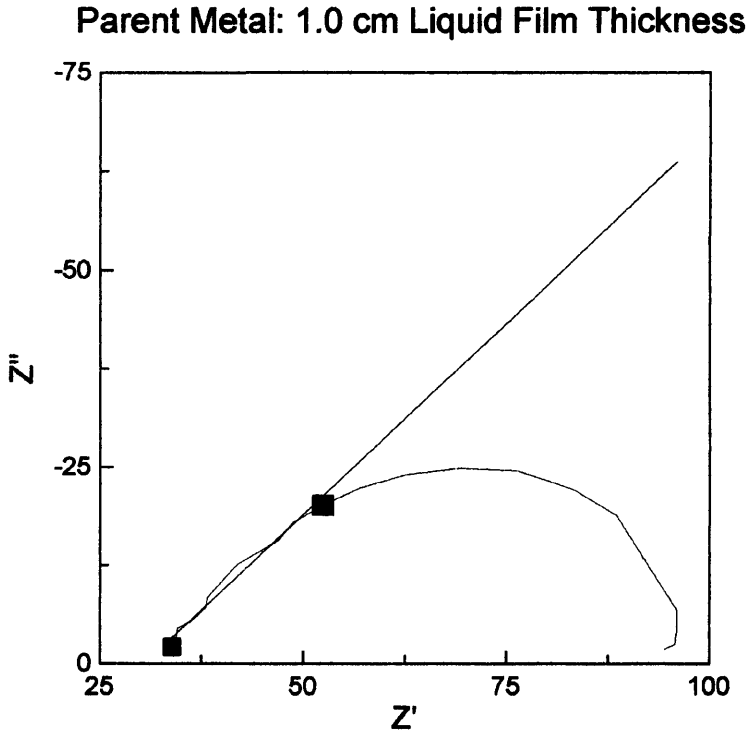

Figure 5.10 Flattening at the high frequency part of the Nyquist plot (no area correction).

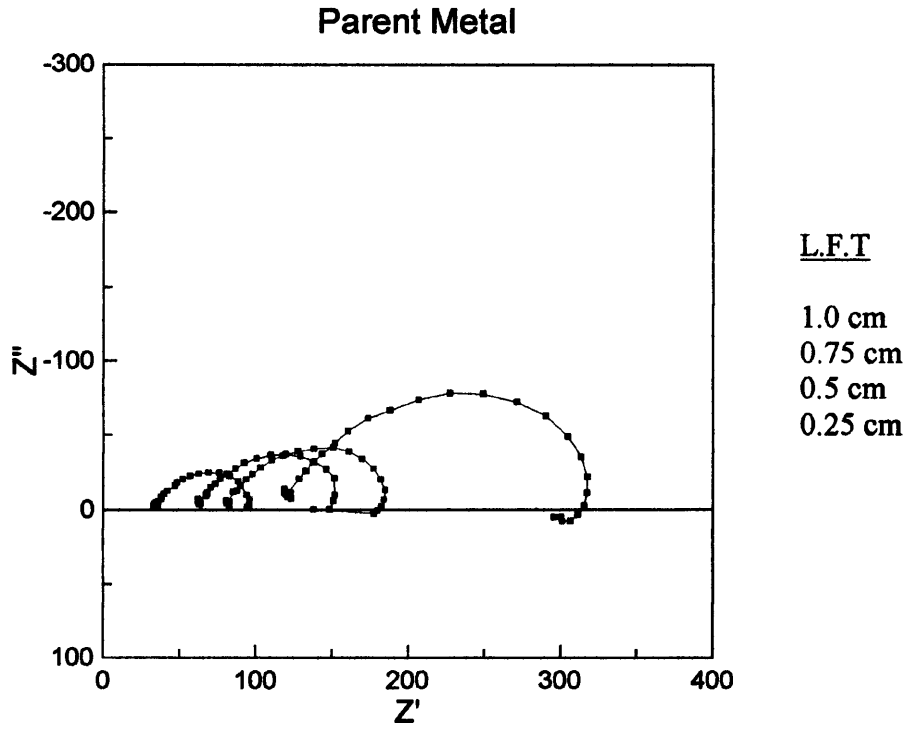

Figure 5.11 a) The Nyquist plots from ac impedance measurements performed at different liquid film thicknesses (no area correction).

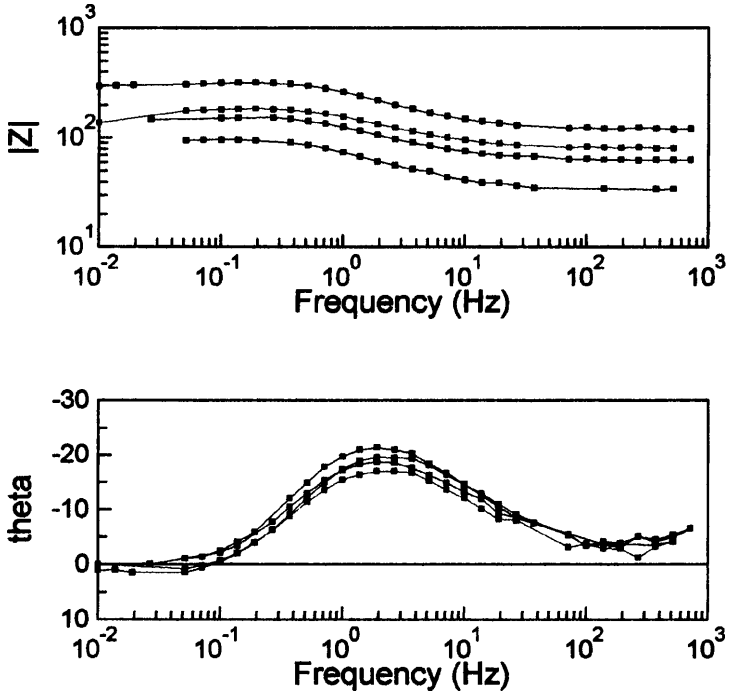

b) The impedance modulus, |Z| and the phase angle, ϕ against frequency.

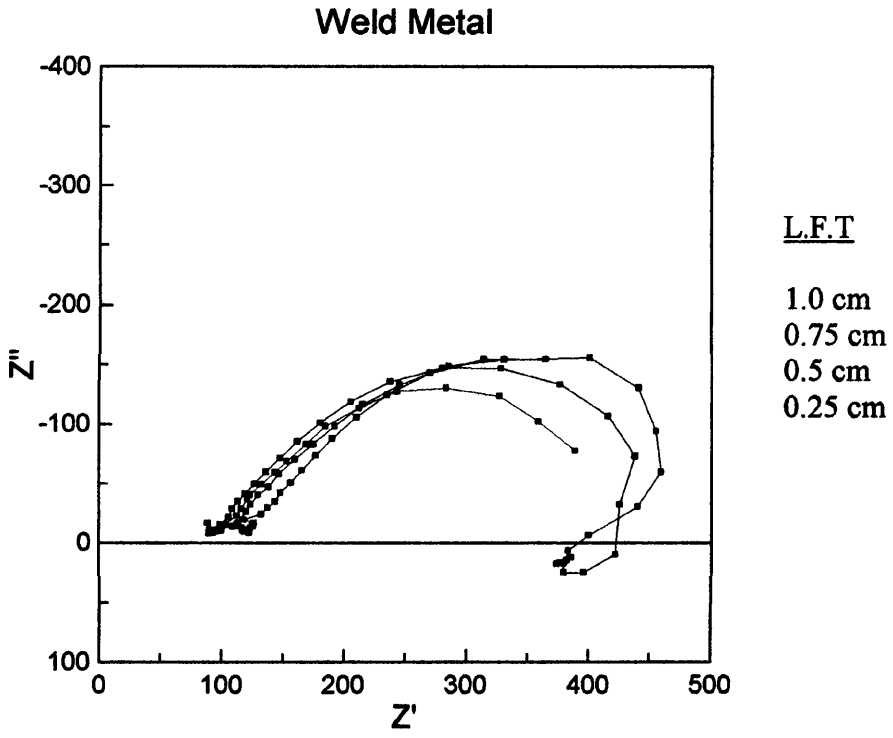

Figure 5.12 a) The Nyquist plots from ac impedance measurements performed at different liquid film thicknesses (no area correction).

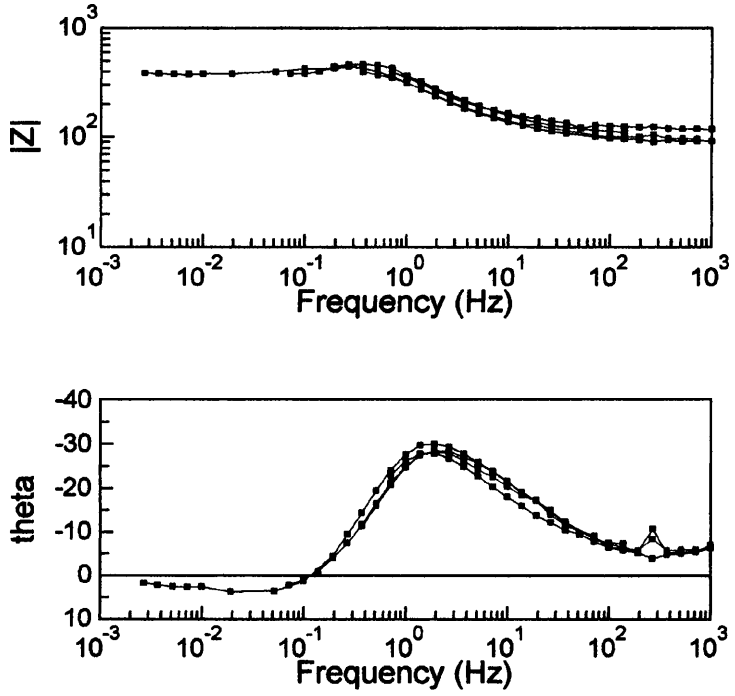

b) The impedance modulus, |Z| and the phase angle, ϕ against frequency.

Table 5.4 Z', Z" and solution resistance taken directly from the Nyquist plots.

	LFT (cm)	Z_{Imeas}	Z_{Rmeas}	R_s
Parent Metal	1.0	22.35	57.00	33.80
	0.75	39.14	127.79	80.57
	0.5	34.23	100.78	64.19
	0.25	73.71	206.93	120.97
Weld Metal	1.0	135.80	237.83	93.53
	0.75	113.62	212.32	103.10
	0.5	142.80	270.06	116.70
	0.25	148.68	285.13	109.29

5.2 The Wide Weldment Electrode

This experiment was performed at ambient room temperature with artificial Waveney solution as the electrolyte initially. The Cl^- content of the solution was increased from 215 ppm of the standard Waveney solution to 2150 ppm and then to 21500 ppm after approximately 9.6 and 11.5 days respectively. The duration of this experiment was 16 days and the galvanic current and potentials at six locations along the length of the weldment electrode were continuously logged at a rate of one measurement per minute. All potentials quoted are with reference to the saturated calomel electrode (SCE).

5.2.1 Potential and Galvanic Current

The coupled potential against time in Figure 5.13 was measured using the reference Luggin 1 - located in the centre of the weld metal. Initially a sharp rise from -718.5 mV to -706 - 8 mV is recorded within 18 hours and the potential remains largely between -706 mV and -709 mV whilst the Cl^- concentration of the solution is 215 ppm. There is little change during the two days after the Cl^- concentration was increased to 2150 ppm. An increase is clearly noticeable after the second addition of NaCl, raising the Cl^- concentration to 21500 ppm. At the end of the analysis the coupled potential appears to have stabilised at approximately -704 mV.

The plots of potentials recorded with reference at Luggins 3 and 6 (Figure 5.15 a and b) would appear to have similar characteristics to the plot of Luggin 1. The reference at Luggin 3 (weld/parent interface) exhibits the same potential behaviour unsurprisingly because of its location, however the potentials are typically 2–3 mV less than the potential in the weld metal centre. In 21500 ppm Cl^-, this potential difference is virtually eliminated.

The reference at Luggin 6 (remote parent) measured subtle differences from the potentials measured by the references at Luggins 1 and 3. There is no initial sharp rise and throughout Cl^- concentrations of 215 ppm and 2150 ppm the potential is largely between -706 and -712 mV, similar to potentials measured at Luggin 3. An immediate 6 mV increase accompanies the increase in Cl^- concentration to 21500 ppm prior to stabilising at –701 mV.

The galvanic current (Figure 5.14) measured between the weld and both parent metals changes from approximately 0 μA to –28 μA and then decreases as rapidly to around –7 μA within just over 50 hours of commencing the experiment. The negative current indicates that the coupled weld and parent metals are the overall cathode and anode respectively. Between 50 and 150 hours, the liquid film thickness and modified LPR measurements are performed daily for five days. Thin peaks are visible in this region that reveal the decrease in current, in some cases to 0 μA which coincides with the reduction in solution thickness for the experiments and in the following 20 hours, the galvanic current at 1.0 cm becomes slightly lower and then reverts back to the overall trend.

During this experimental period the current increases to –26.5 μA at 124 hours and then decreases once more to -15 μA at 230 hours – the time when the Cl^- concentration is increased to 2150 ppm. Initially the addition of Cl^- causes a small increase in current, decreasing over 30 hours and then flattening at around -10 μA.

The further increase in Cl^- concentration to 21500 ppm coincides with a sharp increase in current to -20 μA followed by an equally sharp decrease reaching 16 μA after 30 hours. The measured current remains positive signifying a change in the overall cathode and anode in the couple. Finally there is a small decline and a linear rise in positive current for the final 70 hours of the experiment.

5.2.2 Liquid Film Thickness – Potentials and Galvanic Currents

Figure 5.16 a, b and c shows three plots of the average of two potential measurements taken at the same liquid film thicknesses. There were ten liquid film thicknesses in the range 0.1 – 1.0 cm with the reference at Luggins 1, 2, 3 and 6 for three separate experiments when the weld and both parent metals are coupled.

The change in average measured potential with varying liquid film thickness shown in these plots is summarised for each day and each reference at these Luggins in the Table 5.10 below.

Table 5.10 Summary of Coupled Potential Behaviour at Different Liquid Film Thicknesses

	Day		
Luggin	**1**	**2**	**4**
1	From 1.0 to 0.5 cm, remains at about -708 mV. Increases to –707.7 mV at 0.4 cm. Decreases to –709.3 mV at 0.1 cm	From 1.0 to 0.7 cm, increases from -708.4 to –708 mV. From 0.7 to 0.4 cm, remains at -708 mV. To 0.1 cm, decreases to -708.5 mV.	From 1.0 to 0.1 cm, remains around -708 mV.
2	From 1.0 to 0.4 cm, increases from -710.4 to -709.8 mV. To 0.2 cm, increases more sharply to -709.3 mV. To 0.1 cm, sharp decrease to -710.5 mV.	From 1.0 to 0.4 cm, increases from -710.2 to –710 mV. To 0.1 cm, increases to -709.6 mV.	From 1.0 to 0.4 cm, increases from -710 to –709.6 mV. To 0.1 cm, increases to -708.6 mV.
3	From 1.0 to 0.5 cm, remains around -710 mV. To 0.1 cm decreases to -710.8 mV.	From 1.0 to 0.5 cm, increases from -710.2 to –710 mV. To 0.1 cm, overall decrease to -710.4 mV.	From 1.0 to 0.1 cm, remains around -709.8 mV.
6	From 1.0 to 0.1 cm, an overall decrease from –710.6 to -710.8 mV	From 1.0 to 0.1 cm, an overall decrease from -710.9 to -711.9 mV.	From 1.0 to 0.1 cm, decreases from -710.4 to -710.9 mV.

There is 1.5 - 3 mV difference between values recorded by Luggins 1 and 6. The potentials recorded using Luggin 2 and 3 are located in the region of this potential difference and produce similar results at greater film thicknesses, whereas at lower thicknesses, Luggin 2 potentials are found to be nobler than those at Luggin 3.

From the same experiment, Figure 5.17 shows the average of two measurements of galvanic current at the same liquid film thickness plotted against varying liquid film thickness in the range 0.1 - 1.0 cm. These results are summarised in the Table 5.11 below.

Table 5.11 Summary of Galvanic Current behaviour at Different Liquid Film Thicknesses for the Wide Waveney electrode

Day		
1	**2**	**4**
From 1.0 to 0.1 cm, a smooth change in *ig* from -19.5 to -7 μA.	From 1.0 to 0.1 cm, A smooth change in *ig* from -23 to -9 μA.	From 1.0 to 0.1 cm, A smooth change in *ig* from -23 to -12.5 μA.

It is important to note that as the liquid film thickness is reduced from 1.0 cm the current decreases by a greater amount the lower the thickness. A larger negative current with decreasing thickness is shown overall for days 2 and 4 in comparison with day 1.

5.2.3 Modified LPR Tests and the Application of the Mathematical Model

Table 5.7 a, b and c display the data obtained from the LPR measurements performed using the uncoupled weld and parent 1 metals at four liquid film thicknesses.

The $Rp_{measured}$ are the average of three values taken at the thicknesses 0.25 cm, 0.5 cm, 0.75 cm and 1.0 cm for the weld metal and parent metal 1. $Rp_{measured}$ is plotted against $1/t^{1/2}$ in Figure 5.18 a, b and c according to Equation 5.1.

The value of e_x (x = 2.0 cm), in the case of the parent metal, is the potential change measured between Luggin 5 and Luggin 6 on the electrode. For the weld metal, e_x (x is 1.5 cm) is the potential change between Luggin 1 and Luggin 3.

α is calculated using Equation 2.81 for the weld and parent 1 metals at each liquid film thickness. The increasing solution resistance, with lowering solution thicknesses provides a drop in e_x and gives the increasing values of α.

R_{calc} is calculated using Equation 4.1 and the plots of R_{calc} against 1/t, according to Equation 5.2 in Figure 5.19 a, b and c, illustrate the linearity of the solution resistance increase with decreasing liquid film thickness.

Z_{calc}, the actual Rp of the weld and parent 1 metals is determined using Equation 4.2 and should remain unchanged at different liquid film thicknesses. Z_{calc} of both metals confirm that in general this is found to be true. The weld metal has higher Z_{calc} values than parent metal 1.

5.2.4 Corrosion Rates

The corrosion rates in Table 5.8 were calculated using Z_{calc} values in Equation 4.3. Although these are not absolute values, the corrosion rates suggest that the individual Z_{calc} values therefore the parent would appear to have the highest overall corrosion rate of the two metals.

5.2.5 Uncoupled Potentials

The uncoupled individual potentials of the weld and parent metals (Table 5.9), measured with the references at Luggins 1 and 5 respectively, are used to give a value of potential difference between the metals.

According to these values, the weld metal is the overall cathode with respect to the parent metal and the potential difference on each of the days is approximately 10 mV.

5.2.6 Solution Conductivity

The conductivity (Figure 5.20) is plotted in S cm^{-1} against 1/t (liquid film thickness) and calculated using Equation 2.67. The plots display a generally flat trend with the weld and parent 1 metals having similar behaviour. The solution conductivity remains at a value between 16 and 25 mS cm^{-1} at all liquid film thicknesses. The conductivity of the artificial Waveney solution prior to exposure to the electrode was measured as 4.2 mS cm^{-1}.

5.2.7 pH

The pH of the Waveney solution after immersion of the electrode was 4.9. Prior to the final tests (potentio-dynamic sweeps), the pH was 5.9.

5.2.8 Polarisation Curves

The results of the cathodic and anodic potentio-dynamic sweeps for the uncoupled weld metal and parent 1 metal in bulk solution were plotted on log and linear axes to produce the polarisation curves in Figure 5.21. The weld metal appears to be nobler but the parent metal has a greater current density. Only –900 mV to -200 mV of the polarisation curve is shown on the log x-axis plot due to resistance, flattening the anodic curve at potentials above -200 mV.

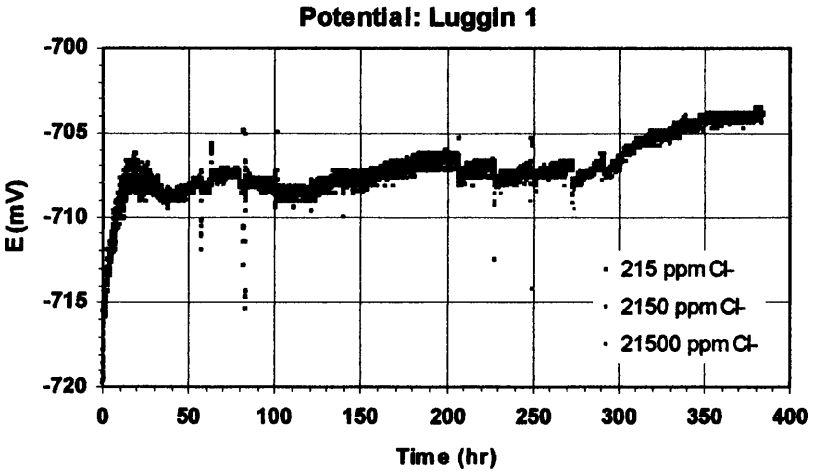

Figure 5.13 The coupled potential measured throughout the experiment with the reference in the weld metal centre.

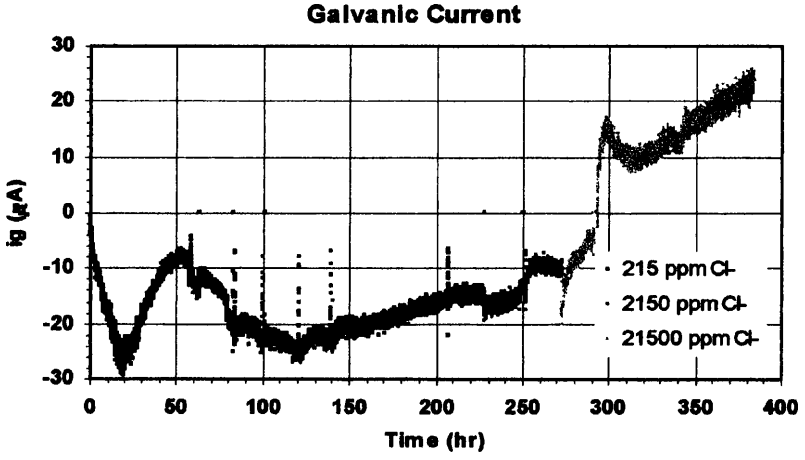

Figure 5.14 The galvanic current measured throughout the experiment between the weld and parent metals.

a)

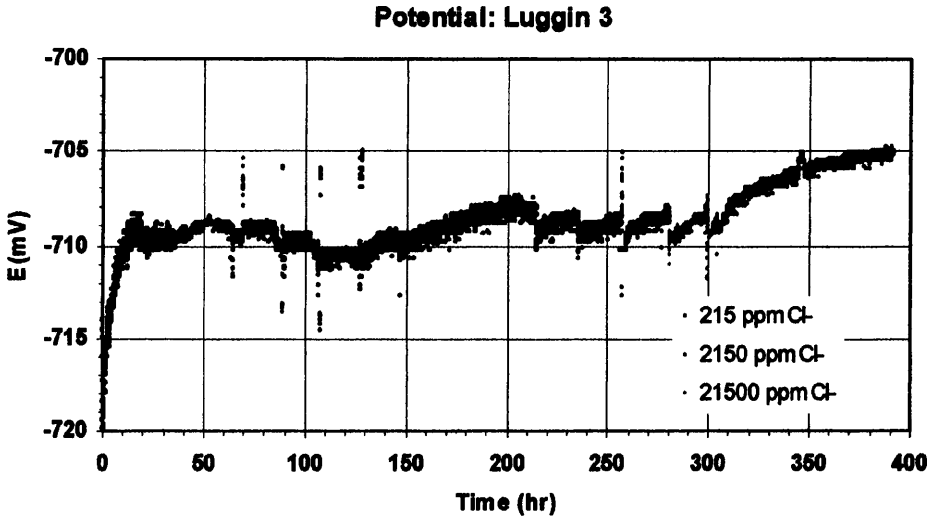

Figure 5.15 (a and b) The coupled potentials throughout the experiment at the weld and parent interface (3) and the remote parent metal (6).

b)

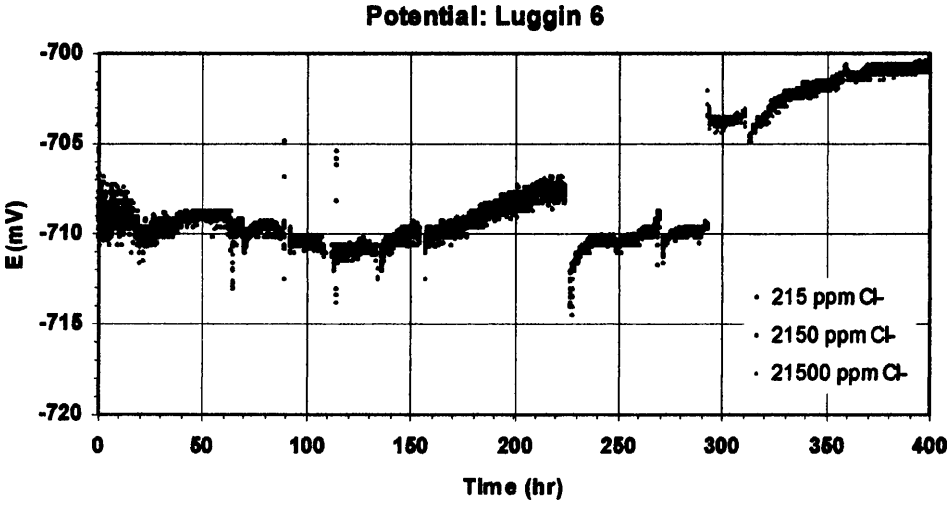

a)

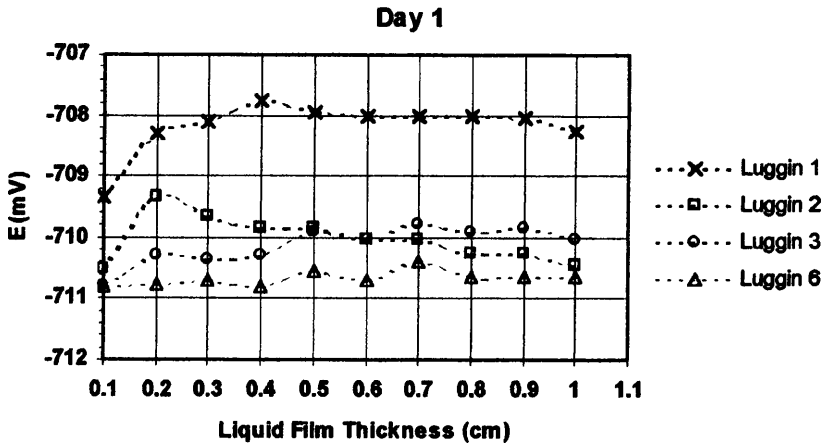

b)

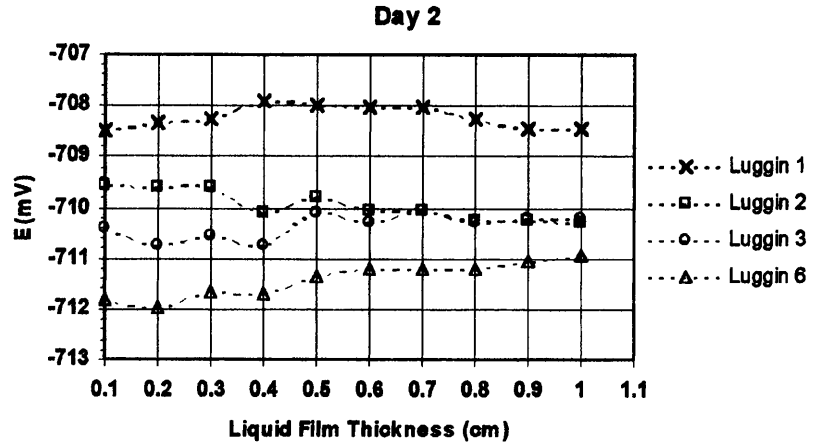

c)

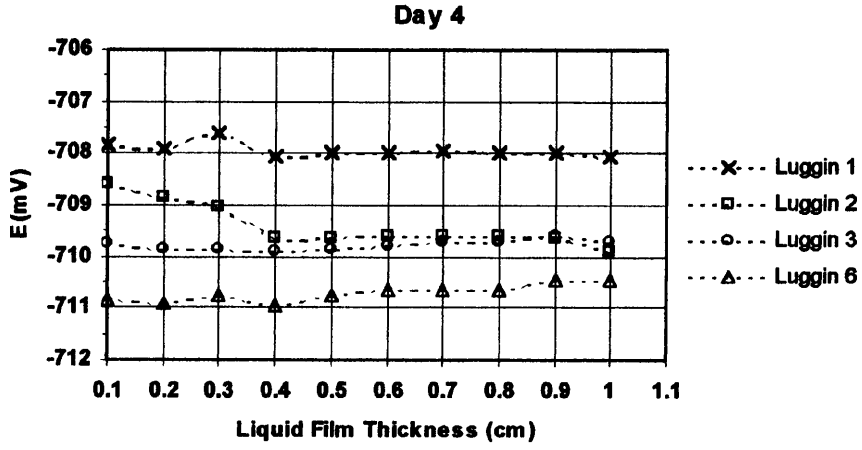

Figure 5.16 (a, b and c) The coupled potentials measured at the weld metal centre (1), the weld and parent interface (3) and the remote parent (6) at different liquid film thicknesses.

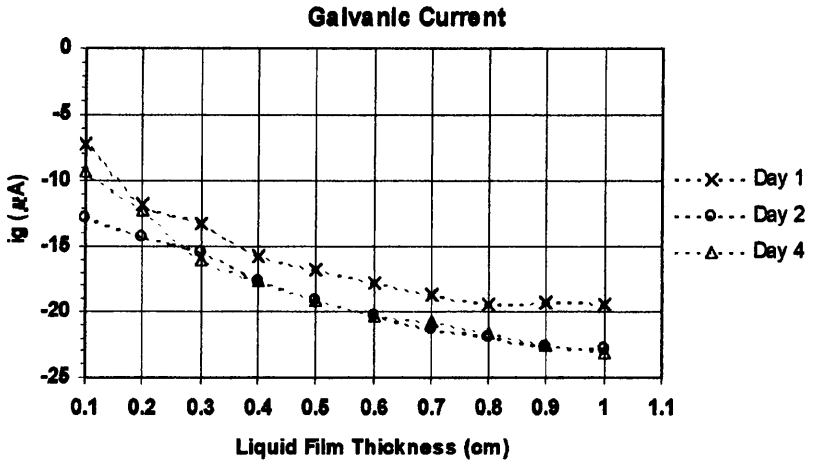

Figure 5.17 The galvanic current between the weld and parent metals measured at different liquid film thicknesses.

Table 5.7 (a, b and c) The measured and calculated data from the modified LPR tests.

a)

Day 1

	Liquid film thickness (cm)	$Rp_{measured}$ (Ohm)	e_x (x = 2.0 cm) e_0 = 20 mV	α calc	R_{calc} (Ohm)	Z_{calc} (Ohmcm^2)
Parent	1	128	9.00	0.40	51	321
	0.75	149	7.67	0.48	72	311
	0.5	204	6.00	0.60	123	339
	0.25	335	6.33	0.57	193	583
			e_x (x = 1.5 cm) e_0 = 20 mV			
Weld	1	176	14.00	0.24	42	740
	0.75	193	12.00	0.34	66	566
	0.5	219	10.67	0.42	92	523
	0.25	313	9.00	0.53	167	589

b)

Day 2

	Liquid film thickness (cm)	$Rp_{measured}$ (Ohm)	e_x (x = 2.0 cm) e_0 = 20 mV	α calc	R_{calc} (Ohm)	Z_{calc} (Ohmcm^2)
Parent	1	106	9.17	0.39	41	272
	0.75	133	8.33	0.44	58	305
	0.5	173	6.67	0.55	95	314
	0.25	222	5.00	0.69	154	321
			e_x (x = 1.5 cm) e_0 = 20 mV			
Weld	1	171	14.00	0.24	41	721
	0.75	193	12.00	0.34	66	567
	0.5	222	10.33	0.44	98	504
	0.25	278	9.00	0.53	148	522

c)

Day 4

	Liquid film thickness (cm)	$Rp_{measured}$ (Ohm)	e_x (x = 2.0 cm) e_0 = 20 mV	α calc	R_{calc} (Ohm)	Z_{calc} (Ohmcm^2)
Parent	1	98	7.67	0.48	47	205
	0.75	113	7.83	0.47	53	241
	0.5	140	6.33	0.57	80	243
	0.25	244	5.17	0.68	165	360
			e_x (x = 1.5 cm) e_0 = 20 mV			
Weld	1	158	13.67	0.25	40	622
	0.75	167	12.67	0.30	51	550
	0.5	225	10.67	0.42	94	536
	0.25	225	9.67	0.48	109	464

a)

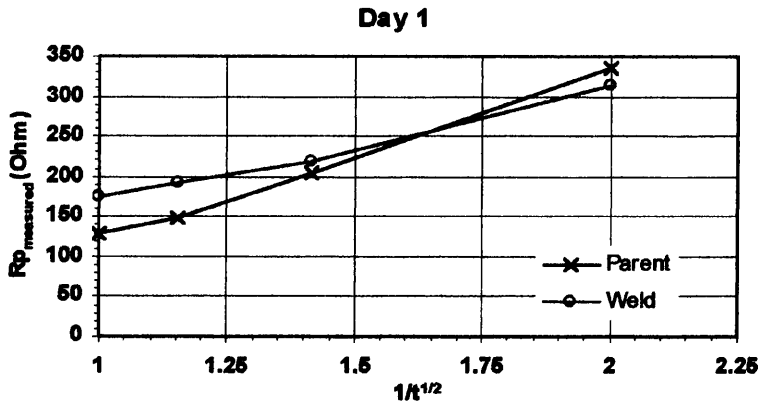

b)

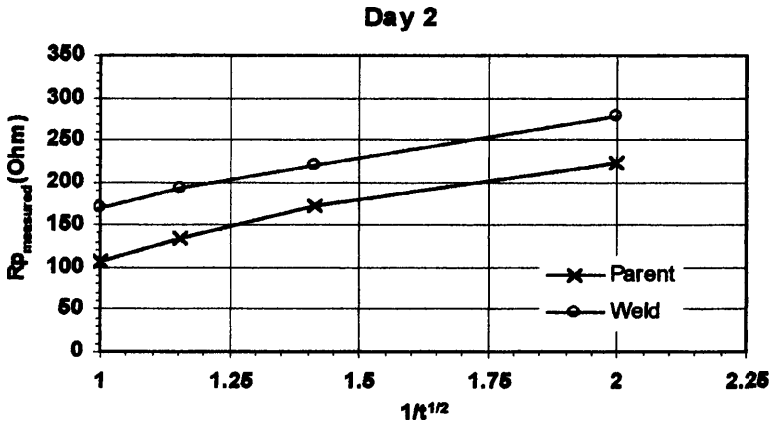

c)

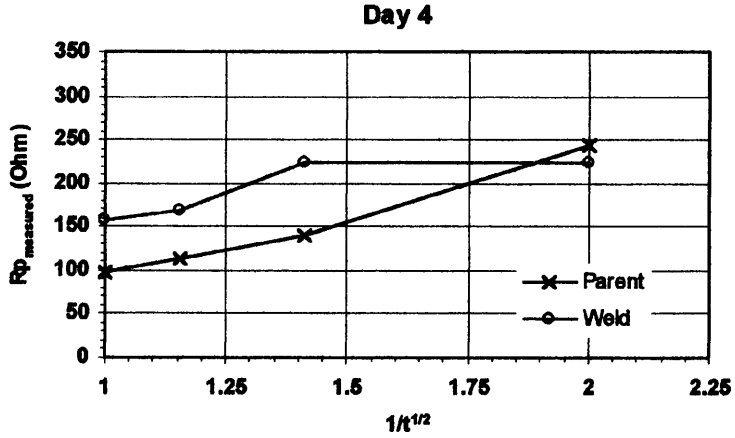

Figure 5.18 (a, b and c) The weld and parent metal 1 measured Rp against liquid film thickness.

a)

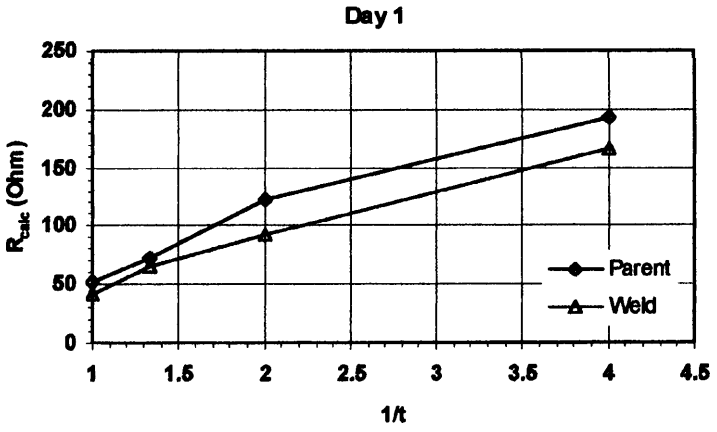

b)

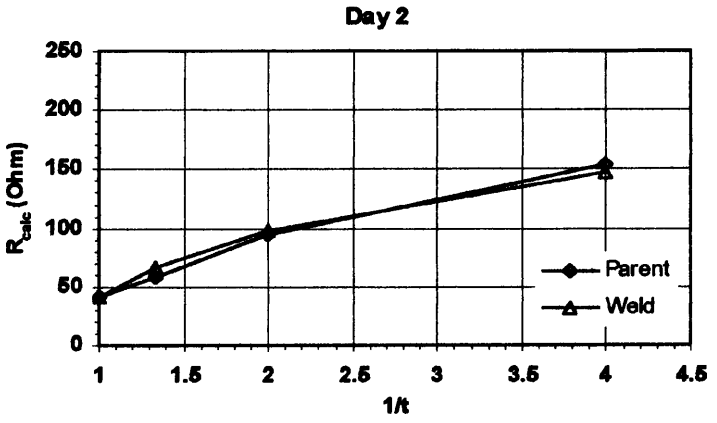

c)

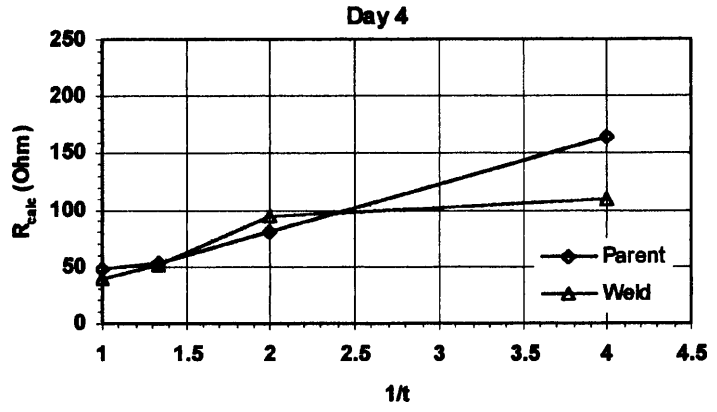

Figure 5.19 (a, b and c) The calculated solution resistance from weld and parent metal 1 R_{calc} data against liquid film thickness.

Table 5.8 The corrosion rates calculated using Z_{calc}.

Corrosion rate (mm y^{-1})			
Day	**L.F.T. (cm)**	**Parent**	**Weld**
1	**1**	0.62	0.27
	0.75	0.64	0.35
	0.5	0.59	0.38
	0.25	0.34	0.34
2	**1**	0.73	0.28
	0.75	0.65	0.35
	0.5	0.63	0.40
	0.25	0.62	0.38
4	**1**	0.97	0.32
	0.75	0.83	0.36
	0.5	0.82	0.37
	0.25	0.55	0.43

Table 5.9 The uncoupled potentials of the weld (1) and parent 1 (5) metals.

	Uncoupled Potential (mV)	
	Luggin 5	**Luggin 1**
Day 1	-711.0	-707.8
Day 2	-711.7	-706.9
Day 4	-710.8	-707.0

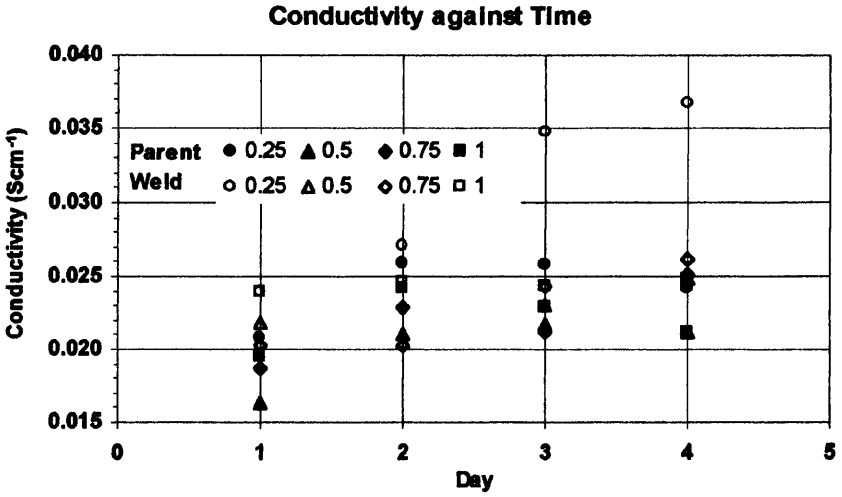

Figure 5.20 The solution conductivities calculated using R_{calc} from the weld and parent metal 1data.

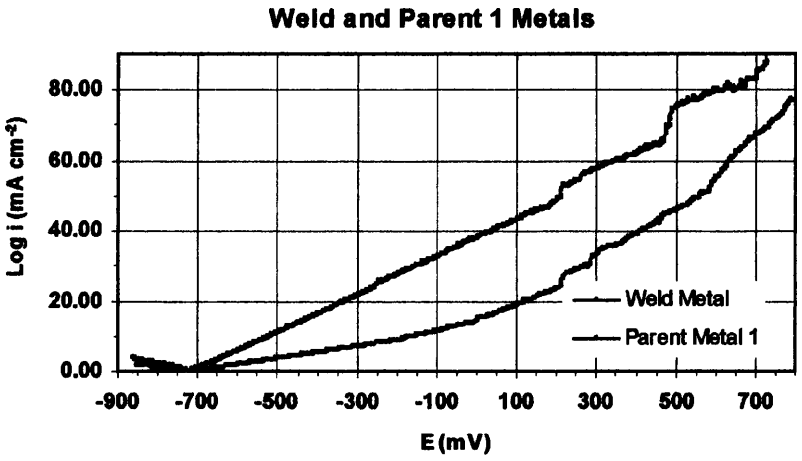

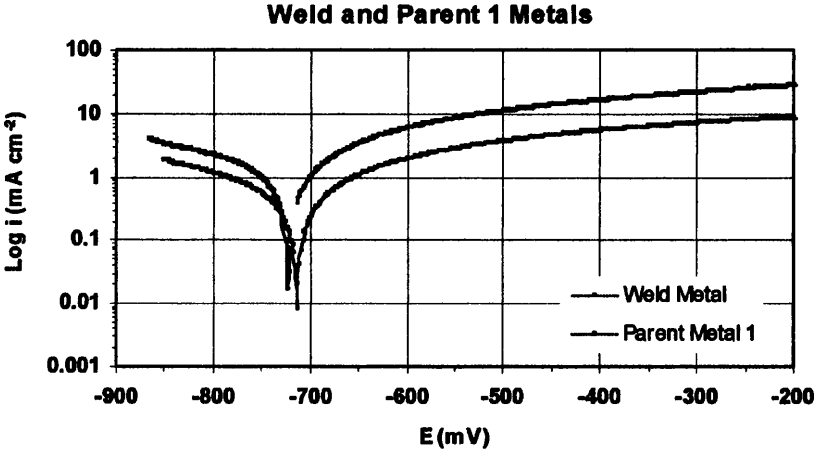

Figure 5.21 The polarisation curves (log scale and linear) of the weld and parent metal 1 in bulk solution.

5.3 The Standard Weldment Electrode at 60° C

The results discussed in this section are taken from experiments using the Standard weldment electrode from joint 3 of the Waveney failure (also used for the experiment at ambient temperature). The dimensions of the electrode were: 6 cm in length, 1.0 cm in width (two parent metals) and 1.0 cm^2 (weld metal). The solution temperature was held at 60° C by immersion in a thermostatically controlled water bath throughout the duration of the experiment (325 hours). References at five Luggins recorded the potentials at locations on the electrode whilst the galvanic current between the parent and weld metals was logged. The electrode potentials and galvanic currents were measured at varying liquid film thicknesses and the weld and parent metals were uncoupled for modified LPR and ac impedance measurements. Finally, cathodic and anodic potentio-dynamic sweeps were performed on the parent metal 1 and the weld metal. All potentials are quoted with reference to the saturated calomel electrode (SCE).

5.3.1 Potential and Galvanic Current

The potential measured at Luggin 1 (adjacent to the weld metal centre) of the coupled weld and parent metals was measured at a rate of one reading per minute (shown in Figure 5.22). On commencing the experiment, the potential is recorded as -680 mV but then falls steeply to approximately –717 mV after 40 hours. After this time the potential climbs back up in stages until 250 hours were passed where the potential is approximately –686 mV. From this time the potential increases at a slower rate towards –680 mV at the end of the experiment. It is in the period between 230 hours and the termination of the data logging that the liquid film thickness and uncoupled LPR measurements were performed.

The potentials logged using Luggins 2 and 5 (parent 1/weld metal interface) are plotted against time in Figure 5.24. Initial potential measurements show a 10 mV difference between these two parts of the electrode, this changes within 10 hours to become only 3 mV. After 50 hours of coupling the potential difference seems to have stabilised at 3 - 4 mV and remains as such until the end. From 40 hours onwards, a time-span of 285 hours, the potential measured at Luggin 2 generally increases from approximately –708 mV to final values of about –680 mV and Luggin 5 from -700 mV to –685 mV. Uncoupling and the periods of temporary variation of the liquid

film thickness appeared to hinder the steady increase in potential measured at both locations.

On commencing the galvanic current logging for the couple, plotted against time in Figure 5.23, measurements appear relatively negative at –20 μA. However the current rapidly becomes less negative in the first 40 hours in a manner similar to the initial potential. In 100 hours the current has changed polarity and peaked at just over 5 μA. The current then decreases and reaches 0 mV at 175 hours and continues this trend and becomes negative until it reaches approximately –5 μA after 250 hours. The experiments which can be distinguished by the vertical peaks, appear to have "broken-up" the steady galvanic current of the couple, therefore between 230 hours and the end of data logging the current plotted in clusters between –2 and –8 μA.

5.3.2 Liquid Film Thickness – Coupled Potentials and Galvanic Currents

The liquid film thickness measurements were taken after approximately eleven days (within the final 125 hours of the experiment) of the current and potential logging because the galvanic current became negative in this period. Figures 5.25 a, b and c show the plots of the change of potential (an average of two measurements taken at the same thickness) at ten thicknesses between 1.0 and 0.1 cm liquid film thickness. The features of these plots of differing potential at Luggins 1, 2 and 5 are summarised in Table 5.16 below.

The potentials measured at Luggins 1 and 2 follow a similar pattern of potential behaviour at the same thicknesses although Luggin 2 measurements are up to 5 mV more negative than 1. The overall potentials appear to change little with reducing thickness with the exception of those taken on day 1. In general, the potentials recorded at all three Luggins increase with each day at the equivalent liquid film thicknesses.

Table 5.16 Summary of coupled potential behaviour at different liquid film thicknesses on the Standard Waveney electrode at 60° C

	Day		
Luggin	1	2	3
1	From 1.0 to 0.5 cm, decreases from -684 to -685.5 mV. At 0.4 cm, -687 mV. At 0.3 cm, rises to -685 mV. To 0.1 cm, drops to -687 mV.	From 1.0 to 0.6 cm, remains about -680 mV. To 0.1 cm, decreases to -683 mV.	From 1.0 to 0.1 cm, remains -680 mV overall.
2	From 1.0 to 0.4 cm, decreases from -685.5 to -687 mV. At 0.3 cm, increased to -685 mV. To 0.1 cm, decreases to -687 mV.	From 1.0 to 0.7 cm, increases from -685 to -682.5 mV. At 0.6 cm, decreased to -685.5 mV. To 0.1 cm, increased overall to -683 mV.	From 1.0 to 0.1 cm, changes little and remains about -683 mV
5	From 1.0 to 0.5 cm, remains about -689 mV. To 0.1 cm, decreases to -691 mV.	From 1.0 to 0.1 cm, decreases from -686 to -690 mV.	From 1.0 to 0.1 cm, decreases from -687 to -690 mV.

The galvanic currents (*ig*) plotted against liquid film thickness in Figure 5.26, recorded simultaneously with the above potentials, are also an average of two measurements at the same liquid film thickness. Figure 5.26 is summarised in the Table 5.17 below.

Day 1 shows a low galvanic current in comparison to the other days because at this point that the overall current was low (Figure 5.23). Between 1.0 and 0.6 cm, the galvanic current is found to be more negative on Day 2 than 3, however this is reversed at thicknesses lower than 0.6cm. Both of these sets of data are very similar therefore such an effect probably insignificant.

Table 5.17 Summary of galvanic current behaviour at different liquid film thicknesses on the Standard Waveney electrode at 60° C

Day		
1	**2**	**3**
From 1.0 to 0.1 cm, *ig* changes overall from –2 to –1 μA.	From 1.0 to 0.3 cm, *ig* changes overall from -7.5 to -4 μA. To 0.1 cm, where ig is -4 μA.	From 1.0 to 0.1 cm, overall *ig* changes from -7.1 to -4.5 μA.

5.3.3 Modified LPR Tests and the Application of the Mathematical Model

Directly after the liquid film thickness measurements, the modified LPR tests were performed when the galvanic current became negative, indicating a cathodic weld metal. The three tables in Table 5.12 a, b and c contain the results of the uncoupled LPR tests on the weld and parent metals and the values calculated using equations from the model.

The $Rp_{measured}$ of the weld and parent metals does not vary significantly between days at each liquid film thickness with the exception of the weld metal at 0.25 cm which is comparatively high. It would appear that the parent metal has the lower Rp therefore a higher corrosion rate but this is not an accurate measurement of the current density of the metal surface due to different electrode geometries.

The plots of $Rp_{measured}$ against $1/t^{1/2}$ according to Equation 5.1 (Figure 5.27 a, b and c) for both weld and parent metals on each day show that, apart from the weld metal on day 1, the measured Rp increases by 50 to 100 Ohm between 1.0 cm and 0.25 cm

e_x, the potential change recorded at the location of Luggin 4 on the parent metal when a 20 mV sweep is performed using the reference at Luggin 5, decreases fairly evenly between 1.0 and 0.25 cm from 11 to 3 mV on all days. The weld metal e_x also has consistent values overall between 13.33 mV and 8.67 mV measured with the reference at Luggin 1 when the polarisation scan is performed with the reference at Luggin 2.

The values of α, calculated using Equation 2.81, for the parent are approximately twice the amounts of the weld metal at the same liquid film thickness. α increases with decreasing liquid film thickness.

R_{calc} values calculated (Equation 4.1) from the results of the weld metal are four or more times greater than the thickness equivalent values of the parent metal. With the exception of the high R_{calc} values at 0.25 cm for the weld metal, the parent and weld solution resistances increase consistently with decreasing thickness. R_{calc} is plotted against 1/t according to Equation 5.2 in Figure 5.28 a, b and c which illustrates the linearity of the R_{calc} increase with lowering solution thickness. It can be seen for the parent metal the R_{calc} at 0.5 cm is approximately twice that at 1.0 cm as predicted.

Z_{calc}, the real Rp of the metals was calculated using Equation 4.2 and, due to the experimental inconsistencies produces a few varying values for both the weld and parent metals.

5.3.4 Corrosion Rates

The corrosion rates of the weld and parent metal 1 in Table 5.13 were calculated using Equation 4.3 and Z_{calc} values. The average corrosion rates on the three days were 0.44 and 0.383 mm y^{-1}, 0.505 and 0.488 mm y^{-1} and 0.543 and 0.505 mm y^{-1} respectively. The corrosion rates of both metals are fairly similar and appear to be increasing with immersion time. The corrosion rate of the metal should not vary with solution thickness but the rates, being proportional to Z_{calc}, show some variation, especially for the parent metal.

5.3.5 Uncoupled Potentials

The potentials listed in Table 5.14 are an average of three values and the potential differences between the parent and weld metals are 3.5, 4.5 and 5.3 mV for the experimental days 1 to 3, where the weld metal is more noble. The individual potential of the weld metal becomes more positive with time as does the parent metal by a lesser amount.

5.3.6 Solution Conductivity

The solution conductivity (Figure 5.29) was calculated (in S cm^{-1}) using Equation 2.67 and R_{calc} values of the weld and parent metal on each day and plotted against *1/t* (liquid film thickness - 1, 0.75, 0.5 or 0.25 cm). The initial solution conductivity was measured as 6.5 mS cm^{-1} shortly after immersion of the electrode. The conductivity does not increase with each day because the iron carbonate had most likely already saturated the solution by the time the LPR tests were performed.

The solution conductivity remains constant with varying liquid film thickness and the values calculated for the parent metal are larger than the those of the weld by three or four times because of the difference between R_{calc} for the weld and parent metals. The parent metal calculation is the most accurate evaluation of the solution conductivity because all of the weld metal values are below the initial measured solution conductivity.

5.3.7 pH

On commencing the experiment, the solution pH was measured as 4.8. At the end of the experiment (before the potentio-dynamic sweeps were performed) the pH was 6.2.

5.3.8 Polarisation Curves

The polarisation curves (Figure 5.30) resulting from the cathodic and anodic potentio-dynamic sweeps of the weld and parent metal were performed in bulk solution. There is some flattening in the parent anodic plot indicating resistance and the current is limited to approximately 28 mA for potentials above –500 mV. The weld metal plot does not display this feature and has a considerably lower current distribution for both the cathodic and anodic curves. The weld metal has the higher corrosion potential and the lower corrosion current according to these curves.

5.3.9 AC Impedance

The Nyquist plots of the weld metal at the four liquid film thicknesses are shown in Figure 5.31 a where the linear response at high frequency is shown clearly. The plots of impedance modulus and phase angle against frequency are also present (b).

Z_{Rmeas} and Z_{Imeas} are the measured real and imaginary parts of the impedance shown in Table 5.15 at each liquid film thickness of the weld metal. Z_{Imeas} is where the complex is no longer linear and also marks the measurement on the x-axis where the $Z_R - R_s$ is taken and R_s is the low intercept part on the x-axis at high frequency.

The parent metal complex plots and impedance modulus and phase against frequency (Figure 5.32 a and b) are very small and demonstrate the response of a larger potential being applied at the location of Luggin 3, 4 cm away from the auxiliary.

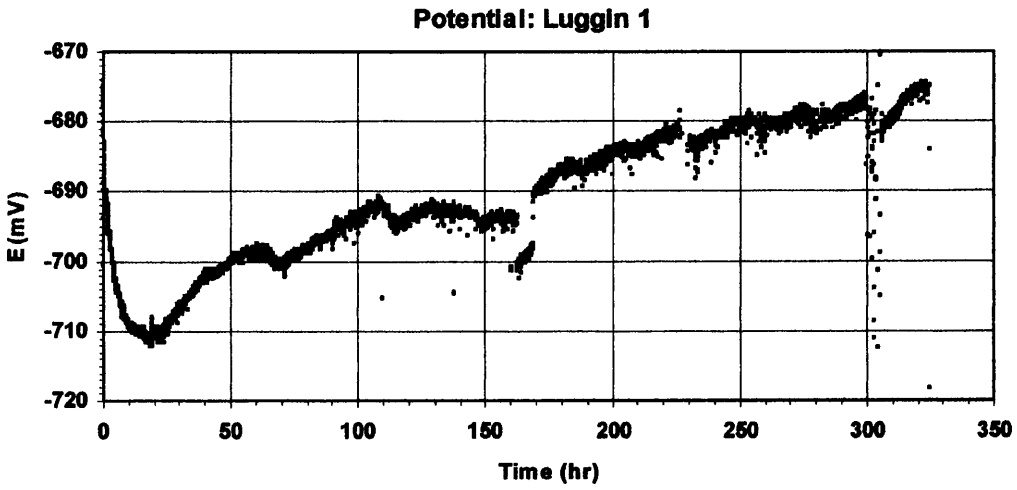

Figure 5.22 The coupled potential measured throughout the experiment with the reference in the weld metal centre.

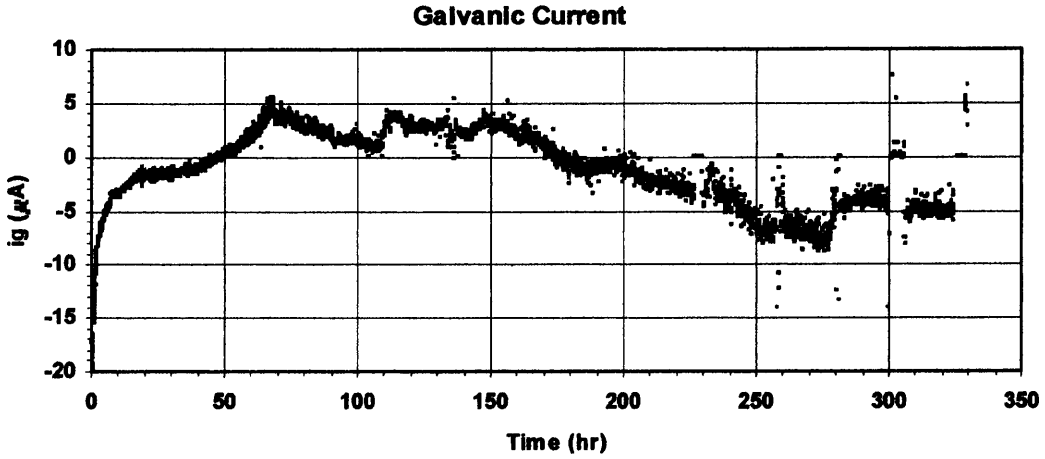

Figure 5.23 The galvanic current measured throughout the experiment between the weld and parent metals.

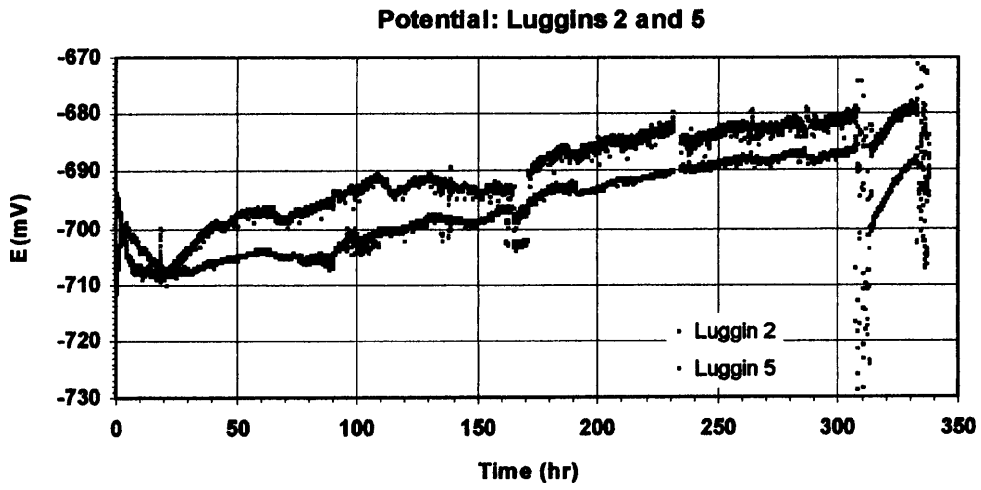

Figure 5.24 The coupled potentials throughout the experiment at the weld and parent interface (2) and the remote parent (5).

a)

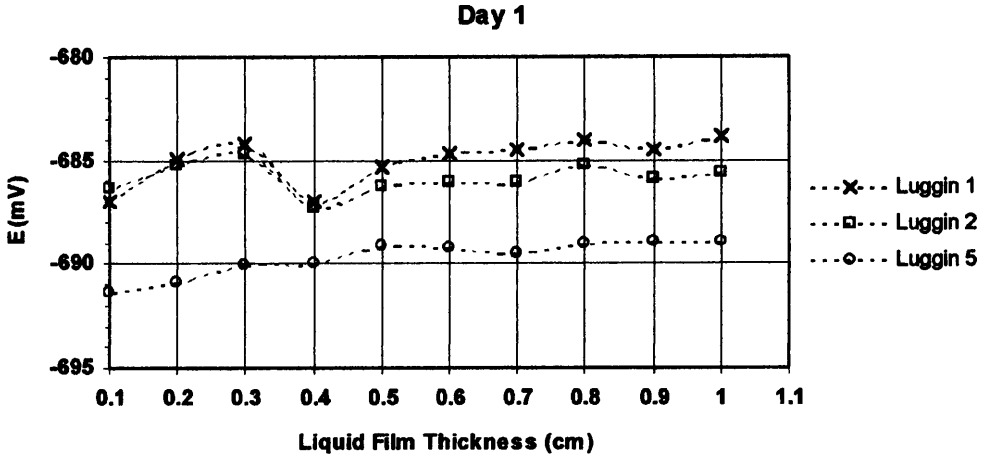

Figure 5.25 (a, b and c) The coupled potentials measured at the weld metal centre (1), the weld and parent interface (2) and the remote parent (5) at different liquid film thicknesses.

b)

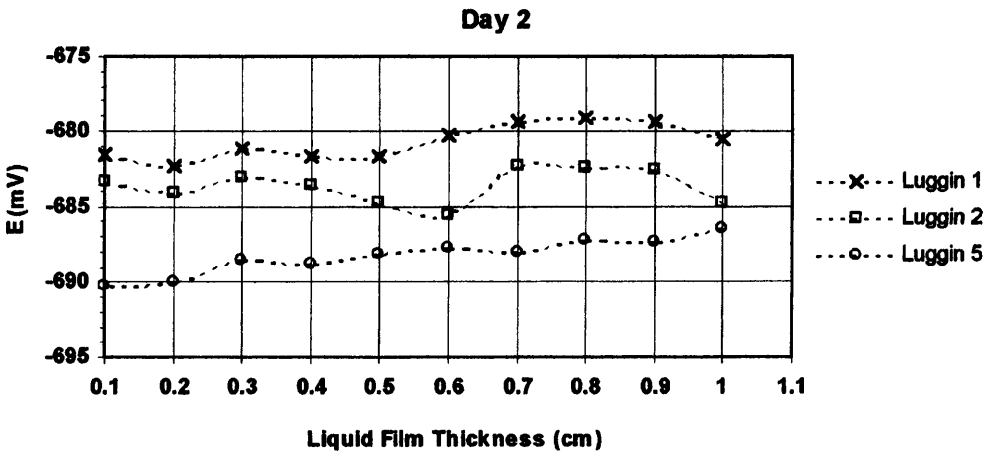

c)

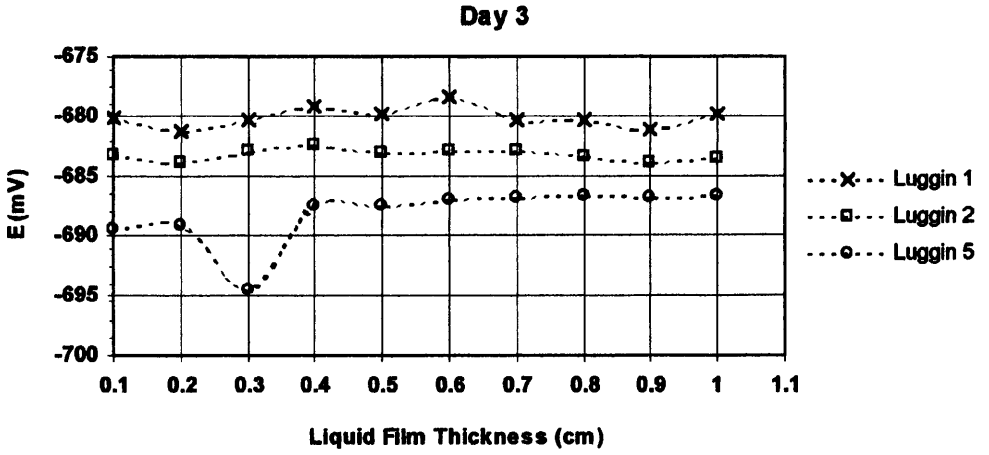

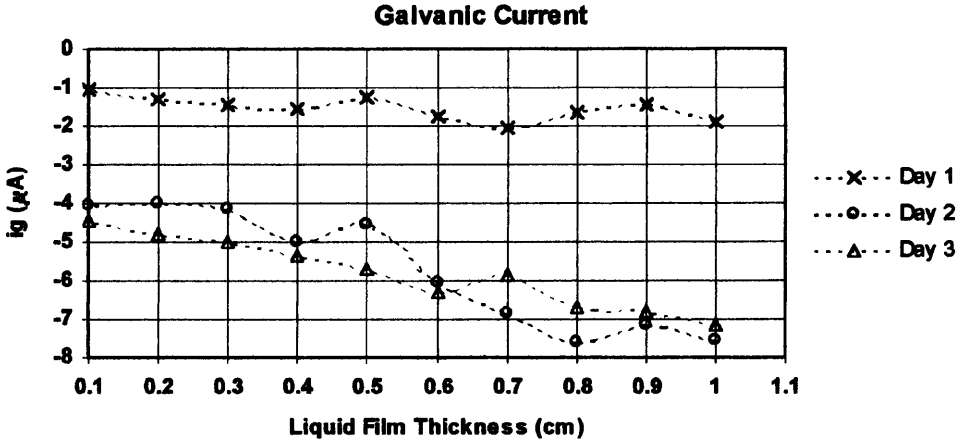

Figure 5.26 The galvanic current between the weld and parent metals measured at different liquid film thicknesses.

Table 5.12 (a, b and c) The measured and calculated data from the modified LPR tests.

a)

Day 1

	Liquid film thickness (cm)	$Rp_{measured}$ (Ohm)	e_x (x = 2.0 cm) e_0 = 20 mV	α calc	R_{calc} (Ohm)	Z_{calc} ($Ohmcm^2$)
Parent	1	181	10.33	0.33	60	548
	0.75	206	8.67	0.42	86	493
	0.5	221	6.67	0.55	122	403
	0.25	314	4.00	0.80	253	390
			e_x (x = 0.5 cm) e_0 = 20 mV			
Weld	1	470	13.33	0.81	381	580
	0.75	471	12.33	0.97	455	487
	0.5	501	11.67	1.08	540	464
	0.25	912	9.00	1.60	1456	571

b)

Day 2

	Liquid film thickness (cm)	$Rp_{measured}$ (Ohm)	e_x (x = 2.0 cm) e_0 = 20 mV	α calc	R_{calc} (Ohm)	Z_{calc} ($Ohmcm^2$)
Parent	1	190	10.67	0.31	60	606
	0.75	222	7.67	0.48	107	464
	0.5	228	5.67	0.63	144	361
	0.25	238	3.67	0.85	202	280
			e_x (x = 0.5 cm) e_0 = 20 mV			
Weld	1	470	13.33	0.81	381	580
	0.75	432	12.67	0.91	395	473
	0.5	474	10.33	1.32	626	359
	0.25	532	8.67	1.67	890	318

c)

Day 3

	Liquid film thickness (cm)	$Rp_{measured}$ (Ohm)	e_x (x = 2.0 cm) e_0 = 20 mV	α calc	R_{calc} (Ohm)	Z_{calc} ($Ohmcm^2$)
Parent	1	186	11.00	0.30	56	622
	0.75	199	9.33	0.38	76	522
	0.5	206	5.33	0.66	136	312
	0.25	228	3.00	0.95	217	241
			e_x (x = 0.5 cm) e_0 = 20 mV			
Weld	1	410	13.00	0.86	353	475
	0.75	404	12.33	0.97	390	418
	0.5	426	11.67	1.08	460	395
	0.25	491	9.33	1.52	748	322

a)

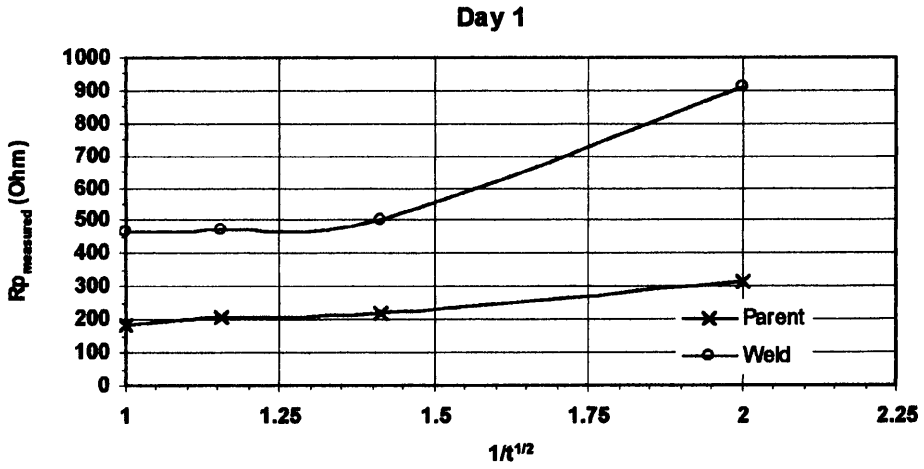

b)

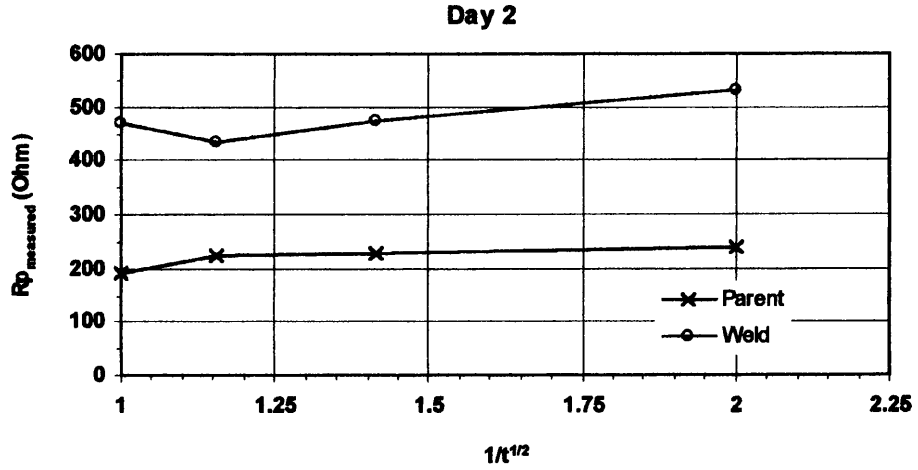

c)

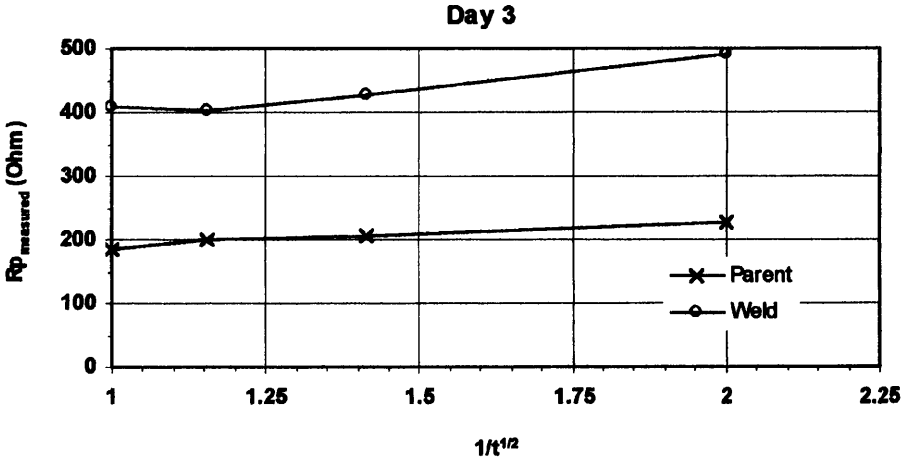

Figure 5.27 (a, b and c) The measured Rp of the weld and parent metal 1 against liquid film thickness.

a)

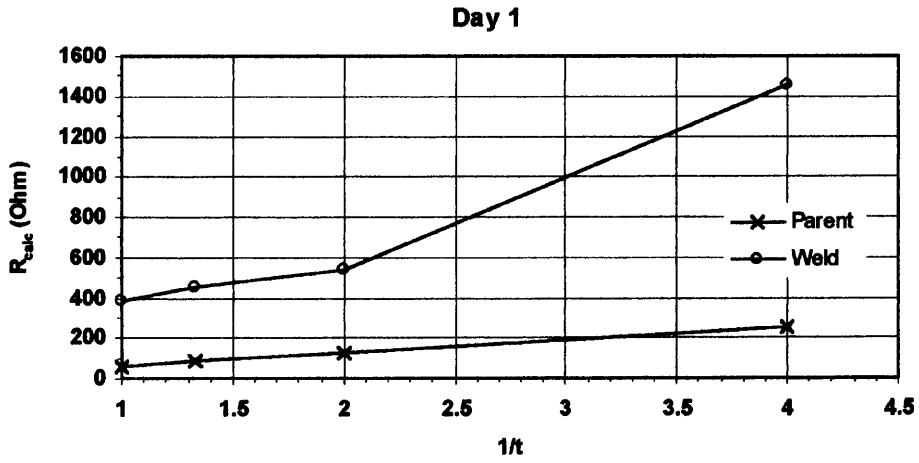

b)

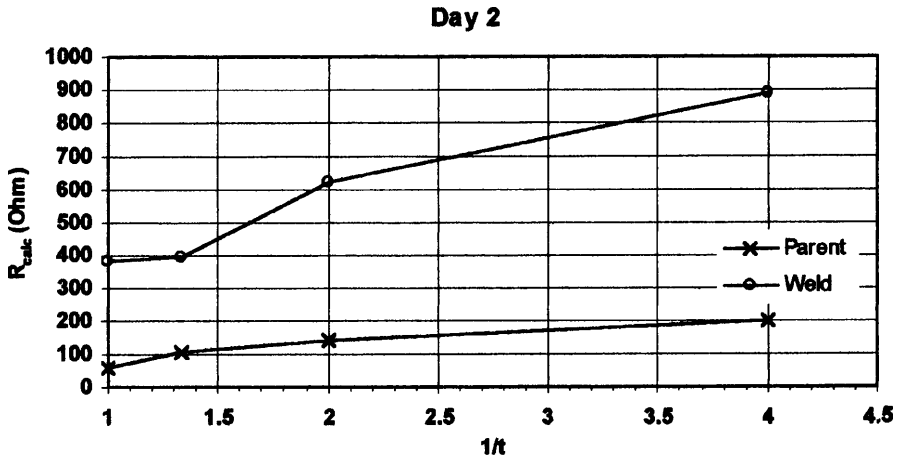

c)

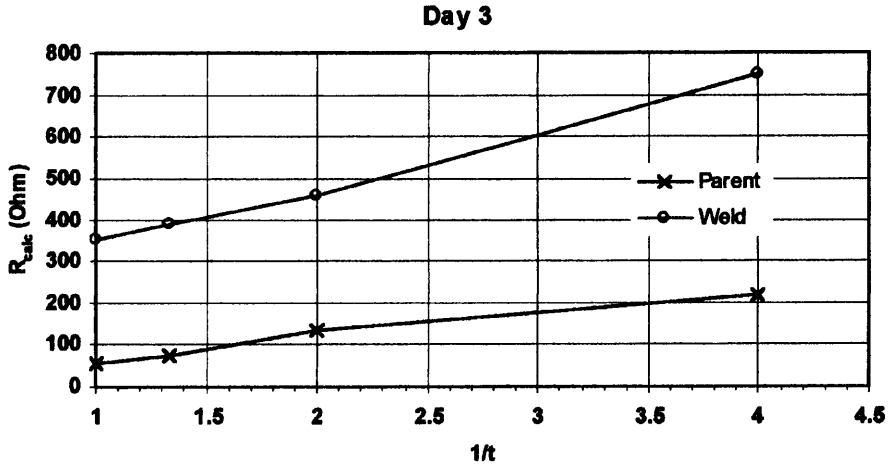

Figure 5.28 (a, b and c) The weld and parent metal 1 R_{calc} values against liquid film thickness.

Table 5.13 The corrosion rates calculated using R_{calc}.

Corrosion rate (mm y^{-1})			
Day	L.F.T. (cm)	Parent	Weld
1	1	0.36	0.34
	0.75	0.40	0.41
	0.5	0.49	0.43
	0.25	0.51	0.35
2	1	0.33	0.34
	0.75	0.43	0.42
	0.5	0.55	0.56
	0.25	0.71	0.63
3	1	0.32	0.42
	0.75	0.38	0.48
	0.5	0.64	0.50
	0.25	0.83	0.62

Table 5.14 The uncoupled potentials of the weld (1) and parent 1 (4) metals.

	Uncoupled Potential (mV)	
Day	Luggin 4	Luggin 1
1	-683.1	-679.6
2	-683.1	-678.6
3	-682.9	-677.4

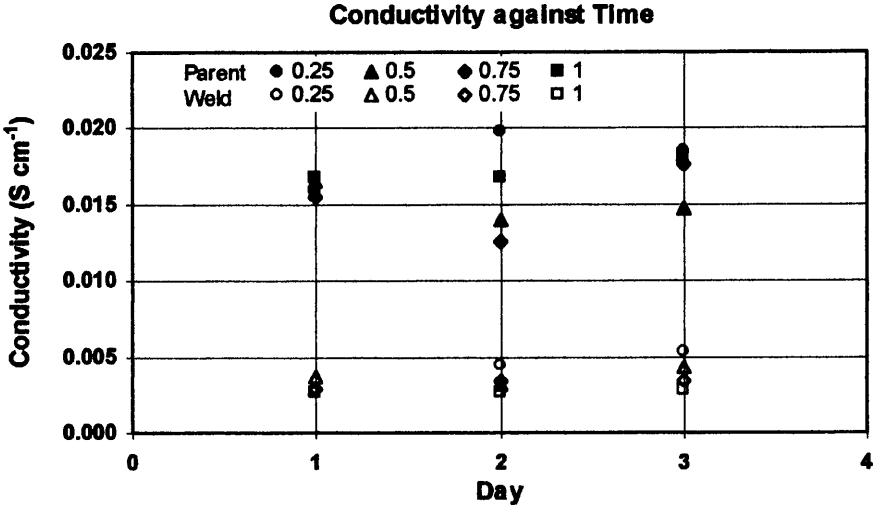

Figure 5.29 The solution conductivities calculated using R_{calc} from the weld and parent metal 1 data at different liquid film thicknesses.

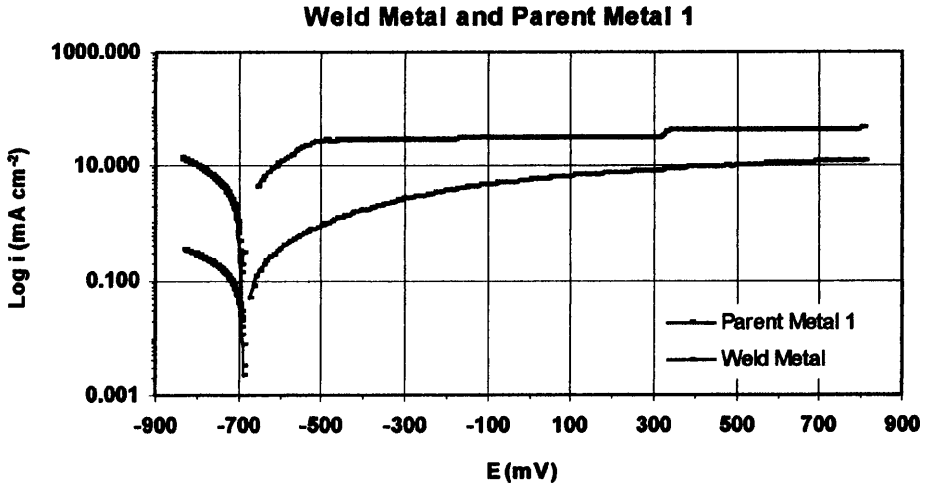

Figure 5.30 The polarisation curves of the weld and parent metal 1 in bulk solution.

Table 5.15 Measured data from the Nyquist plots.

	LFT (cm)	Z_{Imeas}	Z_{Rmeas}	R_s
Weld Metal	**1.0**	32.49	110.15	67.99
	0.75	40.14	116.84	65.66
	0.5	39.95	105.61	57.24
	0.25	86.65	194.56	84.60

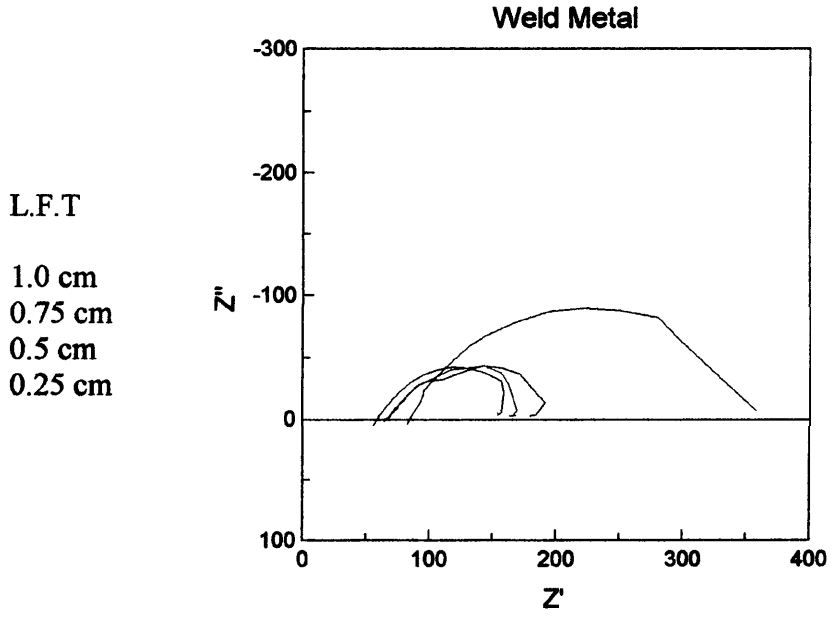

Figure 5.31 a) The Nyquist plots from ac impedance measurements performed at different liquid film thicknesses (no area correction).

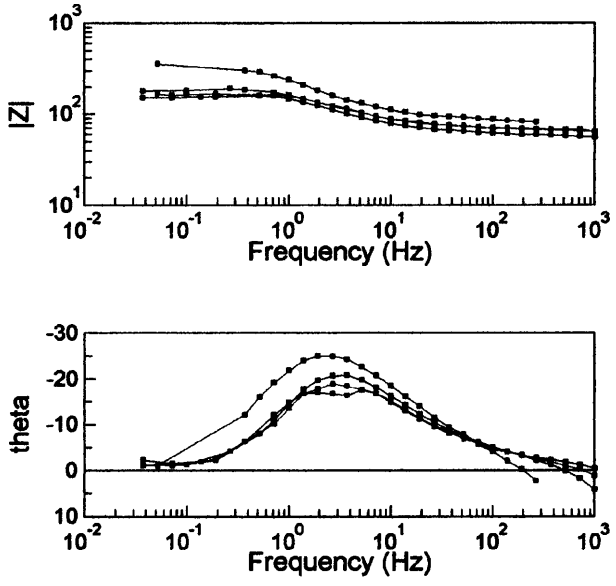

b) The impedance modulus and phase angle plotted against frequency.

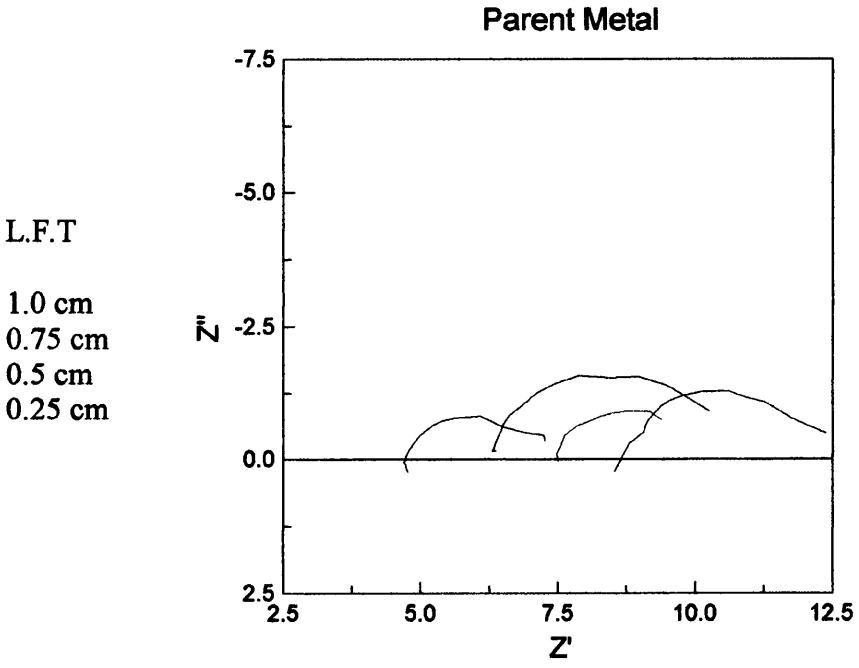

Figure 5.32 a) The Nyquist plots from ac impedance measurements using the reference at Luggin 3 at different liquid film thicknesses (no area correction).

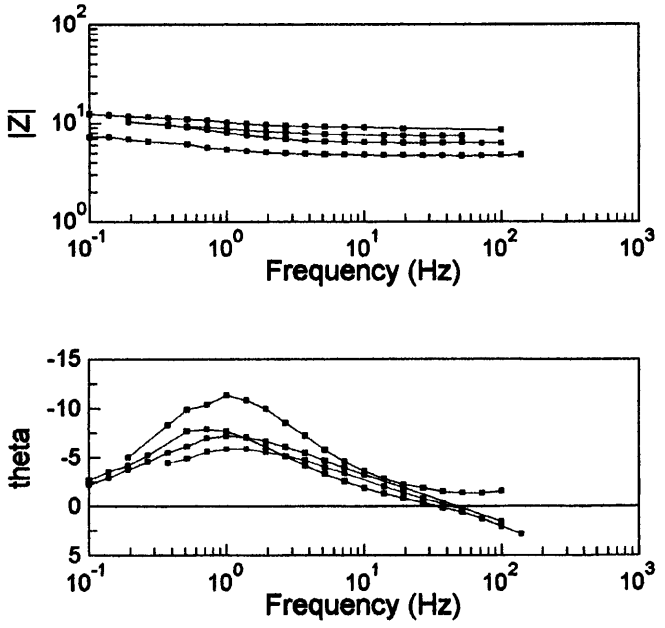

b) The impedance modulus and phase angle plotted against frequency.

6.0 The Results of the Waveney Weld and Parent Coupon Testing

Corrosion monitoring was performed using the Waveney weld and parent metals mounted as conventional coupon electrodes (described in Chapter 3.0) to supplement the work using the segmented weldment electrodes. The reasons for this were as follows:

- To determine accurate Rp using LPR and ac impedance for area corrected weld and parent metals.
- To obtain specimens suitable for examination using SEM-EDX to analyse any surface films and/or characteristics.
- To investigate possible differences in individual potential and Rp between weld and parent metals after long periods of being coupled or uncoupled.

Four experiments were performed with coupled of weld and parent metal coupons, two experiments were performed at ambient temperature and two at 60° C. One experiment at each temperature was coupled via the ACM GalvoGill 12 to measure the coupled potential and galvanic current and was uncoupled to perform the LPR and ac impedance. After approximately 310 hours, the coupled coupons were uncoupled and the previously uncoupled pair was coupled to monitor the galvanic current and potential. The electrolyte was Waveney solution but with 3.5% NaCl to increase solution conductivity. All potentials quoted are with reference to SCE.

6.1 Potentials and Galvanic Currents of the Coupled and Previously Uncoupled Coupons at Ambient Temperature

The coupled potential of the weld and parent coupons, marked in dark blue in Figure 6.1 shows an initial value of -690 mV, which then swiftly decreases to approximately -710 mV within 25 hours. From 70 to 200 hours the coupled potential appears to "saw tooth" above and below -710 mV. Between 200 and 310 hours the coupled potential is recorded in the saw tooth pattern between –705 and –710 mV. At 310 hours the coupled potential plotted (light blue), that of the previously uncoupled weld and parent and the potential immediately decreases to -712 mV. The saw tooth

pattern is seen as the potential increases overall and is -705 mV at the end of the experiment.

The galvanic current between the coupled weld and parent metals (Figure 6.2) (red) at the beginning of the experiment is relatively high at approximately 22 μA, this rapidly declines to 0.5 to 1 μA after 10 hours. The current is clearly anodic indicating that the parent and weld metals are the overall cathode and anode respectively in the couple. The galvanic current of the couple increases throughout the measurement, the maximum value at the end is found to be 4 μA. The peaks present in the data signify the uncoupling of the weld and parent metals when the LPR measurements were performed. The galvanic current data for the previously uncoupled weld and parent metal coupons, plotted in pink displays an initial current of -1 to -1.5 μA, suggesting that in this couple the weld is the overall cathode. This continues to be case until at 400 hours the galvanic current reaches 0 μA and remains in this state of overall zero current for 45 hours. For the final 25 hours a galvanic current has developed and appears to rest at 1 μA implying that the parent metal is the cathode of the couple.

6.2 Potentials and Galvanic Currents of the Coupled and Previously Uncoupled Coupons at 60° C

The data for the coupled parent and weld metal potentials at 60° C is plotted in Figure 6.3. The first potentials recorded are approximately –768 mV which rapidly increases to about –730 mV after 50 hours of measurement. The potential continues to increase steadily to –730 mV when potential logging is ceased. The previously uncoupled parent and weld coupons have a coupled potential of -707 mV on commencing the measurements and remain at this value for 25 hours. It then slowly increases to record approximately –701 mV as the final measurements. The plots for both of the couples are relatively smooth in comparison to the saw tooth pattern at ambient temperature.

The galvanic current recorded for the couple at 60° C (Figure 6.4) appears to vary considerably at any one time but over 310 hours a trend is visible. Initial measurements appear to be between 0 and –10 μA but very quickly rise to 15 μA. It

then returns to between 0 and –10 μA for 20 hours but then the general trend throughout the experiment is an increase of the anodic current and a final measured value is approximately 30 μA. The previously uncoupled parent and weld coupons produced a relatively large cathodic galvanic current peaking at –83 μA within 10 hours of coupling and commencing measurements. The general trend throughout this experiment was current becoming less negative with the final galvanic current measured as approximately –35 μA. There are several peaks in the plots of the first and second galvanic couples caused by the uncoupling of the coupons for LPR measurements.

6.3 Individual Potentials of Coupled and Uncoupled Weld and Parent Metal Coupons

The individual rest potentials plotted against the day of measurement in Figures 6.5 and 6.6 were recorded when the LPR was performed on all of the coupons. The coupled coupons at both ambient temperature and 60° C were uncoupled just prior to the measurements and then immediately re-coupled. The data points plotted in light blue or pink from day 15 to 20 correspond to uncoupling the coupled coupons for the remainder of the experiment and vice versa.

6.3.1 Ambient Temperature

The behaviour of the individual rest potentials of the coupled and uncoupled weld and parent coupons is summarised in Tables 6.1 and 6.2 below.

Table 6.1 Potential behaviour of initially coupled coupons at ambient temperature.

Coupled Coupons		
Days	**Parent Metal**	**Weld Metal**
1	-703 mV	-692 mV
2 - 10	Decreased to -704 mV	Decreased to -704 mV
11 - 14	Increased to -702.5 mV	Decrease to -705 mV
Uncoupled		
15 - 20	Remains at –701 to -700 mV	Remains at –701 mV

The weld and parent metals appear to adopt more negative potentials with immersion time. On day 10 the rest potentials are very similar and continue to be so when they are uncoupled.

Table 6.2 Potential behaviour of initially uncoupled coupons at ambient temperature.

Uncoupled Coupons		
Days	**Parent Metal**	**Weld Metal**
1	-729 mV	-713 mV
2 - 10	Increase to –719 mV	Increase to –706 mV
11 - 14	Increase to –709 mV	Increase to –703 mV
Coupled		
15 - 20	Increases from -706 to -702 mV overall	Remains at –699 mV

The potential difference between the individual potentials of the parent and weld metals is between 16 and 6 mV. When the coupons are coupled during days 15 to 20, the individual potentials of both metals differ by 3 to 6 mV.

6.3.2 60° C

At 60° C, the individual rest potentials of the coupled and uncoupled weld and parent coupons with time are summarised in Tables 6.3 and 6.4 below.

Table 6.3 Potential behaviour of initially coupled coupons at 60° C.

Coupled		
Days	**Parent**	**Weld**
1	-733 mV	-734 mV
2 – 10	Increase from -728 to -717 mV	Increase from –725 to -720 mV
11 - 14	Remains at –715 mV	Increases from –720 to -715 mV
Uncoupled		
15 - 20	Slight increase from -715 to –712 mV	Slight increase from -715 to –712 mV

Both of the metals when coupled display similar rest potentials, which increase with time. When uncoupled the two metals become slightly more noble and have similar rest potentials.

Table 6.4 Potential behaviour of initially uncoupled coupons at 60° C.

Uncoupled		
Days	**Parent**	**Weld**
1	-754 mV	-751 mV
2 – 10	Increase from -726 to -712 mV	Increase from -725 to -704 mV
11 - 14	Slight increase from -710 to –708 mV	Increase from -701 to -696 mV
Coupled		
15 - 20	Increase from -707 to -701 mV	Increase from -698 to -694 mV

The rest potentials of the uncoupled parent and weld metals become nobler than the coupled coupons but with 9 to 13 mV difference. When coupled the individual potentials continue to increase and both metals retain a 7 to 9 mV difference, although this potential difference appears to decline with time.

6.4 Rp of Coupled and Uncoupled Weld and Parent Metal Coupons

Uncoupled Rp for each weld and parent metal coupon at ambient temperature and 60° C was determined. The parent is plotted against time in royal blue and the weld metal in red with the light blue and pink indicating where the coupled coupons were uncoupled and vice versa. The Rp behaviour with time is plotted in Figures 6.7 and 6.8.

6.4.1 Ambient Temperature

The Rp behaviour with time is summarised for the coupled and uncoupled weld and parent metal coupons in the Tables 6.5 and 6.6 below.

Table 6.5 Rp of initially coupled coupons at ambient temperature.

Coupled		
Day	**Parent Metal**	**Weld Metal**
1	750 Ohm	3100 Ohm
2 - 10	600 to 250 Ohm	A sharp reduction from 2200 to 750 Ohm
11 – 14	240 to 250 Ohm	600 to 450 Ohm
Uncoupled		
15 - 20	200 to 175 Ohm	400 to 300 Ohm

The Rp of both metals (weld metal in particular) declines with time and continues this trend after uncoupling.

Table 6.6 Rp of initially uncoupled coupons at ambient temperature.

Uncoupled		
Day	**Parent Metal**	**Weld Metal**
1	250 Ohm	2550 Ohm
2 - 10	250 to 180 Ohm	2900 to 2400 Ohm
11 – 14	170 to 150 Ohm	2400 to 2250 Ohm
Coupled		
15 - 20	150 to 100 Ohm	2250 to 2000 Ohm

The uncoupled parent and weld metal shows decline in Rp with time but the weld metal decrease is less than the coupled weld and is unaffected by long-term coupling.

6.4.2 60° C

The Rp behaviour is summarised for the coupled and uncoupled weld and parent metal coupons in the Tables 6.6 and 6.7 below.

Table 6.7 Rp of initially coupled coupons at 60°C.

Coupled		
Day	**Parent Metal**	**Weld Metal**
1	80 Ohm	65 Ohm
2 - 10	90 to 75 Ohm	70 to 55 Ohm
11 – 14	Approx. 68 to 62 Ohm	Approx. 45 to 55 Ohm
Uncoupled		
15 - 20	68 to 60 Ohm	Remains overall at 55 Ohm

The weld metal Rp is consistently lower than for the parent metal. Rp generally decreases with time for both metals.

Table 6.8 Rp of initially uncoupled coupons at 60° C.

Uncoupled		
Day	**Parent Metal**	**Weld Metal**
1	165 Ohm	115 Ohm
2 - 10	75 to 70 Ohm	60 to 48 Ohm
11 – 14	70 to 65 Ohm	45 to 40 Ohm
Coupled		
15 - 20	Remains overall at 60 Ohm	Increases from 40 to 95 Ohm

In general, the Rp decreases with time with the exception of the originally uncoupled weld metal that records an increase in Rp when coupled to the parent metal coupon.

6.5 Corrosion Rates of Coupled and Uncoupled Weld and Parent Metal Coupons

The corrosion rates of all of the coupons at ambient temperature and 60° C were calculated from the obtained Rp values using Equation 4.3. A Stern-Geary constant of 17 mV was used in the calculation. The corrosion rates with time of the coupled and uncoupled weld and parent metals are plotted in Figures 6.9 and 6.10.

6.5.1 Ambient Temperature

The corrosion rates with time are summarised in Tables 6.9 and 6.10 below.

Table 6.9 The corrosion rate of the initially coupled coupons at ambient temperature.

Coupled		
Day	**Parent Metal**	**Weld Metal**
1	0.3 mm y^{-1}	0.1 mm y^{-1}
2 - 10	0.35 to 1.0 mm y^{-1}	0.1 to 0.3 mm y^{-1}
11 – 14	0.8 to 1.0 mm y^{-1}	0.35 to 0.48 mm y^{-1}
Uncoupled		
15 - 20	1.15 to 1.45 mm y^{-1}	0.5 to 0.75 mm y^{-1}

Both of the coupled weld and parent metals reveal an increase in corrosion rate with time. The parent metal has the higher corrosion rate of the couple at this temperature and the period of uncoupling does not appear to affect the corrosion rate increase.

Table 6.10 The corrosion rate of the initially uncoupled coupons at ambient temperature.

Uncoupled		
Day	**Parent Metal**	**Weld Metal**
1	0.8 mm y^{-1}	0.1 mm y^{-1}
2 - 10	0.9 - 1.3 mm y^{-1}	Remains at 0.1 mm y^{-1}
11 – 14	1.55 to 1.75 mm y^{-1}	Remains at 0.1 mm y^{-1}
Coupled		
15 - 20	1.7 to 2.1 mm y^{-1}	Remains at 0.1 mm y^{-1}

The corrosion rate of the uncoupled parent metal is greater than that of the coupled parent and also increases with time. The uncoupled weld metal remains low and exhibits little change throughout the experiment.

6.5.2 60°C

The corrosion rates with time are summarised in Tables 6.11 and 6.12 below.

Table 6.11 The corrosion rate of the initially coupled coupons at 60° C.

Coupled		
Day	**Parent Metal**	**Weld Metal**
1	2.5 mm y^{-1}	3.0 mm y^{-1}
2 - 10	2.2 to 2.9 mm y^{-1}	2.9 to 4.0 mm y^{-1}
11 – 14	3.0 to 3.2 mm y^{-1}	4.5 to 3.7 mm y^{-1}
Uncoupled		
15 - 20	3.0 to 3.3 mm y^{-1}	Remains at 3.6 mm y^{-1}

The corrosion rates of the coupled weld and parent metals are much higher than at ambient temperature and also increase with time. The weld metal has a higher corrosion rate than the parent at 60° C.

Table 6.12 The corrosion rate of the initially uncoupled coupons at 60° C.

Uncoupled		
Day	**Parent Metal**	**Weld Metal**
1	1.2 mm y^{-1}	1.7 mm y^{-1}
2 - 10	2.7 to 2.9 mm y^{-1}	3.3 to 4.2 mm y^{-1}
11 – 14	2.9 to 3.3 mm y^{-1}	4.6 to 5.0 mm y^{-1}
Coupled		
15 - 20	3.4 to 3.6 mm y^{-1}	4.9 to 2.2 mm y^{-1}

The uncoupled weld and parent metals generally have a higher corrosion rate than the respective coupled coupons. The corrosion rates increase with time and the weld metal has a higher corrosion rate than the parent whilst uncoupled. When the coupling is reversed the weld metal displays a decrease in corrosion rate whereas the other coupons appear unaffected by the change in coupling.

6.6 Polarisation Curves

The results of cathodic and anodic potentio-dynamic sweeps of the parent and weld metal coupons are plotted as polarisation curves in Figure 6.11 a, b, c and d.

6.6.1 Ambient Temperature

The originally uncoupled weld and parent metal appear to have similar cathodic kinetics and the anodic sweep for the weld metal reveals a discontinuity between –400 and –450 mV leading to an increase in the anodic current perhaps implying a surface film breakdown. The originally coupled weld has a more negative cathodic current and slightly less current than the parent metal in the anodic curve.

6.6.2 60° C

The originally uncoupled weld metal has a more negative current than the parent metal as revealed by the cathodic curve, this trend is also observed in the anodic curve where the current is consistently lower than the parent metal.

The originally coupled weld has more negative cathodic current in comparison with the parent metal but its anodic kinetics are more similar to the parent metal than for the uncoupled weld and parent metals.

6.7 AC Impedance

The impedance measurements were taken on day 7 and 8 and the Nyquist and Bode plots of the coupled and uncoupled weld and parent metal coupons at ambient temperature and 60° C are displayed in Figures 6.12 to 6.15. A summary of the results is listed in Table 6.13.

Table 6.13 Measured and calculated data obtained from the impedance measurements.

Temperature		Coupon	R_s (Ohm cm^2)	Z (Ohm cm^2)	C (F)	i (A cm^{-2})	Corrosion Rate (mm y^{-1})
Ambient	Uncoupled	Parent	12.27	161.20	1.00E-03	1.05E-04	1.24
		Weld	52.22	2253.45	8.95E-05	7.54E-06	0.09
	Coupled	Parent	12.11	294.36	6.33E-04	5.78E-05	0.68
		Weld	17.17	1030.54	1.97E-04	1.65E-05	0.19
60° C	Uncoupled	Parent	7.36	59.90	1.90E-03	2.84E-04	3.33
		Weld	6.00	36.18	3.00E-03	4.70E-04	5.51
	Coupled	Parent	8.87	59.82	2.00E-03	2.84E-04	3.33
		Weld	6.00	46.47	2.00E-03	3.66E-04	4.29

6.7.1 Solution Resistance Values

The solution resistance (R_s) at ambient temperature is just over 12 Ohm for both parent metals and is slightly higher for the coupled weld metal at 17 Ohm but is found to be 52 Ohm for the uncoupled weld metal – which has a much higher Rp.

At 60° C the R_s is lower – between 6 and 8.87 Ohm probably due to the larger quantity of dissolved corrosion products increasing the solution conductivity.

6.7.2 Z' Values

At ambient temperature both the coupled and uncoupled weld metal coupons have much higher Z or Rp (polarisation resistance) than the parent metal coupons (Table 6.13). Although the two parent metals can be considered to have similar Rp, the coupled parent metal Rp is over 100 Ohms higher than that of the uncoupled and is consistent with the LPR measurements in this time period. The coupled weld metal showed a sharp decline in Rp in LPR measurements in the period that the impedance was recorded and this is reflected in a value of just over 1000 Ohm cm^2. The Rp provided for the uncoupled weld, although slightly lower, is also consistent with the LPR measurements.

At 60° C both of the parent coupons have virtually identical Rp of nearly 60 Ohm cm^2. The uncoupled weld metal coupon has a lower Rp (10 Ohm) than the

coupled and both of the coupons have a lower Rp than the corresponding parent metals. All of the metals have a slightly lower Rp recorded with impedance than that given by the LPR of the same period because of the distinction of Rp from the solution resistance.

6.7.3 Corrosion Rates

A Stern-Geary constant of 17 mV and the Rp values from the impedance measurements were used to calculate the corrosion rates in mmpy of the weld and parent metals at both temperatures in Table 6.13. It can be inferred from the Nyquist plots at ambient temperature that the weld metals have much lower corrosion rates than the parent metals and at this temperature the overall corrosion rate is much lower than the coupons at 60° C. By studying the plots for the 60° C experiment it is obvious that the weld metals have a higher corrosion rate than the parent metals at the same temperature, this is in agreement with, and quantified by the calculated corrosion rates.

6.8 Surface Analysis of Weld and Parent Metals

The surface of the weld and parent were analysed uncorroded, polished to 1 μm, and after immersion at ambient temperature and 60° C. The solution used at ambient temperature and 60° C was deionised water with 3.5 % NaCl, 49 ppm HCO_3^- and saturated with CO_2. The immersion time for both of the experiments was approximately 150 hours, in this time the weld and parent metals were galvanically coupled.

6.8.1 The Non-Corroded Metal Surface

Scanning electron micrographs and EDX analysis spectra of the weld and parent metals are shown in Figures 6.16 a, b to 6.17 a, b and c. The polishing lines are clearly visible on the micrographs of the weld and parent. There are small, dark areas visible in the micrographs of the parent containing Si, Ca as well as Fe (marked *A* in Figure 6.17 a and in the spectrum, 6.17 c). The features, also seen on the weld metal are approximately 3 to 8 μm in length and are probably the former sites of inclusions that have been removed during polishing. The weld metal spectrum reveals a strong signal for Fe and weaker signals indicating the presence of C, Si, Mn and Ni. In

comparison, the parent metal spectrum suggests a similar composition as expected, but with the absence of Ni.

6.8.2 Corrosion at Ambient Temperature

Scanning electron micrographs and EDX analysis spectra of the weld and parent metals after immersion for 150 hours at ambient temperature are shown in Figures 6.18 a, b to 6.19 a, b. The surface of the weld metal appears porous with some larger, rough porous features and the parent metal surface is more porous has a more uniform roughness than the weld metal. The general weld metal EDX spectrum shows weak signals for C, O, Cl, Cu, Cr, Mo, Cr and Mn in addition to the strong Fe signal and the general parent metal spectrum shows the detection of Si and in addition to the above, but not Cu.

6.8.3 Corrosion at 60° C

Scanning electron micrographs and EDX analysis spectra of the weld and parent metals after immersion for 150 hours at 60° C are shown in Figures 6.20 a and b to 6.21 a, b and c. The main feature of the weld metal consisted of the cubic crystals approximately 15 μm in length and packed together on the metal surface. The parent metal did not appear to have the same features but revealed what appeared to be the actual metal and other surface features. The weld metal spectrum shows the detection of a strong signal for Fe and slightly weaker signals for C, O and Si (probably due to SiO_2). Weak signals for S, Ti, Cr, Mn and Ni were detected on the general surface. EDX analysis spectrum of the apparently amorphous feature approximately 70 x 120 μm in width and length, marked *B* on the parent metal micrograph, shows the most counts for Si followed by O and C. Weaker signals indicate that Fe, Na, Al, S, Cl, K, Ca, Mg and P are present in the feature. EDX analysis spectrum of the region marked *C*, which appears to be bare metal with a non-continuous film has a strong signal for Fe and a slightly weaker signal for O, Si and C. a weak signal for Mn, Cr, Ni, V, Al, Cl and S is detectable.

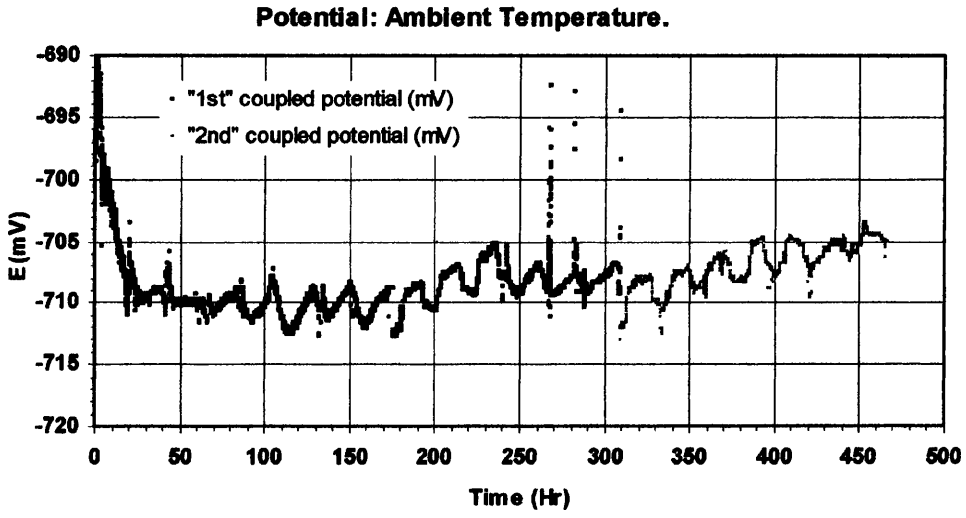

Figure 6.1 The potentials of both pairs of weld and parent metal coupons when coupled.

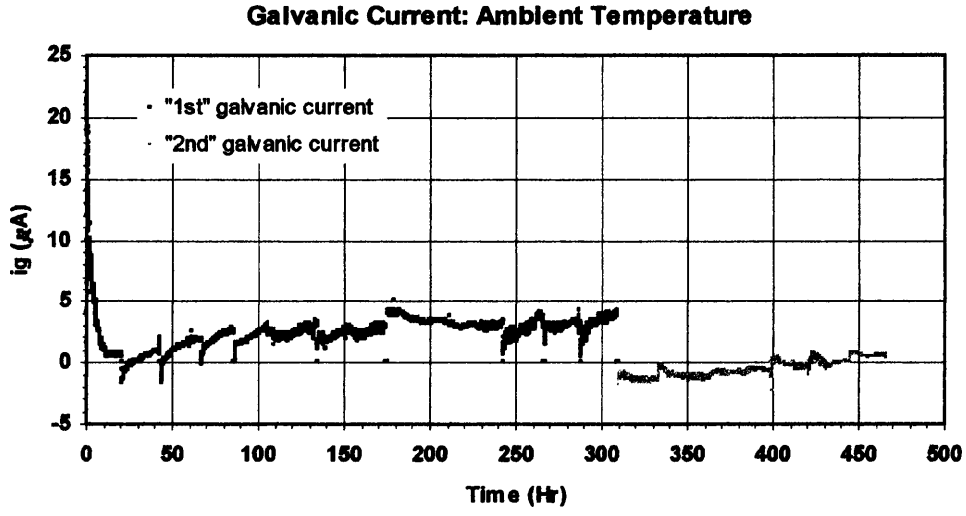

Figure 6.2 The galvanic currents of both pairs of weld and parent metal coupons when coupled.

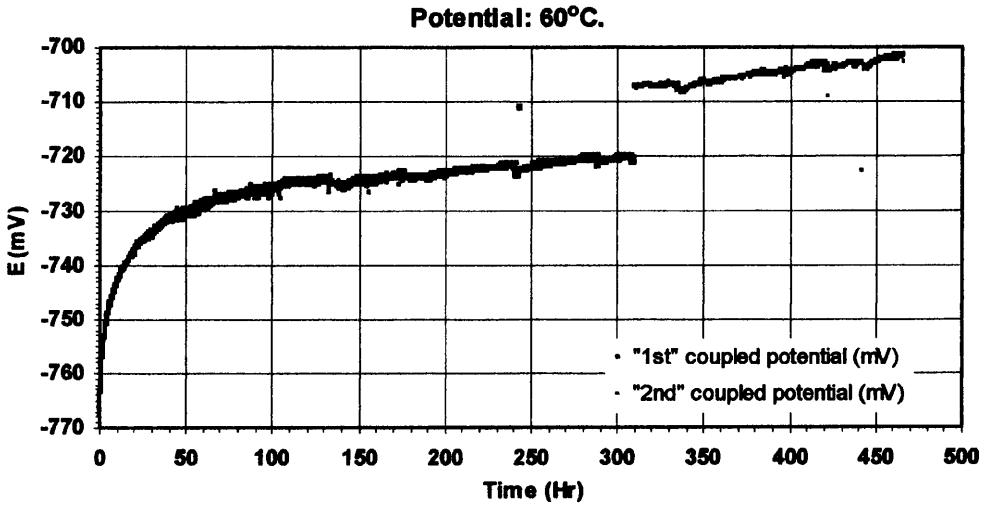

Figure 6.3 The potentials of both pairs of weld and parent metal coupons when coupled.

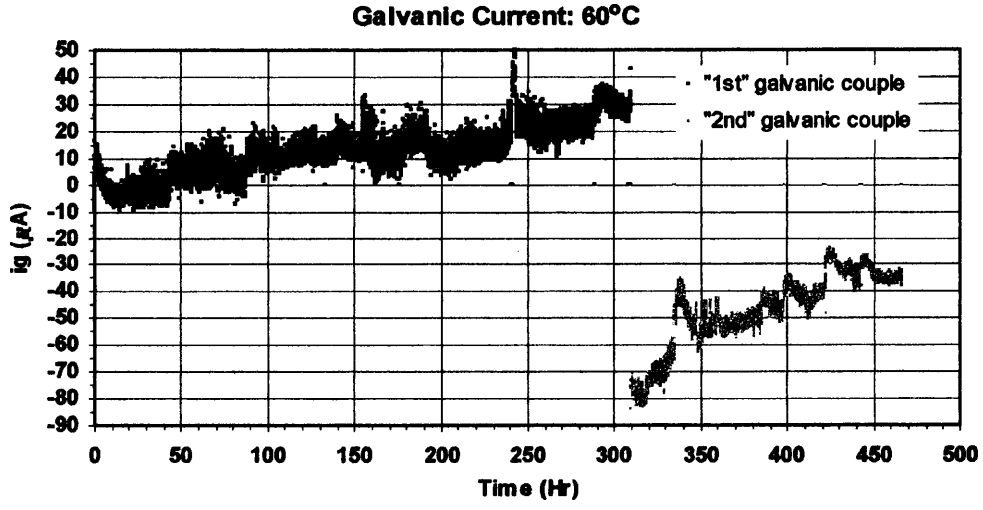

Figure 6.4 The galvanic currents of both pairs of weld and parent metal coupons when coupled.

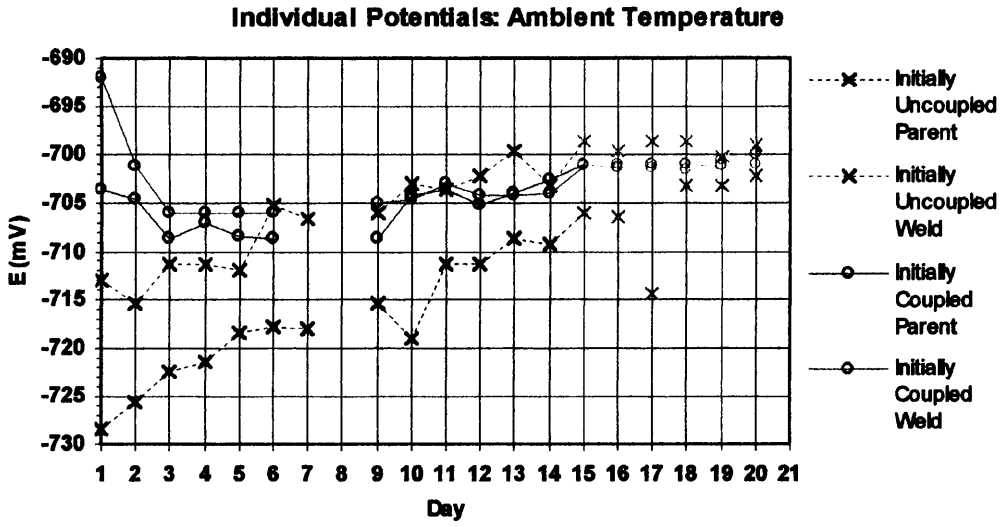

Figure 6.5 The individual measured potentials of the coupled and uncoupled weld and parent metals against time.

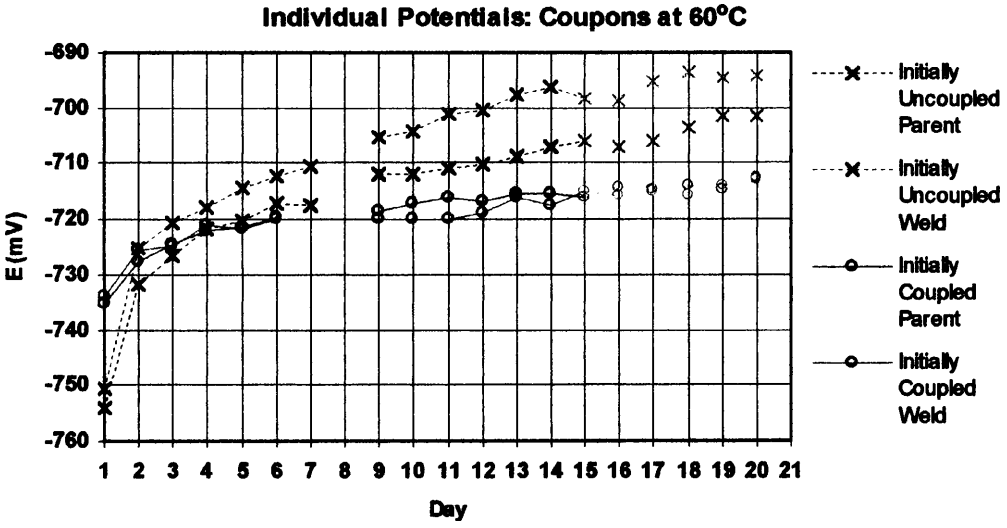

Figure 6.6 The individual measured potentials of the coupled and uncoupled weld and parent metals against time.

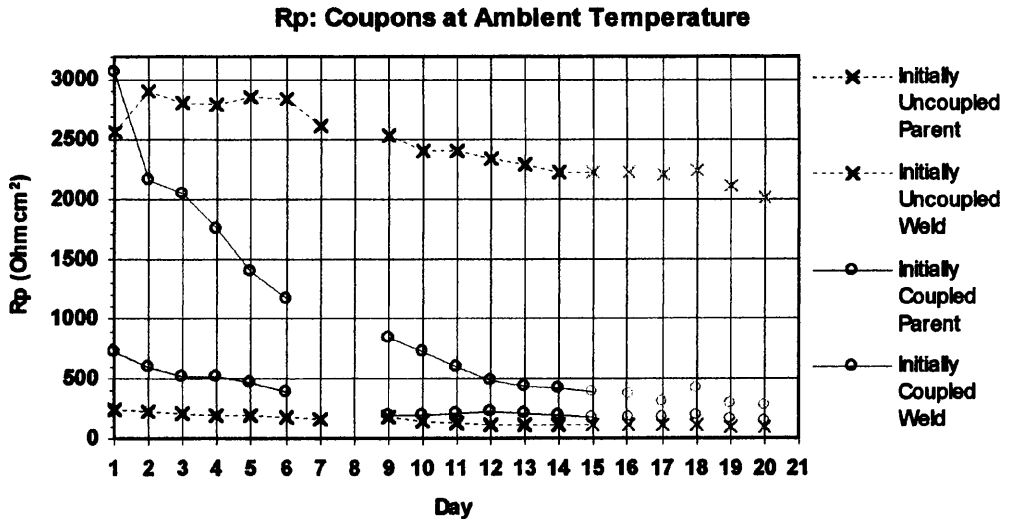

Figure 6.7 The individual measured Rps of the coupled and uncoupled weld and parent metals against time.

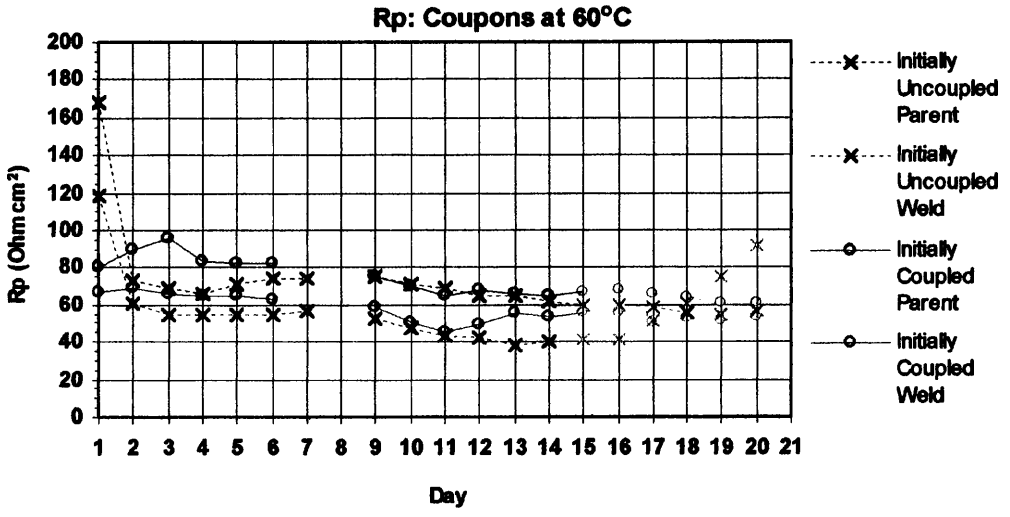

Figure 6.8 The individual measured Rps of the coupled and uncoupled weld and parent metals against time.

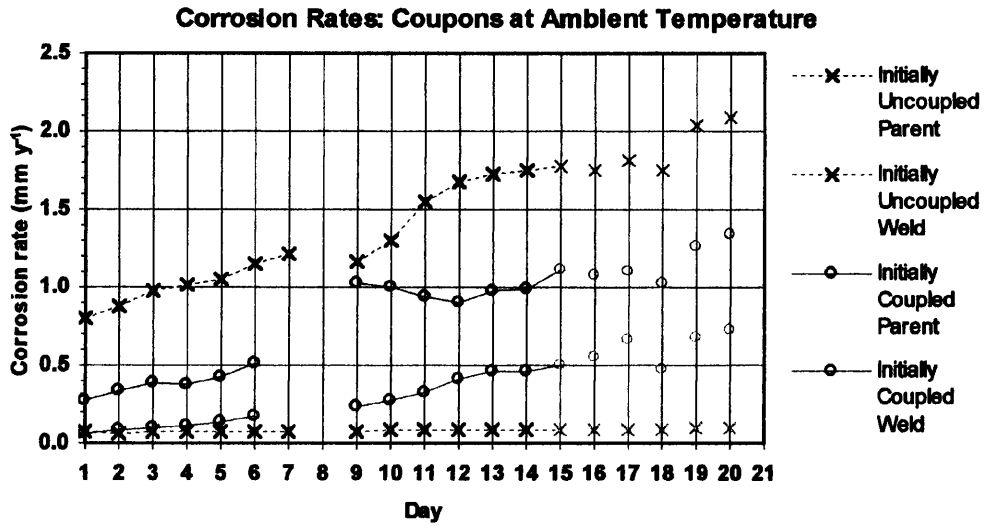

Figure 6.9 The corrosion rates of the coupled and uncoupled weld and parent metals against time.

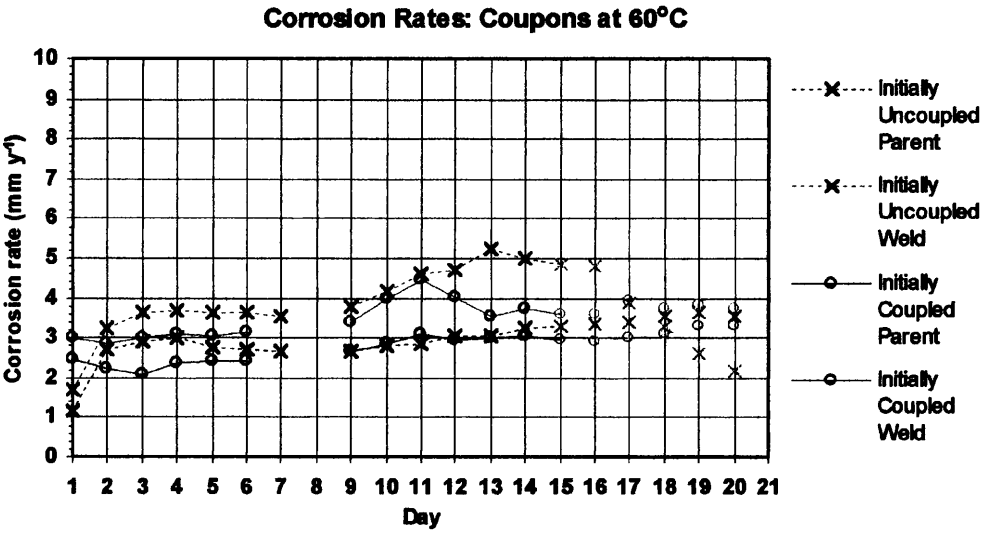

Figure 6.10 The corrosion rates of the coupled and uncoupled weld and parent metals against time.

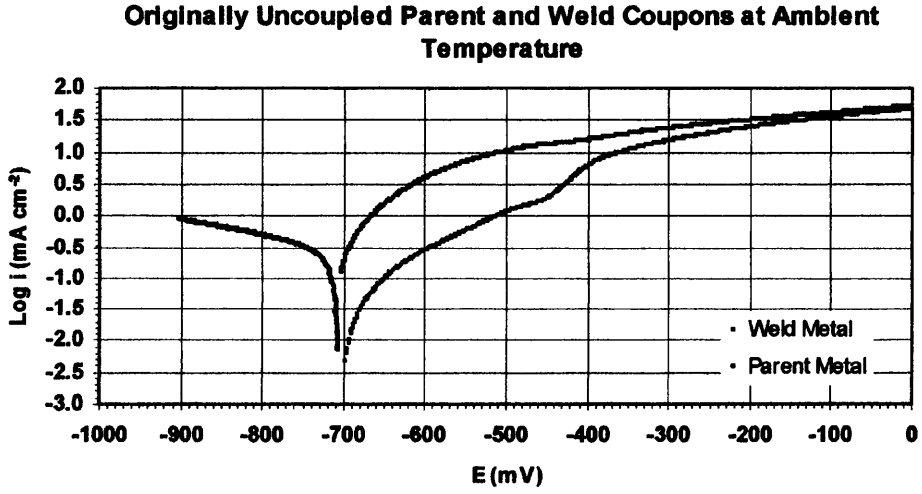
Originally Uncoupled Parent and Weld Coupons at Ambient Temperature
Log i (mA cm-2)
2.0
1.5
1.0
0.5
0.0
-0.5
-1.0
-1.5
-2.0
-2.5
-3.0
-1000
-900
-800
-700
-600
-500
-400
-300
-200
-100
0
E (mV)
Weld Metal
Parent Metal

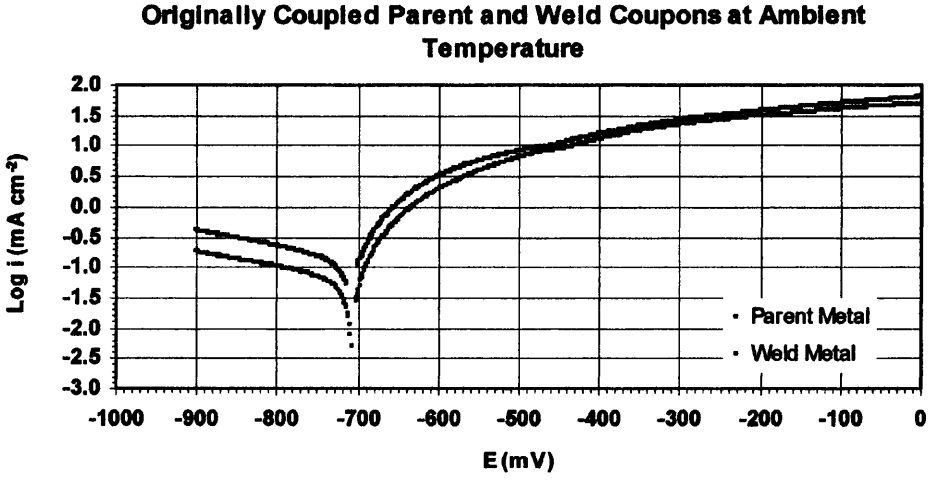
Originally Coupled Parent and Weld Coupons at Ambient Temperature
Log i (mA cm-2)
2.0
1.5
1.0
0.5
0.0
-0.5
-1.0
-1.5
-2.0
-2.5
-3.0
-1000
-900
-800
-700
-600
-500
-400
-300
-200
-100
0
E (mV)
Parent Metal
Weld Metal

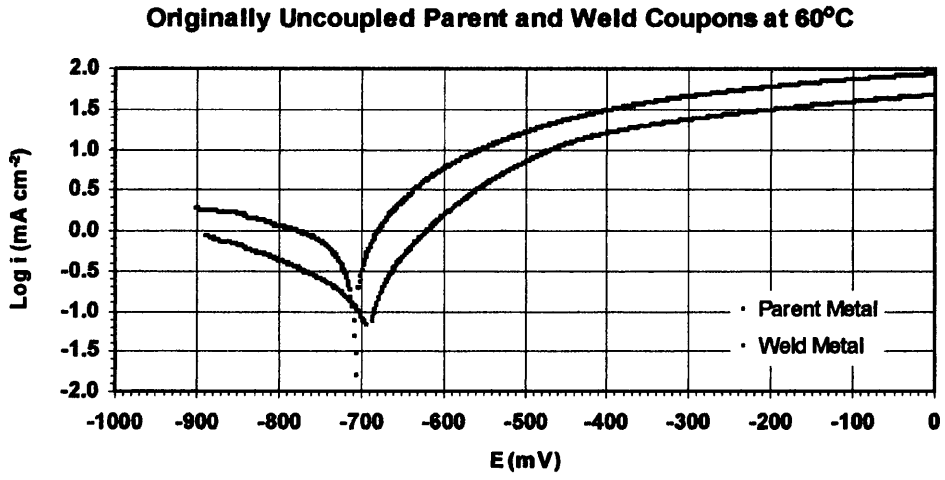

Figure 6.11 (a, b, c and d) Polarisation curves of weld and parent metal from each coupon pair.

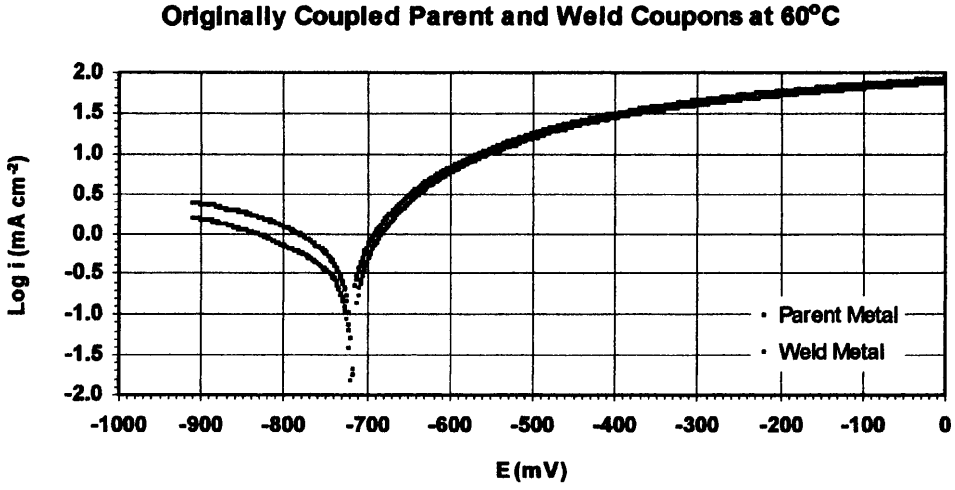

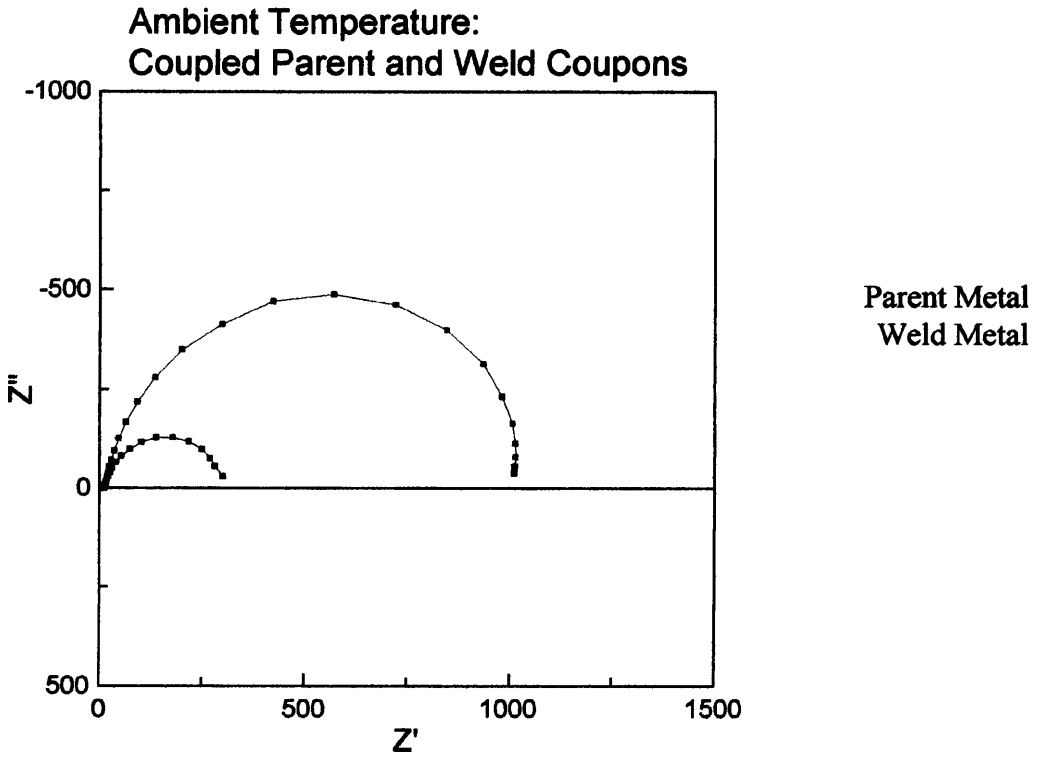

Figure 6.12 a) The Nyquist plots from the ac impedance measurements performed on the initially coupled weld (1.2 cm^2) and parent (1.08 cm^2) metal coupons.

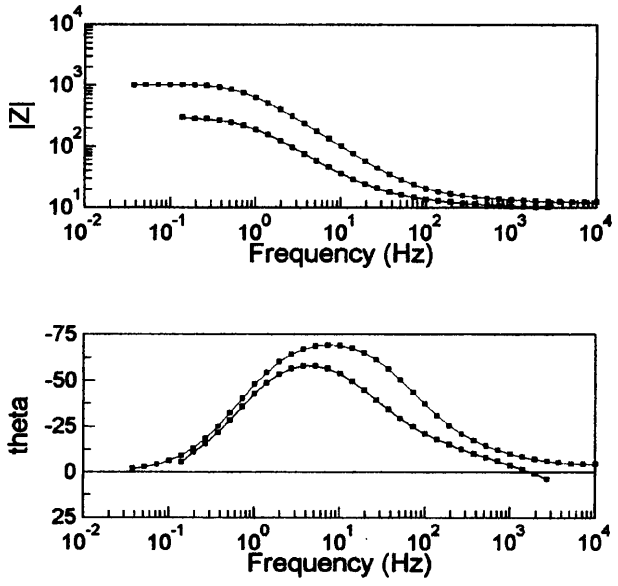

b) The impedance modulus and phase angle plotted against frequency.

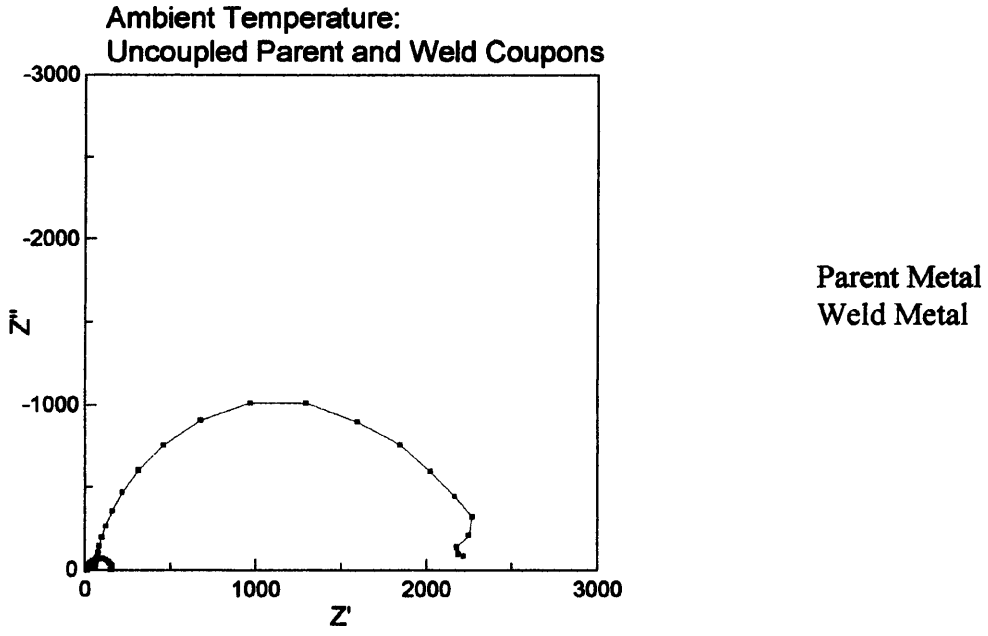

Figure 6.13 a) The Nyquist plots from the ac impedance measurements performed on the initially uncoupled weld (1.8 cm^2) and parent (1.2 cm^2) metal coupons.

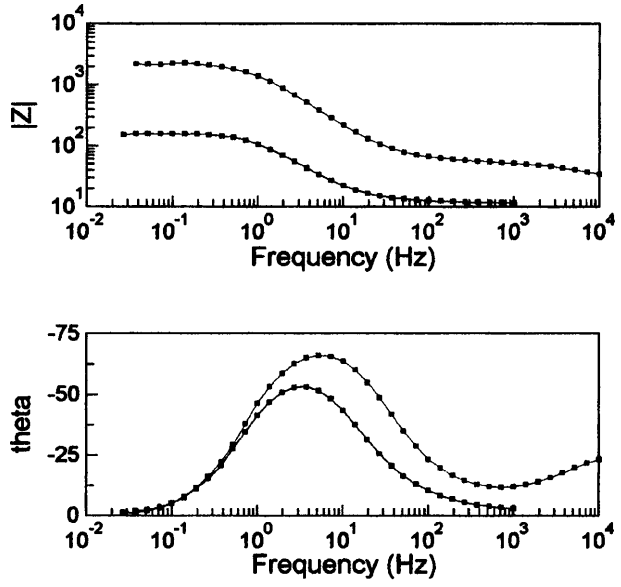

b) The impedance modulus and phase angle plotted against frequency.

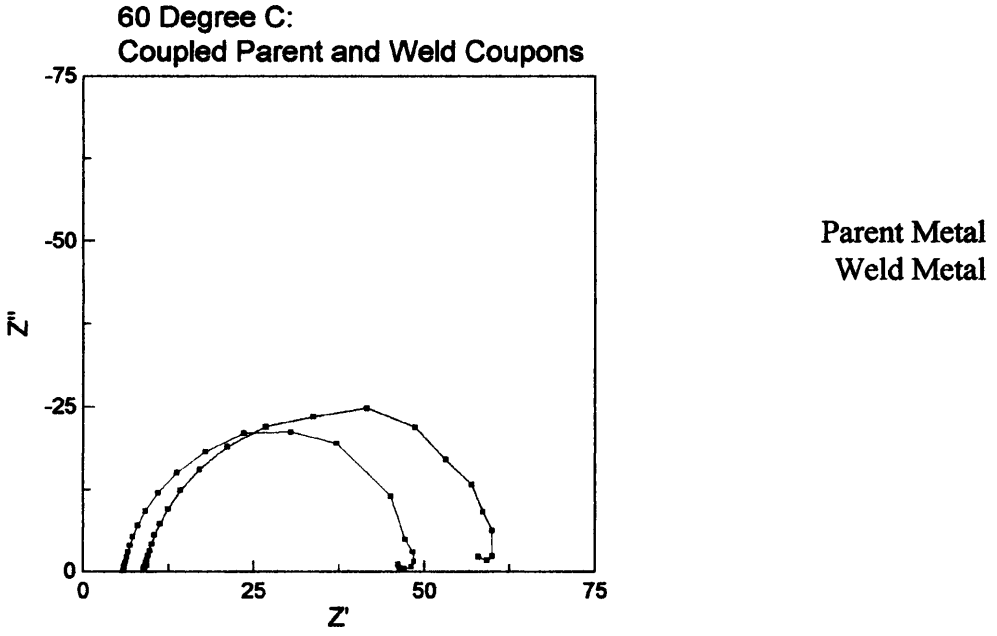

Figure 6.14 a) The Nyquist plots from the ac impedance measurements performed on the initially coupled weld (0.84 cm^2) and parent (1.2 cm^2) metal coupons.

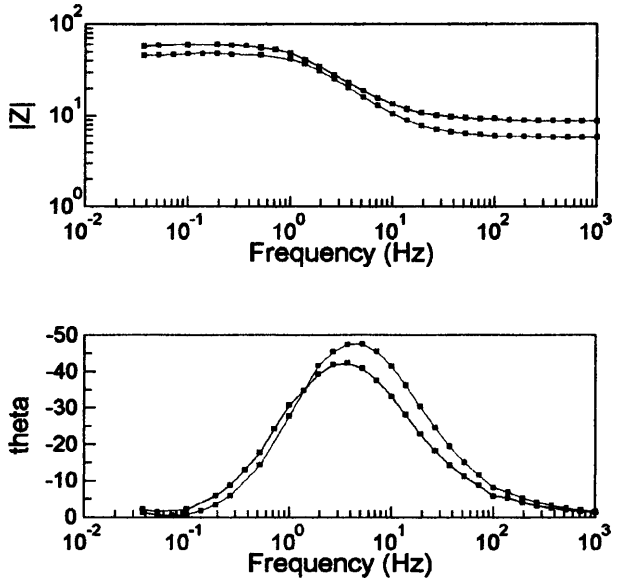

b) The impedance modulus and phase angle plotted against frequency.

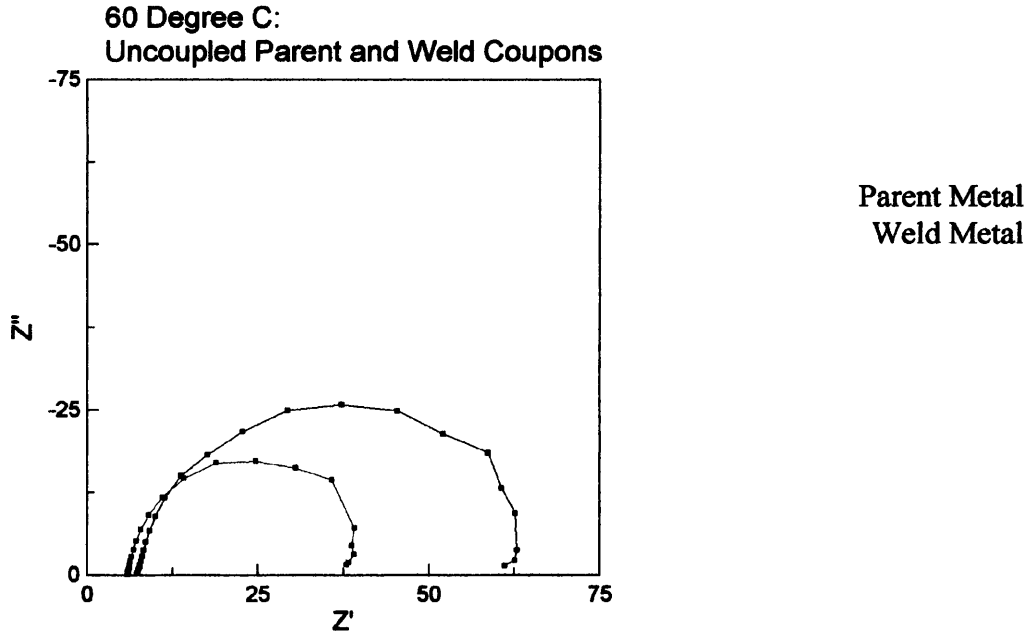

Figure 6.15 a) The Nyquist plots from the ac impedance measurements performed on the initially coupled weld (0.8 cm^2) and parent (1.1 cm^2) metal coupons.

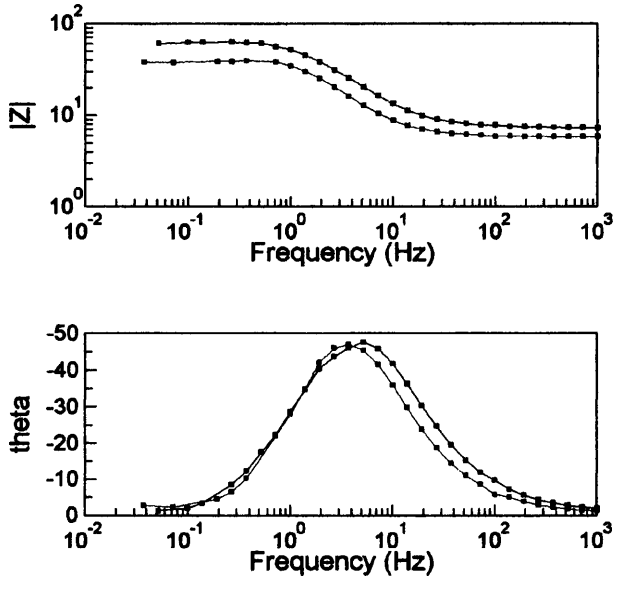

b) The impedance modulus and phase angle plotted against frequency.

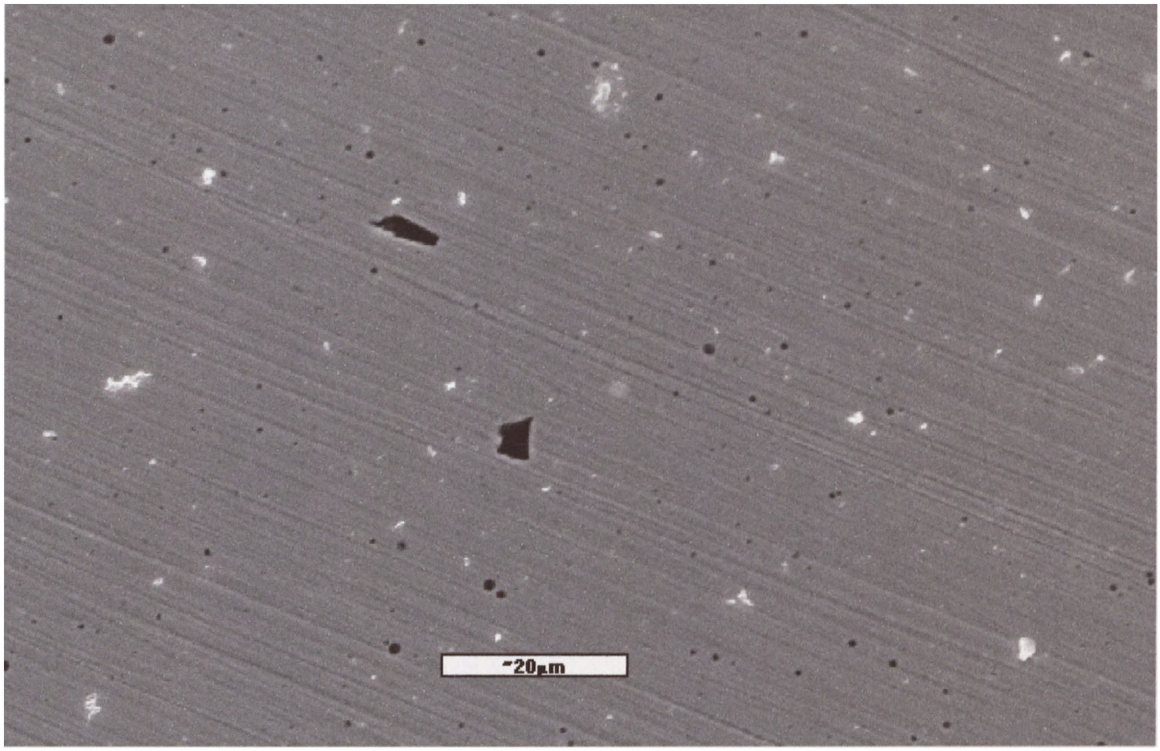

Figure 6.16a) Scanning electron micrograph of the general surface area of the weld metal, polished to 1 µm.

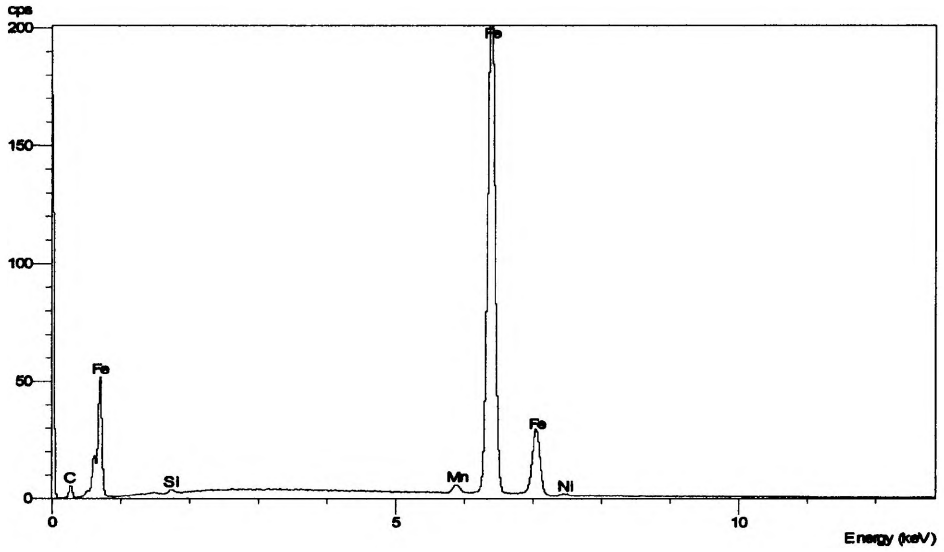

Figure 6.16b) EDX analysis spectrum of the general surface area of the weld metal, polished to 1 µm.

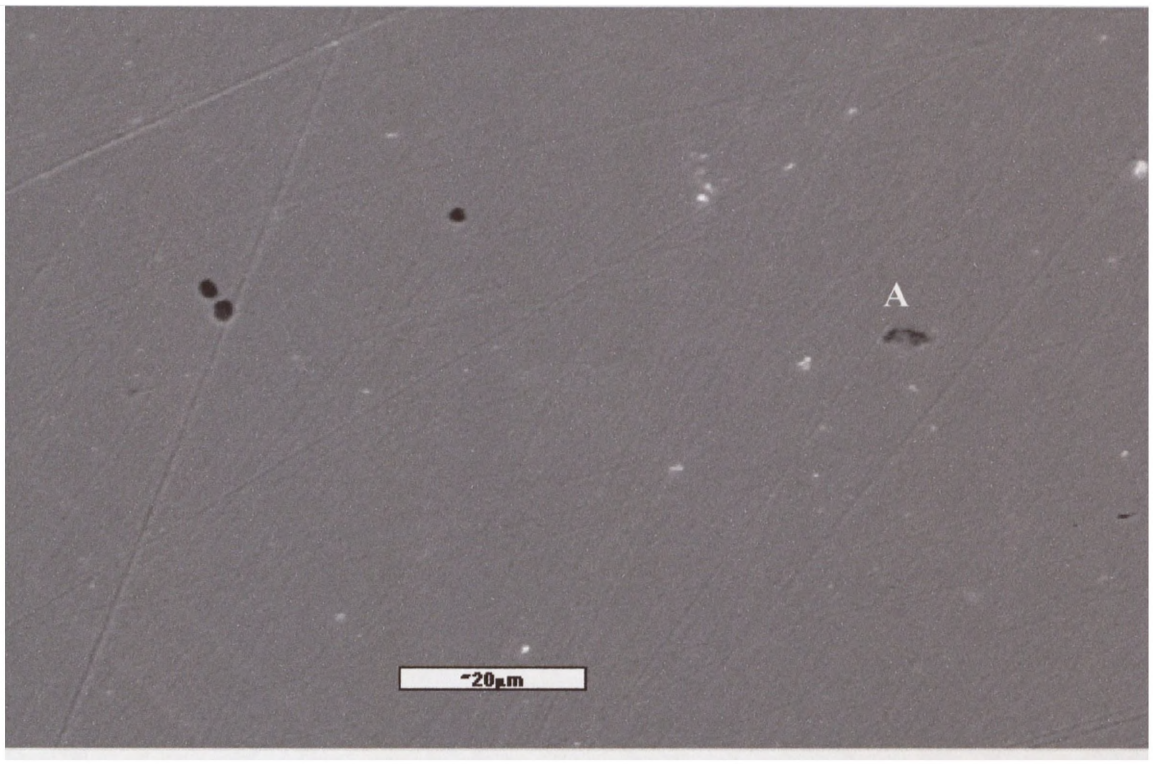

Figure 6.17a) Scanning electron micrograph of the general surface area of the parent metal, polished to 1 µm.

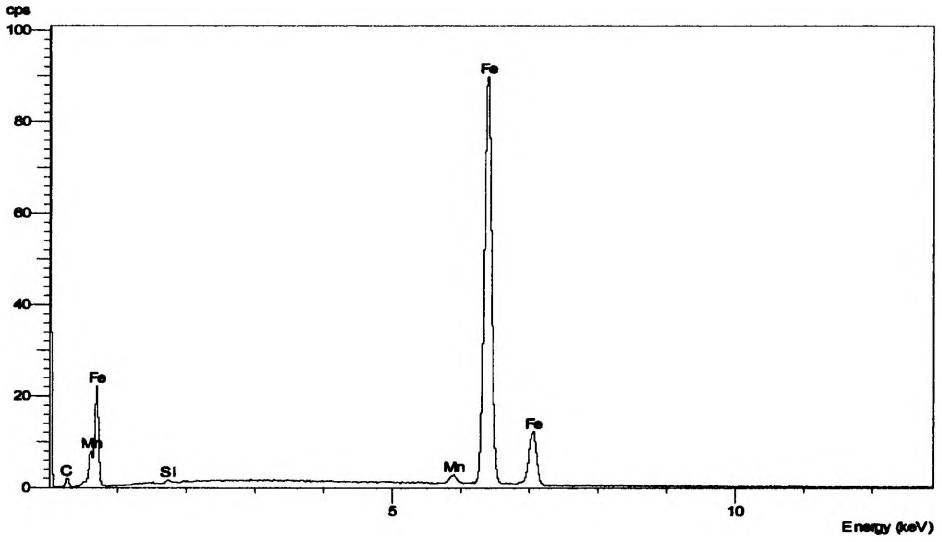

Figure 6.17b) EDX analysis spectrum of the general surface area of the parent metal, polished to 1 µm.

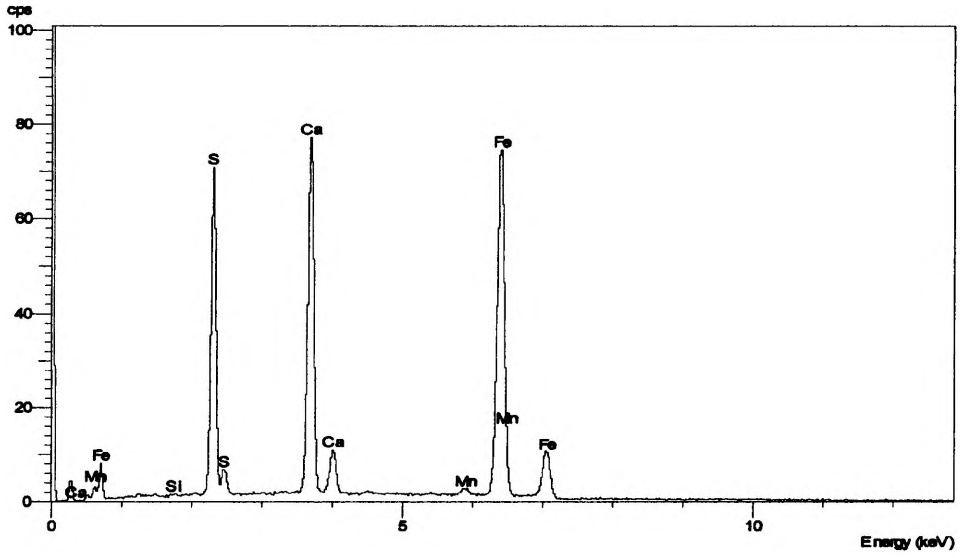

Figure 6.17c) EDX analysis spectrum of an impurity within the parent metal at region A, polished to 1 μm.

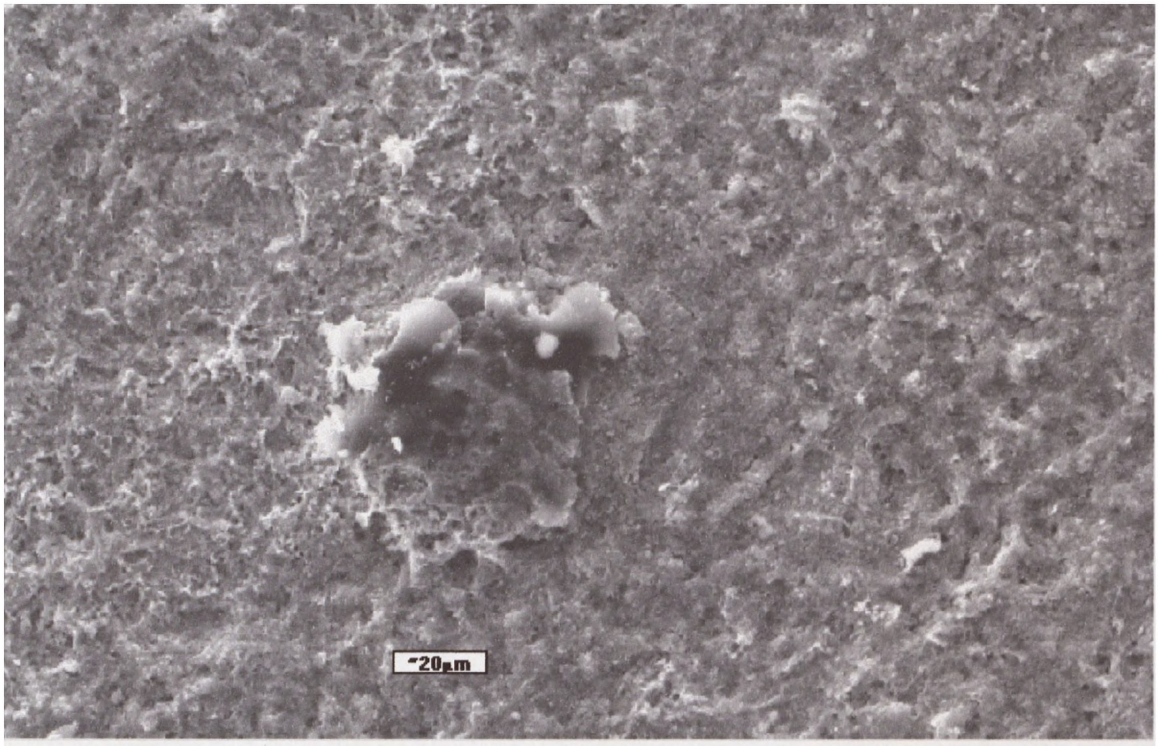

Figure 6.18a) Scanning electron micrograph of the weld metal following immersion in 3.5 % NaCl solution saturated with CO_2 at room temperature for approximately 150 h.

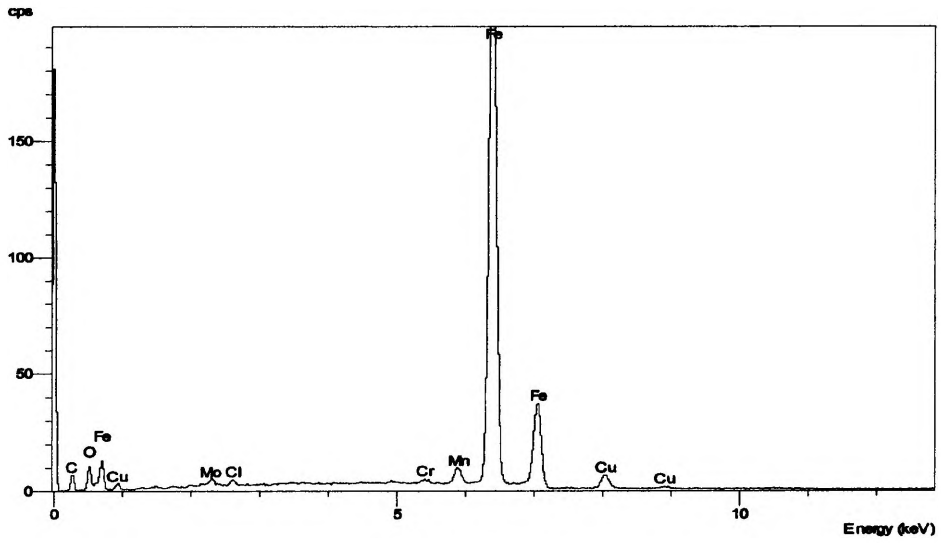

Figure 6.18b) EDX analysis spectrum of the general surface area of the weld metal following immersion in 3.5 % NaCl solution saturated with CO_2 at room temperature for approximately 150 h.

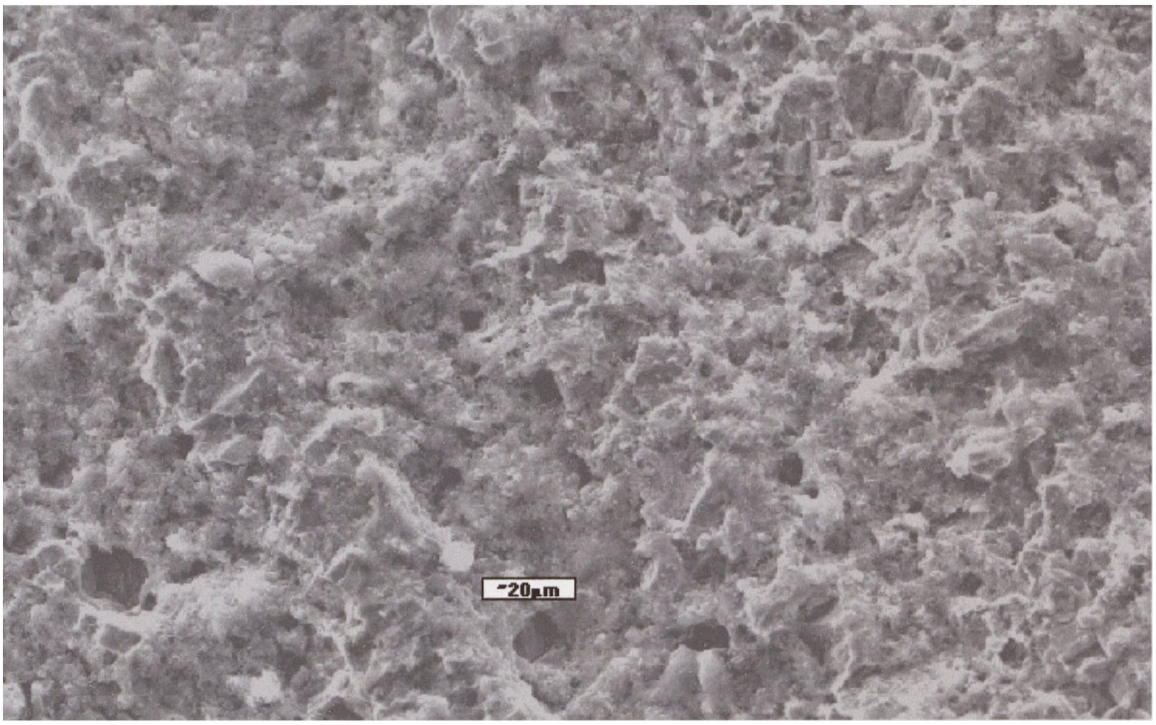

Figure 6.19a) Scanning electron micrograph of the parent metal following immersion in 3.5 % NaCl solution saturated with CO_2 at room temperature for approximately 150 h.

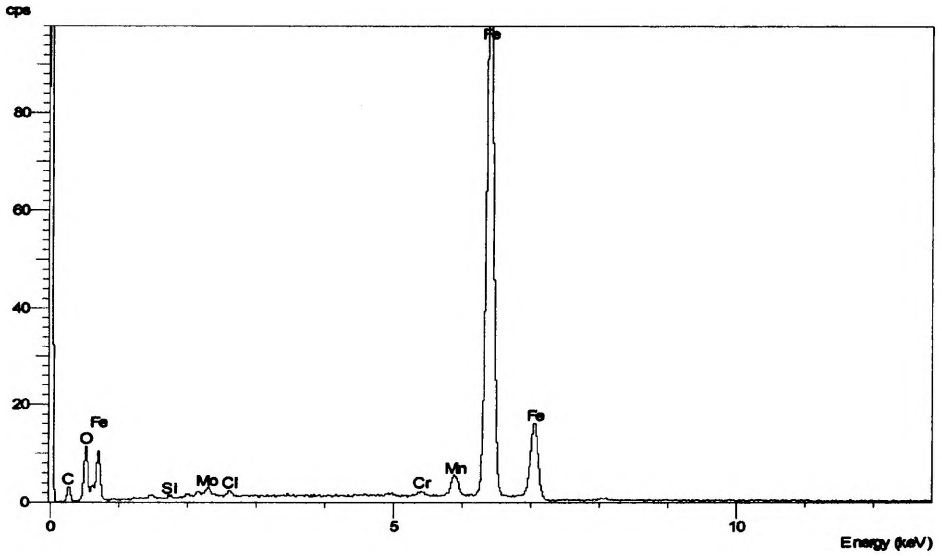

Figure 6.19b) EDX analysis spectrum of the general surface area of the parent metal following immersion in 3.5 % NaCl solution saturated with CO_2 at room temperature for approximately 150 h.

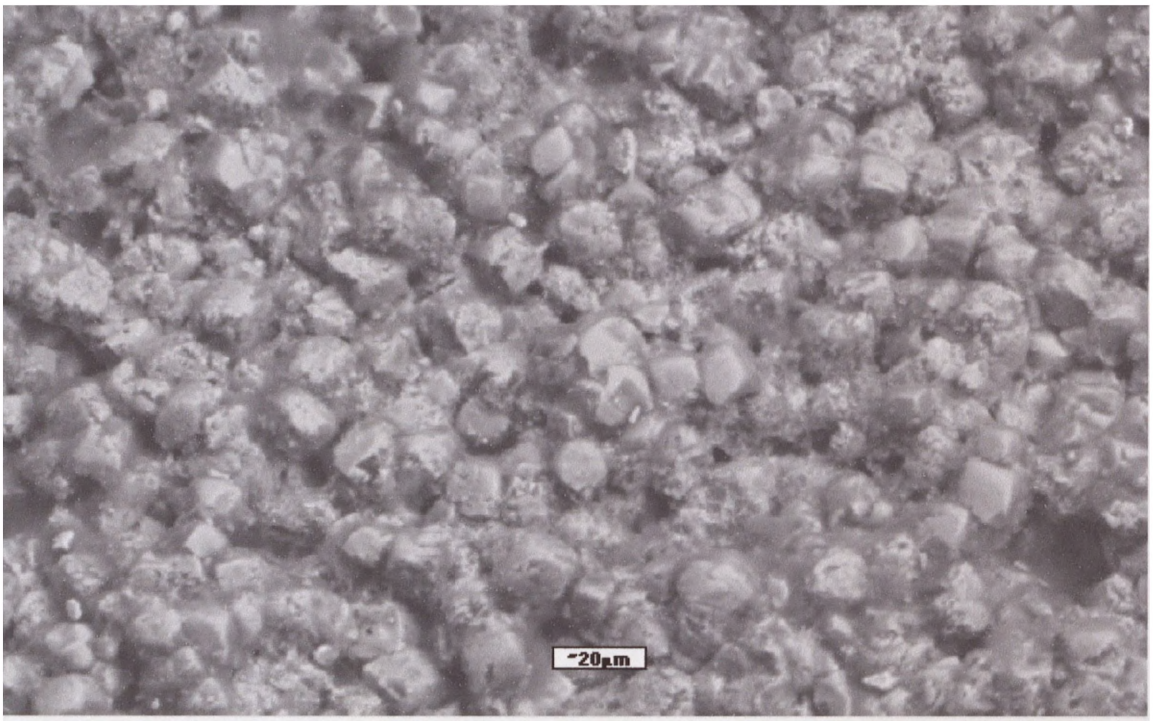

Figure 6.20a) Scanning electron micrograph of the weld metal following immersion in 3.5 % NaCl solution saturated with CO_2 at 60°C for approximately 150 h.

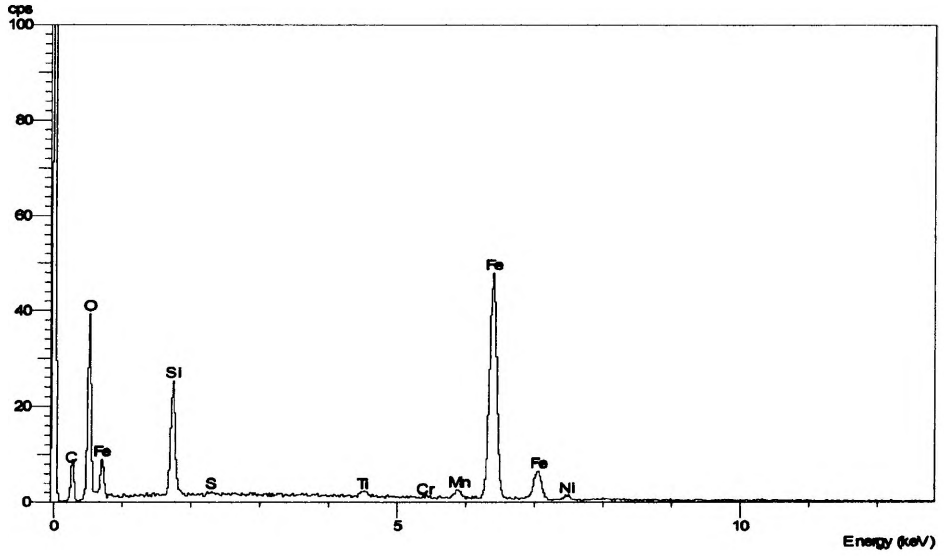

Figure 6.20b) EDX analysis spectrum of the general surface area of the weld metal following immersion in 3.5 % NaCl solution saturated with CO_2 at 60°C for approximately 150 h.

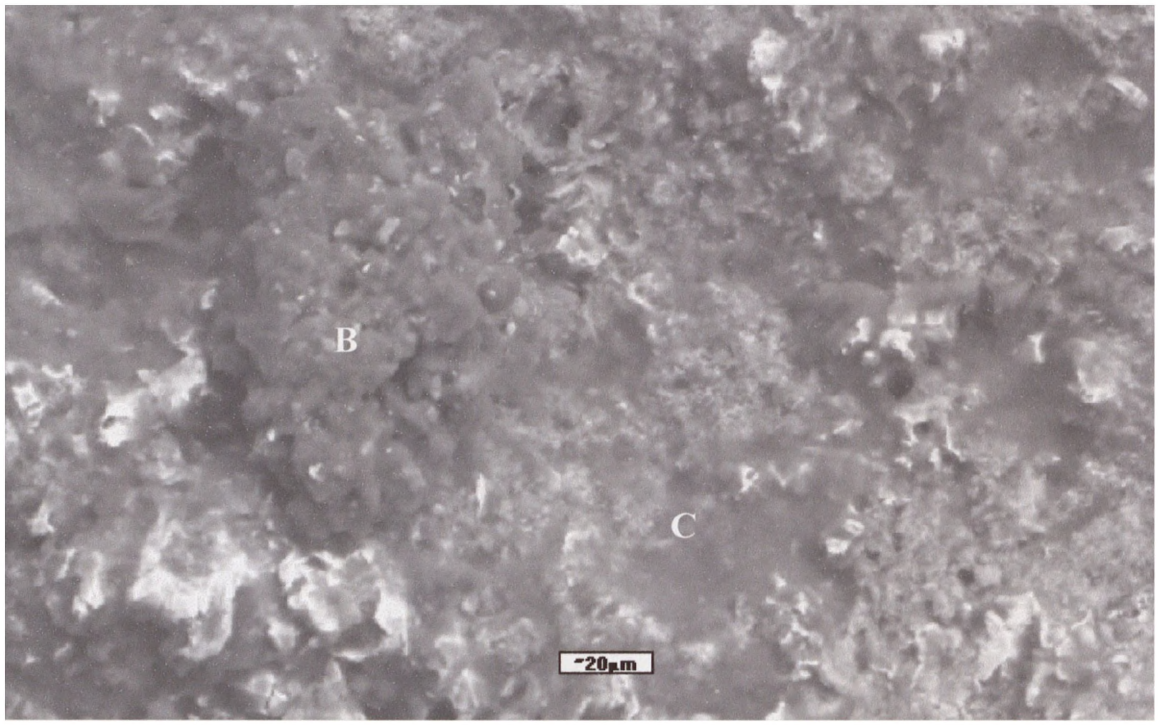

Figure 6.21a) Scanning electron micrograph of the parent metal following immersion in 3.5 % NaCl solution saturated with CO_2 at 60°C for approximately 150 h.

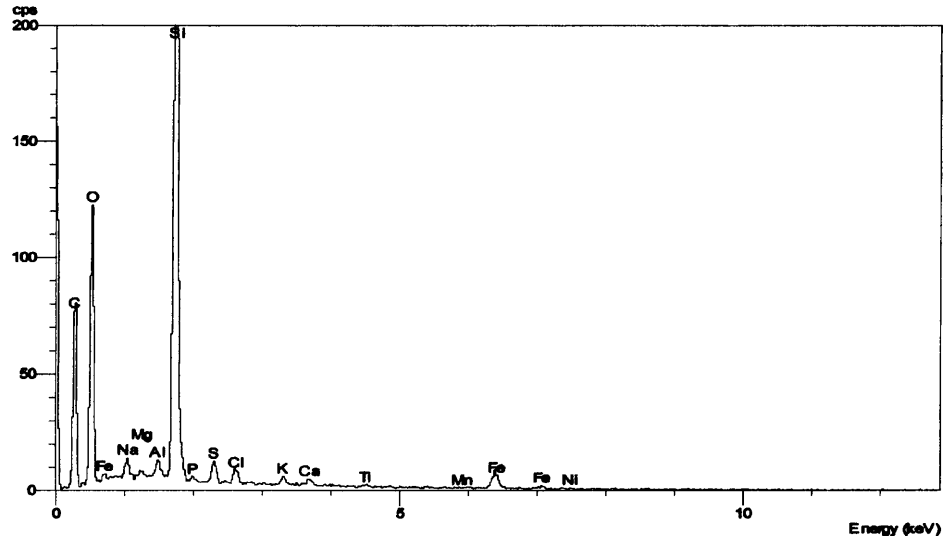

Figure 6.22b) EDX analysis spectrum at region B on the parent metal following immersion in 3.5 % NaCl solution saturated with CO_2 at 60°C for approximately 150 h.

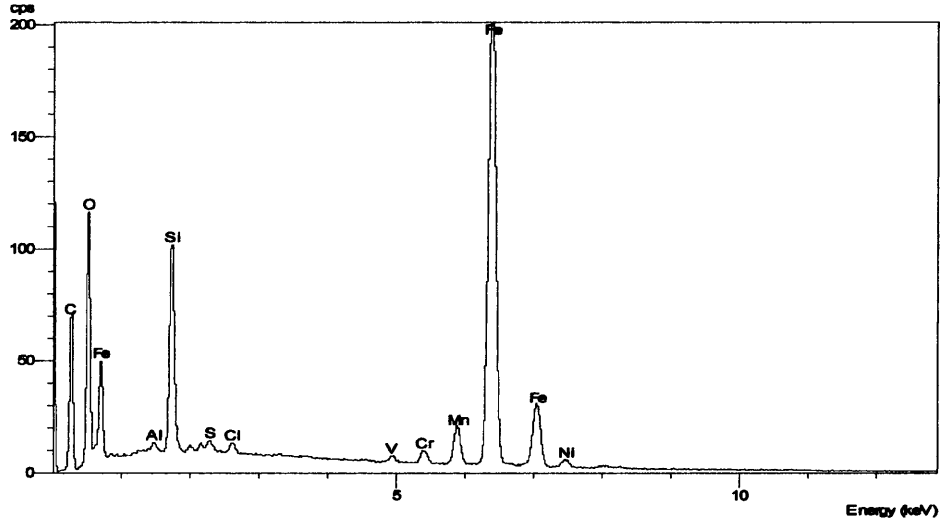

Figure 6.22c) EDX analysis spectrum at region C on the parent metal following immersion in 3.5 % NaCl solution saturated with CO_2 at 60°C for approximately 150 h.

7.0 Discussion of the Galvanic Currents and Potentials with Time for the Artificial and Waveney Electrode Experiments.

The galvanic currents with time between the weld and parent metals of the Artificial weld electrode, the Wide Waveney and the Standard Waveney weldment electrodes (at ambient temperature and 60°C) have been taken from Chapters 4.0 and 5.0 and plotted on the same axes for ease of comparison in Figure 7.1 below.

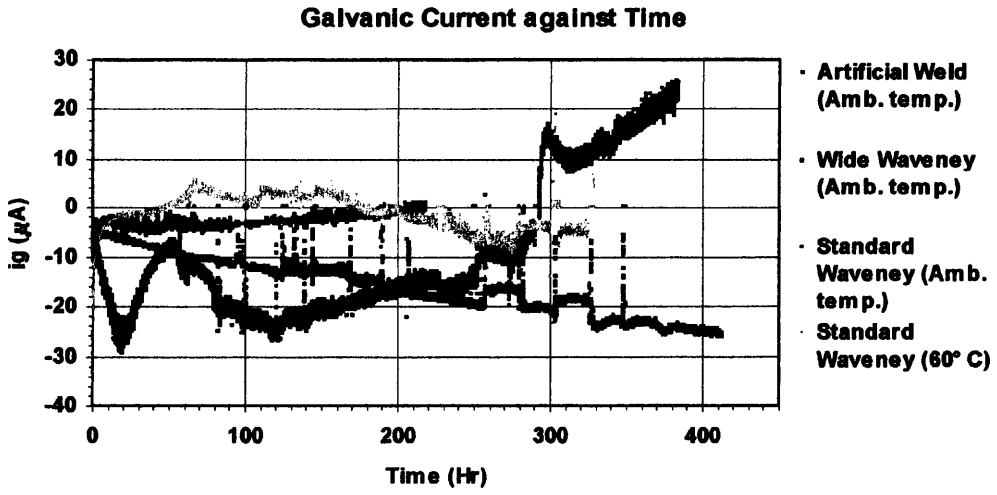

Figure 7.1 The galvanic current between the weld and both parent metals measured during the four experiments.

7.1 The Artificial Weldment Electrode

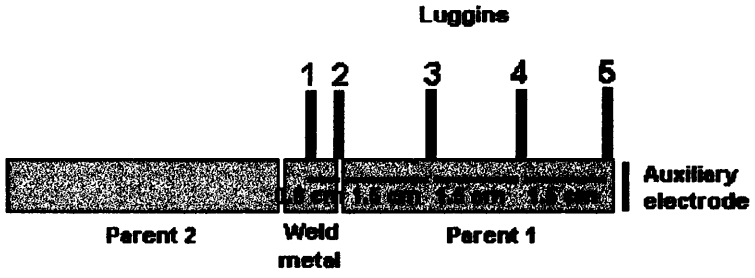

Figure 7.2 The dimensions and Luggin probe location of the Artificial electrode set up.

The Artificial weldment electrode in Figure 7.1, prepared from two low-alloy steels, had a Ni content of 1.7% for the weld component and 0.065% for the two

parent metal components. The surface area of the weld component was 1.0 by 1.0 cm and the parent metals were 1.0 cm by 4.5 cm in length. The electrolyte was CO_2 saturated deionised water.

The Artificial weldment electrode (red in Figure 7.1) shows a negative galvanic current between the weld and parent metals that becomes more negative with immersion time throughout the experiment with the exception of the effects of the liquid film thickness experiments. This negative current behaviour demonstrates the cathodic nature of a weld metal that has small quantities of Ni added in order to ensure a small potential difference between itself and the relatively anodic parent metal.

The increasing negative current with time may be explained by an increase in the number of cathodic reaction sites on the Ni-rich weld metal whilst little change occurs with regard to the cathodic and anodic kinetics of parent metal[68]. In low-alloy steels, Ni atoms are dissolved in the ferrite structure and it is the preferential dissolution of the less noble Fe that produces a porous Ni enriched matrix on the metal surface. The Ni enrichment increases with time and leads to the increasingly cathodic behaviour of the weld metal surface with immersion time.

The coupled potential measured by the reference at Luggin 1, corresponding to the centre of the weld metal shows a broad distribution of measured potentials between -685 and -695 mV for the initial 24 hours of data logging, at a rate of one measurement per minute. However, after this period the values are between –690 and –694 mV and ignoring the effects of the liquid film thickness measurements, the general trend appears to be a slight increase in potential to approximately –690 mV after 400 hours, perhaps indicating an increasingly Ni rich surface matrix.

The effect on the potential and galvanic current by the reduction in liquid film thickness over the surface of the electrode and the uncoupling of the weld and parent metals is visible in the plot of the potential measured with the reference at Luggin 1 against time (Figure 4.1) and in the galvanic current plotted in Figure 7.1 above. The potential and galvanic current in bulk solution returns to stable coupled values after 20 to 30 hours suggesting that the surfaces of the electrode components may be altered

by a short period of uncoupling and also that electrochemical reactions return to a coupled, bulk solution steady state slowly in a low-conductivity electrolyte.

The distance between the Luggins 1, 2 and 5 are shown in Figure 4.2, which also indicates the positions of the Luggins along the length of the weld metal and parent metal 1. The potential difference measured by the references at Luggins 1, 2 and 5 for the coupled parent metal 1 (parent metal 2 is also coupled) and the weld metal is clear from Figures 4.1 and 4.3.

The difference between the measured potentials at Luggins 1 and 2, a distance of 0.6 cm is approximately 15 mV and that between Luggins 2 and 5, a distance of 4.5 cm is approximately 10 mV. The uncoupled potentials of the weld metal and parent metal 1, measured using Luggins 1 and 4, in Table 4.3 show that the average potential difference between the weld metal and parent metal 1 is calculated to be 26 mV, implying that the remote parent metal (Luggin 5) can be considered de-coupled from the weld metal 4.5 cm away.

In a chloride free environment such as this where there is also only one-dimensional current flow, a solution resistance effect would be expected even at a relatively large liquid film thickness of 1.0 cm. It is the high solution resistance that restricts polarisation of the parent metal; even at the edge of the weld and parent the coupled potential is 15 mV more negative than at the weld metal centre. The weld metal centre itself is only polarised by 3 to 5 mV by parent metal 1 if the average uncoupled potential minus the overall coupled potential measured at Luggin 1 is considered.

7.2 The Waveney Weldment Electrodes

The Wide weldment and the Standard weldment electrode (Figure 7.3) are both constructed from the weld (0.85% Ni) and the parent pipe (0.06% Ni) from joint 3 of the Waveney spoolpiece failure and the experiments were conducted in Waveney solution (215 ppm Cl^- and 49 ppm HCO_3^-), which was saturated with CO_2. It is therefore appropriate to draw comparisons of galvanic current and potential behaviour between the Wide and Standard weldment electrodes at ambient temperature and the Standard electrode in the same environment at 60° C.

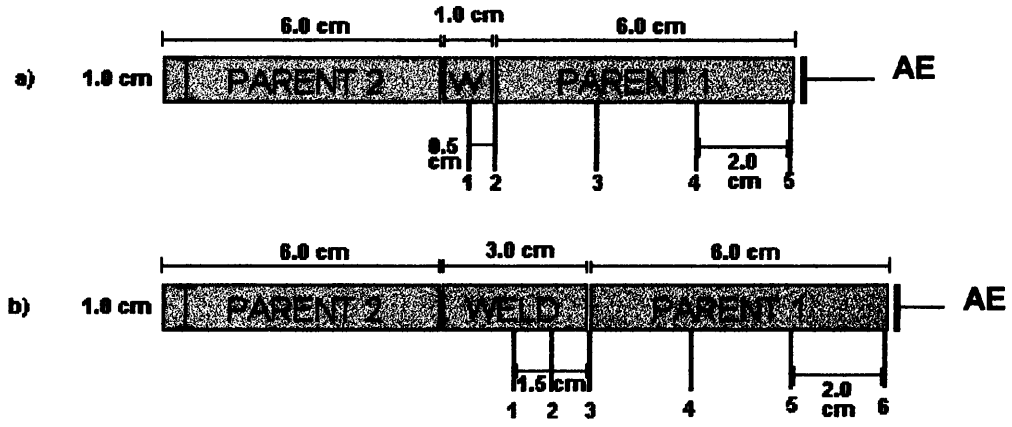

Figure 7.3 The dimensions of the a) Standard and b) Wide weldment electrodes. The locations of the Luggin probes are indicated in red.

From Figure 7.1 it is clear that the Standard electrode (plotted in green) has an galvanic current changing from around –2 μA on commencing measurement to 0 μA whereas the galvanic current of the Wide electrode ranges between –5 and -30 μA in 215 ppm Cl^- Waveney solution. This difference is because the weld metal component of the Standard Waveney electrode was one third of the length of the weld metal component of the Wide Waveney electrode and therefore has a smaller overall cathodic current relative to the parent metal. Because the cathodic reaction in most systems is the rate-determining factor, the 3.0 cm^2 overall cathode generally produces a larger amount of current than a 1.0 cm^2 area.

The change in galvanic current from cathodic to anodic displayed by the Wide Waveney electrode (blue/purple/light blue) when the chloride concentration of the solution was increased to 2150 ppm and then 21500 ppm may have been caused by the polarisation of the edges only of the weld metal at the two junctions with the parent metals in lower conductivity solution. The weld metal centre would have remained unaffected by coupling with the parent metals thus a different surface layer may have developed in comparison to the surface at the coupled weld metal edges. The increase in conductivity after the further addition of Cl^- possibly caused the whole of the weld metal to become part of the galvanic couple. However due to the surface difference at the weld metal centre, the current became anodic relative to the parent metal. By studying the potentials plotted against time measured at Luggins 1, 3 and 6

(Figures 5.13 and 5.15 a and b) it is clear that all three potentials increase but the potential measured with the reference at Luggin 6 flattens out at approximately -701 mV compared to –704 mV at 1 and -705 mV at Luggin 3.

The two sets of galvanic current data for the Standard Waveney electrode at ambient temperature and 60° C (plotted in yellow, Figure 7.1) have initial values of 0 μA and between -18 and -38 μA for each temperature respectively, due to the higher temperature. After the first 10 hours until 220 hours both galvanic currents are found to vary between 5 and –5 μA, with the ambient temperature current generally negative and the 60° C current displaying mostly positive current.

The coupled potentials measured at 60° C with the reference at Luggins 1, 2 and 5 (Figure 5.2 and 5.24) are approximately 4 mV higher than those measured with the same Luggins at ambient temperature (Figures 5.1 and 5.3). At 60° C, the galvanic current became anodic after approximately 50 hours and when the galvanic current became cathodic after 170 to 180 hours the liquid film thickness measurements were performed whilst the current remained in the region of 0 to -10 μA. Roughly the opposite occurred at ambient temperature. The cathodic current of the weld metal steadily decreased and then switched to an anodic current after approximately 205 hours, it is clear from Table 5.3 that the potential difference between the weld and parent metals had decreased slightly by the final uncoupled measurement on day 5.

The coupled potentials measured by all of the Luggin locations on the electrode at both temperatures increase with immersion time and the potentials measured with the reference at Luggins 1 and 2 are very similar to each other in the same conditions with the remote parent having a slightly lower potential. At 60° C the potentials are approximately 25 mV more positive.

7.3 The Comparison of Artificial and Waveney Weldment Behaviour

The plot of the galvanic current with time for the Artificial weldment electrode has a virtually linear negative slope with little natural deviation whereas the Waveney electrode current behaviour appears to experience relatively sudden change and also can become anodic in ordinary Waveney solution. The potentials measured at the weld metal centre, the weld and parent metal interface and the remote parent increase

only slightly for the Artificial weldment electrode throughout the experiment but the equivalent potentials of the Waveney electrodes generally increase significantly more.

The electrolyte is an obvious difference with very low conductivity for the Artificial weldment electrode and slightly higher conductivity for the Waveney solution and the conductivity increases with the accumulation of ions in solution from the electrochemical processes on the metal surface (in particular at 60° C).

The average potential difference between the uncoupled weld and parent metal 1 is almost 26 mV for the Artificial weldment electrode and approximately 10 mV for the Waveney electrodes. This concurs with the Waveney weld and parent metals being of similar composition and the Artificial weld and parent being less alike, although there are the effects of higher resistance solution to consider for the Artificial electrode. It known that the Ni content of the Artificial weld metal is consistent throughout the metal because it has not been subjected to dilution and has twice the amount of Ni of the Waveney weld metal. It may be possible that the second parent metal connection became disconnected and undetected therefore halving the current between the weld and parent metals.

It is assumed that the composition of the filler metal in each pass is identical and that the centre of the weld metal and the greatest dilution of the filler metal occurring at the tip of the "v" on the join, the location of the root and hot pass. However, different filler passes may also lead to differentials in chemical composition across the section of the weld metal.

8.0 Discussion of the Tests Performed Using the Artificial Weldment Electrode

Here the results of the electrochemical tests performed during the 425 hour monitoring of the potential and galvanic current of the Artificial weldment electrode in Chapter 4.0 will be discussed. The tests were: monitoring the galvanic current between the weld and parent metals and potentials with liquid film thickness variation, modified polarisation resistance and potentio-dynamic sweeps of the weld and parent metals.

8.1 The Effect of Liquid Film Thickness Variation

In the three sets of experiments (Figure 4.4 a, b and c), the coupled potential at the weld metal centre increases slightly with decreasing liquid film thickness until 0.4 cm solution thickness due to the de-coupling of the weld and parent metals resulting from increasing the solution resistance, the coupled potential then apparently decreases with further lowering of solution thickness. This lowering potential effect is in general, present in all of the potential measurements and is caused by the liquid film thickness adjuster covering the Luggin interfaces (located in the sidewall) with the solution; preventing potential measurement of the desired location on the electrode.

The coupled potential at the weld and parent interface increases on day 11 with lowering of solution thickness. The solution has higher conductivity because of the presence of corrosion products on day 11; this is perhaps the reason that there is no change on the other days. The conductivity on day 11 was 0.9 mS cm^{-1} (Figure 4.7) and the experiments on day 2 and 3 had measured conductivities of 0.3 and 0.4 mS cm^{-1}. The coupled potential also decreases below 0.4 cm solution thickness.

The remote parent potential does not appear to change with reduction of liquid film thickness, implying that this part of the parent metal is not polarised by the weld metal, which is 4.5 cm away.

The coupled potential in bulk solution (1.0 cm thickness) is approximately -690 mV for the weld metal, measured with the reference at Luggin 1 and –716 mV for the remote parent and the average uncoupled potentials given in Table 4.3 are

-686.5 mV and –712 mV. There is a similar potential difference to when the weld and parent metals are coupled but when uncoupled, both these potentials 3.5 mV more cathodic.

8.2 Potential Shifts on the Weld and Parent Metals

The potential shifts at the weld and parent junction can be calculated using the $Rp_{measured}$ and the ΔE of the weld and parent metals. When the weld and both parent metals are galvanically coupled it is assumed that each parent metal is galvanically coupled to the adjacent half of the weld metal (no current flows across the centre of the weld metal). The $Rp_{measured}$ values of the weld metal are doubled to obtain an Rp for 0.6 cm^2 instead of 1.2 cm^2. Using the results of day 11 at 1.0 cm liquid film thickness the potential shifts can be calculated:

$$\frac{e_{0w}}{e_{0p}} = \frac{Rp_w}{0.5Rp_p} = \frac{636}{425.5} = 1.49 \qquad \textbf{8.1}$$

The ratio of the $Rp_{measured}$ of the weld to the $Rp_{measured}$ of the parent metal 1 is almost 1.5 and the potential shift on the weld metal can be evaluated thus:

$$\frac{e_{0w}}{\Delta E} = \frac{Rp_w}{(Rp_w + 0.5Rp_p)} = \frac{636}{(636 + 425.5)} = 0.6 \qquad \textbf{8.2}$$

$$e_{0w} = \Delta E \times 0.6 = 0.025 \times 0.6 = 0.015 \text{ mV}$$

A potential shift on the weld metal of 15 mV will give a potential shift of 10 mV on the parent metal at the weld and parent junction when the potential difference is 25 mV, which is reflected by the ratio of Rp_w to Rp_p 1.5. The measured values of e_{0w} and e_{0p} are 14 and 11 mV at 1.0 cm liquid film thickness (Figure 4.4 c). The calculated potential shifts at the weld and parent metal junction with a 0.5 cm liquid film thickness are also 15 and 10 mV for e_{0w} and e_{op} respectively, this is because the potential at the two close locations is unaffected by a change in solution resistance caused by altering the liquid film thickness. Figure 4.4 a, b and c show that in general, the potential at the junction measured with the reference at Luggin 2 varies little with solution thickness, with the exception of the measurements at 0.1 to 0.3 cm.

The galvanic currents (*ig*) plotted for the three experiments in Figure 4.5 show a small decrease in cathodic current, between 1.0 and 0.7 cm of liquid film thickness. The subsequent reduction to 0.1 cm of liquid film thickness produces a larger, gradual current decrease. This decrease in measured current is caused by increasing the solution resistance by reducing the solution thickness in a low-conductivity electrolyte thus further restricting the distance and the amount of current that can flow through solution between the coupled metals. The expected galvanic current at 1.0 and 0.5 cm liquid film thickness can be calculated using the potential and Rp from day 11 in Table 4.1 c thus:

$$I_g = \frac{\Delta E}{Rp_w + 0.5Rp_p} = \frac{0.025}{636 + 425.5} = 2.4 \times 10^{-5}\,\mathrm{Acm^{-1}} \qquad \textbf{8.3}$$

A positive current indicates a cathodic weld metal and can be changed to negative to reflect the expected data. The galvanic current between the weld metal and two parent metals at 1.0 cm liquid film thickness is –24 μA, which is close to the measured value of -23 μA. The galvanic current at 0.5 cm liquid film thickness is calculated to be 15.1 μA and the measured value is -15.3 μA.

8.3 Modified Linear Polarisation Resistance

From the values in Table 4.1 a, b and c, it can be seen that the $Rp_{measured}$ of the weld and parent metals increases with halving the liquid film thickness (except the weld metal on day 5), also the parent metal has a consistently higher $Rp_{measured}$ than the weld metal for all experiments implying that the weld metal has the higher corrosion rate of the couple.

The potential change, e_x, recorded at the weld metal centre with the reference at Luggin 1 when the 20 mV potential step is applied with the reference at Luggin 2 is approximately three times greater than the potential recorded with the reference at Luggin 4 when the same potential step is applied with the reference at Luggin 5 on the parent metal. This is because of the diminishing current with increasing distance (x) along the electrode which and can be described by Equation 2.81 (also shown below) for a long electrode, $\alpha l > 1.5$. There are different distances between the Luggin probes, 0.6 cm and 1.5 cm, respectively and different Rp values.

$$e_x = e_0 \exp(-\alpha x) \qquad \textbf{2.81}$$

Where α was previously defined as:

$$\alpha = \left(\frac{R}{Z}\right)^{\frac{1}{2}} \qquad \textbf{2.80}$$

The general Equation 8.4 describes the measured Rp, for a long electrode.

$$Rp_{measured} = \frac{(RZ)^{\frac{1}{2}}}{\tanh\left[\left(\frac{R}{Z}\right)^{\frac{1}{2}} l\right]} \qquad \textbf{8.4}$$

Where l is the length of the weld metal (between the junction with the parent and the centre) and the length of the parent metal (this is considered to be infinite). If αl is large (>1.5) then tanh αl is a value close to 1 therefore Equation 8.5 (Equation 4.2 re-arranged) applies.

$$Rp_{measured} = (RZ)^{\frac{1}{2}} \qquad \textbf{8.5}$$

If αl is small (<0.5), tanh αl will approximate to αl, and:

$$Rp_{measured} = \frac{Z}{l} \qquad \textbf{8.6}$$

The αl values of parent metal 1 are all above 1.5 therefore it is appropriate to calculate R_{calc} and Z_{calc} using Equation 8.5. The αl and tanh αl values of the weld metal for all three days are given in Table 8.1.

Table 8.1 α, αl and tanh αl for the weld metal on selected days for 0.5 cm and 1.0 cm liquid film thickness.

	LFT (cm)	α	αl weld	tanh αl weld
day 2	1	1.39	1.67	0.93
	0.5	1.75	2.10	0.97
day 5	1	1.6	1.92	0.96
	0.5	1.92	2.30	0.98
day 11	1	1.18	1.42	0.89
	0.5	2.01	2.41	0.98

It is clear that with the exception of 1.0 cm liquid film thickness on day 11 that the αl are all above 1.5 therefore the equation for long electrodes - Equation 8.5 applies because of the low solution conductivity, which throughout the experiment is no higher than 1 mS cm^{-1} (Figure 4.7). This suggests that Equation 8.6 is suitable for a short electrode in a more conducting electrolyte.

At the two liquid film thicknesses, many of the calculated solution resistance values (R_{calc}) for the parent metal are significantly higher than those of the weld metal, when they should be the same. This is to be expected in this case if α values of the parent metal are generally similar to those of the weld metal and the $Rp_{measured}$ is consistently higher than the weld metal at the same liquid film thickness. The parent metal values are a more accurate reflection of the actual solution resistances at the different liquid film thicknesses because Equation 8.5 is intended to describe the $Rp_{measured}$ of long electrodes. Also, the R_{calc} of the parent metal approximately doubles when the liquid film thickness is halved in all experiments shown here whereas, with the exception of the experiment on day 11, the weld metal R_{calc} does not. In addition, the e_x for the parent metal is low (~2 mV) thus increasing the magnitude of measurement inaccuracies when using these values to calculate α.

The interfacial impedance, Z_{calc}, of a metal's surface does not change greatly by varying the liquid film thickness and therefore similar corrosion rates are calculated for each metal at 1.0 and 0.5 cm (Table 4.2). The weld metal has a lower Z_{calc} than the parent metal although the parent metal value decreases by a greater amount than the weld metal with time.

8.4 Potential and Current Distribution

Figure 4.6 shows the Rp values measured with the references at Luggins 1-5 at 0.5 cm liquid film thickness. Luggin 5, located at the end of the parent metal component next to the auxiliary electrode measured an Rp of 2550 Ohm, however 1.5 cm away, along the parent metal from this location the Rp measured with the Luggin 4 reference was halved at 1230 Ohm and the measured Rp continues to reduce with increasing distance away from the end of the parent metal. Figure 8.1 illustrates the potential and current behaviour during an LPR measurement.

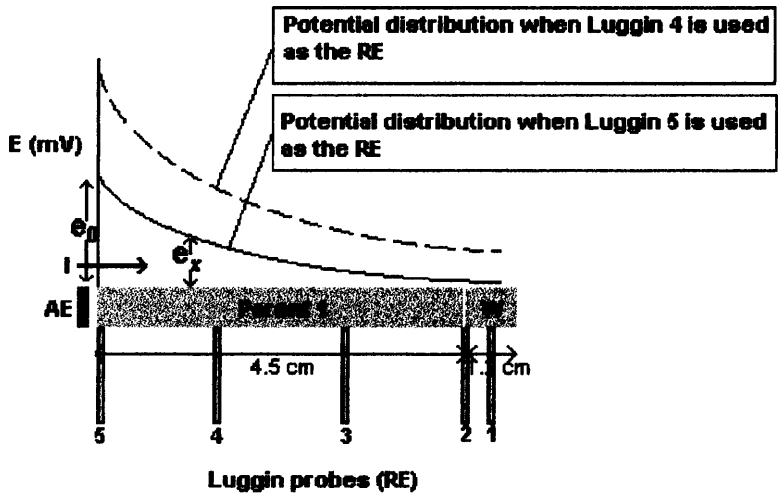

Figure 8.1 The potential distribution when the Luggins 4 and 5 are used as the reference to measure Rp.

The favourable current path is from the current source (auxiliary electrode) to the end of the parent metal because the solution resistance is minimal. When the Rp is measured with the reference at Luggin 5, the measured Rp is the result of a 20 mV step. Figure 8.1 illustrates the potential change 1.5 cm away at the location of Luggin 4 when the Rp is measured and is found to be approximately twice the applied potential of that at the same location on the parent metal when the reference is at Luggin 5. The $Rp_{measured}$ decreases with distance of the Luggin away from the end of the parent metal, caused by the increasing applied current required to maintain a constant potential change and is described by Equation 2.82 where the variables are described by Equations 2.81 and 8.5.

$$I = \frac{e_0}{(RZ_p)^{\frac{1}{2}}} \qquad \textbf{2.82}$$

8.5 Polarisation Curves

The area-corrected polarisation curves of the weld and parent metals in Figure 4.8 confirm that the weld metal is the cathode of the couple and that there is an effect of solution resistance or restricted current density due to the large size of the parent metal.

9.0 Discussion of the Waveney Weldment Experiments

Using the results in Chapter 5.0, this chapter assesses the suitability of applying aspects of the mathematical model to the actual Waveney weldment (joint 3) that failed in service. Three experiments using two electrodes, the Standard electrode (weld metal, 1.0 cm by 1.0 cm and parent metal, 6.0 cm by 1.0 cm) and the Wide weld electrode (weld metal, 3.0 cm by 1.0 cm and parent metal, 6.0 cm by 1.0 cm) were performed. Two experiments using the Standard electrode were performed at ambient temperature and 60° C and the Wide electrode only at ambient temperature. Comparisons can be made with this work and that of the Artificial weldment electrode experiment. The electrolyte used in all of these experiments was Waveney solution (de-ionised water containing 215 ppm Cl^-, 49 ppm HCO_3^{2-} and 160 ppm Na). All potentials are with reference to SCE.

9.1. The Standard Weldment Electrode

The dimensions of the Standard electrode are shown in Figure 9.1. Also the location of the auxiliary electrode and the five Luggin probes are indicated in relation to the weld and parent metals.

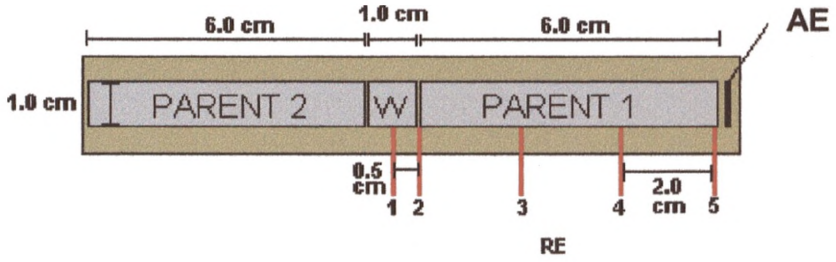

Figure 9.1 The Standard weldment electrode.

9.1.1 The Effect of Liquid Film Thickness Variation and Potential Shifts

The potentials measured with the references at Luggins 1, 2 and 5 (weld metal centre, weld and parent junction and remote parent) increase with time according to Figure 5.4 a, b and c. On day 1 there is a potential difference of 1 to 0.5 mV between the potentials measured with the references at Luggins 1 and 2 (0.5 cm apart) at all liquid film thicknesses. This potential difference decreases with time due to the

increasing solution conductivity, which is a result of the accumulation of corrosion products. The remote parent appears to be polarised by the weld metal when the liquid film thickness is, in general, above 0.8 cm and the extent of the polarisation increases with time, again, due to the higher solution conductivity.

On day 5 the difference between the potentials measured with the references at Luggin 2 and Luggin 5 is 2.1 mV at 1.0 cm liquid film thickness. This potential difference tends towards 3 mV at lower thicknesses because of the de-coupling effect caused by the higher solution resistance hindering the flowing distance of the galvanic current. On the two earlier days, the potential difference between the potentials measured with references at Luggins 2 and 5 are between 3 and 5 mV. The ratio of the potential shifts on the weld and parent are calculated to be 5.01 for day 3 using Equation 8.1.

It is clear from the plot of potentials against liquid film thickness on day 3 in that the solution potential shift on the weld metal at the junction due to coupling is not five times the size of that on the parent metal at the junction. The large $Rp_{measured}$ of the weld metal causes the calculation to be incorrect.

From Equation 8.2, e_{0w}, the potential shift on the weld metal can be calculated to be 4.7 mV, however the potential at the junction is found to be virtually identical to the weld metal Luggin on day 3 and the shift on the parent metal is approximately 4 mV at 1.0 cm solution thickness. The solution potential shift ratios and the calculated shifts on the weld metal at the junction are listed in Table 9.1.

The measured galvanic currents between the weld and both parent metals at varying liquid film thicknesses for the three experiments are plotted in Figure 5.5. The current is negative, indicating a cathodic weld relative to the parent metal. There is little change in galvanic current between 1.0 and 0.7 cm of solution thickness and a decline from –3.5 to –4.5 μA to between –2.2 and –2.7 μA from 0.7 to 0.1 cm. The increasing solution resistance appears to affect the galvanic current at solution thicknesses lower than 0.7 cm because the solution conductivity is higher than the Artificial weldment solution. The galvanic current is calculated using Equation 8.3 for

day 3 and the galvanic currents calculated for the three lower liquid film thicknesses are listed next to the measured values for this experiment, also in Table 9.1.

Table 9.1 The calculated potential shifts and galvanic currents for the Standard electrode at the five liquid film thicknesses.

Liquid film thickness (cm)	Potential shift ratio	Calculated potential shift on weld metal (mV)	Calculated total galvanic current (Ig, μA)	Measured total galvanic current (Ig, μA)
1.0	5.01	4.7	-12	-4.2
0.75	3.65	4.5	-11.4	-4.3
0.5	4.72	4.7	-11.6	-3.9
0.25	2.45	4.0	-9.5	-3.3

The calculated galvanic currents are considerably larger than the measured values because of the unusually small Rp values measured for the parent metal. It is possible that the connection on the lower parent metal became detached from the electrode therefore only the galvanic current between the upper parent and one half of the weld metal was measured.

9.1.2 Modified Linear Polarisation Resistance

If the measured Rp values of the Standard weldment electrode are compared with those of the Wide weldment electrode, as expected, the two sets of parent metal $Rp_{measured}$ should be similar because they are the same metal in identical conditions with the same dimensions. The weld metal $Rp_{measured}$ for the Standard weldment electrode are at least twice the parent metal $Rp_{measured}$ whereas the weld metal $Rp_{measured}$ values of the wide weld are virtually the same as the parent metal at the equivalent liquid film thickness. The Standard electrode $Rp_{measured}$ parent metal exhibits an approximate doubling with halving the liquid film thickness for days 1 and 5 (Figure 5.6 a, b and c) but the weld metal $Rp_{measured}$ does not, although overall the Rp increases slightly by lowering the solution thickness. The $Rp_{measured}$ of the weld and parent metal 1 are plotted against $1/t^{1/2}$ according to Equation 5.1. The points in the plot would be expected to produce a straight line because of the solution resistance doubling when the thickness is halved and being four times that at 0.25 cm. However the plots resemble Figure 9.2 because when the liquid film thickness increases the measured $(RZ)^{1/2}$ decreases and when it is above 1.0 cm the measured resistance is

equivalent to the interfacial impedance according to Equation 8.6, where l is the length and because the width is 1 cm, it is also the surface area. The solution resistance will be insignificant as it is only the distance between the Luggin interface and the metal surface. ρ is the solution resistivity, which is constant and related to the solution resistance, R by Equation 2.67. Because the width of the weld and parent metals is 1.0 cm, the area is equal to t.

$$Rp_{measured} = \frac{Z}{l} \qquad 8.6$$

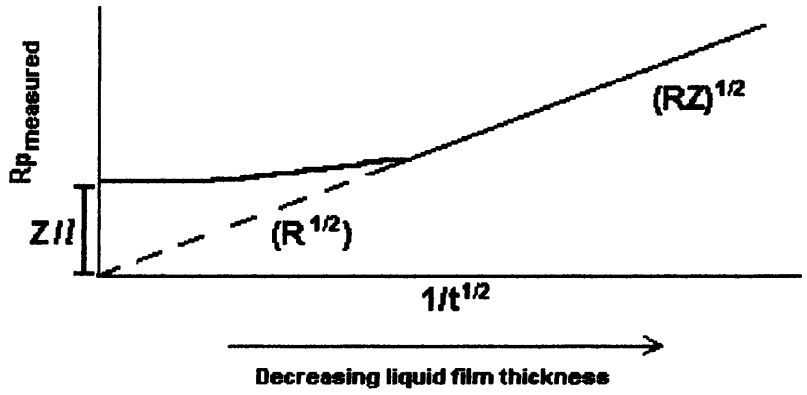

Figure 9.2 The components of the measured Rp with changing liquid film thickness.

The parent metal shows change between 1 and 0.5 cm solution thickness on the plots in Figure 5.6 a, b and c but, of course, the weld metal does not. This highlights the difference in weld metal $Rp_{measured}$ compared to the wide weld metal, where there is little difference between the values of the weld and parent metal due to the wide weld having a similar current distribution to the parent.

9.1.3 Potential Distributions

The change in solution potentials (e_x) measured using the reference at Luggin 5 when the reference at Luggin 4 undergoes a potential step of 20 mV (e_0) in a LPR measurement, are listed in Table 5.1 a, b and c and can be described by Equation 2.81.

The behaviour of the potential distributions on the electrode during the 20 mV potential step, are illustrated in Figure 9.3 for the parent metal (Luggins 5 and 4) and for the same measurement on the weld metal (Luggins 2 and 1), where the potential steps are performed with the references at Luggins 5 and 2 respectively.

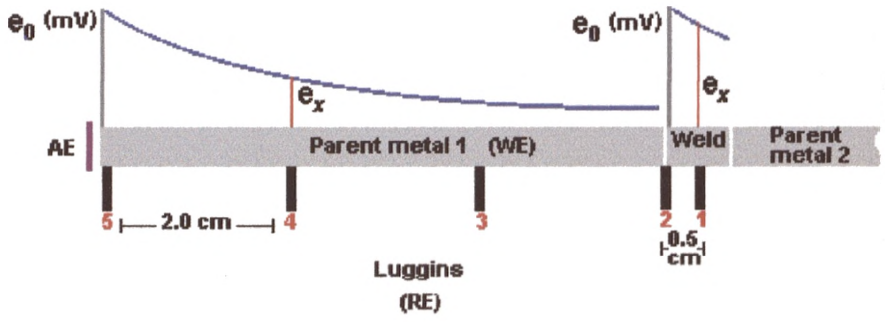

Figure 9.3 The potential distribution on the electrode when the reference at Luggin 5 and 2 are used as the references in the individual LPR tests.

The distance between Luggins 5 and 4 is 2 cm and between Luggins 2 and 1 is 0.5 cm, e_x, the potential change, measured with the reference at Luggin 4 in 1.0 cm liquid film thickness ranges from 8 to 10 mV for each day and decreases to 3.5 to 5.5 mV in 0.25 cm. e_x measured with the reference at Luggin 1 ranges from 13 to 13.67 mV in 1.0 cm of liquid film thickness and 7 to 10 mV in 0.25 cm. e_x decreases overall with the reduction in thickness because of the effective increase in solution resistance and it is larger for the weld metal measurements as the distance between the Luggin probes is a quarter of that between Luggin probes 5 and 4 and therefore this part of the electrode "sees" a greater potential change.

α is calculated using Equation 2.81, knowing e_0, e_x and x being the distance between the Luggin probes. Using α and the solution resistance (R_{calc}) the actual interfacial impedance (Z_{calc}) can be calculated using Equation 8.5 for the different liquid film thicknesses.

Larger α values are expected at lower liquid film thicknesses and the difference between the α values relate to the difference between the $Rp_{measured}$ at the different thicknesses because Z will remain unchanged for a particular metal.

The $Rp_{measured}$ can be defined with general Equation 8.4 but if αl is >1.5, tanh (αl) is 0.91 or above and close to 1and Equation 8.5 applies. This equation is suitable for the parent metal to calculate Z, having what is considered infinite length. α, αl and tanh (αl) for the weld metal are listed in Table 9.2 where l is 1.0 cm.

Table 9.2 α, αl and tanh αl for the weld metal for the four liquid film thicknesses from the results of day 3.

Liquid film thickness (cm)	α	αl	**Tanh** αl
1.0	0.79	0.79	0.66
0.75	0.94	0.94	0.74
0.5	1.29	1.29	0.86
0.25	1.39	1.39	0.88

When αl is between 1.5 and 0.5 for the weld metal as it is in Table 9.2, more accurate solution resistance (R) and interfacial impedance (Z) at the different liquid film thicknesses can be calculated by using Equation 2.76 which is suitable for calculating α for shorter electrodes in reasonably conducting solutions as opposed to Equation 8.5, which applies to infinitely long electrodes.

$$e_x = \frac{e_0 \cdot \cosh[-\alpha(x-l)]}{\cosh(\alpha l)} \qquad \textbf{2.76}$$

α is obtained using Solver in MS Excel by knowing e_x, x and l. The new α enables calculation of R and Z at different liquid film thicknesses with Equations 9.1 and 2.81.

$$Rp_{measured} = \frac{\alpha Z}{\tanh(\alpha l)} \qquad \textbf{9.1}$$

The new calculated values for the weld metals are listed for day 3 in Table 9.3 with the original parent and weld metal values resulting from Equation 8.5. The new

values of Z at all four liquid film thicknesses are all similar and lower than those calculated using Equation 8.5, they are also lower overall, than the equivalent parent metal values. The new solution resistance values, R, are higher than originally calculated because the new α is larger.

Table 9.3 R_{calc} and Z_{calc} for the weld and parent metal from Table 5.1 b and the new values calculated for the weld metal using Equations 2.76, 9.1 and 2.81.

	Parent Metal		
Liquid film thickness (cm)	$Rp_{measured}$ (Ohm)	R_{calc} (Ohm)	Z_{calc} (Ohmcm^2)
1	158	72	345
0.75	214	138	331
0.5	172	111	266
0.25	349	225	540
	Liquid film thickness (cm)	Weld Metal	
	1	311	503
	0.75	368	416
	0.5	523	315
	0.25	593	309

Liquid film thickness (cm)	$Rp_{measured}$ (Ohm)	α calc	Rcalc (Ohm)	Z_{calc} (Ohmcm^2)
1	396	1.15	370	282
0.75	391	1.28	429	261
0.5	406	1.58	589	236
0.25	428	1.66	662	240

9.1.4 Solution Resistance and Impedance

The R_{calc}, the solution resistance (R) is calculated using Equation 4.1 for both the weld and parent metals and plotted against the inverse of the liquid film thickness for days 1, 3 and 5 according to Equation 5.2 in Figure 5.7 a, b and c.

A straight line passing through zero on the y-axis would be expected if 1.0 cm liquid film thickness were considered bulk solution conditions. However there will be an effect from the inherent solution resistance even when the Luggin probe and the electrode surface are in close proximity.

There is an approximate halving of R_{calc} when the liquid film thickness is halved for the parent metal plot indicating that the solution resistance is proportional to the liquid film thickness. This pattern is less clearly defined for the weld metal plot.

There is a large difference in the solution resistances calculated using the data for the weld and parent metal. This is because the values of α and $Rp_{measured}$ for the weld metal are larger than those of the parent metal so solution resistance calculated using Equation 4.1 produces higher values. When α is calculated using Equation 2.76 it is clear that the R_{calc} values for the weld metal are slightly larger than those plotted in Table 5.7 a, b and c, although this equation gives smaller Z_{calc} than the parent metal. When Z is calculated from Equation 9.1, the values are lower than those calculated using the Equation (4.2 or 8.5) that is suitable for the infinitely long electrode and lower than the parent values.

Of the two plots it is probable that the parent metal plot of R_{calc} against the inverse of the liquid film thickness is the most accurate reflection of actual solution resistance at the different liquid film thicknesses due to the solution conductivity measurement and calculations explained below.

9.1.5 Solution Conductivity

The conductivity of the Waveney solution prior to immersion was measured as 4.1 mS cm^{-1}. Conductivities for each day were calculated, after three days of immersion, with R_{calc} for both the weld and parent metals using Equation 2.67, they are plotted in Figure 5.8. The area is equal to the liquid film thickness assuming the width of each component (considered to be the length for this calculation) is 1.0 cm. The conductivity should be constant for the weld and parent metals at any one time and the conductivity will increase with immersion time.

The calculated conductivity peaks at just over 20 mS cm^{-1} using the parent metal results and 7 mS cm^{-1} using the weld metal results from day 3. The difference between the two sets of calculated conductivity is related to the different R_{calc} for weld and parent metals. The larger $Rp_{measured}$ and α of the weld metal provide the larger R_{calc} and hence lower calculated conductivities. The correct value of conductivity for

each day is most likely given by the parent metal calculations because some of the values are below the original measurement of 4.1 mS cm^{-1} and it can be speculated that the accumulation of ions in the solution would raise the conductivity by more than 3 mS cm^{-1} after several days immersion.

9.1.6 Polarisation Curves

It is clear from the area-corrected polarisation sweeps of the weld and parent metals in Figure 5.9 that the weld is the overall cathode of the two metals. The parent metal has slightly higher cathodic current and there is an effect of solution resistance or restricted current density due to the large size of the parent metal. An apparent film breakdown is visible on the anodic curve of the parent metal at potentials more noble than –370 mV. This is probably due to the occurrence of an oxide film that was able to form when the ac impedance was performed which necessitated removal of the CO_2 gas bubbler from the solution.

9.1.7 AC Impedance

The linearity in the high frequency part of the Nyquist plots in Figures 5.11 a) and 5.12 a) are caused by the "damping" of the ac signal at high frequency. The alternating signal does not affect the electrode potential some distance along the electrode due to the large admittance at high frequency and the resulting plot is the capacitance effect of a short rather than long electrode. At lower frequencies, the signal is able to penetrate along the length of the electrode so the complex plot changes from being flattened to more semi-circular in shape. This behaviour is indicative of the transmission line effect.

Such plots characterise porous electrodes[74, 75, 78] and the cause of the linearity is identical. The linear response at high frequency and the corrected responses are shown for the parent and weld metals in Figures 9.4 a, b, c and d and 9.5 a, b, c and d. The measured impedance, Z_{Rmeas} is equal to $(RZ)^{1/2}$, where R is R_{calc}, the solution resistance at different liquid film thicknesses, Z is the true impedance of the metal and the phase angle, ϕ, is half that of a usual complex plot of an electrode in bulk solution at approximately 45° (the plots in Figure 5.11). Equation 9.3 is used to double ϕ and the square of the measured impedance modulus, $|Z|^2_{meas}$, can be obtained from

Equation 9.2 using the values Z_{Rmeas}, Z_{Imeas} and R_s estimated from the linear part of the Nyquist plots. These values are listed in Table 9.4, using the values in Table 5.4

$$|Z|^2_{meas} = (Z_{Rmeas} - R_s)^2 + Z^2_{Im\,eas} \qquad \textbf{9.2}$$

ϕ can be determined thus:

$$\sin\phi = \frac{\left(\frac{Z_I}{|Z|_{meas}}\right)}{\pi 180} \qquad \textbf{9.3}$$

Table 9.4 The impedance modulus and phase angle of the uncorrected Nyquist plots in Figures 5.11 and 5.12.

	LFT (cm)	$\|Z\|_{meas}$	ϕ
Parent Metal	1.0	32.21	43.93
	0.75	61.33	39.65
	0.5	50.11	43.09
	0.25	113.24	40.61
Weld Metal	1.0	198.15	43.26
	0.75	157.60	46.13
	0.5	209.55	42.96
	0.25	230.27	40.22

New real (Z_R) and imaginary (Z_I) points are calculated from $|Z|_{meas}$ and ϕ using Equations 9.4 and 9.5 and used to produce a corrected complex plot.

$$Z_R = +|Z|^2_{meas} \cdot \cos(2\varphi) \qquad \textbf{9.4}$$

$$Z_I = -|Z|^2_{meas} \cdot \sin(\varphi) \qquad \textbf{9.5}$$

A corrected complex can be plotted where Z_R and Z_I are the real and imaginary components of the measured impedance. The resulting plots (Figures 9.4 and 9.5) have a ϕ of approximately 90° (although some are larger than this due the estimation of measured values) and a semi-circle is plotted instead of a linear region

at high frequency. Z_R (the high minus the low intercepts in the plots), which can also be considered as equal to $(RZ)^{1/2}$, is used to calculate true Z using Equation 9.6 and values of R_{calc} (R) taken from the modified LPR measurements on day 3. The results are tabulated in Table 9.5.

$$Z = \frac{Z_R^{\ 2}}{R} \qquad \textbf{9.6}$$

Table 9.5 (RZ), R_{calc} from day 3, used to calculate true Z.

	Parent metal			Weld metal		
LFT (cm)	(RZ)	R_{calc} (Ohm)	Z (Ohm cm^2)	(RZ)	Rcalc (Ohm)	Z (Ohm cm^2)
1	3843	72	53	127816	311	411
0.75	9889	138	72	76691	368	208
0.5	9582	111	86	74901	523	143
0.25	35998	225	160	121116	593	204

(RZ) for the parent metal is obviously lower than for the weld metal at all liquid film thicknesses. This may be explained by the parent being six times the length of the weld metal as in the case of the modified LPR experiments.

a)

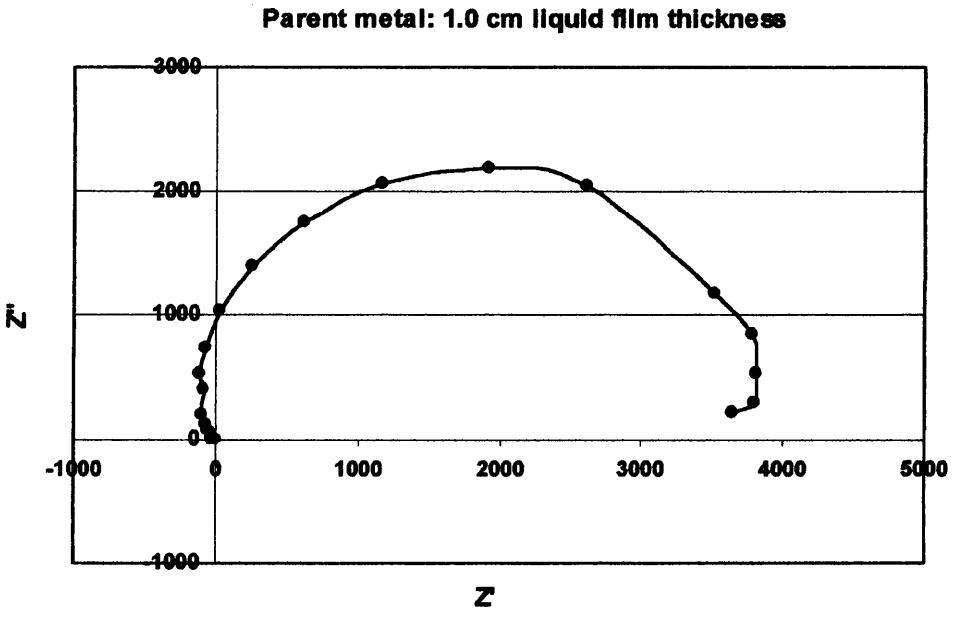

Figure 9.4 The corrected Nyquist plots for the parent metal from ac measurements at four liquid film thicknesses.

b)

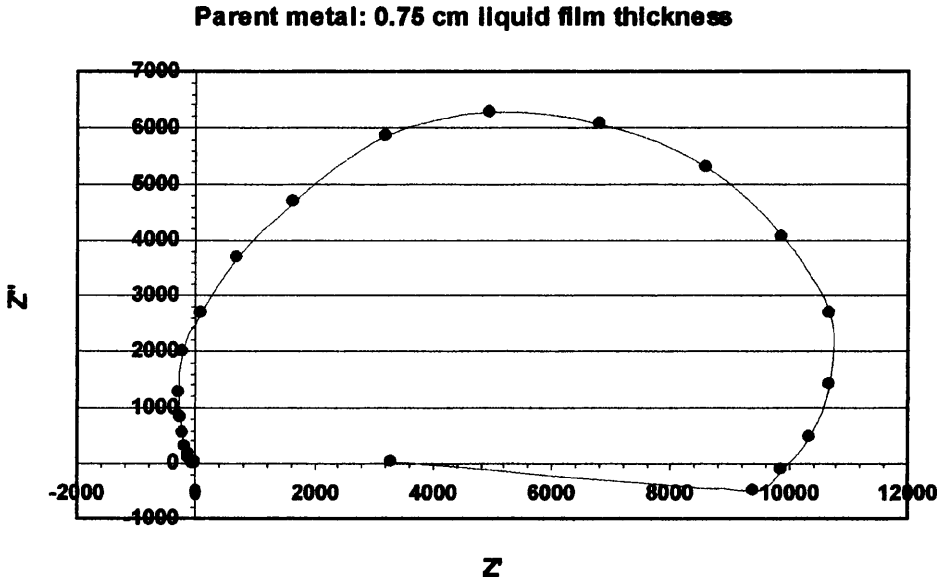

c)

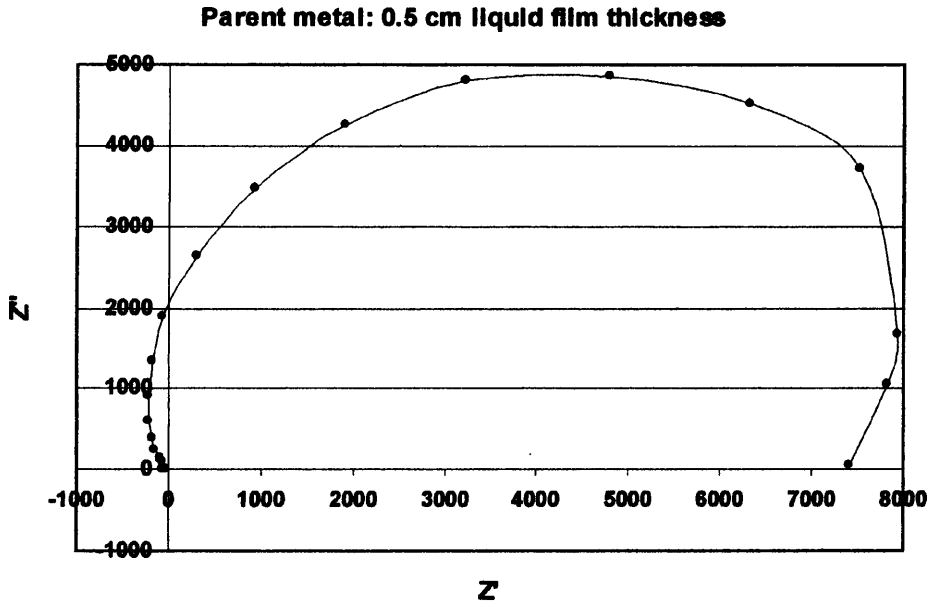
Parent metal: 0.5 cm liquid film thickness
5000
4000
3000
2000
1000
0
-1000
-1000
0
1000
2000
3000
4000
5000
6000
7000
8000
Z'

d)

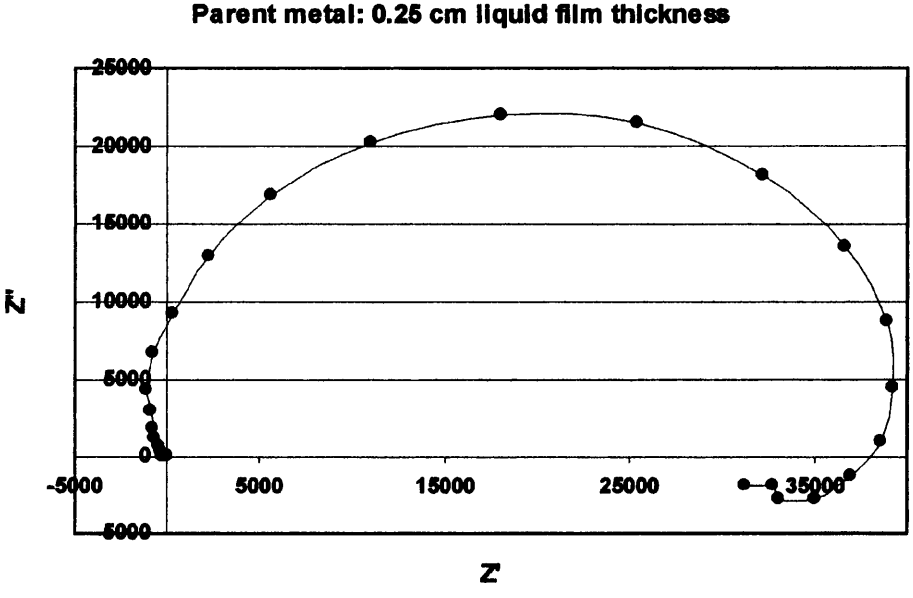
Parent metal: 0.25 cm liquid film thickness
25000
20000
15000
10000
5000
0
-5000
-5000
5000
15000
25000
35000
Z'

a)

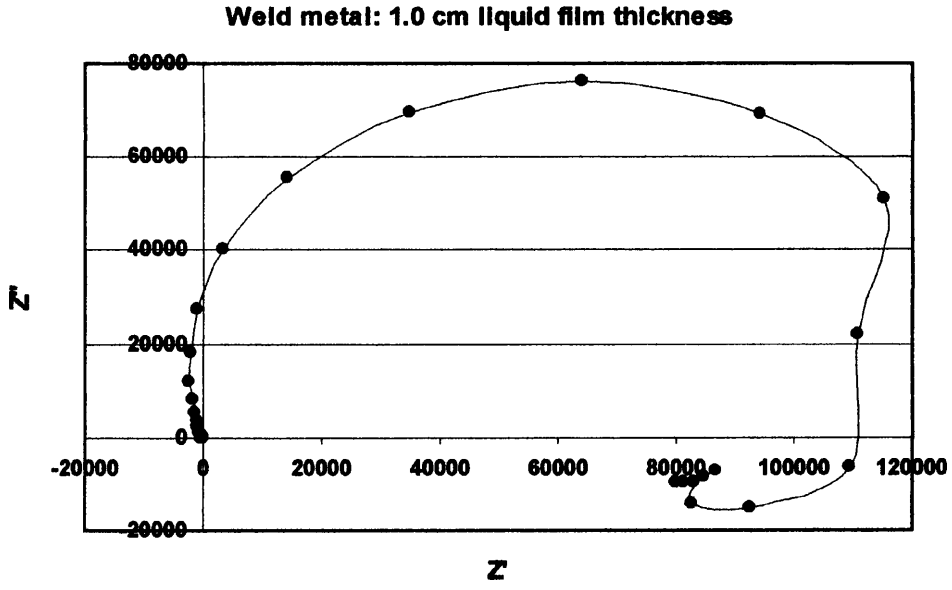

Figure 9.5 The corrected Nyquist plots for the weld metal from ac measurements at four liquid film thicknesses.

b)

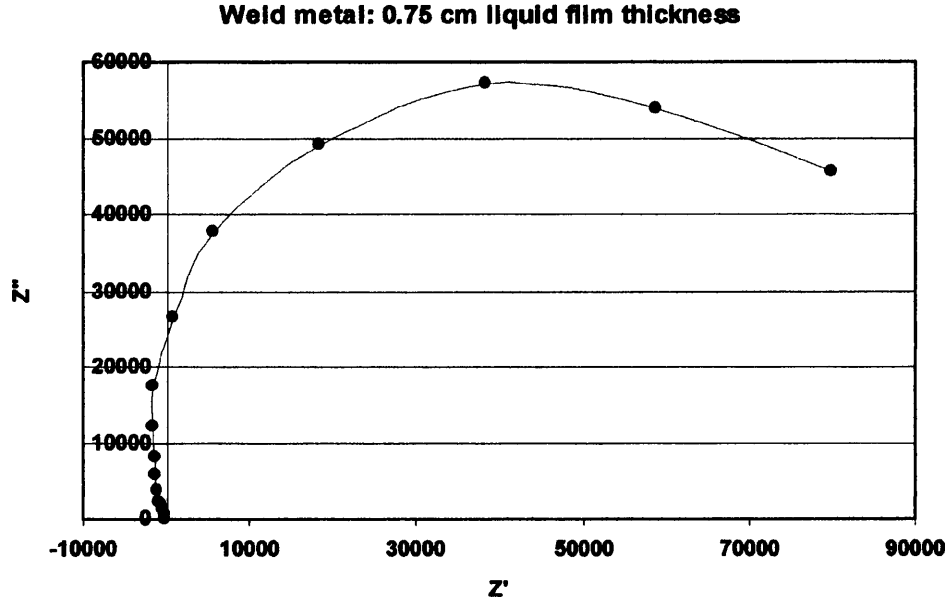

c)

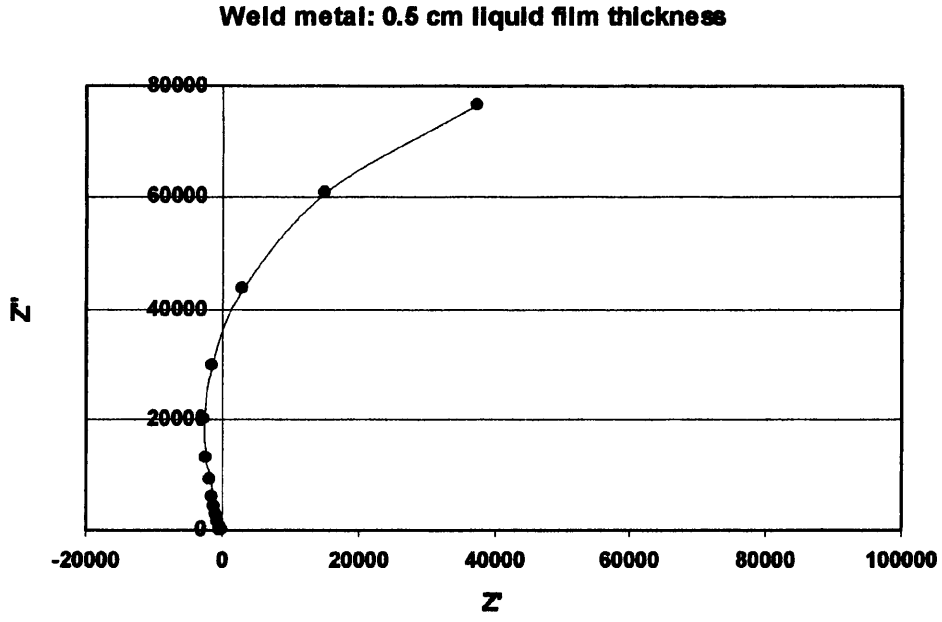
Weld metal: 0.5 cm liquid film thickness
80000
60000
40000
20000
0
Z'
-20000
0
20000
40000
60000
80000
100000

d)

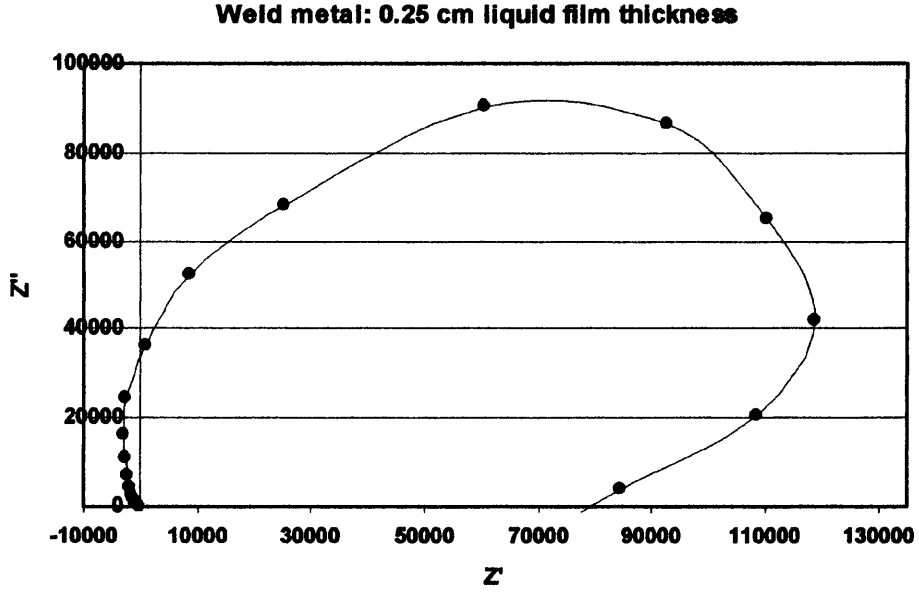
Weld metal: 0.25 cm liquid film thickness
100000
80000
60000
40000
20000
0
Z'
-10000
10000
30000
50000
70000
90000
110000
130000

9.2 The Wide Waveney Electrode

The Wide Waveney electrode is shown schematically in Figure 9.6. The duration of the test was 16 days and when the tests discussed below were performed, the Cl^- content of the Waveney solution was 215 ppm and the HCO_3^- content was 49 ppm, (with the exception of the polarisation curves).

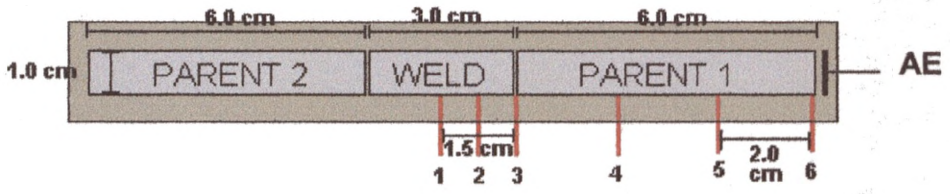

Figure 9.6 The Wide weldment electrode.

9.2.1 The Effect of Liquid Film Thickness Variation and Potential Shifts

The liquid film thickness experiments (Figure 5.16, a, b and c) for the Wide weld metal electrode measure a potential difference of approximately 2 mV between the weld metal centre (Luggin 1) and 0.75 cm along the weld metal, closer to the parent metal (Luggin 2). The potentials measured with changing solution thickness with the reference at Luggin 2 are similar to those with the reference at Luggin 3 – the weld and parent metal junction. The remote parent potential, measured with the reference at Luggin 6, is less than one millivolt more negative than at the locations of Luggins 2 and 3. The remote parent potential appears to decrease by 0.5 to 1.0 mV with the decrease in solution thickness from 1.0 to 0.4 cm suggesting that the weld metal gradually polarises the parent metal at this location because the solution conductivity of Waveney solution is sufficiently high.

The coupled potential at the weld and parent metal junction does not change with decreasing liquid film thickness (except below 0.4 cm due to the effects of the spacer). The thickness of the divider between each component is 12 μm therefore the distance between the weld and parent metals at the junctions is only slightly greater than this due to the additional adhesive resin securing the divider during fabrication. The relatively small distance between the edges of the components allows the galvanic current to flow with minimum resistance at low liquid film thicknesses

where galvanic current between more remote parts of the weld and parent metals would be restricted because of the high solution resistance.

The potential shifts caused by coupling at the weld and parent junctions are calculated using the $Rp_{measured}$ and the average ΔE between the uncoupled weld and parent metals. Half the length of the weld metal is considered (1.5 cm) and the $Rp_{measured}$ of the weld metal is doubled. The ratio of potential shift values on each component can be evaluated according to Equation 8.1 for day 4 using the $Rp_{measured}$ at 1.0 cm liquid film thickness in this example.

The calculated ratio of 3.22 indicates that the potential shift on the weld metal is over three times greater than that of the parent metal at the junction. The weld metal shift is calculated to be 0.76 using Equation 8.2. The average potential difference (ΔE) between the weld and parent metal is 4 mV from Table 5.9. Therefore the potential shift on the weld metal adjacent to the parent metal potential is calculated to be 3.04 mV and the shift on the parent metal should be 0.96 mV.

The actual potential measured at the weld and parent metal junction in 1.0 cm solution thickness with the reference at Luggin 3 is -709.8 mV. The average uncoupled potentials of the weld and parent metal 1 are –707.2 mV and -711.2 mV respectively, giving potential shifts of 2.6 mV on the weld edge and 1.4 mV on the parent edge. The calculated potential shift ratio and the shift on the weld metal at all four liquid film thicknesses on day 4 are displayed in Table 9.6 below.

The galvanic current for days 1,2 and 4, plotted in Figure 5.17 is negative, indicating a cathodic weld metal. The current on day 2 is found to be higher overall than on day 1 by 2 to 5 μA, but does not increase between days 2 and 4. There is a smooth decrease in galvanic current with each incremental reduction in solution thickness due to the effective increase in solution resistance reducing the distance over which the current may travel.

Table 9.6 The calculated potential shifts, the shift on the weld metal and the galvanic current for day 4.

Liquid film thickness (cm)	Potential shift ratio	Calculated potential shift on weld metal (mV)	Calculated total galvanic current (Ig, μA)	Measured total galvanic current (Ig, μA)
1.0	3.22	2.4	-19.32	-23.00
0.75	2.96	2.4	-17.9	-21.50
0.5	3.21	2.43	-13.56	-19.00
0.25	1.84	2.08	-11.53	-14.50

The galvanic current between the weld metal and both parent metals is calculated for the parent metal with 1.0 cm liquid film thickness using Equation 8.3. A positive value of galvanic current indicates a cathodic weld.

The calculated and measured galvanic currents for the other liquid film thicknesses are listed in Table 9.6 above. The sign of the calculated Ig is changed to reflect the expected data where a cathodic weld would have a negative current. The calculated galvanic currents for the four liquid film thicknesses are lower than the actual values obtained from the plot of galvanic current against liquid film thickness but they are comparable.

9.2.2 Modified Linear Polarisation Measurements

The $Rp_{measured}$ (Figure 5.7, a, b and c) of the Waveney weld and parent metals increase with decreasing liquid film thickness but the values are generally lower than those of the Artificial weldment electrode. This is due to the apparently lower interfacial impedance of the Waveney weld and parent metals as well as the Waveney solution, because of the ion content, having a higher conductivity than the solution used in the Artificial weldment experiment, which was CO_2 saturated deionised water. The $Rp_{measured}$ for the weld and parent metal 1 is plotted against $1/t^{1/2}$ (t is the liquid film thickness) in Figure 5.18 a, b and c, to demonstrate the relationship between $Rp_{measured}$ and $(RZ)^{1/2}$ according to Equation 5.1. The expected nature of the plot is shown in Figure 9.2.

When the liquid film thickness is >1.0 cm the solution on the electrode surface is considered to be bulk solution therefore the measured Rp will become constant and can be described by Equation 8.6. There is little difference between the plots of the weld metal and parent metal because here $l = 3$ cm^2 so Z is reduced for the Wide electrode compared to the Standard weldment electrode. ρ is the solution resistivity, which is constant and related to the solution resistance (R) in one-dimensional thin liquid films by Equation 2.67.

9.2.3 Potential Distributions

The change in solution potential recorded at a reference when a 20 mV potential step is applied using a reference electrode x distance away is described by Equation 2.81. The distance, x, between Luggins 1 and 3 is 1.5 cm and 2.0 cm between Luggins 5 and 6. The average change in solution potential measured with the reference at Luggin 5 when 20 mV (e_0) is applied to parent metal 1 with the reference at Luggin 6 (the remote parent) is generally just less than 10 mV in 1.0 cm solution thickness. In comparison, when the same potential is applied with the reference at the weld and parent metal junction (Luggin 3) in 1.0 cm solution thickness, the solution potential change recorded with the reference at the weld metal centre (Luggin 1) is 14 mV, with three quarters of the distance. e_x decreases with decreasing liquid film thickness for the weld and parent metal because of the increasing solution resistance effect. Figure 9.7 illustrates solution potential (e) distributions with distance from the applied potential change. The Rp is also slightly larger for the weld metal because it has half of the surface area of parent metal 1 and the $Rp_{measured}$ increases with decreasing liquid film thickness.

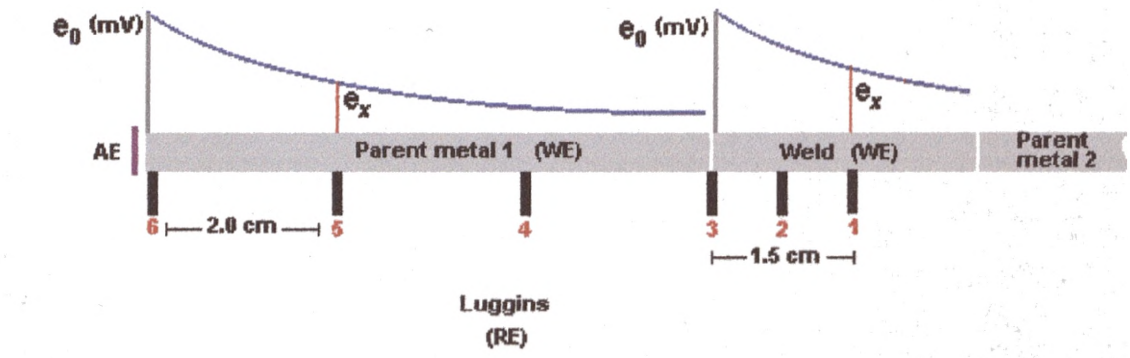

Figure 9.7 The potential distribution on the electrode when the reference at Luggin 6 and 3 are used as the references in the individual LPR tests.

α is calculated using Equation 2.81 and α is defined in Equation 2.80. A relatively low αl would be expected when the solution conductivity is high and/or for a short electrode. The calculated α values for the weld metal are generally lower than the parent metal because of the larger e_x at concurrent solution thicknesses and α also increases with decreasing liquid film thickness.

The absolute values of $Rp_{measured}$ are clarified in Equation 8.4. The parent metal, where (l) is an infinite length of electrode and therefore αl is >1.5 and tanh αl is close to 1 so Equation 8.5 can be used to calculate the interfacial impedance, Z. The l of the weld metal (width) is 3.0 cm, subsequently values of tanh αl are mostly below 1 and the calculated Z values are unlikely to be accurate using Equation 8.5.

Table 9.7 α, αl and tanh αl for day 4.

Liquid film thickness (cm)	**α**	**αl**	**tanh αl**
1.0	0.25	0.75	0.64
0.75	0.30	0.90	0.72
0.5	0.42	1.26	0.85
0.25	0.48	1.44	0.89

Equation 8.6 applies when αl is <0.5 and solution resistance is considered insignificant. The αl calculated for the weld metal on day 4 (Table 9.7) at all four liquid film thicknesses are between 0.5 and 1.5 (although at 0.25 cm is close), so that tanh (αl) will not approximate to 1 and Z calculated using Equation 8.5 would be too high. Therefore neither Equation 8.5 nor 8.6 necessarily apply so Equation 2.76 can be used to obtain new values for α at the different liquid film thicknesses in Table 9.8.

Table 9.8 The new values of α and the old and new R_{calc} and Z_{calc} values for the weld metal for day 4.

Liquid film thickness (cm)	$Rp_{measured}$ (Ohm)	1st Method R_{calc} (Ohm)	1st Method Z_{calc} ($Ohmcm^2$)	New α calc	New Rcalc (Ohm)	New Z_{calc} ($Ohmcm^2$)
1	158	40	622	0.37	48	341
0.75	167	51	550	0.42	60	339
0.5	225	94	536	0.52	106	397
0.25	225	109	464	0.57	121	368

New values of R_{calc} and Z_{calc} can be calculated using the new α in Equations 9.1 and 2.80. The new values of Z_{calc} are lower than those calculated with the first method and the values are within 60 Ohm cm^2 of each other at all four liquid film thicknesses. Also the new R_{calc} are still very similar to the original values and therefore similar to the R values calculated for the parent metal, unlike the Standard weldment electrode.

9.2.4 Solution Resistance and Impedance

The R_{calc}, the solution resistance (R) is calculated using Equation 4.1 for both the weld and parent metals and plotted against the inverse of the liquid film thickness according to Equation 5.2 in Figure 5.19, a, b and c.

The plot illustrates, in general, a doubling of solution resistance by halving the solution thickness with the plots for weld and parent metals being approximately linear. At 1.0 cm liquid film thickness and above the R_{calc} is equivalent to the bulk solution resistance of the Waveney solution. It was not possible to measure the solution conductivity directly and therefore calculate the resistivity of the Waveney

solution. However, 1 cm solution thickness is taken to be sufficient thickness to be described as bulk solution.

The plots also demonstrate that the values of R_{calc} for the weld and parent metals at different solution thicknesses are very similar to each other, in comparison, the plots of $Rp_{measured}$ against $1/t^{1/2}$ for the weld and parent metal, the weld metal exhibits the higher $Rp_{measured}$ of the two. The apparently larger Z constituent of the weld $Rp_{measured}$ is a result of a smaller potential change required to reach the end of the shorter electrode for the LPR measurement because Rp was measured in Ohm instead of Ohm cm^2.

9.2.5 Solution Conductivity

The conductivity (measured using a meter) of the Waveney solution prior to immersion was 5 mS cm^{-1}. Conductivities for each day were obtained, three days after immersion, using R_{calc} for both the weld and parent metals with Equation 2.67 and plotted in Figure 5.20. The area is equal to the liquid film thickness because the width is 1.0 cm therefore the conductivity should be constant for the weld and parent metals at each thickness on a particular day.

Calculated conductivities range between 15 and 25 mS cm^{-1} on day 1 and increase to between 20 and 28 mS cm^{-1} on day 2 with the conductivity remaining in this range throughout days 3 and 4 suggesting that the Waveney solution was saturated with corrosion products by day 2, the fifth day of immersion.

9.2.6 Polarisation Curves

It is clear from the area-corrected polarisation curves of the weld and parent metals (Figure 5.21) that the weld is the overall cathode of the two metals. The parent metal has higher anodic and cathodic currents but the anodic curves are affected by solution resistance or restricted current density due to the large size of the parent metal. This test was performed in 21500 ppm Cl^- therefore higher solution conductivity giving a larger current at i_{corr} than the Standard and Artificial weldment electrodes.

9.3 The Standard Weldment Electrode at 60° C

The dimensions and features of the Standard weldment electrode are shown in Figure 9.8. The temperature of the tests was held at 60° C by immersion in a thermostatically controlled water bath and the total experiment lasted 325 hours. It is the same electrode as discussed earlier, the only difference between the experiments is the temperature at which work was performed.

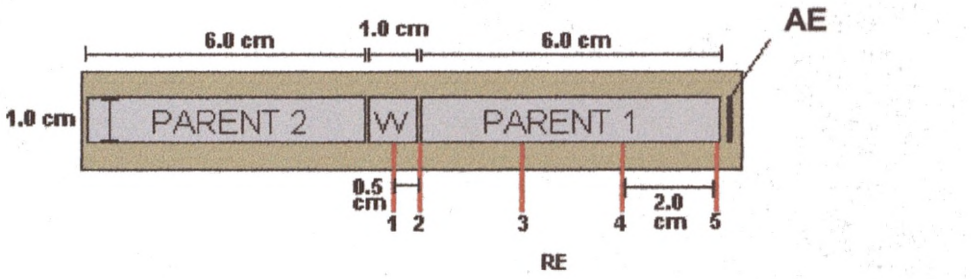

Figure 9.8 The Standard weldment electrode.

9.3.1 The Effect of Liquid Film Thickness Variation and Potential Shifts

The potentials measured with the reference electrodes at Luggins 1,2 and 5 (Figure 5.25, a, b and c) are all approximately 30 mV more noble than those measured at the same locations at ambient temperature. Above 0.5 cm liquid film thickness, the potential difference between the weld metal centre and the coupled potential at the weld and parent junction is 3 to 4 mV and the potential at the remote parent metal is 10 to 12 mV more negative than at the junction.

The parent metal is polarised by the weld metal above 0.5 cm liquid film thickness by 2 to 3 mV compared to potential values below this thickness. The potential values measured at the weld metal centre increase over days 1,2 and 3 and the potential difference between this location and the junction increases to 3 to 5 mV.

The ratios of the potential shifts at the weld and parent junction in relation to the weld and parent metals are calculated from Equation 8.1 using the Rp values in Table 5.12 c for day 3 and the uncoupled potential difference (15 mV) between the weld and parent metals. The results for the four different liquid film thicknesses are listed in Table 9.9 below. The potential shift on the weld at the junction with the

parent is not ~12 mV as calculated using Equation 8.2. The shifts are due to the large $Rp_{measured}$ values of the weld metal compared to those of the parent metal.

Table 9.9 The calculated potential shifts, the shift on the weld metal and the galvanic current for day 3.

Liquid film thickness (cm)	**Potential shift ratio**	**Potential shift on weld metal (mV)**	**Calculated Ig (μA)**	**Measured Ig (μA)**
1.0	4.41	12.3	-29.8	-7.2
0.75	4.06	12.0	-24.9	-6.4
0.5	4.14	12.15	-23.8	-5.8
0.25	4.31	12.15	-20.9	-5.0

The measured galvanic current (Table 9.9) increases between days 1 and 2. On day 1 there is an overall change in current when the liquid film thickness is reduced from –2 to -1 μA, and on days 2 and 3 the current changes from over –7 μA to between –4 and -5 μA. Using Equation 8.3, the calculated (weld metal, one parent metal) and measured (both parent metals) galvanic currents for day 3 are listed in Table 9.9. As is similar to the same experiment at ambient temperature, the galvanic current is calculated to be much larger than actually measured, as suggested earlier, the Standard weldment electrode may have a loose connection on one of the parent connections hence giving a lower than expected galvanic current between the weld and parent metals.

9.3.2 Modified Linear Polarisation Measurements

The $Rp_{measured}$ data for the parent and weld metals presented in Table 5.12 a, b and c is broadly similar to the $Rp_{measured}$ data for the same electrode at ambient temperature. The weld metal values are approximately twice the size of those for the parent metal. The $Rp_{measured}$ is plotted against decreasing liquid film thickness ($1/t^{1/2}$) in Figure 5.27 a, b and c. In comparison with the plots at ambient temperature in Figure 5.6 a, b and c, the curves bear greater similarity to the illustration than the same plots at ambient temperature but the Rp values at 60°C appear to be less affected by reducing liquid film thickness.

9.3.3 Potential Distributions

The potential distributions were recorded in the same locations as the ambient temperature experiments during the potential step of 20 mV (e_0). Because of the identical geometry, LPR measurements and therefore the solution potential behaviour in this experiment, can also be represented by Figure 9.3. The potential measured at the location of Luggin 4, e_x, is slightly higher at 1.0 cm liquid film thickness at 60 °C than at ambient temperature and slightly lower at 0.25 cm thickness, but such small amounts are most likely due to experimental differences. e_x values measured on the weld metal at the location of Luggin 1 are also comparable with those at ambient temperature.

α values, calculated using Equation 2.81, are also comparable with those calculated at ambient temperature because e_x and e_0 are similar and x is identical. Also tanh αl for the weld metal does not approximately equal one, as is seen in Table 9.10 because l is 1 cm as opposed to infinitely long in the case of the parent metal. Therefore, again, Equation 8.4 cannot apply.

Table 9.10 α, αl and tanh αl for the weld metal for the four liquid film thicknesses from the results of day 2.

Liquid film thickness (cm)	α	αl	**tanh** αl
1	0.81	0.81	0.67
0.75	0.91	0.91	0.72
0.5	1.32	1.32	0.87
0.25	1.67	1.67	0.93

The alternative method for calculating α using Equation 2.76 produces values for the weld metal α on day 2 listed in Table 9.11 and the R and Z values calculated from Equation 9.1 using these new values at the four different liquid film thicknesses.

Table 9.11 The recalculated α, R and Z for the weld metal on day 2.

	Liquid film thickness (cm)	$Rp_{measured}$ (Ohm)	R_{calc} (Ohm)	Z_{calc} ($Ohmcm^2$)	New α calc	New R_{calc} (Ohm)	New Z_{calc} ($Ohmcm^2$)
Parent	1	190	60	606			
	0.75	222	107	464			
	0.5	228	144	361			
	0.25	238	202	280			
Weld	1	470	381	580	1.17	452	331
	0.75	432	395	473	1.26	462	292
	0.5	474	626	359	1.61	703	272
	0.25	532	890	318	1.91	970	267

Because α is larger when recalculated, the new R_{calc} values are also much larger than previously calculated from $Rp_{measured}$ and it therefore follows that Z_{calc} will be smaller. The new Z_{calc} values are more similar values to each other at different liquid film thicknesses in addition to being smaller than the calculated parent metal Z values. Unusually, the values in Table 9.11 are comparable with those at ambient temperature (Table 9.3) because at 60 °C it would be expected that the kinetics of the metal surface would be more rapid.

The originally calculated Z values of the weld metal are generally similar to the parent but the recalculated values are somewhat lower than the parent metal. This may be a more accurate reflection of actual Rp values and therefore the actual corrosion rates of the weld and parent metals.

9.3.4 Solution Resistance and Impedance

The R_{calc} is plotted against the inverse of the liquid film thickness, according to Equation 5.2, using the values of $Rp_{measured}$ and α in Equation 4.1 for the parent and weld metals. The plots in Figure 5.28 a, b and c are fairly linear and resemble the blue

line in Figure 9.2 although neither the data of the parent and weld passes through zero at 1 cm thickness, which might be considered bulk solution and the values of the weld metal are four times those of the parent metal. The alternative weld metal R_{calc} values are slightly larger still than those plotted because the $Rp_{measured}$ is larger than and α is similar to the parent metal values. As reflected in the results for the same electrode at ambient temperature, the short weld metal, relative to the infinitely long parent metal requires less applied current during LPR measurement to reach the far end of the electrode to the auxiliary in order to accomplish the specific potential change at the relevant RE. Therefore when the Rp is being measured in Ohm instead of Ohm cm^2 in this manner, more current is applied in order to change the potential at the reference so the potentiostat calculates lower interfacial impedance for the larger electrode.

9.3.5 Solution Conductivity

The solution conductivity was calculated using the original R_{calc} values using Equation 2.67 and plotted against the inverse of the liquid film thickness in Figure 5.29. The initial solution conductivity, prior to the immersion of the weldment electrode was 6.5 mS cm^{-1}.

The parent metal data gives conductivities of between 12 and 20 mS cm^{-1} over the three days and the weld metal data ranges between 2 mS cm^{-1} to just over 5 mS cm^{-1}. Similar calculated solution conductivities were calculated from the Standard weldment electrode experiment at ambient temperature.

There is uncertainty as to which of the sets of data are more accurate but the initial solution conductivity suggests that the weld metal values are not correct because they are too low and the recalculated R_{calc} would be even lower. It is probable that the parent metal values are more realistic reflection of the actual conductivities because the calculation is intended for infinitely long electrodes. The conductivity does not appear to show an increase with time indicating that the solution had already become saturated with corrosion products when the tests were performed.

9.3.6 Polarisation Curves

The area-corrected polarisation curves in Figure 5.30 indicate a greater anodic and cathodic current density for the parent metal than the weld metal. There is also

high solution resistance or restricted current density characterised by the flattening of the anodic curve of the parent metal at more noble potentials. The curves also indicate the more positive rest potentials of the weld and parent metals at 60 °C than of the same metal at ambient temperature. The weld metal is still the cathode also reflected by the uncoupled potentials (Table 5.14).

9.3.7 AC Impedance

Flattening is evident at the high-frequency part of the Nyquist plots of the weld metal at the four liquid film thicknesses (Figure 5.31 a), the same as that observed on the same electrode at ambient temperature. The measured impedance modulus, $|Z|_{meas}$, and the phase angles, ϕ, at all four thicknesses were calculated using the values that were estimated from the plots in Table 5.15 with Equations 9.2 and 9.3. The phase angles would be expected to be 45° in the high frequency linear response instead of 90° in a normal high frequency response.

Table 9.12 The impedance modulus and phase angle of the uncorrected Nyquist plots in Figures 5.31 and 5.32.

	LFT (cm)	$\|Z\|_{meas}$	ϕ
Weld Metal	1.0	53.23	37.62
	0.75	65.04	38.11
	0.5	62.73	39.55
	0.25	140.00	38.24

After correction was applied using the calculations Equations 9.4 and 9.5, the new points were re-plotted in Figure 9.9 a, b, c and d. R_{calc} (R), was taken from the modified LPR measurements on day 3 and Z_R, obtained from the difference between the high and low intercepts in the corrected plots (Z_R is equal to $(RZ)^{1/2}$).

It is clear from the true Z values, listed for each liquid film thickness in Table 9.13 below, that true Z is lower than those for the weld metal of the same electrode at ambient temperature because of the hastened kinetics at the metal surface. These results indicate higher corrosion rates than those given by the recalculated interfacial impedances in Table 9.11 above. Some of the corrected plots have larger than 90° phase angles, this is due to the estimation of the factors used to calculate $|Z|_{meas}$.

Table 9.13 (RZ) and R_{calc} from day 3, used to calculate true Z.

	Weld metal		
LFT (cm)	(RZ)	R_{calc} (Ohm)	Z (Ohm cm^2)
1	13421	353	38
0.75	14064	390	36
0.5	12647	460	27
0.25	40388	748	54

The parent metal impedance analysis was performed using Luggin 3 as the reference to study the effect of increasing applied potential with distance and decreasing liquid film thickness at a distance of 4 cm (x) away from the end of the electrode and the auxiliary. The small R_s and Z values in the complex plots in Figure 5.32 a, are a result of the increasing solution resistance with increasing distance away from the auxiliary electrode. Table 9.14 lists the results of applying Equations 9.7 and 9.8. The α values obtained for the parent metal at the different liquid film thicknesses on day 3 are used to calculate the actual voltage change at the parent metal at the end closest to the auxiliary so that the potential change at the parent metal measured with the reference at Luggin 3 is 10 mV.

$$y = 10\exp(-\alpha x) \qquad \textbf{9.7}$$

and

$$mV_{applied} = \left(\frac{10}{y}\right) \times 10 \qquad \textbf{9.8}$$

Table 9.14 The calculated applied potential on the parent metal when Luggin 3 is used as the reference.

Parent Metal			
LFT (cm)	α (Day 1)	y (4.0 cm)	$mV_{applied}$
1	0.3	3.01	33.20
0.75	0.38	2.19	45.72
0.5	0.66	0.71	140.13
0.25	0.95	0.22	447.01

y is the voltage change measured with the reference at Luggin 3 if only 10 mV was applied at the end of the electrode (with the reference at Luggin 6). The actual applied potential on the electrode is much larger than that measured with the reference at Luggin 3 therefore a larger overall current response is recorded giving lower R_s and Z values. The applied potential increases with the increasing solution resistance (distance from auxiliary electrode) with reduction in liquid film thickness.

a)

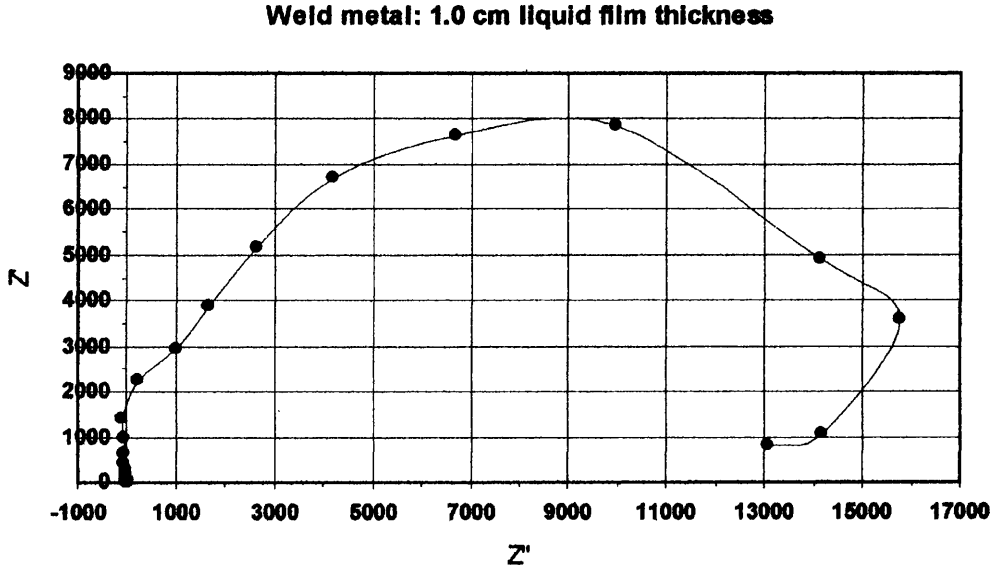

Figure 9.9 The corrected Nyquist plots for the weld metal from ac measurements at four liquid film thicknesses.

b)

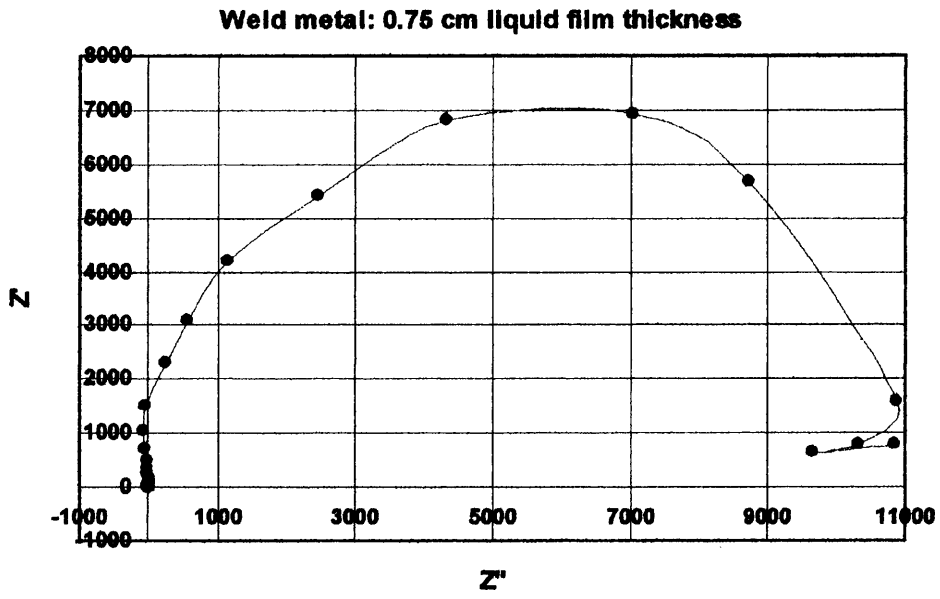

c)

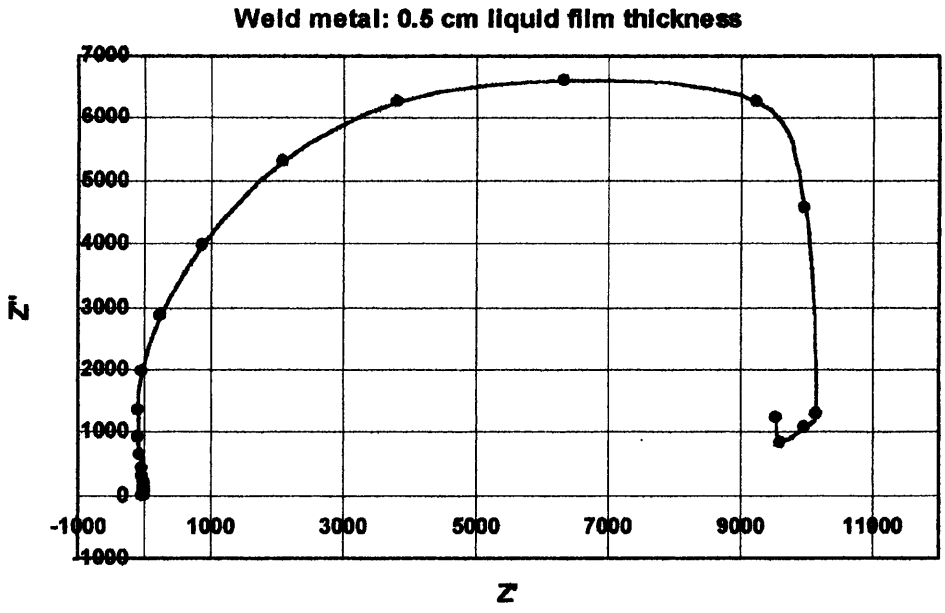
Weld metal: 0.5 cm liquid film thickness
7000
6000
5000
4000
3000
2000
1000
0
-1000
1000
3000
5000
7000
9000
11000
-1000
Ñ
Z'

d)

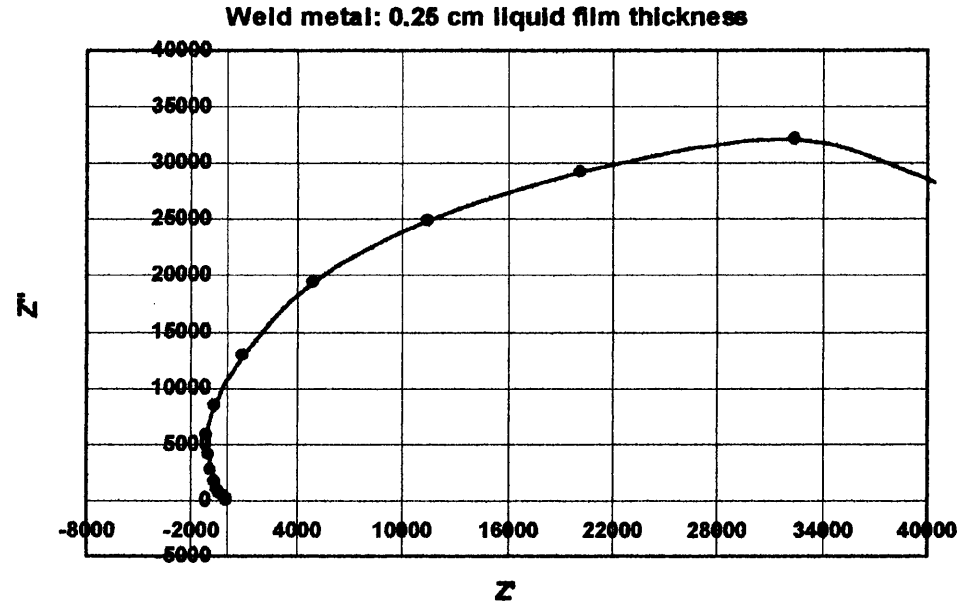
Weld metal: 0.25 cm liquid film thickness
40000
35000
30000
25000
20000
15000
10000
5000
0
-8000
-2000
4000
10000
16000
22000
28000
34000
40000
-5000
Ñ
Z'

10.0 Weld and Parent Metal Coupons – Ambient Temperature and 60° C

For these experiments, eight coupons with an area of approximately 1.0 cm^2 were used; four weld and four parent pipe metals. Coupled and uncoupled weld and parent metal samples were set up in pairs in 1L electrochemical cells immersed in CO_2 saturated 3.5% NaCl solution at ambient temperature and at 60° C. The coupling of the weld and parent metal coupons was switched after 14 days immersion. LPR tests and potential and galvanic monitoring was used to study the possible effects of coupling on individual metals. The total duration of the experiment was 470 hours (23 days) and all potentials are with reference to SCE.

Separately, the results of the SEM-EDX analysis will be discussed of weld and parent metal coupons that were examined after polishing to 1 μm with diamond paste, coupled at ambient temperature and again, after re-polishing, at 60° C.

10.1 The Appearance of the Weld and Parent Metals

After completion of the experiment, both of the weld metals that underwent testing at ambient temperature exhibited a dull, blackened corrosion product at the edges of the metal surface whilst the central area of the metal remained almost completely mirror-bright. The surfaces of both of the parent metals were more blackened with some uncorroded metal visible at the edges on the initially uncoupled parent and on the centre of the initially coupled parent metal surface.

The surfaces of all the coupons tested at 60° C were completely covered with a porous black layer, some of which had dissolved away from the metal surface in small patches on the initially coupled weld metal.

The blackened layer on the metals at ambient temperature is Fe_3C, cementite from the ferritic or martensitic phase. It is the same corrosion layer on the metals at 60° C in addition to $FeCO_3$ that is unlikely to deposit as a film on the metal surface at lower temperatures because insufficient Fe is present in the solution for it to become saturated with $FeCO_3$.

10.2 Coupled Potentials

At ambient temperature the potential of the initially coupled coupons decreased from –690 mV to -710 mV and remained around this value for the rest of the coupling (Figure 6.1). However at 60° C (Figure 6.3) the coupled potential is initially much lower and increases to around –720 mV. There is little difference in coupled potential between the initially coupled coupons at ambient temperature and the weld and parent metal when coupled after 14 days. At 60° C the initially uncoupled pair show an increasing potential. The short period of uncoupling each day to take measurements caused a slight vacillation in the coupled potential at ambient temperature, suggesting an effect on the coupled potential from uncoupling but the length of this effect is related to the duration of the uncoupling. At 60° C there appears to be no effect from uncoupling.

10.3 Galvanic Current

Where a negative galvanic current indicates a cathodic weld metal, the galvanic current at ambient temperature (Figure 6.2) of the initially coupled weld and parent coupon becomes negative after the first few hours and positive again but with a low value. The galvanic coupling of the second pair of electrodes reveals a current close to zero suggesting that there is little difference in composition between the weld and parent metals in general. At 60° C (Figure 6.4) the initial coupling increases in positive current, indicating an anodic weld metal, but the second coupling has a negative galvanic current, thus a cathodic weld metal but this current is decreasing and, speculatively, may become positive if the duration of the coupling experiment was longer.

10.4 Summary of Coupon Testing

10.4.1 Uncoupled Individual Potentials

The uncoupled individual potentials of the four coupons at ambient temperature (Figure 6.5) indicate that the initially coupled weld and parent coupons develop increasingly similar potentials with time and remain so after they have been uncoupled. The potential difference between the initially uncoupled weld and parent coupons was approximately 10 mV prior to coupling and they also appear to be tending towards similar individual potentials during the six days of coupling.

At 60° C (Figure 6.6) the potentials of the initially coupled weld and parent metals increase in by 30 mV and like the initially coupled coupons at ambient temperature, remain similar throughout the test. The initially uncoupled weld and parent metals generally have 5 to 10 mV difference but follow the same potential pattern and appear unaffected by coupling over the final six days.

The increase in metal surface reactions caused by elevated temperature is reflected by the initially lower potentials although for the final few days of the tests all potentials are around -700 mV, except the initially coupled coupons at 60° C which are just less than -710 mV. This may be due to the development of Fe_3C on the metal surface and a $FeCO_3$ film providing some degree of protection.

10.4.2 Linear Polarisation Resistance and Corrosion Rates

Unusually, at ambient temperature the initial Rp values measured for the weld metal coupons (Figure 6.7) are high compared to the parent metal values. However, the Rp of the initially coupled weld metal coupon does decrease dramatically during the 20 days from over 3000 Ohm cm^2 to just over 500 Ohm cm^2 and the initially uncoupled weld metal, also decreases but only from 3000 to 2000 Ohm cm^2.

The Rp value of the initially coupled parent metal is higher than the initially uncoupled parent metal but after approximately nine days this value reduced to around 200 Ohm cm^2, whilst the former remained at 150 Ohm cm^2. The reduction in Rp values may be a result of coupling. However little change was observed in the initially uncoupled weld and parent metals after coupling although this coupling was over a shorter length of time.

As expected, at 60° C (Figure 6.8) the Rp values are much lower than those at ambient temperature. The initially uncoupled weld and parent coupons had higher Rp values measured on day 1 than the coupled but then decreased quickly to relatively lower values. The weld metals generally have lower Rps than both parent metals - a reverse of the situation at ambient temperature both weld metals consistently have higher Rps than the parent metals. On day 17 the initially uncoupled weld Rp begins to increase to just over 90 Ohm cm^2 when the test is ended. This is a possible

indication of the effect of changing the metal from uncoupled to coupled and may be related to the formation of a protective film. The other coupons appear to develop similar Rp values to each other after day 16, which may also be an effect of coupling.

10.4.3 Corrosion Rates

The corrosion rates were calculated using the results from the individual Rp measurements in Figures 6.7 and 6.8. These values reflect the general increase in corrosion rate with immersion time for all metals at both temperatures. At ambient temperature (Figure 6.9) the maximum corrosion rate is 2.1 mm y^{-1} for the initially uncoupled parent metal at the end of the experiment and the minimum was 0.15 mm y^{-1} for the initially uncoupled weld metal at the beginning of the experiment and changed little throughout. The initially coupled weld and parent had similar corrosion rates, which may be an effect of long-term coupling. The weld metal is unlikely to have the highest corrosion rate of the two at ambient than at service temperature whether coupled or not.

The maximum corrosion rate of all four coupons at 60° C (Figure 6.10) is for the initially uncoupled weld metal on day 13 with a value of 5.2 mm y^{-1}, which subsequently decreases to just over 2 mm y^{-1}. This is possibly due to the rapid dissolution of ferrite, initially and exposing Fe_3C in the corrosion layer thus enabling a protective $FeCO_3$ to result from the Fe^{2+} saturated solution. From day 2 onwards, the corrosion rates of all the coupons are above 2 mm y^{-1} and all (except initially uncoupled weld) are between 3 and 4 mm y^{-1} at the end of the test, reflecting the higher corrosion rates at elevated temperature.

10.4.4 Polarisation Curves

The polarisation curves in Figure 6.11 a, b, c and d for the ambient temperature tests indicate a possible film breakdown on the initially uncoupled weld metal during the anodic polarisation at about –550 mV. The current changes from ~2 mA cm^2 to above 6 mA cm^2 at –480 mA cm^2 when it becomes similar to the parent metal instead of exhibiting high resistance. Some areas on the surface of the weld metal remained bright through the duration of the test and it is possible that more active areas galvanically protected these areas; this could be due to slight chemical or microstructural differences in the passes from weld fabrication.

10.4.5 AC Impedance

The solution resistance (R_s) obtained from the area corrected Nyquist plots in Figures 6.12, 6.13, 6.14 and 6.15 indicate that the solution was quite conducting, more so for the tests at 60° C because of the greater saturation of corrosion products. The impedance, Z, reflects the general values and trends of the LPR measurements, as do the capacitance and the corrosion current density for all coupons in Table 6.13. The corrosion rates highlight the slightly greater rates on days 7 and 8 than might be expected in the plot of corrosion rates calculated from the LPR measurements, this is due to the effect of the inclusion of solution resistance in polarisation resistance testing.

The polarisation curves were performed at the end of the experiment by which time the initially coupled weld metals at both temperatures had similar measured Rp values as the corresponding parent metal. It would appear from the anodic and cathodic polarisation curves that the parent metal had the greatest current density of the two metals at equivalent potentials. In general, the potentials of the weld metals are more noble than those of the parent metal and the coupons that were initially coupled have a slightly more negative potential than those that were initially uncoupled.

There is also the flattening of the curve at positive potentials because of solution resistance effects with high current densities.

10.5 The Calculated Galvanic Current

The galvanic current was calculated using Equation 10.1 below. The weld and parent metal individual Rp values and potentials for each day and the solution resistance, R_s obtained from the impedance measurements are used. The assumed distance of 4 cm between the coupons is for all of the coupon pairs, coupled and uncoupled.

$$ig = \frac{\Delta E}{(4 \times Rs) + (Rp_p + Rp_w)} \qquad \textbf{10.1}$$

The galvanic current plotted against time is shown in Figures 6.22 and 6.23 including the predicted current when coupons were uncoupled.

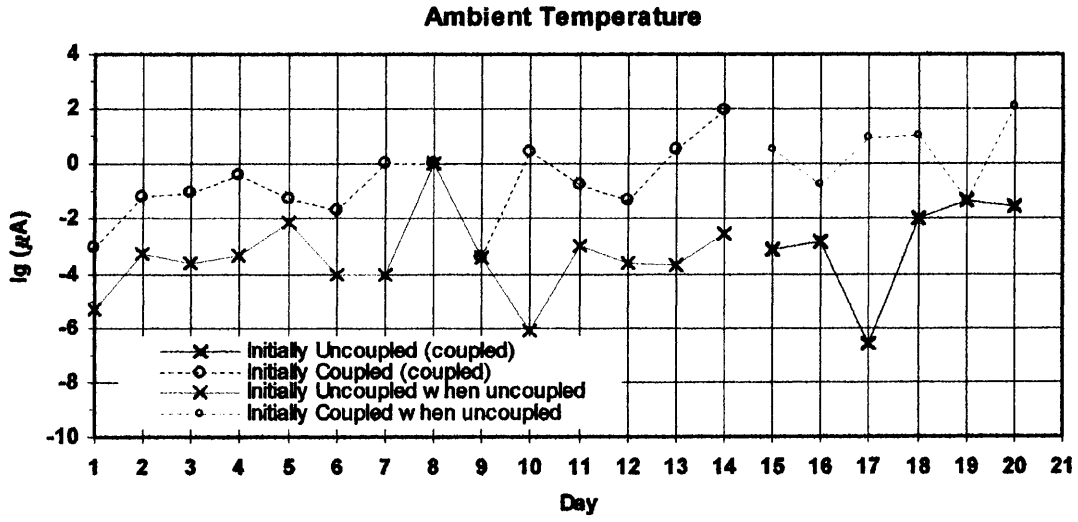

Figure 6.22 The calculated and predicted (lighter blue) galvanic current during coupling and uncoupling of weld and parent metal coupons at ambient temperature.

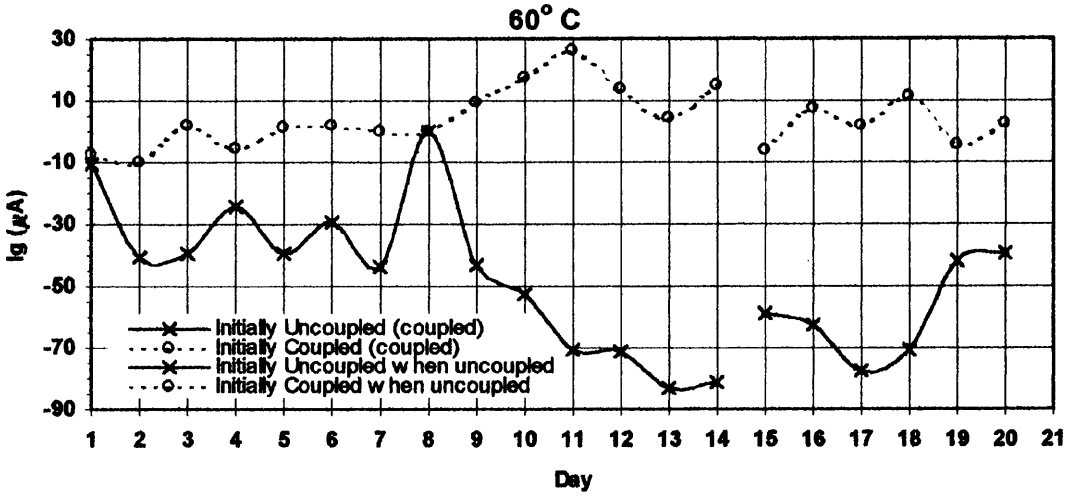

Figure 6.23 The calculated and predicted (lime) galvanic current during coupling and uncoupling of weld and parent metal coupons at ambient temperature.

10.5.1 Ambient Temperature

In comparison to the measured galvanic currents of the coupons in Figure 6.2, the calculated current of the initially coupled coupons at ambient temperature tend

towards a slightly negative or zero current instead of positive. The current generally becomes slightly more positive with time and after uncoupling the predicted current continues this trend.

The predicted galvanic current of initially uncoupled coupons is slightly more negative than that calculated for the coupled coupons. As with the measured galvanic currents, the initially uncoupled coupons have a more negative calculated galvanic current than the initially coupled coupons.

10.5.2 60° C

At 60° C the calculated galvanic currents are very similar to those measured in Figure 6.4. A possible effect of coupling on the behaviour of the metals is noticeable in that when uncoupled, the initially uncoupled pair are predicted to have an increasing negative galvanic current with time, indicating a cathodic weld metal. When they are coupled the measured and calculated galvanic current decreases from around –80 μA to -30 μA, suggesting that coupling altered the cathodic behaviour of the weld metal.

The predicted galvanic current of the initially uncoupled weld and parent metals is approximately –10 μA at the beginning of the experiment with the initially coupled pair have the same value from measurement and calculation. The galvanic current of the initially coupled coupons becomes increasingly positive with time indicating that in this coupling the weld metal is the overall anode. However, after uncoupling the current is predicted to reduce to less than 10 μA from a maximum of 30 μA. Therefore it may be possible that the weld and parent metals can revert to uncoupled characteristics once coupling has ceased.

It would appear that effects of coupling and uncoupling are more clearly observed at service temperature than at ambient temperature.

10.6 SEM EDX

The SEM-EDX images of weld and parent metal samples after polishing to 1 mm with diamond paste, immersion at ambient temperature and at 60° C are shown in Figures 6.16 a and b to 6.21 a, b and c.

The alloy additions to the Waveney weld and pipe steel are shown in Table 10.1 the values are taken from a chemical analysis using LECO Spectromat/GDS 750 after the failed weldments were removed from the spoolpiece.

Table 10.1 The chemical analysis of the weld and parent (pipe) metals in addition to Fe.[71]

%	C	Si	Mn	P	S	Cr	Mo	Ni	Cu	V
Weld	0.05	0.31	1.19	0.012	0.008	<0.01	0.01	0.85	0.02	<0.003
Pipe	0.15	0.32	1.39	0.015	<0.003	0.11	0.01	0.06	0.04	0.033

It is thought that the increasing concentration of Ni, Cu and C will increase the corrosion rate of the steel surface.

10.6.1 The Non-Corroded Surface

The amorphous black sites on the parent metal surface may be the sites of inclusions, marked *A* in Figure 6.17a, that have been removed during the polishing process and may have been MnS. It is clear from the spectrum and the composition table that Mn is present and S is found at 60° C post corrosion. The weld metal image (6.16a) shows what might to be sites of gas bubbles from the filler passes which are not present in the parent metal image.

All of the elements listed in Table 10.1 are detected in the EDX spectrum for the weld metal (6.16b) where the content is listed as 0.05 % and above. However the parent pipe spectrum (6.17 b and c) has only detected Mn, C, Si in addition to Fe and Mn, S and Ca at the site of the impurity.

10.6.2 Corrosion at Ambient Temperature

After 150 hours immersion in 3.5 % NaCl, CO_2 saturated water the surface of the weld metal (Figure 6.18a) appears to be less porous than the parent metal (Figure 6.19a) in the same conditions but has some larger features randomly sited on the surface instead of the uniform porosity found on the parent. There are small quantities of alloying elements detected by the EDX such as Cr, Mo, Mn and Cu (only in the weld spectrum, Figure 6.18b) but there is no signal for Ni in either the weld or parent metal spectra. There is a small signal for Si only present in the parent spectrum (Figure 6.19b). Cl is detected in both spectra from the solution and C and O are also present perhaps as small quantities of FeC_3 and $FeCO_3$ although the latter is unlikely to form in great quantities at ambient temperature. O may also be present from slight oxidation after the coupons were removed from the solution. The proportions of the metal surface composition of the parent and weld (Table 10.2) show that Ni is present in the weld metal but not the parent. It is present is lower quantities than stated in Table 10.1, this is possibly due to non-mixing between the filler passes or dilution leading to non-uniform Ni distribution across the weldment.

Table 10.2 Composition of the weld (in red) and parent metals detected by EDX.

Element	Elemental%	Atomic%
Si	0.37 / 0.33	0.74 / 0.66
Mn	1.68 / 1.39	1.7 / 1.41
Fe	98.04 / 97.76	97.65 / 97.44
Ni	0 / 0.51	0 / 0.49

10.6.3 Corrosion at 60° C

The surface of the weld metal (Figure 6.20a) appears to consist almost entirely of $FeCO_3$ crystals. The $FeCO_3$ has recrystalised on the FeC_3 layer due to a rise in pH and saturation of Fe^{2+} in the solution. The presence of Cr, Mn and Ni is detected by the EDX (Figure 6.20b), although no Cu is present in the spectrum after exposure to tests at this temperature. The Si concentration in the corrosion layer and on the metal surface of the weld and parent metals has increased substantially from the uncorroded state. The amorphous particle (B) on the parent metal visible in Figure 6.21a consists

mainly of Si, and has remained on the metal surface after the surrounding Fe has dissolved. It also contains C, O and small quantities of impurities and alloying elements (Figure 6.21b). The spectrum of the bare parent metal, *C* (Figure 6.21c), detects the presence of $FeCO_3$ and Mn, Cr, Ni, V, Al, s and Cl.

The $FeCO_3$ layer is patchier on the parent metal compared to the uniform coverage on the weld metal. The parent may have a less adherent film due to the presence of martensite which does not allow a $FeCO_3$ film to build up as rapidly as ferrite and pearlite. The weld metal most likely has a mainly ferrite-pearlite microstructure that promotes formation of the $FeCO_3$ film due to the quick accumulation of Fe^{3+} which provides good anchoring sites for the film and offers some protection. However there is little Cr remaining in the weld to stabilise the film.

The coupons were cut from various parts of the weld metal after sectioning; which may explain some of the differences in corrosion behaviour for two reasons;

1) There may be differences in composition in different weld metal due to mixing between different weld passes during fabrication. In the early runs where the root pass (absent in all the Waveney joint failures) and hot pass (also largely removed) would have contained 0.8% Ni and other elements, subjected to dilution by the parent metal. In effect, there would be gradients of alloying element of varying concentrations in directions into the weld and longitudinally across it.

2) It is possible that martensitic microstructures in the edges of the weld metal, next to the HAZ were present in some of the coupons hence increasing local corrosion rates.

11.0 Conclusions

1. From the results of the modified LPR and ac impedance measurements, the current and potential behaviour of a long electrode, with restricted solution thickness on the metals surface is similar to that of a porous electrode.[74, 75, 78]

2. Equation 2.81 is suitable for calculating potential distributions on an infinitely long electrode such as the parent metal but not a short electrode like the weld metal, with regards to the Waveney weldment electrodes. The calculated effective solution (R_{calc}) and the true polarisation resistance (Z_{calc}) are too high for the weld metal using this equation if compared with the values of the parent metal. The parent metal values may be prone to errors but they are a reasonable approximation.

$$e(x) = e_{0p}\exp(-\alpha_p x) \qquad \textbf{2.81}$$

3. Equations 2.76 and 9.2 can be used to obtain more representative and consistent values of Z_{calc} for the weld metal at varying liquid film thickness, but the R_{calc} values obtained by this method are relatively high and do not concur with those of the parent metal.

$$e_x = \frac{e_0.\cosh[-\alpha(x-l)]}{\cosh(\alpha l)} \qquad \textbf{2.76}$$

$$Rp_{measured} = \frac{\alpha Z}{\tanh(\alpha l)} \qquad \textbf{9.2}$$

Also, the galvanic current at different solution thicknesses can be calculated using Equation 2.79 and has been found to be concurrent with the measured galvanic current.

$$Ig = \frac{e_{0p}}{(RZ_p)^{\frac{1}{2}}}\tanh(al) \qquad \textbf{2.79}$$

4. Equation 2.81 was suitable for representing the potential behaviour of the weld and parent metal 1 in the Artificial weldment electrode. The cathodic weld metal has a higher corrosion rate than the parent, an approximate doubling of R_{calc} is demonstrated when the liquid film thickness is halved and the de-coupling effect on the weld and parent metals is apparent in measured coupled potentials. This experiment was more successful in comparison to the real weldment experiments because the electrolyte had high inherent solution resistance and a greater potential difference between the Artificial weld and parent metals thus confining current and potential distributions.

5. The Artificial weld and parent metal probably had a predictably uniform chemical and metallurgical composition, therefore the potential difference between them was quite distinct, whereas the Waveney weld metal was cut from the passes further into the weld because the root and hot passes had been preferentially removed in service. The root and hot passes may have contained different quantities of Ni, Cr, Cu and perhaps other alloying elements. Therefore the weld metal actually used in the electrodes may have differed only slightly from the parent pipe.

6. Generally, the individual potentials of weld and parent metal coupons became increasingly similar, after coupling together for long periods, an effect that appears to continue after permanent uncoupling. The Wide weldment electrode also displayed changes in the potential and galvanic current when the conductivity of the solution was increased, enabling the previously "uncoupled" weld metal centre to be included in galvanic behaviour with the parent metal.

7. The measured galvanic current was negative for most experiments, indicating that the weld metal was the cathode of the weld and parent metal couple. However, the weld and parent metals in the Standard weldment electrode did appear to change polarity during experiments. The galvanic current switched from negative to positive during monitoring at ambient temperature and at 60° C the current behaved in the reverse manner to this.

8. At ambient temperature, the parent metal coupons generally had higher corrosion rates than the weld metal coupons though the opposite occurred in tests at 60° C.

11.1 Recommendations for Further work

1. Similar liquid thickness tests should be performed in flowing conditions because potentials will differ from those obtained in static tests.

2. If the solution is refreshed there will not necessarily be saturation of corrosion products. This will promote a stable conductivity and prevent any protection offered by corrosion products depositing on the metal surface, which might not happen in the service environment.

3. The plots of galvanic current against time for the coupons (Figures 6.2 and 6.4) indicate that a polarity change occurs between ambient temperature and 60° C. It may be possible to perform tests at temperatures between these points to establish a critical temperature at which this change occurs.

4. The chloride content of the Waveney solution increased the electrolyte conductivity compared with the solution used in the Artificial weldment electrode experiment. But it is unclear whether increasing Cl^- concentration actually raises the intrinsic corrosion rates of low-alloy steels. Simple tests may clarify the effect of Cl^- on charge transfer resistance.

5. The effect of lowering or increasing the amount of Ni in steel should be analysed with regard to potential, corrosion rate and the galvanic current when coupled to the parent metal.

6. Long-term tests using unsegmented weldments in a solution that is held at low liquid film thickness. If the individual potentials and Rps of the metals are known and the solution resistance of the electrolyte, the galvanic current and sites of preferential attack can be predicted. These results can be compared to the results of a physical examination using a microscope or resin to observe the depth of attack of the long-term tests.

12.0 References

1. Fontana, M. G., Greene, N. D., "Corrosion Engineering." 3rd edition. McGraw-Hill. 1986.
2. Atkins, P. W. "Physical Chemistry." 5th edition. Oxford University Press. 1994.
3. Pourbaix, M. "Atlas of Electrochemical Equilibria in Aqueous Solutions." 2nd English edition. NACE, Houston, TX. 1974.
4. Bard, A.J., Faulkner, L,R. "Electrochemical Methods." John Wiley and Sons. 1980.
5. Wagner, C., Traud, W. Electrochem. Vol. 44. p.391. 1938.
6. Shreir, L.L., Jarman, R.A., Burstein, G.T. "Corrosion; Metal / Environment Reactions." 3rd Edition. Vol. 1. Butterworth-Heinemann Ltd. Oxford. 1995.
7. Stern, M. "A Method for Determining Corrosion Rates from Linear Polarisation Data." Corrosion. NACE. Vol.14. 1958.
8. Brown, R. H., Mears, R. B. " The Electrochemistry of Corrosion." Trans. Electrochem. Soc. 1938.
9. Baboian, R. "Predicting Galvanic Corrosion Using Electrochemical Techniques."
10. Cottis, R. A., Turgoose, S. "Electrochemical Noise and AC Impedance." Awaiting publication.
11. Kermani, M. B., Smith, L. M. (Eds.) "CO_2 Corrosion Control in Oil and Gas Production." Design Considerations. Fed. of Corr. Publications No. 23, Inst. of Mat. Book no. 688. 1997.
12. Kern, D. M. "The Hydration of Carbon Dioxide." J. Chem. Ed. 37. January 1960.
13. De Waard, C., Milliams, D. E. "Carbonic Acid Corrosion of Carbon Steel." Corrosion. NACE International. Volume 31, No. 5. P 177. May 1975.
14. Schmitt, G., Rothmann, B. "Studies on the Corrosion Mechanism of Unalloyed Steel in Oxygen-Free Carbon Dioxide Solutions." Part 1. "Kinetics of the Liberation of Hydrogen." Werkstoffe und Korrosion., Volume 29. (1978) in "CO_2 Corrosion in Oil and Gas Production – Selected Papers, Abstracts and References." Newton, L. E., Hausler, R. H. (Eds.). NACE T13. NACE International. 1984.

15. Crolet, J. L., Thevenot, N., Nesic, S. "Role of Conductive Corrosion Products in the Protectiveness of Corrosion Layers." Corrosion - Vol. 54, No. 3. March 1998. NACE International.
16. Ikeda, A., Mukai, S., Ueda, M. "Prevention of CO_2 Corrosion of Linepipe and Oil Country Tubular Goods." Paper no. 289. CORROSION 84. NACE International. 1984.
17. Dugstad, A. "The Importance of $FeCO_3$ Supersaturation on the CO_2 Corrosion of Carbon Steels". Paper no. 14. CORROSION 92. NACE International. 1992.
18. Ikeda, A., Ueda, M., Mukai, S. "CO_2 Corrosion Behaviour and Mechanism of Carbon Steel and Alloy Steel." Paper no. 45. CORROSION 83. NACE International. 1983.
19. De Moraes, F. D., Shadley, J. R., Chen, J., Rybicki, E. F. "Characterisation of CO_2 Corrosion Product Scales Related to Environmental Conditions." Paper no. 30. CORROSION 2000. NACE International. 2000.
20. Videm, K., Dugstad, A. "Effect of Flow Rate, pH, Fe^{2+} Concentration and Steel Quality on the CO_2 Corrosion of Carbon Steel." Paper no. 42. CORROSION 87. NACE International. 1987.
21. Dugstad, A., Lunde, L., Videm, K. "Influence of Alloying Elements upon the CO_2 Corrosion Rates of Low-Alloyed Carbon Steels." Paper no. 473. CORROSION 91. NACE International. 1991.
22. Kimura, M., Saito Y., Nakano, Y. "Effects of Alloying Elements on Corrosion Resistance of High Strength Linepipe Steel in Wet CO_2 Environments." Paper no. 18. CORROSION 94. NACE International. 1994.
23. Crolet, J. L., Olsen, S., Wilhelmsen., W. "Influence of a Layer of Undissolved Cementite on the Rate of Corrosion of Carbon Steel." Paper no. 4. CORROSION 94. NACE International. 1994.
24. Videm, K., et al. "Surface Effects on the Electrochemistry of Iron and Carbon Steel Electrodes in Aqueous CO_2 Solutions." CORROSION 96. Paper No. 1.,NACE International. 1996.
25. Schmitt, G., Engels, D. "SEM/EDX Analysis of Corrosion Products for Investigations on Metallurgy and Solution Effects in CO_2 Corrosion." CORROSION 88. Paper No. 149. NACE International. 1988.
26. Cross, D. E. "Mesa-Type CO_2 Corrosion and its Control." CORROSION 93. Paper No. 118. NACE International. 1993.

27. Ueda, M., Ikeda, A. "Effect of Microstructure and Cr Content in Steel on CO_2 Corrosion." Paper no. 13. CORROSION 96. NACE International. 1996.
28. Takabe, H., Ueda, M. "The Formation Behaviour of Corrosion Films of Low Cr Bearing Steels in CO_2 Environments." Paper no. 1066. CORROSION 2001. NACE International. 2001.
29. Palacios, C. A., Shadley, J. R. "Characteristics of Corrosion Scales on Steels in a CO_2-Saturated NaCl Brine." Corrosion - Vol. 47, No. 2. February 1991. NACE International.
30. Takabe, H., Ueda, M. "Effect of Environmental Factors and Microstructure on Morphology of Corrosion Products in CO_2 Environments." Paper no. 13. CORROSION 99. NACE International. 1999.
31. Heuer, J. K., Stubbins, J. F. "Microstructure Analysis of Coupons Exposed to Carbon Dioxide Corrosion in Multiphase Flow." Corrosion - Vol. 54, No. 7. NACE International. July 1998.
32. Al-Hassan, S., Mishra, B., Olson, D. L., Salama, M. M. "Effect of Microstructure on Corrosion of Steels in Aqueous Solutions Containing Carbon Dioxide." Corrosion - Vol. 54, No. 6. NACE International. June 1998.
33. Crolet, J. L. "Which CO_2 Corrosion, Hence Which Prediction?", "Progress in the Understanding and Prevention of Corrosion." Vol. 1. Inst. of Mat. For the Soc. Espanola de Quimica Industrial on behalf of Eur-Fed. Of Corr. Costa, J. M., Meier, A. D. (Eds). UK. 1993.
34. Chitwood, G. B., Hilts, R. L. "A Case History Analysis of Using Plain Carbon and Alloy Steel for Completion Equipment in CO_2 Service." Paper no. 20. CORROSION 94. NACE International. 1994.
35. Schmitt, G., Mueller, M., Papenfuss, M. "Understanding Localized CO_2 Corrosion of Carbon Steel from Physical Properties of Iron Carbonate Scales." Paper no. 38. CORROSION 99. NACE International. 1999.
36. Videm, K. "The Influence of the State of the Surface on the Electrochemistry of Iron and Steel Electrodes in Aqueous CO_2 Solutions." 335, p. 235 – 240. Surface Science. 1995.
37. Paisley, D., Barrett, N., Wilson, O. "Pipeline Failure: The Roles Played by Corrosion, Flow and Metallurgy." Paper no. 18. CORROSION 99. NACE International. 1999.

38. Schmitt, G., Gudde, T., Strobel-Effertz, E. "Fracture Mechanical Properties of CO_2 Corrosion Product Scales and Their Relation to Localised Corrosion." Paper no. 9. CORROSION 96. NACE International. 1996.
39. Burke, P. A., Hausler, R. H. " Assessment of CO_2 Corrosion in the Cotton Valley Limestone Trend." CORROSION 84. Paper no. 288. NACE International. 1984.
40. Hausler, R. H., Garber, J. D. "The COPRA Correlation Revisted." CORROSION 90. Paper no. 45, NACE International. 1990.
41. Daniel, B. "Corrosion of Carbon Steel Welds." Winfrith., UK Atomic Energy Authority. 1988.
42. Easterling, K. "Introduction to the Physical Metallurgy of Welding." Butterworths and Co. 1983.
43. Garverick, L. (Ed.). "Corrosion in the Petrochemical Industry." ASM International. The Materials Information Society. December 1994.
44. Palmer, J. W., Dawson, J. L., Fowler, C. M., Dicken, G. "Challenges for Corrosion Inhibition." Capcis Ltd. IIR Conference "CORRPIPE '96". 1996.
45. Rothwell, A. N. "Weld Corrosion: Causes and Solutions." Corrosion Prevention and Control. October 1992.
46. Robinson, J. L. "Preferential Corrosion of Welds." The Welding Institute Research Bulletin. January 1979.
47. Backman, G., Leimalm, A., Lundin, S. "Corrosion Resistance of High Tensile Steel Ships." Svetsaren English Edition. (2-3 1971). 2.
48. Uusitalo, E. "Effect of Flow Rate on the Galvanic Corrosion of Low-Carbon Steels in Seawater." Corrosion, Volume 17. 1961.
49. Rasanen, E., Relander, K. "Development of Shipbuilding Steel Plates for Use on Arctic Seas." Scandinavian Journal of Metallurgy. Volume 7. 1978.
50. Alasaarela, P., Saarinen, A. "The Effect of Carbon, Manganese and Silicon on the Austenite Content of the Heat-Affected Zone in Structural Steels." Scandinavian Journal of Metallurgy. Volume 1. 1972.
51. Saarinen, A., "The Effect of Microstructure on the HAZ Corrosion of Shipbuilding Steel." Trans. ISIJ. Volume 11. 1971.
52. Lundin, S., Utterberg, B. "The Influence of Microstructure on the Corrosion Resistance of Welded Structural Steels." Svetsaren in English. Volume 4. 1968.

53. Rothwell, A. N., Dawson, J. L., Eden, D. A., Palmer, J. W. "Interpreting Electrochemical Impedance Spectra from Segmented Electrode Arrangements." Electrochemical Impedance Analysis and Interpretation. Scully, Silverman and Kendig (Editors). ASTM. March 1993.

54. Joosten, M. W., Kolts, J., Humble, P. G., (Conoco Ltd), Marlow, J., (Marshall Marlow Assoc. Ltd), "Aspects of Selective Weld and HAZ Attack in CO_2 Containing Production Environments." Paper No. 79. CORROSION 96. NACE International. 1996.

55. Stegman, D. W., et al. "Laboratory Studies on Flow Induced Localised Corrosion in CO_2/H_2S Environments, 1) Development of Test Methology." CORROSION 90. Paper No. 5. NACE International. 1990.

56. Jasinski, R., "Corrosion of N80-Type Steel by CO_2/Water Mixtures." CORROSION 87. Paper No. 4. NACE International. 1987.

57. Joosten, M. W., Payne, G. "Preferential Corrosion of Steel in CO_2 Containing Environments." Paper No. 211. CORROSION 88. NACE International. 1988.

58. Savva, G. C., Weatherly, G. C., Aust, K. T. "Heat-Affected Zone Corrosion Behaviour of Carbon-Manganese Steels." *Corrosion Engineering.* Corrosion, Volume 45, No. 3. NACE International. March 1989.

59. Alhajji, J. N., Reda, M. R. "The Effect of Alloying Elements on the Electrochemical Corrosion of Low-Residual Carbon Steels CO_2-Saturated Brine." *Corrosion Science,* Vol. 34, No. 11, pp. 1899-1911. 1993.

60. "Preferential Corrosion of Carbon Steel Weldments in Oil and Gas Production Systems." TWI and Capcis report. 1989.

61. Backman, G., Leimalm, A., Lundin, S. "Corrosion Resistance of High Tensile Steel Ships." Svetsaren English edition. (2-3 1971). 2.

62. Nice, P. I., Takabe, H., Ueda, M. "The Development and Implementation of a New Alloyed Steel for Oil and Gas Production Wells." CORROSION 2000, Orlando, Florida. Paper no. 154. NACE. 2000.

63. Denpo, K., Ogawa, H. "Effects of Nickel and Chromium on Corrosion Rate of Linepipe Steel." Corrosion Science. Vol. 35. No. 1-4. p. 285-288. 1993.

64. Kimura, M., Saito, Y., Nakano, Y. "Effects of Alloying Elements on Corrosion Resistance of High-Strength Linepipe Steel in Wet CO_2 Environments." CORROSION 94, Paper no. 18. NACE International. 1994

65. Kermani, M.B., Gonzales, J. C., Linne, C., Dougan, M., Cochrane, R. "Development of Low Carbon Cr-Mo Steels with Exceptional Corrosion Resistance for Oilfield Applications." CORROSION 2001. Paper No. 1065. NACE International. 2001.

66. Gainer, L., Wallwork, G. R., "Effect of Alloy Element Additions on the Pitting Corrosion of Mild Steel." Corrosion. Vol. 36. No. 7. July. 1980.

67. Sydberger, T., Edwards, J. D., Bjørnøy, O. "Modes of CO_2 Corrosion Damage: Consequences for Corrosion Control Strategies." CORROSION 96. Paper No. 28. NACE International. 1996.

68. Krijgsman, A. D. "Metallurgical Aspects of Preferential Weld Attack of Carbon Steels in CO_2 Environments." June 1996.

69. Rahn, H. N., Mayer, E. H., Frame, J. W., J. of Amer. Ceramic Society. Vol. 45. p. 581. 1962.

70. Waveney Weld Corrosion Investigation Preliminary Inspection Photographs, Line No. –6"-GP-F6-1001. Arco British Ltd. June 1999.

71. Investigation of Root Weld Corrosion. ASAMS Test Report. ASAMS Ltd. June 1999.

72. Palmer, J. W. Risk of Preferential Weldment Corrosion of Ferritic Steels in CO_2-Containing Environments. Review. The Sponsor Group. Nov. 2000.

73. Abou-Zour, M. Risk of Preferential Weldment Corrosion of Ferritic Steels in CO_2-Containing Environments. Progress Report 2. The Sponsor Group. May 2001.

74. De Levie, R. "On Porous Electrodes in Electrolyte Solutions." Electrochimica Acta. Vol. 8, p.751 – 780. 1963.

75. De Levie, R. "On Porous Electrodes in Electrolyte Solutions – IV." Electrochimica Acta. Vol. 9, p.1231 – 1245. 1964.

76. MacDonald, D. D., McKubre, M. C., Urquidi-MacDonald, M. Corrosion, Vol. 44. No. 2. 1988.

77. Issacs, H. S., Davenport, A. J. J. Electrochem. Soc. 137, 2196. 1990.

78. De Levie, R. "Electrochemical Response of Porous and Rough Electrodes." Advances in Electrochemistry and Electrochemical Engineering. Vol. 6. Delahay, P., Tobias, C. W. (Eds). Wiley. 1967.

79. Hampson, N. A., McNeil, A. J. S. "The Electrochemistry of Porous Electrodes: Flooded, Static (Natural) Electrodes." Electrochemistry. Vol. 8. Specialist Periodical Reports. RSC. 1983.
80. Candy, J-P., Fouilloux, P., Keddam, M., Takenouti, H. "The Characterisation of Porous Electrodes by Impedance Measurements". Electrochimica Acta. Vol. 26, p.1029 – 1034. 1981.
81. Test Certificate. C&S Steels. Wolverhampton Ltd.
82. Analysis of Waveney (Produced) Water from the Test Specimen. SGS. Sept. 1999.